James Henry Barrington

Design and fabrication of optical fibre long period gratings for CO_2 sensing

PhD Thesis

2018

James Henry Barrington

Design and fabrication of optical fibre long period gratings for CO_2 sensing

Centre for Engineering Photonics
School of Aerospace, Transport and Manufacturing

PhD Thesis

Academic Years :	2015 to 2018
Supervisors:	Prof. Stephen W. James
	Dr. Matthew Partridge
	Prof. Ralph P. Tatam
Submission:	June 2018

This thesis is submitted in partial fulfilment of the requirements for the Degree of Doctor of Philosophy

Abstract

This thesis investigated the repeatability of the overwrite long period grating (LPG) fabrication method and highlighted the advantage it offers in its ability to tune spectral features thus allowing the manufacture of bespoke sensors. Moreover, LPGs with periods ranging from 100 - 200 μm were written and a novel technique for mapping the transmission data was presented. This method gave a unique overview into the period mediated evolution of attenuation features, which, when designing LPGs that operate at the sensitive phase matching turning point, is invaluable. Further exploration into the overwrite method revealed that the UV irradiation duty cycle used in the fabrication of LPGs was found to influence the presence of harmonics, where a duty cycle of 25% maximised coupling to 2^{nd} order transmission features. LPGs which possessed these additional spectral features within a small wavelength range (600 - 1000 nm) were assessed for their suitability in performing multi-parameter sensing.

Ionic liquids were explored as an LPG CO_2 sensitive coating. It was shown that these materials demonstrate a refractive index change upon exposure to CO_2 which was maintained following mechanical stabilisation using a gelling agent. A coating system for applying the gelled ionic liquid to the surface of an optical fibre was developed and techniques to improve the coating deposition were explored. The sensor demonstrated an 8 nm wavelength shift in response to 20% CO_2, which was reversible by reducing the partial pressure of CO_2 for 25 min.

Acknowledgements

Firstly, I would like to thank Ralph Tatam for taking a chance on me, without which, I would not have had the pleasure (and occasional frustration) to undertake this work. His experience and knowledge of the PhD process has been invaluable throughout. I am also indebted to Matt Partridge and Steve James for their expertise and enthusiasm, and for allowing me to occupy large chunks of their time discussing anything from the fundamentals of long period gratings to the state of English cricket.

I would like to express my appreciation to all the Engineering Photonics staff who were always happy to help and regularly brought delicious cake to coffee breaks. I am also grateful to Steve Staines for his practical expertise during the fabrication of equipment used in my experiments and for the numerous chats about woodworking.

It is fair to say that this experience would not have been the same without my fellow PhD students. Their help, general conversation, and multiple Tequila nights made my time as a student even more enjoyable.

Personally, I would also like to thank my family for their endless support and providing a feast whenever I visited. And finally Fiona, for being an eternal optimist and always listening to (tolerating) needlessly long-winded ramblings when things weren't going to plan.

Contents

List of Figures

List of Tables

List of Acronyms

$[BF_4]$	Tetrafluoroborate
[Bmim]	1-butyl-3-methylimidazolium
$[C_6mim][Tf_2N]$	1-hexyl-3-methylimidazolium bis(trifluoromethylsulfonyl)imide
$[PF_6]$	Hexaflourophosphate
AMPS	(3-Aminopropyl)trimethoxysilane
CO_2	Carbon dioxide
CRDS	Cavity ringdown spectroscopy
ESA	Electrostatic self-assembly
eSEM	Environemntal scanning electron microscopy
FBG	Fibre Bragg grating
FET	Field effect transistor
IPA	Isopropyl alcohol
LB	Langmuir-Blodgett
LMOG	Low molecular-weight organic gelator
LoD	Limit of detection
LP	Linearly polarised cladding mode
LPG	Long period grating
MOF	Metal organic framework
MOS	Metal oxide semi-conductor
NDIR	Non-dispersive infrared

OMS	Ordered mesoporous silica
OSA	Optical spectrum analyser
PCF	Photonic crystal fibre
PEI	Polyethylenimine
PMTP	Phase matching turning point
RIU	Refractive index units
SA	Synthetic air
SBU	Secondary building unit
SD	Standard deviation
SiO_2	Silica nano-particles
TDLAS	Tuneable diode laser absorption spectroscopy
TNBSA	2,4,6-trinitrobenzene sulfonic acid

List of Symbols

A	Generic environmental parameter	145
A_f	Optical fibre cross-sectional area	135
$A(\lambda)$	Absorbance	17
$A_{vj,i}$	Arbitary field constant	37
B	Generic environmental parameter	145
b	Gradient of calibration curve	205
β	Propagation constant	33
$\boldsymbol{\lambda}$	Wavelength determination matrix	147, 148
$B_{vj,i}$	Arbitary field constant	37
C	Gas concentration	17
c	Speed of light in vacuo	33
C_{bulk}	Fractional concentration of bulk sucrose solution	138
C_{exp}	Expected sucrose concentration	138
CI	Confidence intervals	138
C_n	Condition number	145
$\boldsymbol{C_v}$	Generic Bessel function	37
$\boldsymbol{C'_v}$	Derivative of generic Bessel function	37
D	Deposition solution's physio-chemical characteristics	73
Δ	Determinant of $\mathbf{K}$	147, 148
δA	Error in measuring environmental parameter A	147, 148
δB	Error in measuring environmental parameter B	148
δK	Errors within $\mathbf{K}$	147
$\Delta\lambda_i$	Change in central wavelength of resonance band i	145
$\delta\lambda_i$	Wavelength measurement precision of attenuation band i	148
Δ^*	Determinant of $\mathbf{K}$ errors	148

δ_{iA}	Standard error of the matrix coefficient for attenuation band i and environmental parameters A	148
δ_{iB}	Standard error of the matrix coefficient for attenuation band i and environmental parameters B	148
$\delta\lambda$	Errors in determining wavelength	147
$\boldsymbol{D_v}$	Generic Bessel function	37
$\boldsymbol{D'_v}$	Derivative of generic Bessel function	37
E	Rate of evaporation experienced by deposition solution	72
ϵ	Axial strain	42
η_g	Ionogel viscosity	183
E_v	Cell volatge	15
F	Faraday's constant	15
f	frequency	33
G	Young's modulus of silica glass	135
g	Gravitational acceleration	135
$\gamma_{vj,i}$	Magnitude of transverse wavenumber	37
γ_g	Ionogel surface tension	183
h_0	Deposition thickness	72
$I_B(\lambda)$	Baseline spectrum wavelength associated intensity	110
I_v	Modified Bessel function of the first kind	37
$I_F(\lambda)$	Final spectrum wavelength associated intensity	110
J_v	Ordinary Bessel function of the first kind	37
$\mathbf{K}$	Sensor characteristic matrix	145, 147, 148
k	Wavenumber	33
k_0	Wavenumber in free space	33
κ_i	Coupling constant for the ith mode	34
K_v	Modified Bessel function of the second kind	37
k_i	Solution composition constant	72
K_{iA}	Coefficient of environemntal parameter A for resonance band i	145, 148

K_{iB}	Coefficient of environemntal parameter B for resonance band i	145, 148
$\|\mathbf{K}\|$	Norm of matrix $\mathbf{K}$	145
$\|\mathbf{K}^{-1}\|$	Inverse norm of matrix $\mathbf{K}$	145
K_T	True value of $\mathbf{K}$	147
L_g	Grating length	34
L	Optical path length	17
Λ	LPG period	34
λ_0	Wavelength in free space	33
λ_i	Combined wavelength shift of attenuation band i in response to environmental parameters A and B	148
λ_T	True wavelength value	147
$\lambda_{(x)}$	Resonance band central wavelength	34
m	Mass	135
$M_{i,i+i}$	Waveguide matrix	38
N	Order of diffraction	34
n	Generic refractive index	33
n_1	Core refractive index	31
n_2	Cladding refractive index	31
n_3	Surrounding refractive index	33
$n_{clad(x)}$	Cladding effective refractive index for xth cladding mode	34
n_{core}	Core's effective refractive index	34
n_e	Number of electrons	15
n_i	Refractive index of dielectric layer i	37
Φ_v	Azimuthal component of the electric field	37
ϕ	Azimuthal angle	37
$\Psi_{vj,i}$	Wave function	37
Q_i	Q_i transfer matrix factor	38
$R_{vj,i}$	Radial component of the electric field	37
r	Radial distance	37

R_c	Gas constant	15
ρ_g	Ionogel density	183
SE	Standard error	139
$\sigma(\lambda)$	Gas absorption coefficient	17
S_w	Substrate width	73
T	Temperature	40
θ_c	Critical angle	32
T_i	Transmission loss of resonance band associated with ith mode	34
t_{n-1}	Two tailed t-value	139
$U_{vj,i}$	Transverse electric field	37
u	Withdrawal speed	73
v	Positive arbitrary azimuthal number	37
V_{dose}	Cumulative dose volume	138
V_{samp}	Cumulative sample volume	138, 139
V_{wt}	Initial volume of water	138
$\bar{x}$	Mean dose %	139
Y_v	Ordinary Bessel function of the second kind	37

Chapter 1

Introduction

The ability to detect carbon dioxide (CO_2) is of vital importance in numerous situations, ranging from patient health monitoring (capnography) [1] to environmental research [2], and ensuring safe working conditions during industrial procedures [3]. This is often performed with commercial devices based on non-dispersive infrared (NDIR) [4, 5] or electrochemical processes [6]. Although these techniques are well suited to many of the environments previously mentioned, situations that require remote sensing or necessitate electrical isolation would render these methods inappropriate. Furthermore, in certain situations, an array of sensors is desirable, where either the devices operate synergistically (simultaneously measuring parameters which interfere with the analyte of interest) or are designed to detect a number of separate analytes. Typically, this requires a substantial container in which to house the numerous sensing elements, therefore making multi-parameter detection with these devices impractical in circumstances where space or weight is limited. It is in these situations that optical fibre sensors can provide an attractive solution.

1.1 Optical fibre sensors

Optical fibres have revolutionised communication technology allowing the transfer of high data rates over long distances with minimal signal losses. Furthermore, unlike their copper counterparts, optical fibres are relatively immune to electromagnetic interference and, due to their ability to transfer larger bandwidths, generally require less space [7]. It is these attributes that stimulated research into the use of optical fibres as a sensing medium. The ever-growing interest in fibre-based sensors can be clearly seen, where a basic Scopus search for "Optical Fiber Sensor" reveals that over 60% more articles were published in 2017 (3111) than in 2007 (1913).

The types of fibre sensor available vary from point-based elements, which include inline-interferometers (Mach-Zehnder, Michelson, Fabry-Perot) and fibre gratings, to distributed fibre sensors employing time- and frequency-domain reflectometry (Brillouin and Raman scattering) [8].

Although numerous optical fibre sensing methods exist, the ability to detect CO_2 requires the transmitted light to interact with the environment in which the gas is present. One method commonly used to achieve this is to alter the physical properties of the fibre by removing the cladding through etching or tapering [9]. Both of these fibre sensing methods have been successfully implemented for the detection of chemical and biological species [10, 11]. Nevertheless, a reduction in cladding material significantly increases the fragility of the sensing device and the fabrication process used to create these modified-fibre elements is often difficult [9, 12].

Gratings offer another technique in which to adapt optical fibres to facilitate modal interactions with the surrounding environment. Unlike devices that require a portion of the cladding to be removed, fibre gratings can be formed without the need to significantly disrupt its structure. Furthermore, they offer the potential for multiplexing along a single optical fibre using wavelength division multiplexing [13, 14]. These in-fibre elements are comprised of periodic changes to the refractive index of the fibre's core and are generally classified into two basic types defined by the periodicity of the grating, namely, fibre Bragg gratings (FBGs) and long period gratings (LPGs) [15]. FBGs have periods which are typically sub-micron and act to promote back-reflected core modes at a wavelength that matches the Bragg condition [16], while LPGs possess longer periods in the order of hundreds of micrometres and act to couple core guided light to forward propagating cladding modes [17] (Fig. 1.1).

Through the use of gratings, changes in the fibre's properties (physical elongation, refractive index variation) induced by external parameters (temperature, strain, surrounding refractive index etc.) are translated into properties of light that can be measured, including, wavelength, intensity and phase [18]. Fibre-based chemical sensing generally requires the environment surrounding the fibre to be monitored. While LPGs are inherently sensitive to perturbations in refractive index surrounding the fibre [19], FBGs are not, and therefore must be inscribed at an angle relative the fibre's axis, named tilted FBGs, to augment this form of sensing [20]. Furthermore, LPGs demonstrate superior sensitivities with values up to 10^4 nm·RIU^{-1} (where RIU stands for refractive index unit) in comparison to 10^2 nm·RIU^{-1} observed in tilted FBGs [21]. Moreover, since LPGs are created using longer periods, the fabrication process allows for gratings with unusual periods and structures to be

created permitting them to be altered for specific purposes [22, 23].

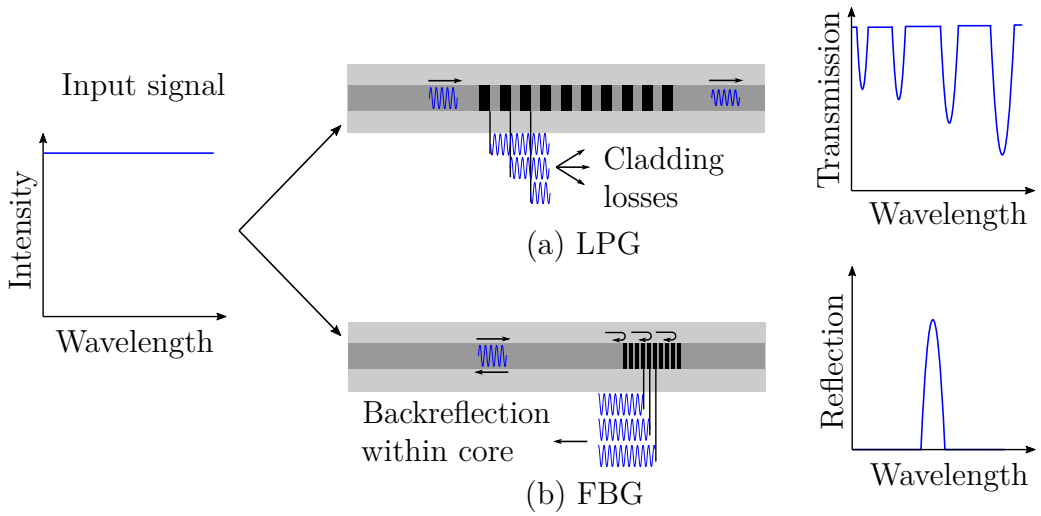

Figure 1.1: Operating principle of an LPG (a), where each modulation produces discrete wavelengths to couple into the cladding resulting in multiple attenuation bands in the transmission feature and an FBG (b), where each refractive index modulation (dark bands) causes back-reflections resulting in a detectable reflected peak. Adapted from [13]

The greatest drawback of LPGs is that they are also inherently sensitive to temperature, strain, and bending, thus creating difficulties for successful single analyte measurements [17]. Nevertheless, as the transmission of an LPG possesses many resonance bands, it is possible to utilise the feature-rich spectrum to monitor more than one measurand simultaneously [24]. LPGs are not intrinsically sensitive to specific chemicals and therefore respond to general changes in external refractive index [25]. However, by coating the grating with a material that exhibits a refractive index change in response to a particular chemical, it is possible to create a highly sensitive and selective device [26, 27]. The ability to tailor the response of an LPG in this manner further highlights their suitability as a sensing platform.

To date, there has been minimal research on the efficacy of LPGs for the detection of CO_2 [28, 29, 30]. Considering the desirable attributes these in-fibre gratings possess for chemical sensing and the need for real-time CO_2 monitoring, LPGs have the potential to be a cheap, viable alternative CO_2 sensor.

1.2 Thesis aims and objectives

The main aim of this project was to develop a fibre optic CO_2 sensor. The intention was that this device could eventually be integrated with a prototype LPG ammonia breath sensor being developed within the Centre for Engineering Photonics. Utilised

for this purpose, the CO_2 sensor would improve sampling reliability through the identification of specific lung regions based on exhaled CO_2 concentrations. Typically, the air sampled from the alveolar region is utilised for analyte quantification, since this part of the exhaled air has been in contact with alveoli blood, and can be recognised through a plateaued CO_2 concentration around 4% [1]. It is therefore required that the CO_2 sensor is able to detect concentrations between 0 - 15% with an accuracy of ±0.2% (based on the specification of a CO_2 sensor utilised in [31] for breath sampling analysis). Additionally, the device here must possess a response/recovery time of <0.1 s in order to determine the magnitude of the CO_2 response required to accurately identify the aforementioned plateau in a single breath [32]. Finally, it is also important that the fibre based sensor is assessed for its cross-sensitivity with ammonia and humidity (since human breath is water saturated) [33].

In order to achieve these aims, the following research objectives were proposed:

i Investigate the reproducibility of LPG fabrication methods and assess the suitability of this technique for creating highly sensitive devices.

ii Evaluate the applicability of higher order features as technique for multi-parameter sensing using a single LPG element as a means to compensate for interfering environmental parameters.

iii Explore a number of materials for their appropriateness as a CO_2 sensitive LPG coating.

iv Characterise the newly manufactured device's response to CO_2, temperature, and humidity.

v Disseminate novel findings via appropriate academic conferences and in suitable peer-reviewed journals.

1.3 Thesis novelty

The following points highlight the aspects of the thesis which are considered to be novel:

i A representation technique which looks to highlight the crucial resonance features from sequential LPG transmission data in order to aid in the future fabrication of complex and coated LPGs (Chapter 5).

ii A theoretical and experimental demonstration that the UV irradiation duty cycle during LPG fabrication governs which harmonic features are present in

the transmission spectrum (Chapter 6).

iii The demonstration of a CO_2 induced refractive index change in the ionic liquid 1-hexyl-3-methylimidazolium bis(trifluoromethylsulfonyl)imide (Chapter 7).

iv The design and development a coating technique to apply the ionic liquid gel to an optical fibre surface (Chapter 7).

v The detection of 20% CO_2 using an ionic liquid gel coated LPG (Chapter 7).

1.4 Chapter summary

Chapter 2 reviews the various types of CO_2 sensors which have been developed and summarises the key advantages and disadvantages of each technology.

Chapter 3 covers the theory of LPGs by outlining operating mechanisms, inherent sensitivities, examples of different LPG types, fabrication techniques, and a number of multi-parameter sensing schemes.

Chapter 4 discusses common methods of applying coatings to optical fibres and reviews materials which display an affinity for CO_2.

Chapter 5 presents the first experimental work investigating the repeatability and the advantages of fabricating LPGs using the overwrite method. Additionally, through the fabrication of numerous LPGs, a novel technique for portraying fabrication data is outlined from which a number of key LPG characteristics can be inferred.

Chapter 6 investigates and identifies the fabrication parameters necessary to consistently produce an LPG with higher order diffraction features, where an LPG possessing these additional features is assessed for its ability to perform simultaneous measurements.

Chapter 7 outlines the development of an LPG CO_2 sensor from initial material suitability evaluations, to the creation of a coating system, and finally, the characterisation of the sensing device.

Chapter 8 summarises the results presented in the thesis and details future experiments in which to further the work presented here.

1.5 References

[1] B. Buszewski, M. Kesy, T. Ligor, and A. Amann. Human exhaled air analytics: biomarkers of diseases. *Biomedical Chromatography*, 21(6):553–566, 2007.

[2] H. Chen, J. Winderlich, C. Gerbig, A. Hoefer, C. Rella, E. Crosson, A. Van Pelt, J. Steinbach, O. Kolle, V. Beck, *et al.* High-accuracy continuous airborne measurements of greenhouse gases (CO2 and CH4) using the cavity ring-down spectroscopy (CRDS) technique. *Atmospheric Measurement Techniques*, 3(2), 2010.

[3] J. Hodgkinson, R. Smith, W. O. Ho, J. R. Saffell, and R. P. Tatam. Non-dispersive infra-red (NDIR) measurement of carbon dioxide at 4.2 μm in a compact and optically efficient sensor. *Sensors and Actuators B: Chemical*, 186(1):580–588, 2013.

[4] J. Puton, T. Palko, A. Knap, K. Jasek, and B. Siodlowski. Module for measurement of CO2 concentration in exhaled air. In *Optoelectronic and Electronic Sensors V*, vol. 5124, pp. 278–283. International Society for Optics and Photonics, 2003.

[5] L. B. Mendes, N. W. Ogink, N. Edouard, H. J. C. Van Dooren, I. F. F. Tinôco, and J. Mosquera. NDIR gas sensor for spatial monitoring of carbon dioxide concentrations in naturally ventilated livestock buildings. *Sensors*, 15(5):11239–11257, 2015.

[6] H. B. Shim, J. H. Kang, J. W. Choi, and K. S. Yoo. Characteristics of thick-film CO2 sensors based on NASICON with Na2 CO3-CaCO3 auxiliary phases. *Journal of Electroceramics*, 17(2-4):971–974, 2006.

[7] A. D. Kersey. A review of recent developments in fiber optic sensor technology. *Optical Fiber Technology*, 2(3):291–317, 1996.

[8] H.-E. Joe, H. Yun, S.-H. Jo, M. B. Jun, and B.-K. Min. A review on optical fiber sensors for environmental monitoring. *International Journal of Precision Engineering and Manufacturing-Green Technology*, 5(1):173–191, 2018.

[9] K. Mullaney. *The fabrication of micro-tapered optical fibres for sensing applications.* Ph.D. thesis, Cranfield University, 2016.

[10] J. Yuan and M. A. El-Sherif. Fiber-optic chemical sensor using polyaniline as modified cladding material. *IEEE Sensors Journal*, 3(1):5–12, 2003.

[11] A. Urrutia, K. Bojan, L. Marques, K. Mullaney, J. Goicoechea, S. James, M. Clark, R. Tatam, and S. Korposh. Novel highly sensitive protein sensors based on tapered optical fibres modified with Au-based nanocoatings. *Journal of Sensors*, 2016(1), 2016.

[12] W. C. Wong, W. Zhou, C. C. Chan, X. Dong, and K. C. Leong. Cavity ringdown refractive index sensor using photonic crystal fiber interferometer. *Sensors and Actuators B: Chemical*, 161(1):108–113, 2012.

[13] T. Kissinger. *Range-resolved optical interferometric signal processing*. Ph.D. thesis, Cranfield University, 2015.

[14] J. Hromadka, S. Korposh, M. C. Partridge, S. W. James, F. Davis, D. Crump, and R. P. Tatam. Multi-parameter measurements using optical fibre long period gratings for indoor air quality monitoring. *Sensors and Actuators B: Chemical*, 244(1):217–225, 2017.

[15] V. Bhatia and A. M. Vengsarkar. Optical fiber long-period grating sensors. *Optics Letters*, 21(9):692–694, 1996.

[16] Y. Kashyap. *Fiber Bragg Gratings*. Academic Press, London, UK, 1st ed., 1999.

[17] S. W. James and R. P. Tatam. Optical fibre long-period grating sensors: characteristics and application. *Measurement Science and Technology*, 14(5):R49–61, 2003.

[18] A. D. Kersey, M. A. Davis, H. J. Patrick, M. LeBlanc, K. Koo, C. Askins, M. Putnam, and E. J. Friebele. Fiber grating sensors. *Journal of Lightwave Technology*, 15(8):1442–1463, 1997.

[19] A. M. Vengsarkar, P. J. Lemaire, J. B. Judkins, V. Bhatia, T. Erdogan, and J. E. Sipe. Long-period fiber gratings as band-rejection filters. *Journal of Lightwave Technology*, 14(1):58–65, 1996.

[20] E. Chehura, S. W. James, and R. P. Tatam. Temperature and strain discrimination using a single tilted fibre Bragg grating. *Optics Communications*, 275(2):344–347, 2007.

[21] J. Albert, L.-Y. Shao, and C. Caucheteur. Tilted fiber Bragg grating sensors. *Laser and Photonics Reviews*, 7(1):83–108, 2013.

[22] R. Y. N. Wong. *Advanced fibre optic long period grating sensors; design, fabrication and sensing*. Ph.D. thesis, Cranfield University, 2014.

[23] M. Partridge, S. W. James, J. H. Barrington, and R. P. Tatam. Overwrite fabrication and tuning of long period gratings. *Optics Express*, 24(20):22345–22356, 2016.

[24] V. Bhatia, D. K. Campbell, D. Sherr, T. D'Alberto, N. Zabaronick, G. A. Ten Eyck, K. A. Murphy, and R. O. Claus. Temperature-insensitive and strain-insensitive long-period grating sensors for smart structures. *Optical Engineering*, 36(7):1872–1877, 1997.

[25] S. W. James and R. P. Tatam. Fibre optic sensors with nano-structured coatings. *Journal of Optics A: Pure and Applied Optics*, 8(7):S430–S444, 2006.

[26] S. Korposh, R. Selyanchyn, W. Yasukochi, S.-W. Lee, S. W. James, and R. P. Tatam. Optical fibre long period grating with a nanoporous coating formed from silica nanoparticles for ammonia sensing in water. *Materials Chemistry and Physics*, 133(2-3):784–792, 2012.

[27] M. Partridge, R. Wong, S. W. James, F. Davis, S. P. Higson, and R. P. Tatam. Long period grating based toluene sensor for use with water contamination. *Sensors and Actuators B: Chemical*, 203(1):621–625, 2014.

[28] L. Melo, G. Burton, B. Davies, D. Risk, and P. Wild. Highly sensitive coated long period grating sensor for CO2 detection at atmospheric pressure. *Sensors and Actuators B: Chemical*, 202(1):294–300, 2014.

[29] C.-W. Wu and C.-C. Chiang. Application of Notched Long-Period Fiber Grating Based Sensor for CO2 Gas Sensing. *Fiber and Integrated Optics*, 35(1):22–28, 2016.

[30] J. Hromadka, B. Tokay, R. Correia, S. P. Morgan, and S. Korposh. Carbon dioxide measurements using long period grating optical fibre sensor coated with metal organic framework HKUST-1. *Sensors and Actuators B: Chemical*, 255(1):2483–2494, 2018.

[31] W. Filipiak, A. Filipiak, C. Ager, H. Wiesenhofer, and A. Amann. Optimization of sampling parameters for collection and preconcentration of alveolar air by needle traps. *Journal of Breath Research*, 6(2):027107, 2012.

[32] G. Schmalisch. Current methodological and technical limitations of time and volumetric capnography in newborns. *Biomedical Engineering Online*, 15(104):1–13, 2016.

[33] C. Lourenço and C. Turner. Breath analysis in disease diagnosis: methodological considerations and applications. *Metabolites*, 4(2):465–498, 2014.

Chapter 2

Carbon dioxide detection methods

Monitoring concentrations of CO_2 is essential in numerous situations, ranging from leak detection in underground CO_2 storage reservoirs [1] to environmental research [2], and ensuring safety in enclosed industrial environments (fermentation vats, freezers, mines) [3]. In each circumstance, the location, desired sensitivity, and number of devices ultimately governs the size and type of sensor most suited for the purpose. In order to meet the wide-ranging demand, various CO_2 detection technologies have been developed from small, simple low-cost units to expensive, highly accurate tools. This chapter reviews the most-widely used techniques for the detection of CO_2 in order to help clarify the design and requirements for a novel CO_2 sensor.

2.1 Non-optical techniques

Numerous CO_2 sensors are based on changes in the electrical properties of materials (conductance, resistance) rather than spectroscopic absorption. These devices are often cheap to produce and are small in size, making it easy to incorporate them into electronic systems and allowing widespread deployment [4]. However, they tend to suffer from cross sensitivity with coexisting gases and often deteriorate with time, leading to a short-life span [5]. There are a number of important performance parameters associated with sensors that require definition prior to a review on CO_2 sensors, namely, limit of detection (LoD), response time, and selectivity. Firstly, LoD is generally defined as the lowest concentration that a device can detect. The response time of a sensor is the time required for a 10% to 90% change of the test signal at equilibrium following exposure to the target gas. Finally, selectivity is described as the extent to which a device can determine a particular analyte in a mixture or composition without interference from competing substances. All definitions were

obtained from [6].

2.1.1 Metal oxide semi-conductors

Metal oxide semi-conductor (MOS) devices have attracted substantial attention in the field of gas sensing due to their low-cost, ease-of-use, and quick production. Furthermore, the majority of MOS sensors demonstrate longevity and resistance to poisoning [7]. To understand the basic operation of these devices, a brief description of band theory is required. Band theory proposes that within a lattice, the energy states present form bands rather than discrete energies and that for conduction to occur, electrons must be able to pass from the valence band into the conduction band. Between the bands there exists a gap which requires excitation to bridge and depending on the class of material (conductor, semi-conductor, insulator), this gap can vary in the amount of energy required to traverse it (Fig. 2.1). In the case of

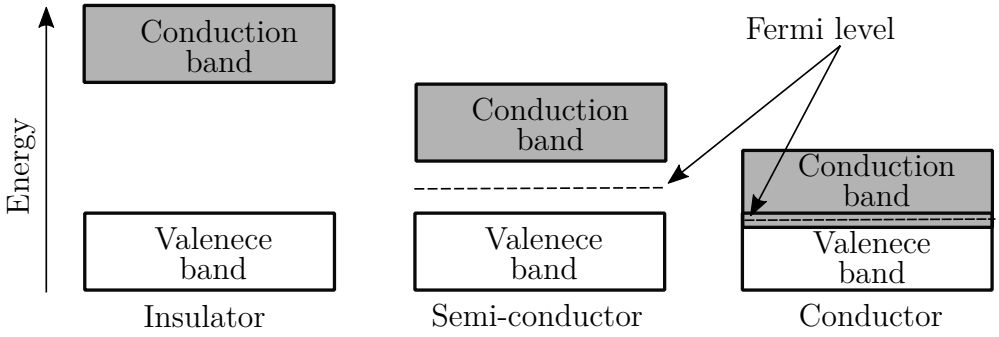

Figure 2.1: Schematic representation of the conduction and valence band for the three main classes of material. The large gap observable in the insulator means no electrons are able to transfer to the conduction band, whereas with sufficient energy this transfer may occur in the semi-conductor. Conductors possess overlapping bands thus not requiring external stimuli to achieve conductance [8]

semi-conductors, the gap is small enough (typically in the region of 0.5 - 5.0 eV) such that during excitation it is possible for electrons to inhabit the conduction band but large enough that below the Fermi level (the highest electron energy level at a specific temperature) conduction is not present [8, 9].

An arrangement for a typical MOS sensor can be seen in Fig. 2.2, although other structures, such as tubes and bead-shapes, have been successful applied [10]. Sensing is accomplished in MOS sensors via surface reactions between the adsorbed surface oxygen species and the target gas. This causes the molecule of interest to dissociate into charged ions, which results in the transfer of electrons to the conduction band producing a change in the resistivity of the sensitive layer [11]. The device is operated at high temperatures (>250°C) and is optimised for the target gas for

fast, reproducible device operation (Table 2.1) [4, 11]. The change in resistivity is

Table 2.1: Influence of sensor operating temperature on gas sensitivity for a tin oxide sensor. Gas concentrations in air are 0.8% hydrogen (H_2), 0.2% C_3H_8, 0.5% methane (CH_4) and 0.02% carbon monoxide (CO). Data obtained from graphical interpretation [12]

Analyte	**Temperature (°C)**
H_2	320
C_3H_8	360
CH_4	440
CO	350

governed by the choice of semi-conductor (p-type, n-type) and whether the target gas is a reducing or an oxidising agent. For example, an n-type semi-conductor will experience an increase in resistivity in the presence of an oxidising gas, whereas a p-type material will demonstrate a decrease [8]. CO_2 can be detected by various metal oxides (e.g. Al, Bi, Cd). However, none of these materials respond specifically to CO_2 and may react with many other gaseous species [13]. These 'pure' materials can be doped with noble metals (Au, Pl etc.) to improve sensitivity and selectivity [14]. This ability to alter sensing characteristics through the variation in dopants has allowed the realisation of numerous MOS CO_2 sensors with varying degrees of sensitivity and specificity.

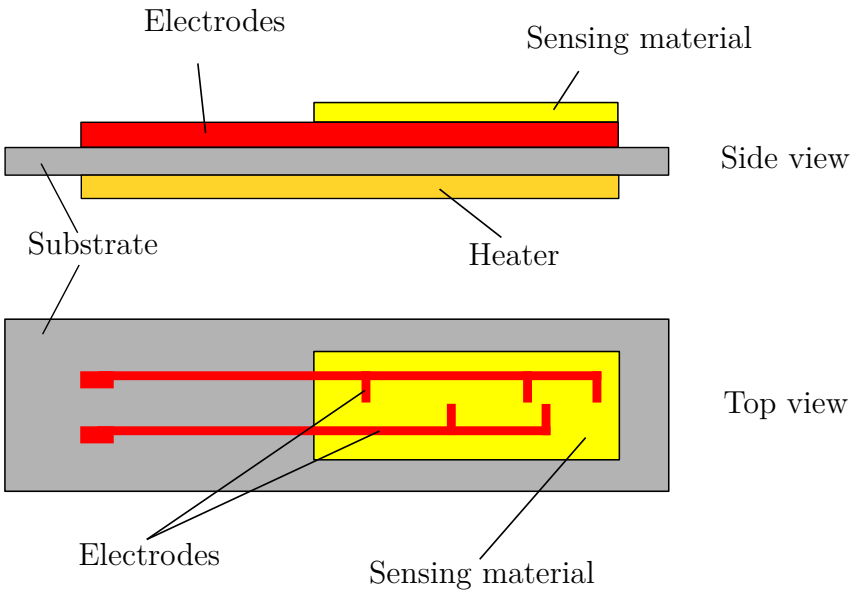

Figure 2.2: Schematic of a typical MOS sensor. Electrodes are integrated into the sensing layer which is deposited onto a insulating substrate provided with a heater [11]

MOS sensors can detect CO_2 in concentrations ranging from 500 - 50,000 ppm

depending on the metal oxide chosen [15, 16, 17, 18]. However, they suffer from cross-sensitivity with humidity and other gaseous species (e.g. carbon monoxide). Reduction of carbon monoxide induced responses in SnO-based MOS gas sensors has been achieved by doping the semi-conductor material with La [19]. Generally, MOS sensors display response times ∼60 s, although this can be influenced by the structure (surface-to-volume ratio) of the metal oxide layer [20].

2.1.2 Field effect transistors

First utilised to detect gaseous hydrogen [21], field effect transistors (FETs) have been adapted for use in CO_2 sensing. These transistors consist of a silicon body with two doped channels (either p- or n-type silicon depending on the FET) and three terminals: source, drain and gate. An insulator (typically SiO_2) separates the source and drain allowing a flow of current in the channel region between the two to be controlled by the gate terminal through the application of a potential difference (Fig. 2.3). Once the applied potential difference reaches a certain voltage threshold, a high density layer of negative charge forms, allowing current to flow between the source and drain. In gas sensing, the gate is comprised of a material which demonstrates an affinity for the target gas (i.e. palladium for hydrogen sensing [21]). Contact with the target gas induces either a physical or chemical change in the material, causing the required potential difference for current to flow.

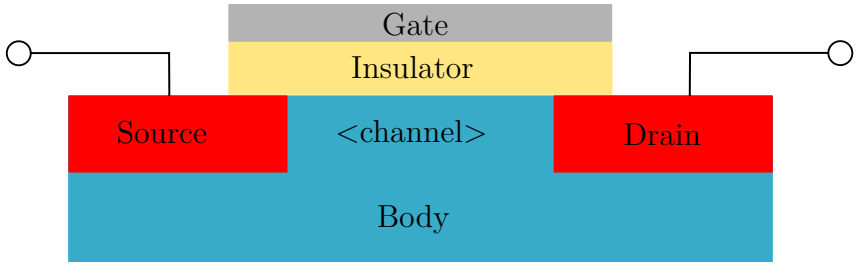

Figure 2.3: Basic FET structure

In the case of CO_2 FET sensors, the sensitive region can be created through a number of materials, including amine-functionalised carbon nanotubes, ionic liquids and amine-starch polymers [22, 23, 24, 25]. Typically, FETs are able to detect CO_2 from approximately 500 ppm with response times in the region of a few seconds [22]. Additionally, unlike MOS sensors, FETs are able to operate at room temperature,

improving device lifetime and power consumption. Furthermore, a variety of sensing materials can be used, broadening the possibility for selective sensing [26]. However, these devices often suffer from hysteresis originating from humidity interference and analyte saturation of the sensitive material [22, 27].

2.1.3 Solid electrolyte potentiometers

Traditionally, potentiometric electrochemical cells based on solid electrolytes operate via redox reactions with redox-active gases (e.g. oxygen) by surface conductivity. However, CO_2 is redox-inactive and therefore requires a different strategy to achieve detection [28]. This has been accomplished through the use of solid electrolytes that possess alkaline charge carriers, such as sodium ion conductors [29]. The simplest CO_2 potentiometric sensors are based on a sensitive layer of bicarbonate, typically sodium or lithium bicarbonate, separating a sensing electrode and a reference electrodes. Determination of CO_2 concentrations can be achieved via monitoring the cell voltage (E_v) which is determined by the difference in carbonate concentration at the two electrodes governed by the Nernest equation [30],

$$E_v = \frac{R_c T}{n_e F} \ln \left(\frac{[CO_3^{2-}]_{sens}}{[CO_3^{2-}]_{ref}} \right) \tag{2.1}$$

where R_c is the gas constant, T is temperature, F is Faraday's constant and n_e is the number of electrons ($n_e = 2$ for CO_3^{2-}). To obtain a stable reference signal, essential for a reliable CO_2 concentration measurement, a reference gas of CO_2 and O_2 with stable partial pressures is typically used. However, this approach requires gas separation between sensing and reference electrodes, complicating the sensor design and limiting its effectiveness in diverse environments [30].

To overcome this, an alternate method was devised through the development of solid-state reference electrodes that establish potential via metal oxide (e.g. NaO) activity. This allows only the sensing electrode to display CO_2 sensitivity, rather than both, on the assumption that the sensing and reference electrodes are exposed to the same oxygen partial pressure. In this design, the electrochemical cell relies on sodium conducting ions rather than carbonates via the use of alkali metal electrolytes. In the case of sodium, common ion conducting electrolytes are NASICON ($Na_{1+x}Zr_2Si_xP_{3-x}O_{12}$ $(0 < x < 3)$) and Na-β-alumina ($Na_2O{\cdot}11Al_2O_3$). Combining the electrolyte with an auxiliary phase, typically comprised of Na_2CO_3, sodium ions are exchanged at the interface of the two materials in order to maintain equilibrium between sodium and CO_2 (Fig. 2.4). Although more complex, this electrochemical cell

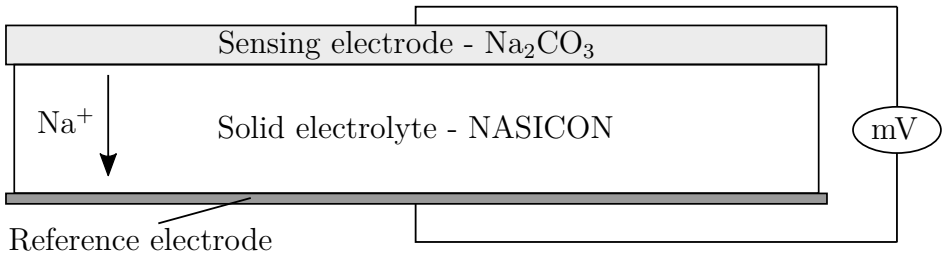

Figure 2.4: Basic CO_2 pellet solid electrolyte potentiometer design with Na^+ flow indicated [31]

system only requires O_2 as a reference gas removing the necessity for gas separation [29]. Further improvements in reference electrode stability have been proposed by removing the reference gas dependency entirely (i.e. only the sensing electrode is gas sensitive) by fixing the O_2 activity through the use of silica or zirconia incorporated materials (e.g. $Na_2Si_2O_5$) [29].

These devices are generally operated at high temperatures ($>400°C$) as ion conductivity, response magnitude and sensitivity are all improve with increasing temperatures [30]. Detection generally occurs in the 100 - 10,000 ppm range with response times <2 min [32, 33]. However, both NASICON and β-alumina react with hydrogen sulfide to form sodium sulfate, resulting in irreversible degradation of these electrolytes [34]. Additionally, operating life is often limited due to chemical reactions between the auxiliary and electrolyte phases and decomposition of the sensing electrode [35].

2.1.4 Summary of non-optical techniques

CO_2 sensors based on non-optical techniques generally offer a cost-effective detection scheme, particularly if numerous devices are necessary. Additionally, it is possible to alter their sensing characteristics through varying the chemical composition of the sensor. However, the greatest drawback with non-optical based CO_2 sensors are their susceptibility to cross-sensitivity with humidity and other gaseous species.

It is clear that the aforementioned techniques are not suitable for the current project since they would not be able to be multiplexed with the proposed LPG-based ammonia breath sensor, in addition to their inherent humidity sensitivity.

2.2 Optical techniques

Optical techniques can be broadly separated into two approaches; direct absorption, or transduction (sensing a change in an intermediate functional material caused by the analyte rather than assessing the analyte directly). The former approach, with careful design, provides a highly specific sensor that experiences negligible cross sensitivity with other gaseous species, far surpassing that of non-optical methods [36]. However, these devices are difficult to miniaturise and tend to be more expensive [11]. Optical techniques that utilise transduction can be easily adapted by changing the functional material thereby allowing the sensors' characteristics to be tailored to specific requirements. Nevertheless, this intermediate material is often vulnerable to cross-sensitivity.

2.2.1 Non-dispersive infrared

Non-dispersive infrared (NDIR) CO_2 sensors are the most mature of the detection techniques and have been implemented in various environments from assessing CO_2 in livestock buildings [37] to capnography [38]. The basic operating principle of NDIR relies on the absorption strength of mid-IR radiation to determine the gas concentration of CO_2 as it demonstrates strong absorption in this region ($\sim$4.2 μm) [39]. A schematic of a simple linear NDIR sensor can be seen in Fig. 2.5. Typically, an NDIR device consists of a broadband source (e.g. microbulb), cavity, and a dual-channelled detector (active and reference). Optical filters are placed over the detectors, one covering a narrow absorption band specific to CO_2 (active channel) and the other pertaining to a neighbouring wavelength range distinct from the one used on the active channel (reference channel). By carefully selecting the filter's transmission wavelength, it is possible to avoid cross-sensitivity with other gases [40].

Quantification of CO_2 concentration is governed by the Beer-Lambert law which can be expressed as [41],

$$A(\lambda) = \sigma(\lambda)CL \tag{2.2}$$

in this case $A(\lambda)$ is absorbance, L is the optical path length, $\sigma(\lambda)$ is the gas absorption coefficient in standard state and C is the gas concentration in parts per volume. In comparison to other optical techniques, NDIR sensors are low cost and require only a few components allowing compact designs to be manufactured [40]. However, further reductions in size are desired. Miniaturisation of NDIR sensors is difficult due to the path length sensitivity of these devices (as can be seen in Equation 2.2). Nevertheless,

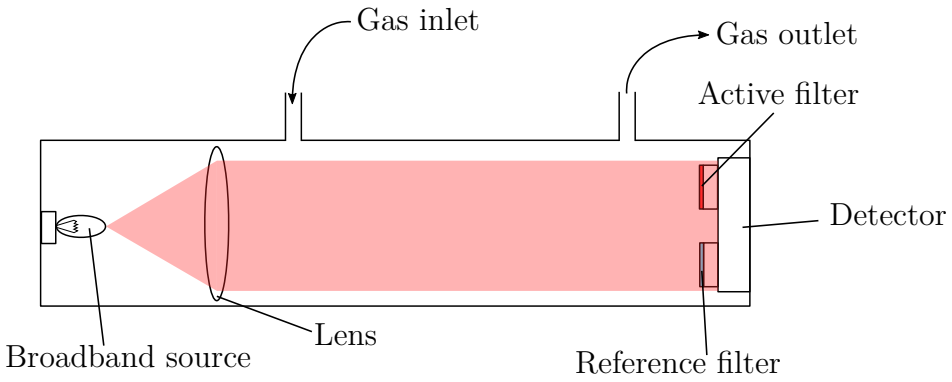

Figure 2.5: Diagram of a simple linear NDIR CO_2 gas sensor [40]

novel designs have been realised which conform to industry standard gas sensor dimensions (20 mm diameter x 16.5 mm) while achieving a limit of detection of 1 ppm [40].

The sensitivity dependence on path length allows devices to be tailored for certain concentration levels, where shorter path lengths (20 mm) are suited for higher concentrations (5 - 100%) while longer path lengths (70 mm) allow for more accurate detection at lower concentrations (200 - 50,000 ppm) [42]. NDIR based CO_2 sensors which have been compactly designed (limiting path length) show higher LoD (1 ppm with a response time of 23 s [40]) than physically larger NDIR devices. In contrast, by using the bigger (length = 10 cm) sensors, it is possible to obtain a LoD of 0.007 ppm with a response time of $\sim$2 min [39]. Regardless of physical size, NDIR CO_2 sensors using the CO_2 absorption band at 4.2 μm demonstrate negligible cross-sensitivity with other gases or water vapour [42].

2.2.2 Tuneable diode laser absorption spectroscopy

Gas absorption measurement using tuneable diode laser spectroscopy (TDLAS) is achieved by scanning the output of a tuneable diode laser across the target gas line and subtracting the resulting signal from a zero reference measurement over the same range [43]. Tuning the diode's emission is accomplished by ramping the input current or by varying the temperature of the laser, where typically these sources have a narrow linewidth (usually 20 - 25 MHz) and a small tuning wavelength range. Diode lasers are available in various wavelength ranges in the infrared, mid-infrared and red visible regions [44].

The simplest method for measuring gas concentrations using TDLAS is via direct absorption. This technique involves the swept source undergoing a single pass through

the sample gas contained in a gas cell prior to reaching the detector. Although straight forward, this technique suffers from poor sensitivity when analysing low concentrations due to the difficulty in extracting the small absorption signal from background noise [43]. One technique to improve this is to use wavelength modulation spectroscopy where the emission wavelength is modulated sinusoidally over the absorption line and gas is detected by the harmonic spectrum obtained from a lock-in amplifier [36].

Another strategy to improve the sensitivity of TDLAS is to use a multi-pass gas cell, such as a Herriott or White cell (Fig. 2.6 (a) and (b) respectively). These cells typically consist of two or more mirrors which reflect the incident beam multiple times, increasing the optical path length that contains the stable gas sample. Using these devices path lengths of 56 m have been accomplished during CO_2 isotope detection [45]. However, multi-pass gas cells require precise alignment to operate effectively, thus limiting their commercial applications. In contrast, integrating spheres are able to tolerate such misalignment. Integrating spheres are spherical cavities constructed of materials which possess high diffuse reflectivity with two or more ports for sources and detectors (Fig. 2.6 (d)) [46]. The indecent beam is initially scattered upon hitting the internal sphere wall and reflected round the cavity, increasing the optical path length; although not to the same distances as other multi-pass cells [36]. It is this spherically diffuse reflective surface that permits high alignment tolerances, as following the initial beam strike in the cavity, uniform irradiance over the surface is achieved within a few passes [47]. Hawe *et al.* [48] utilised a 50 mm integrating sphere for the successful detection of CO_2 in a concentration range between 7% and 100%

Longer optical path lengths have been achieved through use of cavity ringdown spectroscopy (CRDS). Using a high finesse cavity (typically containing mirrors with reflectivity >99.99%), light enters the cavity through a partial mirror and is allowed to build-up over time while being monitored by an external photo-detector behind a second partial mirror (Fig. 2.6 (c)). Once a sufficient intensity has been achieved, the source is interrupted and the slow intensity decay (caused by cavity mirrors with less than 100% reflectivity and slight mirror misalignments) is tracked. If a sample gas is present within the cavity, the intensity decays more rapidly [49]. The advantages of CRDS are that this technique is insensitive to fluctuations in source power, as measurements are based on relative decay. Additionally, the thousands of reflections inside the cavity provide CRDS with optical path lengths of kilometres [36]. However, the cavity mirrors must remain completely clear of surface contamination for maintained performance. In terms of CO_2 sensing, CRDS can detect concentrations

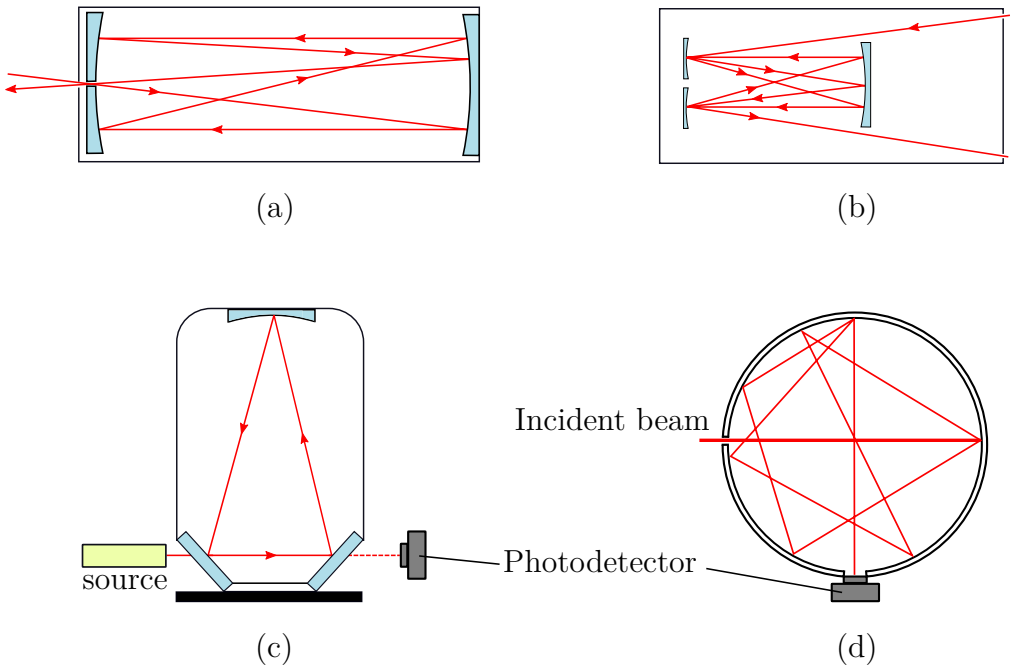

Figure 2.6: Examples of commonly used gas cells and cavity enhancement techniques for improving absorption sensitivity: (a) Herriott cell; (b) White cell; (c) Cavity ringdown spectroscopy and; (d) Integrating spheres

of 100 ppb with a response time of 5 s [49].

2.2.3 Fibre optics

Optical fibres are able to carry data of over large distances (kms) with minimal losses (0.2 dB·km^{-1} in single mode fibre) [50]. In terms of gas sensing, this ability to carry data has been exploited through the multiplexing of gas cells allowing a single, expensive source to be shared among numerous cells, reducing the overall cost per sensor head [36]. However, optical fibres can also be adapted in order to serve as the transducer element for sensing purposes rather than just acting as data conduits. This can be achieved by various means (see [51] for a review of fibre sensor technologies). However, only techniques pertinent to CO_2 sensing are outlined in the subsequent section.

Although fibre optic CO_2 sensors are not currently commercially available, various schemes and technologies have been investigated. Fig. 2.7 depicts a number of techniques used to adapt optical fibres for the purpose of CO_2 gas sensing. These modulation techniques either operate through evanescent fields interacting with the surrounding environment (Fig. 2.7 (a), (c), (d)) or via a change in optical path length (Fig. 2.7 (b)) to distinguish CO_2 concentrations. The sensitive coatings

depicted in Fig. 2.7 interact with the gaseous CO_2 producing either a significant colour change [52] or a shift in refractive index [53, 54, 55, 56] which is detected by the aforementioned schemes. In order to recognise these changes, optical fibre based CO_2 sensors generally require a source (broadband emission, laser) and an interrogation system (OSA, spectrophotometer). Additionally, optical fibre CO_2 sensors, like the majority of fibre-based sensors, are able to access remote and hard-to-reach environments which would not be achievable for other device forms. Additionally, depending on the modulation technique used, it is possible to multiplex a number of sensor elements thus allowing numerous sites to be monitored via the same fibre [55].

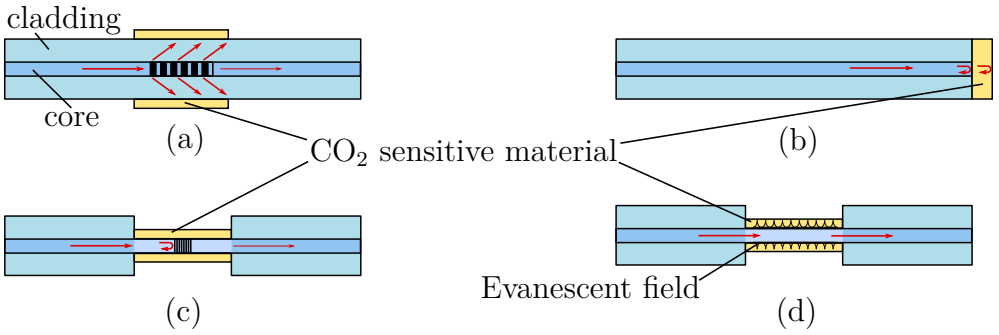

Figure 2.7: Various techniques that have been employed in CO_2 sensors to cause light propagating in the core to interact with the surrounding environment: (a) LPG [54]; (b) extrinsic Fabry-Perot cavity [53]; (c) FBG [55] and; (d) etched cladding [52]. All the examples here use a material which demonstrates CO_2 sensitivity and the subsequent change in coating upon exposure to CO_2 is sensed by the interacting light

Optical fibre devices tested at lower CO_2 concentrations (200 - 4000 ppm) typically showed response times between 2 - 3 min with an estimated limit of detection of 75 ppm [52, 55]. Fibre optic CO_2 sensors assessed in higher concentration ranges (7.6 - 87%) demonstrated response times of 0.5 - 1 min with resolutions of 200 pm·%CO_2^{-1} [53]. Typically, response times of fibre-based CO_2 sensors are limited by the performance of the CO_2 sensitive material (CO_2 affinity, CO_2 absorption/diffusion rate) applied to the device, as the majority of fibre technologies utilise interrogation methods that operate at speeds <1 s. However, the necessary use of CO_2 sensitive coating materials often causes cross-sensitivity with water vapour [53] or other gaseous species [52].

LPG-based CO_2 sensors are of particular interest to this project, as this fibre transduction method would provide the simplest means of multiplexing with the ammonia breath sensor (thought the utilisation of the same source and interrogator). Minimal research has been previously conducted on utilising this technology for CO_2

sensing [54, 56]. These devices were used to detect CO_2 concentrations of 500 - 40000 ppm [56] and 25 - 100% CO_2 [54] by employing metal organic framework (MOFs) and polystyrene cladding depositions, respectively, both demonstrating response times of 1 - 2 min. Furthermore, similar to other fibre-based schemes, the coating of these sensors displayed cross-sensitivity to ambient humidity. Since there are a number of CO_2 sensitive materials available (as described in Section 4.2) that have not been applied to LPGs, there is scope to produce an LPG-based CO_2 sensor that uses a novel coating material that could improve on the sensing performance noted in [54, 56].

2.2.4 Summary of optical techniques

Direct spectroscopic techniques, such as NDIR and TDLS, offer superior CO_2 detection specificity and sensitivity in comparison to non-optical methods. Nevertheless, this enhanced performance is obtained at the cost of miniaturisation and a greater financial burden. Optical fibre derived CO_2 sensors on the other hand, are dimensionally small (diameters below 1 mm) and can possess multiple sensors on a single fibre array. Concentrations in the ppm range have been detected with these sensors, however, the transduction method relies on a form of CO_2 sensitive material that increases response times and demonstrates cross-sensitivity. Nonetheless, a fibre-based CO_2 sensor would be most appropriate for the current work due to their ability to be multiplexed.

2.3 Summary and conclusions

This chapter has outlined techniques which are currently used for detecting gaseous CO_2. Non-optical methods demonstrate a durable, cost-effective solution for determining CO_2 concentrations albeit with issues of cross-sensitivity. Optical-based sensors posses the selectivity and sensitivity not presently obtainable in their non-optical counterparts, yet this increased performance comes with a larger financial cost. Table 2.2 summarises the important aspects of each technique described in Sections 2.1 and 2.2.

This literature review has highlighted that the CO_2 sensor market is saturated. However, fibre optic-based sensors demonstrate the greatest potential for this project since they can be multiplexed with other fibre sensors and share a single interrogation unit and source. Additionally, since the CO_2 sensor is intended to be integrated with

an LPG sensor, it is practical that this sensor should also utilise this method of fibre transduction. Although a number of LPG-based CO_2 sensors have been previously developed through the application of varying sensitive coatings, these devices do not possess the require response times demanded of breath analysis. Nevertheless, the limiting factor in these sensors is the functional deposition and not the underlying optical technique. Therefore, through the utilisation of a novel coating material that shows a faster response/recovery time (<1 s) and does not demonstrate a humidity response, it could be possible to create a fibre-based CO_2 sensor that would be ideally suited for breath analysis.

Table 2.2: Comparison of existing CO_2 sensor technologies. Abbreviations: Metal oxide semiconductors (MOSs), Solid electrolyte potentiometers (SEPs), Field effect transistors (FETs), Non-dispersive infrared (NDIR), Tuneable diode laser absorption spectroscopy (TDLAS), Limit of detection (LoD), Response time (RT), Advantage (+), Disadvantage (−)

Technique	**LoD**	**RT**	**Comments**
Non-optical			
MOSs [15, 16, 17, 18]	500 ppm	∼1 min	(+) Cheap and easy to produce (+) Long sensor life (−) High operating temperature (−) Cross-sensitivity to humidity and other gases
FETs [22]	500 ppm	<5s	(+) Operate at room temperature (+) Various materials can be applied adapting selectivity and sensitivity
SEPs [32, 33]	100 ppm	<2 min	(+) High sensitivity (−) Suffers humidity degradation (−) Cross-sensitivity (−) Short operating life (1-3 yrs)
Optical			
NDIR [39, 40, 42]	7 ppb	<1 s	(+) Highly sensitive (+) Fast response time (+) Long-term stability (+) Minimal humidity cross-sensitivity (−) Can be affected by particulates in the beam path (−) Expensive in comparison to FETs and MOS sensors
TDLAS [49, 48]	100 ppb	<5 s	(+) CO_2 specific through appropriate choice of laser diode (+) Highly sensitive (+) Fast response times (−) Affected by temperature fluctuations and vibration (−) Gas cell systems require regular maintenance for optimum performance
Fibre optics [52, 55, 56]	75 ppm	∼1 min	(+) Deployable in hard-to-reach areas (+) Potential for multiplexing (−) Fragile without suitable packaging (−) Rely on coating for CO_2 detection - degradable, requires refreshing

2.4 References

[1] R. Chadwick, R. Arts, M. Bentham, O. Eiken, S. Holloway, G. Kirby, J. Pearce, J. Williamson, and P. Zweigel. Review of monitoring issues and technologies associated with the long-term underground storage of carbon dioxide. *Geological Society, London, Special Publications*, 313(1):257–275, 2009.

[2] H. Chen, J. Winderlich, C. Gerbig, A. Hoefer, C. Rella, E. Crosson, A. Van Pelt, J. Steinbach, O. Kolle, V. Beck, *et al.* High-accuracy continuous airborne measurements of greenhouse gases (CO2 and CH4) using the cavity ring-down spectroscopy (CRDS) technique. *Atmospheric Measurement Techniques*, 3(2), 2010.

[3] J. L. Scott, D. G. Kraemer, and R. J. Keller. Occupational hazards of carbon dioxide exposure. *Journal of Chemical Health and Safety*, 16(2):18–22, 2009.

[4] P. Moseley. Solid state gas sensors. *Measurement Science and Technology*, 8(3):223, 1997.

[5] A. Azad, S. Akbar, S. Mhaisalkar, L. Birkefeld, and K. Goto. Solid-state gas sensors: A review. *Journal of the Electrochemical Society*, 139(12):3690–3704, 1992.

[6] X. Zhao, B. Cai, Q. Tang, Y. Tong, and Y. Liu. One-dimensional nanostructure field-effect sensors for gas detection. *Sensors*, 14(8):13999–14020, 2014.

[7] S. M. Kanan, O. M. El-Kadri, I. A. Abu-Yousef, and M. C. Kanan. Semiconducting metal oxide based sensors for selective gas pollutant detection. *Sensors*, 9(10):8158–8196, 2009.

[8] G. F. Fine, L. M. Cavanagh, A. Afonja, and R. Binions. Metal oxide semiconductor gas sensors in environmental monitoring. *Sensors*, 10(6):5469–5502, 2010.

[9] R. Martin. *Electronic Structure: Basic Theory and Practical Methods*. Cambridge University Press, Cambridge, UK, 2004.

[10] N. Yamazoe, J. Fuchigami, M. Kishikawa, and T. Seiyama. Interactions of tin oxide surface with O2, H2O and H2. *Surface Science*, 86(1):335 – 344, 1979.

[11] S. Neethirajan, D. Jayas, and S. Sadistap. Carbon dioxide (CO2) sensors for the agri-food industry–a review. *Food and Bioprocess Technology*, 2(2):115–121, 2009.

[12] A. P. Lee and B. J. Reedy. Temperature modulation in semiconductor gas sensing. *Sensors and Actuators B: Chemical*, 60(1):35 – 42, 1999.

[13] G. Eranna, B. C. Joshi, D. P. Runthala, and R. P. Gupta. Oxide Materials for Development of Integrated Gas Sensors - A Comprehensive Review. *Critical Reviews in Solid State and Materials Sciences*, 29(3-4):111–188, 2004.

[14] A. Kolmakov, X. Chen, and M. Moskovits. Functionalizing nanowires with catalytic nanoparticles for gas sensing application. *Journal of Nanoscience and Nanotechnology*, 8(1):111–121, 2008.

[15] U. Hoefer, G. Kühner, W. Schweizer, G. Sulz, and K. Steiner. CO and CO2 thin-film SnO2 gas sensors on Si substrates. *Sensors and Actuators B: Chemical*, 22(2):115–119, 1994.

[16] T. Krishnakumar, R. Jayaprakash, T. Prakash, D. Sathyaraj, N. Donato, S. Licoccia, M. Latino, A. Stassi, and G. Neri. CdO-based nanostructures as novel CO2 gas sensors. *Nanotechnology*, 22(32):325501, 2011.

[17] R. Dhahri, S. Leonardi, M. Hjiri, L. El Mir, A. Bonavita, N. Donato, D. Iannazzo, and G. Neri. Enhanced performance of novel calcium/aluminum co-doped zinc oxide for CO2 sensors. *Sensors and Actuators B: Chemical*, 239(1):36–44, 2017.

[18] D. Y. Kim, H. Kang, N.-J. Choi, K. H. Park, and H.-K. Lee. A carbon dioxide gas sensor based on cobalt oxide containing barium carbonate. *Sensors and Actuators B: Chemical*, 248(1):987–992, 2017.

[19] A. Marsal, A. Cornet, and J. Morante. Study of the CO and humidity interference in La doped tin oxide CO2 gas sensor. *Sensors and Actuators B: Chemical*, 94(3):324–329, 2003.

[20] T. Karthik, L. Martinez, and V. Agarwal. Porous silicon ZnO/SnO2 structures for CO2 detection. *Journal of Alloys and Compounds*, 731(1):853–863, 2018.

[21] I. Lundstrom, S. Shivaraman, C. Svensson, and L. Lundkvist. A hydrogen-sensitive MOS field-effect transistor. *Applied Physics Letters*, 26(2):55–57, 1975.

[22] A. Star, T.-R. Han, V. Joshi, J.-C. Gabriel, and G. Grüner. Nanoelectronic carbon dioxide sensors. *Advanced Materials*, 16(22):2049–2052, 2004.

[23] N. Kiga, Y. Takei, A. Inaba, H. Takahashi, K. Matsumoto, and I. Shimoyama. CNT-FET gas sensor using a functionalized ionic liquid as gate. In *2012 IEEE*

25th International Conference on Micro Electro Mechanical Systems (MEMS, pp. 796–799. IEEE, 2012.

[24] S. S. Sabri, J. Guillemette, A. Guermoune, M. Siaj, and T. Szkopek. Enhancing gas induced charge doping in graphene field effect transistors by non-covalent functionalization with polyethyleneimine. *Applied Physics Letters*, 100(11):1–3, 2012.

[25] A. Inaba, G. Yoo, Y. Takei, K. Matsumoto, and I. Shimoyama. A graphene FET gas sensor gated by ionic liquid. In *2013 IEEE 26th International Conference on Micro Electro Mechanical Systems (MEMS)*, pp. 969–972. IEEE, 2013.

[26] P. Feng, F. Shao, Y. Shi, and Q. Wan. Gas sensors based on semiconducting nanowire field-effect transistors. *Sensors*, 14(9):17406–17429, 2014.

[27] P. Bondavalli, P. Legagneux, and D. Pribat. Carbon nanotubes based transistors as gas sensors: state of the art and critical review. *Sensors and Actuators B: Chemical*, 140(1):304–318, 2009.

[28] M. Holzinger, J. Maier, and W. Sitte. Potentiometric detection of complex gases: application to CO2. *Solid State Ionics*, 94(1-4):217–225, 1997.

[29] J. Zosel, W. Oelßner, M. Decker, G. Gerlach, and U. Guth. The measurement of dissolved and gaseous carbon dioxide concentration. *Measurement Science and Technology*, 22(7):1–45, 2011.

[30] J. W. Fergus. A review of electrolyte and electrode materials for high temperature electrochemical CO2 and SO2 gas sensors. *Sensors and Actuators B: Chemical*, 134(2):1034–1041, 2008.

[31] J. Ramirez-Salgado and P. Fabry. Study of CO2 electrodes in open devices of potentiometric sensors. *Solid State Ionics*, 158(3-4):297–308, 2003.

[32] Y. Sadaoka, Y. Sakai, and T. Manabe. Detection of CO2 using a solid-state electrochemical sensor based on sodium ionic conductors. *Sensors and Actuators B: Chemical*, 15(1-3):166–170, 1993.

[33] H. B. Shim, J. H. Kang, J. W. Choi, and K. S. Yoo. Characteristics of thick-film CO2 sensors based on NASICON with Na2 CO3-CaCO3 auxiliary phases. *Journal of Electroceramics*, 17(2-4):971–974, 2006.

[34] C. Park, S. Akbar, and W. Weppner. Ceramic electrolytes and electrochemical sensors. *Journal of Materials Science*, 38(23):4639–4660, 2003.

[35] H.-H. Mobius. Galvanic solid electrolyte cells for the measurement of CO2 concentrations. *Journal of Solid State Electrochemistry*, 8(2):94–109, 2004.

[36] J. Hodgkinson and R. P. Tatam. Optical gas sensing: a review. *Measurement Science and Technology*, 24(1):1–59, 2013.

[37] L. B. Mendes, N. W. Ogink, N. Edouard, H. J. C. Van Dooren, I. F. F. Tinôco, and J. Mosquera. NDIR gas sensor for spatial monitoring of carbon dioxide concentrations in naturally ventilated livestock buildings. *Sensors*, 15(5):11239–11257, 2015.

[38] J. Puton, T. Palko, A. Knap, K. Jasek, and B. Siodlowski. Module for measurement of CO2 concentration in exhaled air. In *Optoelectronic and Electronic Sensors V*, vol. 5124, pp. 278–283. International Society for Optics and Photonics, 2003.

[39] C. Hummelgard, I. Bryntse, M. Bryzgalov, J.-A. Henning, H. Martin, M. Noren, and H. Rodjegard. Low-cost NDIR based sensor platform for sub-ppm gas detection. *Urban Climate*, 14:342 – 350, 2015. New Sensing Technologies and Methods for Air Pollution Monitoring.

[40] J. Hodgkinson, R. Smith, W. O. Ho, J. R. Saffell, and R. P. Tatam. Non-dispersive infra-red (NDIR) measurement of carbon dioxide at 4.2 μm in a compact and optically efficient sensor. *Sensors and Actuators B: Chemical*, 186(1):580–588, 2013.

[41] H. Xia, W. Liu, Y. Zhang, R. Kan, M. Wang, Y. He, Y. Cui, J. Ruan, and H. Geng. An approach of open-path gas sensor based on tunable diode laser absorption spectroscopy. *Chinese Optics Letters*, 6(6):437–440, 2008.

[42] D. Gibson and C. MacGregor. Self powered non-dispersive infra-red CO2 gas sensor. In *Journal of Physics: Conference Series*, vol. 307, p. 012057. IOP Publishing, 2011.

[43] P. Werle, F. Slemr, K. Maurer, R. Kormann, R. Mücke, and B. Jänker. Near- and mid-infrared laser-optical sensors for gas analysis. *Optics and Lasers in Engineering*, 37(2-3):101–114, 2002.

[44] H. Nasim and Y. Jamil. Recent advancements in spectroscopy using tunable diode lasers. *Laser Physics Letters*, 10(4):1–14, 2013.

[45] J. McManus, D. Nelson, J. Shorter, R. Jimenez, S. Herndon, S. Saleska, and M. Zahniser. A high precision pulsed quantum cascade laser spectrometer for measurements of stable isotopes of carbon dioxide. *Journal of Modern Optics*, 52(16):2309–2321, 2005.

[46] N. M. Davis, J. Hodgkinson, D. Francis, and R. P. Tatam. Sensitive detection of methane at 3.3 μm using an integrating sphere and interband cascade laser. In *Optical Sensing and Detection IV*, vol. 9899, pp. 1–6. International Society for Optics and Photonics, 2016.

[47] J. Hodgkinson, D. Masiyano, and R. P. Tatam. Using integrating spheres as absorption cells: path-length distribution and application of Beer's law. *Applied Optics*, 48(30):5748–5758, 2009.

[48] E. Hawe, P. Chambers, C. Fitzpatrick, and E. Lewis. CO2 monitoring and detection using an integrating sphere as a multipass absorption cell. *Measurement Science and Technology*, 18(10):3187, 2007.

[49] E. Crosson. A cavity ring-down analyzer for measuring atmospheric levels of methane, carbon dioxide, and water vapor. *Applied Physics B*, 92(3):403–408, 2008.

[50] T. Kissinger. *Range-resolved optical interferometric signal processing*. Ph.D. thesis, Cranfield University, 2015.

[51] K. Grattan and T. Sun. Fiber optic sensor technology: an overview. *Sensors and Actuators A: Physical*, 82(1-3):40–61, 2000.

[52] H. Segawa, E. Ohnishi, Y. Arai, and K. Yoshida. Sensitivity of fiber-optic carbon dioxide sensors utilizing indicator dye. *Sensors and Actuators B: Chemical*, 94(3):276–281, 2003.

[53] W. Ma, R. Wang, Q. Rong, Z. Shao, W. Zhang, T. Guo, J. Wang, and X. Qiao. CO2 gas sensing using optical fiber Fabry-Perot interferometer based on polyethyleneimine/poly(vinyl alcohol) coating. *IEEE Photonics Journal*, 9(3):1–8, 2017.

[54] L. Melo, G. Burton, B. Davies, D. Risk, and P. Wild. Highly sensitive coated long period grating sensor for CO2 detection at atmospheric pressure. *Sensors and Actuators B: Chemical*, 202(1):294–300, 2014.

[55] B. Shivananju, S. Yamdagni, R. Fazuldeen, A. Sarin Kumar, G. Hegde, M. Varma, and S. Asokan. CO2 sensing at room temperature using carbon nanotubes coated core fiber Bragg grating. *Review of Scientific Instruments*, 84(065002):1–7, 2013.

[56] J. Hromadka, B. Tokay, R. Correia, S. P. Morgan, and S. Korposh. Carbon dioxide measurements using long period grating optical fibre sensor coated with metal organic framework HKUST-1. *Sensors and Actuators B: Chemical*, 255(1):2483–2494, 2018.

Chapter 3

Long period gratings: Theory and fabrication

It was highlighted in Chapter 2 that LPGs would be the most suitable sensing platform for this project. Therefore a review of this technology is warranted.

First proposed by Vengsarkar *et al.* [1] in 1996, LPGs have gained considerable interest over the past two decades, where these in-fibre gratings have been utilised, not just for fibre sensing, but also as band rejection filters [1] and optical switches [2]. Nevertheless, this chapter will apply particular emphasis on the sensing applications of LPGs in order to provide a foundation for the subsequent experimental work outlined in this thesis. Initially, a description of the basic theory of light propagation in an optical fibre and the fundamental properties of an LPG will be presented. Additionally, the numerical modelling of LPGs will be described, followed by a discussion on the sensitivity of LPGs to environmental perturbation and a review of the various methods that have been implemented for their fabrication. Finally, a review of multi-parameter sensing using LPGs will be provided.

3.1 Principle of optical fibre operation

Optical fibres operate through the propagation of modes, which are self-consistent electromagnetic waves that propagate energy in a waveguide [3]. Using ray theory, it is possible to glean a mechanistic understanding of modal propagation in an optical fibre.

Fig. 3.1 shows a typical design of a step index fibre where the high refractive index core (n_1) is surrounded by cladding (n_2) with a lower index. The difference in

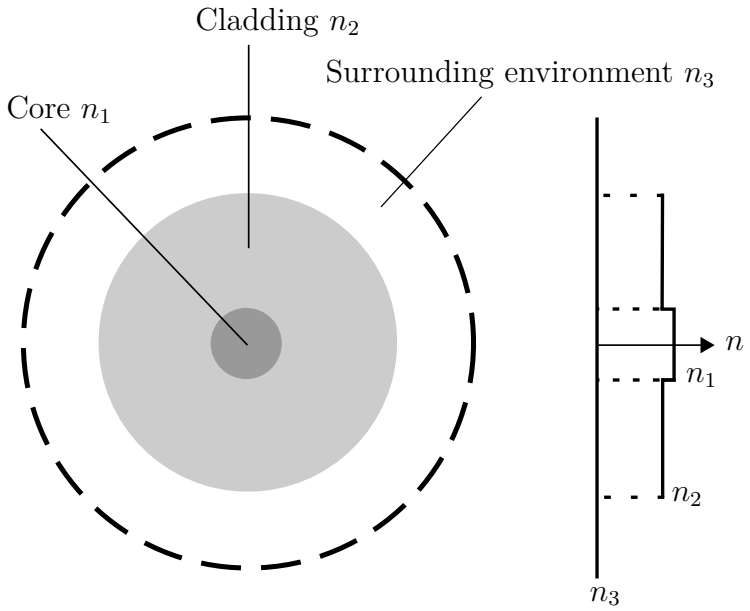

Figure 3.1: Typical structure of a step-index optical fibre with accompanying refractive index profile highlighting the difference in refractive index between core and cladding.

refractive index at the core-cladding dielectric boundary confines the ray inside the fibre on the condition that the angle of the incident between the two media is greater than the critical angle (θ_c) of the fibre, where θ_c is defined as $\theta_c = \sin^{-1}(n_2/n_1)$ [4]. Certain optical fibres, termed multi-mode, are able to support numerous modes (Fig. 3.2a) depending on the wavelength of the incident beam and the fibre's physical parameters (core radius, n_1 and n_2). Although multi-mode fibre allows for more efficient coupling (large core radius and numerical aperture), this type of waveguide suffers from modal dispersion causing pulses of light to spread due to the higher order modes travelling slower than their lower order counterparts.

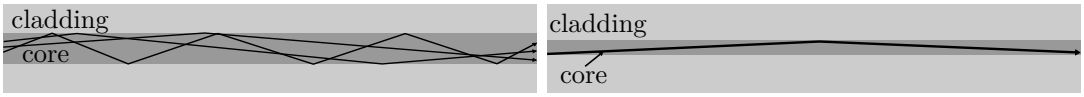

(a) Multi-mode fibre **(b)** Single-mode fibre

Figure 3.2: Geometrical comparison between multi-mode (a) and single-mode (b) fibre highlighting the ray propagation in each instance. Single-mode fibre allows only the fundamental mode to propagate where as multi-mode can support numerous modes of varying orders. Adapted from [5]

Utilisation of single-mode optical fibre, which possess a small core radius (in the region of a few micrometers), allows core propagation of only a single, fundamental mode at wavelengths above the fibre's cut-off frequency (Fig. 3.2b), consequently removing the issue of modal dispersion. To gain a more detailed understanding of the propagation characteristics in a single-mode fibre, Maxwell's equations and

appropriate boundary conditions must be employed [6].

A brief description of the pertinent aspects of the propagation of electromagnetic radiation in optical fibres is provided below. Numerous sources are available in which a detailed explanation and full derivation can be found [3, 6, 5]. Since optical fibres possess cylindrical symmetry, it is convenient to represent the wave equation using the cylindrical coordinate system. As we are concerned with the propagation of light along the fibre's axis (z-component), the wave equation can be expressed in terms of the axial components of the electric (E_z) and magnetic fields (H_z), taking the form [3],

$$\frac{\partial^2\psi}{\partial r^2} + \frac{1}{r}\frac{\partial\psi}{\partial r} + (k^2 - \beta^2 - \frac{1}{r^2})\psi = 0, \tag{3.1}$$

where $\psi = E_z, H_z$, r is the radial coordinate, β is the propagation constant, $k = \omega^2 n^2/c$, where in this case c is the speed of light in free space and ω is the angular frequency $= 2\pi f$, with f indicating frequency. Solutions to Equation 3.1 provide discrete values of β dependant on the wavelength of light and the physical parameters of the optical fibre given by,

$$\beta = \frac{\omega n_{eff}}{c} = \frac{2\pi n_{eff}}{\lambda_0}, \tag{3.2}$$

where n_{eff} is the effective refractive index of the waveguide and λ_0 is the wavelength in free space. The discrete β values of modes propagating in the core are confined to $n_2 k_0 < |\beta| < n_1 k_0$ where k_0 is the propagation constant of free space and is defined as $k_0 = 2\pi/\lambda$ [7]. In addition to core modes, radiation modes are also solutions to the wave equation. These non-propagating modes cause a continual loss of power from the core when the refractive index of the environment surrounding the fibre (n_3) is greater than that of the cladding; however, if $n_3 < n_2$ (e.g. when the medium surrounding the cladding is air) these radiation modes, termed cladding modes, are bound to the cladding and are able to propagate within this region with discrete propagation constants confined to, $n_3 k_0 < |\beta| < n_2 k_0$ [8, 9]. It is possible for energy transfer to occur between core and cladding modes if their associated electric fields overlap. Utilising suitable modulation to the fibre's physical parameters allows phase matching of the electric fields to occur and is the basic principle of operation for LPGs [10].

3.2 Long period gratings

LPGs are formed of periodic refractive index perturbations in the core of the optical fibre with a typical periodicity between 100 - 1000 μm [11]. A standard LPG consists of a single element with a uniform period for the entire length of the grating (Fig. 3.3). These in-fibre phase gratings cause the core mode of the fibre to interact with a set of forward propagating cladding modes.

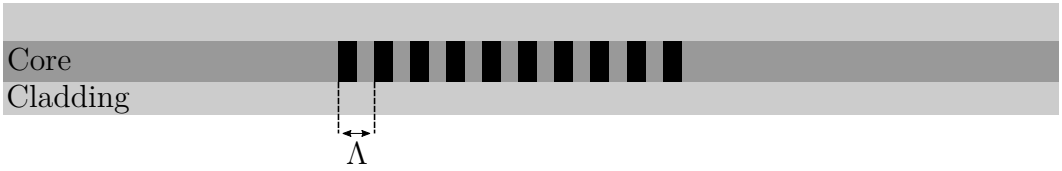

Figure 3.3: A uniform LPG with period Λ, where dark sections indicate refractive index perturbations. Adapted from [12]

However, cladding modes are more susceptible than the core mode to extinction through losses created by scattering, bending, and the refractive index of materials surrounding the cladding, and are therefore rapidly attenuated [13]. As a result, distinct attenuation bands are visible in the transmission spectrum centred at particular wavelengths governed by the phase matching expression [14],

$$\lambda_{(x)} = \frac{(n_{core} - n_{clad(x)})\Lambda}{N}, \tag{3.3}$$

where $\lambda_{(x)}$ is the central wavelength of the attenuation band, n_{core} is the effective refractive index of the mode propagating in the core, $n_{clad(x)}$ is the effective refractive index xth radial cladding mode, Λ is the period of the grating, and $N = 1, 2, 3 \ldots$ is the order of diffraction. An example of a typical transmission spectrum can be seen in Fig. 3.4.

The transmission loss, T_i, of the resonance bands in an LPG spectrum is dependent on the strength of the coupling constant and the grating length [15].

$$T_i = 1 - \sin^2(\kappa_i L_g), \tag{3.4}$$

where κ_i is the coupling constant for ith mode and L_g is the length of the grating. The coupling constant κ_i is a function of the overlap integral of the core and cladding modes and also the amplitude of the refractive index modulation [11].

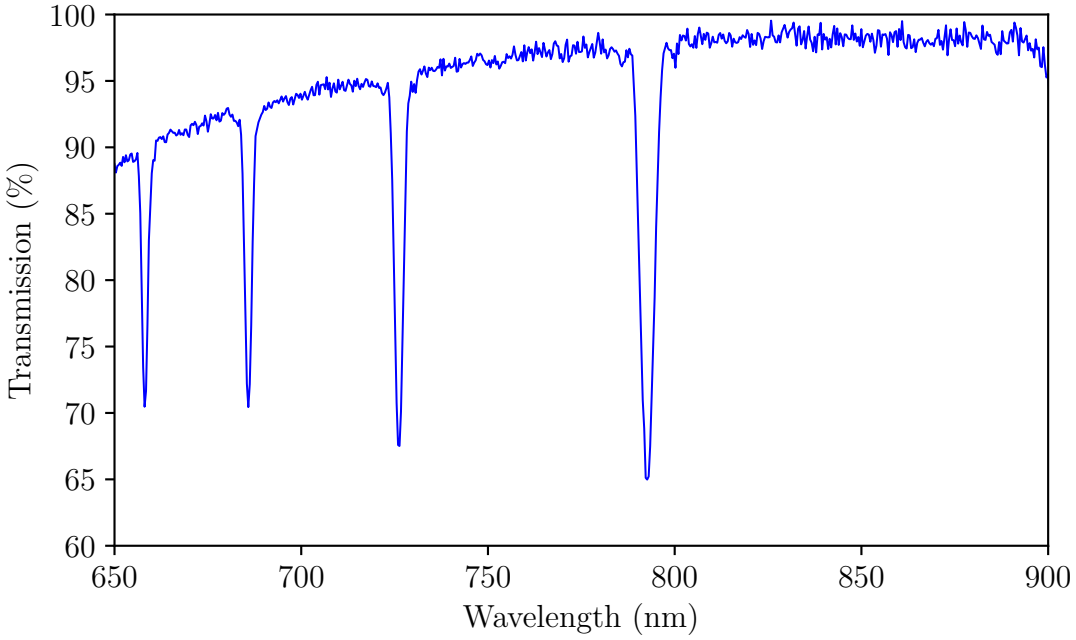

Figure 3.4: The transmission spectrum of a LPG of 40 mm length and period 160 μm.

3.3 Numerical analysis of long period gratings

Accurate prediction of the resonance bands' central wavelengths is essential for determining the period needed to produce an LPG with the desired spectral features. There are two broad mathematical approaches that are used to describe the behaviour of an LPG. The first method, and the simplest, considers the fibre in two layers where the cladding modes are calculated using only the parameters of the cladding and surrounding environment [16]. This approach is based on a number of assumptions: the core is neglected on the basis it is dimensionally small relative to the cladding and the majority of the cladding mode profile propagates in the cladding; the grating has a uniform period; the refractive index profile has circular symmetry; the induced index modulation is small; and the waveguide is considered weakly guiding [9]. Under the conditions of weak guidance, the modes are linearly polarised in the transverse field and are termed LP_{vj} modes (where v and j represent azimuthal and radial order respectively) on the assumption $\Delta \ll 1$, where [16]

$$\Delta = \frac{n_{core} - n_{clad}}{n_{core}}. \tag{3.5}$$

Although this approach allows for rapid calculation of dispersion curves, in reality there is a significant overlap between core and cladding modal fields, as such, the presence of the core has a significant influence on the cladding mode properties thus

this method is more appropriate for qualitative analysis .

The second method involves the use of a three-layer system. This approach is correspondingly more complex than the two-layer system and takes the core, cladding and surrounding environment into consideration. A general three-layer numerical method for calculating transmittance of UV-induced gratings without azimuthal field variations in step-index fibres is extensively described in [13]. However, alternative methods to UV irradiation for fabricating LPGs (see section 3.5) have been shown not to produce a uniform change in cross sectional refractive index, as such, have an azimuthal dependence. Through the use of the transfer matrix method, Anemogiannis *et al.* [17] showed that it is possible to simulate LPG structures with azimuthal and radial refractive index variations. Additionally, this generalised model can be used to describe the behaviour of an LPG with an overlay applied to the cladding surface [18].

The accuracy of the numerical model is highly dependant upon the waveguide parameters (core/cladding refractive indices and radii). In commonly used optical fibre (e.g. SMF28), the manufacturing process is highly repeatable and therefore these parameters are known to a sufficient level of accuracy to allow accurate modelling of the resonance features. However, in more specialist fibre (e.g. PS750) this is not the case and thus resulting in a disparity between modelled and empirical data (this is further discussed in Chapter 5).

All numeric modelling undertaken in this thesis was based upon the methods outlined in [17], and therefore a comprehensive description can be found below.

3.3.1 Formulation

The LP approximation was applied to a cylindrical dielectric waveguide where the validity of the approximation is still appropriate for lower orders even where the refractive index difference between the cladding and ambient air is non-negligible. Propagating along the z-axis, the transverse electric field component for LP_{vj} mode is given by [17],

$$\begin{aligned} U_{vj,i}(r,\phi,z) &= exp(-j\beta_{vjz})\Psi_{vj,i}(r,\phi) = exp(-j\beta_{vjz})\Phi_v(\phi)R_{vj,i}(r) \\ &= exp(-j\beta_{vjz}) \begin{Bmatrix} \cos(v\phi) \\ \sin(v\phi) \end{Bmatrix} \\ &\times \begin{Bmatrix} A_{vj,i}J_v(r\gamma_{vj,i}) + B_{vj,i}Y_v(r\gamma_{vj,i}) & when\ \beta_{vj} < k_0 n_i \\ A_{vj,i}I_v(r\gamma_{vj,i}) + B_{vj,i}K_v(r\gamma_{vj,i}) & when\ \beta_{vj} > k_0 n_i \end{Bmatrix} \end{aligned} \tag{3.6}$$

where β_{vj} is the longitudinal propagation constant of mode LP_{vj}, $\gamma_{vj,i} = \sqrt{|k_0^2 n_i^2 - \beta_{vj}^2|}$ is the magnitude of the transverse wavenumber, ϕ is the azimuthal angle and $A_{vj,i}$ and $B_{vj,i}$ are arbitrary field coefficients within each cylindrical layer, i. $J_v(r\gamma_{vj,i})$ and $Y_v(r\gamma_{vj,i})$ are the ordinary Bessel functions of the first and second kind of order v, and $I_v(r\gamma_{vj,i})$ and $K_v(r\gamma_{vj,i})$ are the modified Bessel functions of the first and second kind of order v with v being a non-negative integer.

In order to determine the propagation constants for LP modes, the transfer matrix formula was applied. The radial field for an LP_{vj} mode is written as

$$\begin{aligned} R_{vj,i}(r) &= A_{vj,i}\boldsymbol{C_v}(r\gamma_{vj,i}) + B_{vj,i}\boldsymbol{D_v}(r\gamma_{vj,i}) \\ &= \begin{Bmatrix} A_{vj,i}J_v(r\gamma_{vj,i}) + B_{vj,i}Y_v(r\gamma_{vj,i}) \\ A_{vj,i}I_v(r\gamma_{vj,i}) + B_{vj,i}K_v(r\gamma_{vj,i}) \end{Bmatrix} \quad \begin{matrix} when\ \beta_{vj} < k_0 n_i \\ when\ \beta_{vj} > k_0 n_i \end{matrix} \end{aligned} \tag{3.7}$$

where $\boldsymbol{C_v}$ and $\boldsymbol{D_v}$ are either ordinary or modified Bessel functions depending on which fibre region the propagating mode is confined to. Continuity of tangential fields across the interface of two consecutive cylindrical layers must be applied so that R and $\frac{dR}{dr}$ are equivalent at radius $r = r_i$ satisfying the equations,

$$\begin{aligned} R_{vj,i} &= R_{vj,i+1} \\ &\Rightarrow A_{vj,i}\boldsymbol{C_v}(r_i\gamma_{vj,i}) + B_{vj,i}\boldsymbol{D_v}(r_i\gamma_{vj,i}) \\ &= A_{vj,i+1}\boldsymbol{C_v}(r_i\gamma_{vj,i+1}) + B_{vj,i+1}\boldsymbol{D_v}(r_i\gamma_{vj,i+1}) \end{aligned} \tag{3.8}$$

and

$$\begin{aligned} \frac{dR_{vj,i}(r_i)}{dr} &= \frac{dR_{vj,i+1}(r_i)}{dr} \\ &\Rightarrow \gamma_{vj,i}[A_{vj,i}\boldsymbol{C'_v}(r_i\gamma_{vj,i}) + B_{vj,i}\boldsymbol{D'_v}(r_i\gamma_{vj,i})] \\ &= \gamma_{vj,i+1}[A_{vj,i+1}\boldsymbol{C'_v}(r_i\gamma_{vj,i+1}) + B_{vj,i+1}\boldsymbol{D'_v}(r_i\gamma_{vj,i+1})], \end{aligned} \tag{3.9}$$

where $\boldsymbol{C'_v}$ and $\boldsymbol{D'_v}$ denote derivatives with respect to r. The matrix equation for a single homogeneous cylindrical layer is derived through solution of Equations 3.8 and 3.9 and is written as,

$$\begin{aligned} \begin{pmatrix} A_{vj,i} \\ B_{vj,i} \end{pmatrix} &= \begin{pmatrix} \frac{m_{11}^{i,i+1}(\beta_{vj})}{Q_i} & \frac{m_{12}^{i,i+1}(\beta_{vj})}{Q_i} \\ \frac{m_{21}^{i,i+1}(\beta_{vj})}{Q_i} & \frac{m_{22}^{i,i+1}(\beta_{vj})}{Q_i} \end{pmatrix} \begin{pmatrix} A_{vj,i+1} \\ B_{vj,i+1} \end{pmatrix} \\ &= M_{i,i+i} \begin{pmatrix} A_{i+1} \\ B_{i+1}, \end{pmatrix} \end{aligned} \tag{3.10}$$

where the elements of the matrix, $M_{i,i+i}$ and Q_i are defined as,

$$\begin{aligned}
m_{11}^{i,i+1}(\beta_{vj}) &= \gamma_{vj,i}\boldsymbol{D'_v}(r_i\gamma_{vj,i})\boldsymbol{C_v}(r_i\gamma_{vj,i+1}) - \gamma_{vj,i+1}\boldsymbol{D_v}(r_i\gamma_{vj,i})\boldsymbol{C'_v}(r_i\gamma_{vj,i+1}) \\
m_{12}^{i,i+1}(\beta_{vj}) &= \gamma_{vj,i}\boldsymbol{D'_v}(r_i\gamma_{vj,i})\boldsymbol{D_v}(r_i\gamma_{vj,i+1}) - \gamma_{vj,i+1}\boldsymbol{D_v}(r_i\gamma_{vj,i})\boldsymbol{D'_v}(r_i\gamma_{vj,i+1}) \\
m_{21}^{i,i+1}(\beta_{vj}) &= \gamma_{vj,i+1}\boldsymbol{C_v}(r_i\gamma_{vj,i})\boldsymbol{C'_v}(r_i\gamma_{vj,i+1}) - \gamma_{vj,i}\boldsymbol{C'_v}(r_i\gamma_{vj,i})\boldsymbol{C_v}(r_i\gamma_{vj,i+1}) \\
m_{22}^{i,i+1}(\beta_{vj}) &= \gamma_{vj,i+1}\boldsymbol{C_v}(r_i\gamma_{vj,i})\boldsymbol{D'_v}(r_i\gamma_{vj,i+1}) - \gamma_{vj,i}\boldsymbol{C'_v}(r_i\gamma_{vj,i})\boldsymbol{D_v}(r_i\gamma_{vj,i+1}) \\
Q_i &= \begin{cases} \frac{2}{\pi r_i} & when\ \beta_{vj} < k_0 n_i \\ \frac{-1}{r_i} & when\ \beta_{vj} > k_0 n_i. \end{cases}
\end{aligned} \tag{3.11}$$

The global matrix that relates the inner layer, $i = 1$ (core), to the outermost ambient layer, $i = N + 1$, can be expressed as

$$\begin{pmatrix} A_{vj,1} \\ B_{vj,1} \end{pmatrix} = M_{1,2}M_{2,3}\cdots M_{N,N+1}\begin{pmatrix} A_{vj,N+1} \\ B_{vj,N+1}. \end{pmatrix} \tag{3.12}$$

Thus for a three layer waveguide

$$\begin{pmatrix} A_{vj,1} \\ B_{vj,1} \end{pmatrix} = M_{1,2}M_{2,3}\begin{pmatrix} A_{vj,3} \\ B_{vj,3}. \end{pmatrix} \tag{3.13}$$

For finite fields, the coefficients $A_{vj,N+1}$ and $B_{vj,1}$ must be zero, therefore the propagation constants, β_{vj}, of the waveguide for a particular azimuthal number, v, can be determined by satisfying the following condition,

$$m_{22}^{1,N+1}(\beta_{vj}) = 0 \tag{3.14}$$

where the solutions can be obtained through use of a root solving algorithm (e.g. bisection method).

Table 3.1: PS750 fibre parameters used in the generation of phase matching curves. Data obtained from [12]

Parameter	**Value**
Core radius (μm)	2.0
Cladding radius (μm)	62.6
Core refractive index	1.4533
Cladding refractive index	1.4583
Ambient refractive index	1.0003
Cut-off wavelength (nm)	650

Obtaining the propagation constants allows the effective refractive index of the core

and cladding modes to be deduced for a specific wavelength. Solving Equation 3.3 with the calculated effective refractive indices allows phase matching curves to be calculated (Fig. 3.5). The curves were generated using a Python script (Appendix A) applying parameters of Fibercore PS750 (photosensitive fibre doped with B-Ge) which were used to guide the fabrication of all the LPGs utilised in this thesis (Table 3.1). It can be seen in Fig. 3.5 that the wavelength at which cladding modes are coupled to depend on the period of the LPG. Furthermore, coupling to higher order modes can be achieved through the use of shorter periods and that the resonance bands associated with these modes display a greater wavelength sensitivity to variations in period (as noted by the reduced gradients) than lower order cladding modes.

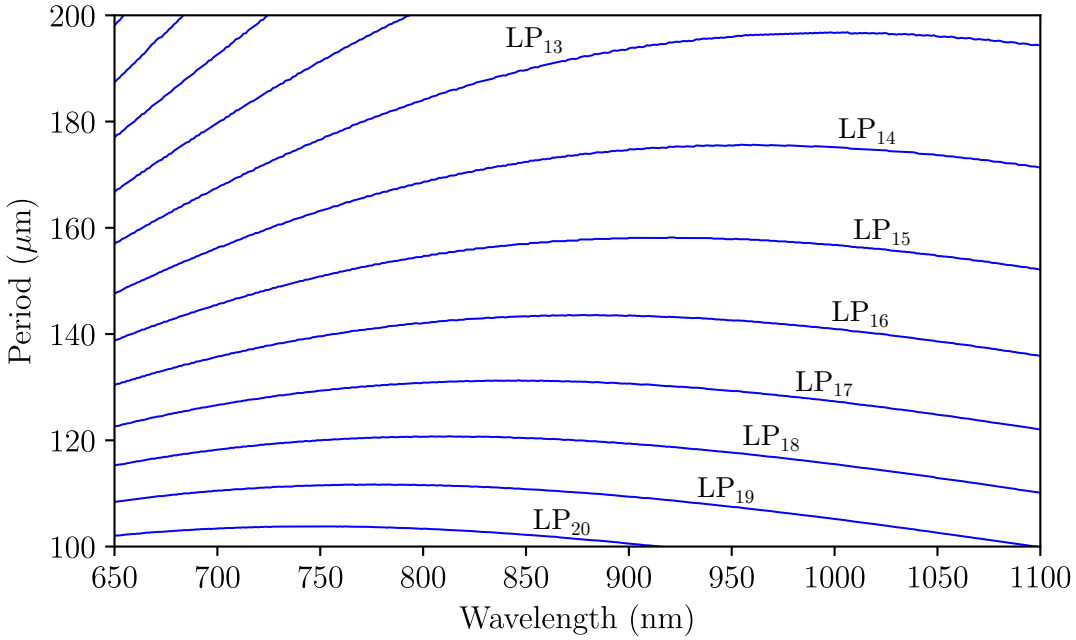

Figure 3.5: Calculated phase matching curves for cladding modes LP_{13} - LP_{20} in PS750 optical fibre

3.4 Long period grating sensitivity characteristics

LPGs are ideally suited as sensing elements due to their innate sensitivity to various physical perturbations such as temperature, strain, bending, and changes in surrounding refractive index. Alteration in one or more of these parameters induces a response in the transmission spectrum via a wavelength shift or a change in the extinction of the resonance bands. Whilst both responses can be used for sensing, wavelength change is an absolute measure and thus preferable, whereas intensity

tracking is susceptible to fluctuations in light source power and connection losses [19].

Although the ability of LPGs to respond to multiple measurands makes them suitable for a multitude of sensing applications, they do, however, require additional considerations in order minimise cross sensitivity. Indeed, various methods have been proposed to desensitise the LPG to a particular measurand while maintaining sensitivity to the parameter of interest e.g. use of expensive temperature insensitive photonic crystal fibre (PCF) [20] or hybrid FBG/LPG sensing system [21]. Alternatively, appropriate choice of LPG parameters (period, amplitude of refractive index change) and suitable interrogation techniques can be employed to discriminate between different physical parameter mediated resonance band responses.

3.4.1 Temperature sensitivity

The temperature sensitivity of LPGs manifests itself in the form of a spectral shift displayed by the resonance bands. To understand the root of temperature sensitivity, it is necessary to differentiate the phase matching expression (Equation 3.3) with respect to temperature, T, [22],

$$\frac{d\lambda}{dT} = \frac{d\lambda}{d(\delta n_{eff})}\frac{d(\delta n_{eff})}{T} + \Lambda\frac{d\lambda}{d\Lambda}\frac{1}{L_g}\frac{dL_g}{dT}, \tag{3.15}$$

where δn_{eff} is the differential effective index between core and cladding modes. Temperature sensitivity exhibited by LPGs is comprised of material and waveguide contributions which are the first and second terms on the right-hand side of Equation 3.15 respectively. The former is related to the change in refractive index of the core and cladding through the thermo-optic effect and arises due to the fibre's composition. This change is also dependent on modal order where the response of lower order modes are greatly dominated by the material contribution while higher order modes are negligibly affected [22]. The waveguide contribution is dependent on the variation in the period caused by thermal expansion/contraction of the core material, and thus, the magnitude and sign of wavelength shifts mediated through temperature responses are dependent upon the cladding mode order [7]. For gratings with period <100 μm the resonance band responds with a positive shift whereas LPGs with periods greater than this show a negative spectral change [23].

With careful consideration of the factors affecting temperature sensitivity, it is possible to fabricate LPGs which are able to respond with positive and negative wavelength shifts. Typically, the temperature response of LPGs is linear with each cladding mode

displaying a different thermal coefficient (Fig. 3.6). Additionally it can be seen from Fig. 3.6 that LPGs display a larger temperature sensitivity than Bragg gratings. It

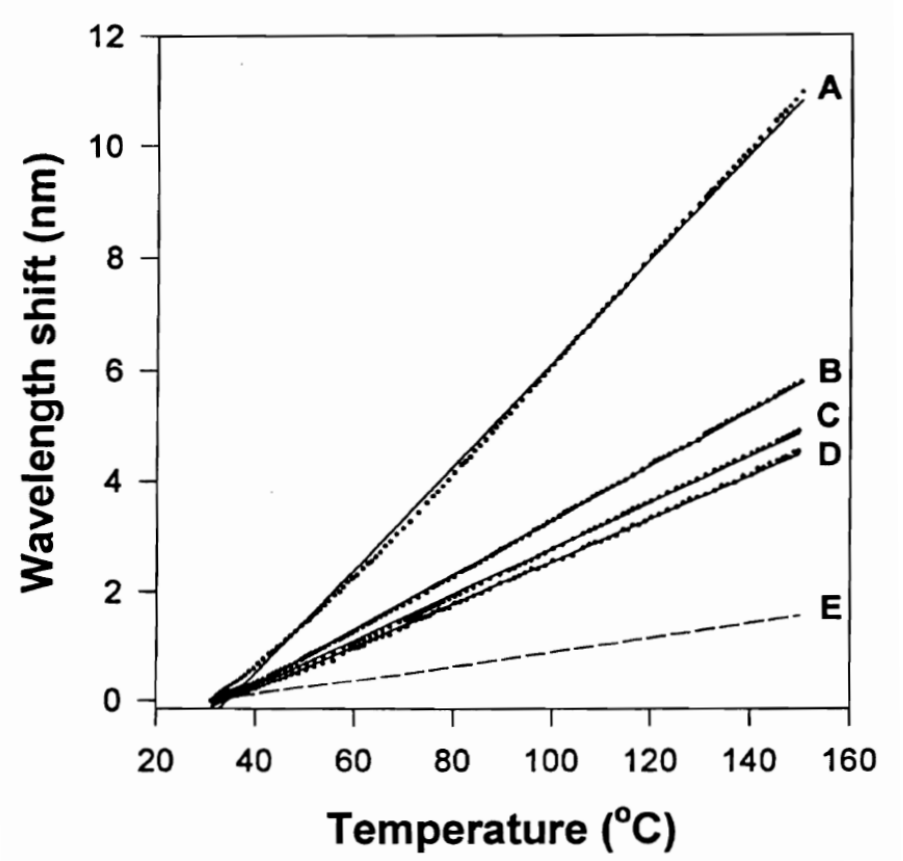

Figure 3.6: The attenuation bands, A-D, of an LPG with period 280 μm show a linear response to changes in temperature. E corresponds to the temperature response of a Bragg grating. Taken from [7]

has been previously shown that it is possible to suppress the temperature sensitivity of LPGs to 0.002 nm·°C^{-1} by adjusting the dopant concentrations of GeO_2 and B_2O_3 in the composition of the fibre [24]. In addition to altering the fibre's composition, it also possible to minimise an LPGs temperature sensitivity by applying a suitable material to the cladding of the fibre [24]. The temperature compensation is achieved through the utilisation of an LPGs susceptibility to variations in surrounding refractive index (discussed further in Section 3.4.3). If the fibre displays a blue shift (negative shift) to a temperature increase produced by its composition then application of a coating material that induces a red shift under the same temperature change can be used to compensate for the thermal mediated spectral transformation. Finally, it is possible to fabricate LPG sensors in relatively temperature insensitive PCF, therefore removing the need for additional compensatory schemes or discriminatory techniques [25].

3.4.2 Strain sensitivity

Similarly to temperature sensitivity of LPGs, axial strain, ϵ, induced effects are dependent on both material and waveguide contributions. Differentiating Equation 3.3 with respect to strain the following expression is obtained [22],

$$\frac{d\lambda}{d\epsilon} = \frac{d\lambda}{d(\delta n_{eff})}\frac{d(\delta n_{eff})}{d\epsilon} + \Lambda\frac{d\lambda}{d\Lambda}, \tag{3.16}$$

The first term on the right-hand side is the material contribution. Axial strain on the fibre changes the core and cladding refractive indices through the strain-optic effect. Additionally, unlike temperature sensitivity, the radii significantly contributes to material effects as the applied strain reduces the core and cladding's transverse dimensions. The second term on the right-hand side describes the waveguide effect, where its contribution arises from the gradient of the dispersion term and is dependent on the period and the cladding mode order [22]. Typically, strain-induced wavelength changes elicit a linear response from attenuation bands with each cladding mode possessing a different coefficient. For LPGs with periods >100 μm, the waveguide effect is positive while material contribution is negative [11]. It is therefore possible, with suitable choice of fibre composition and grating periodicity, to fabricate LPGs with resonance bands that respond to the application of axial strain with positive, negative or zero shifts in wavelength.

The response of different modes can be seen in Fig. 3.7 where each attenuation band provided a different response. Interestingly, the resonance band corresponding to LP_{05} displayed a negligible wavelength change to the application of strain. This ability of certain resonance bands not to produce a wavelength shifts opens up the possibility for multi-parameter sensing (discussed in Section 3.7) through the isolation of the desired measurand. LPGs with appropriate parameter selection typically demonstrate greater sensitivity than FBGs with sensitivities in the region of 2.2 pm$\cdot\mu\epsilon^{-1}$ [11].

3.4.3 Refractive index sensitivity

The origins of an LPG's sensitivity to changes in the surrounding refractive index derives from the dependence of the phase matching condition on the effective refractive index of the cladding. Since this is a function of the the cladding and surrounding refractive indices, any change in the latter can have a significant effect on the coupling wavelength through the phase matching expression. The change in coupling

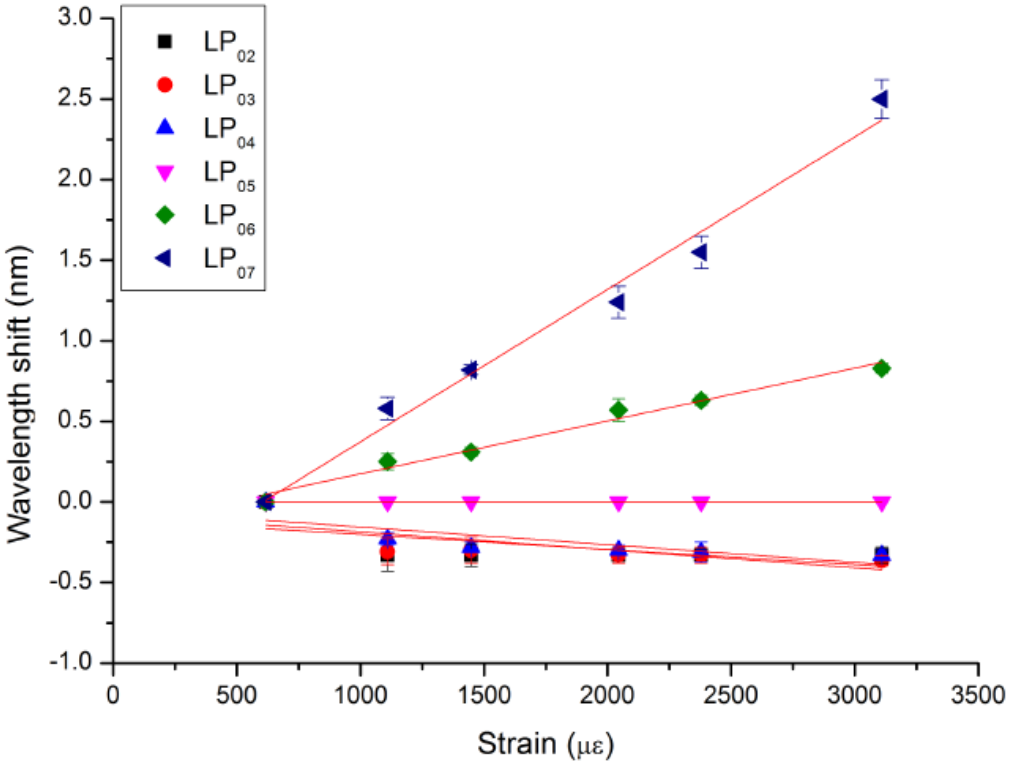

Figure 3.7: The response of resonance bands LP_{02} to LP_{07} to the application of axial strain. The uniform LPG with a period of 400 μm was written in Fibrecore PS750. Taken from [12]

wavelength produced by a change in ambient refractive index can be given by,

$$\frac{d\lambda}{dn_3} = \frac{d\lambda}{dn_{clad}} \frac{dn_{clad}}{dn_3}, \tag{3.17}$$

where n_3 is the surrounding refractive index and n_{clad} is the effective refractive index of the cladding. The expression for refractive index sensitivity is simpler than for temperature and strain due to the grating remaining unchanged under the influence of any ambient refractive index disturbance ($\frac{d\Lambda}{dn_3} = 0$) [7]. Ambient refractive index mediated variations in resonance band central wavelengths are modal dependent, where higher order modes generally display greater sensitivity to perturbations [26]. This susceptibility of higher order modes is due to a larger part of the field interacting with surrounding environment. As such, it is possible to tailor the sensitivity of an LPG through the use of shorter periods in order to couple to these higher-order modes. As the ambient refractive index approaches that of the cladding, the magnitude of the wavelength shifts experienced by the attenuation bands is increased in a non-linear fashion (Fig. 3.8). Once $n_3 = n_2$, the cladding appears to become infinite, losing its ability to support discrete modes resulting in the disappearance of the resonance features [11].

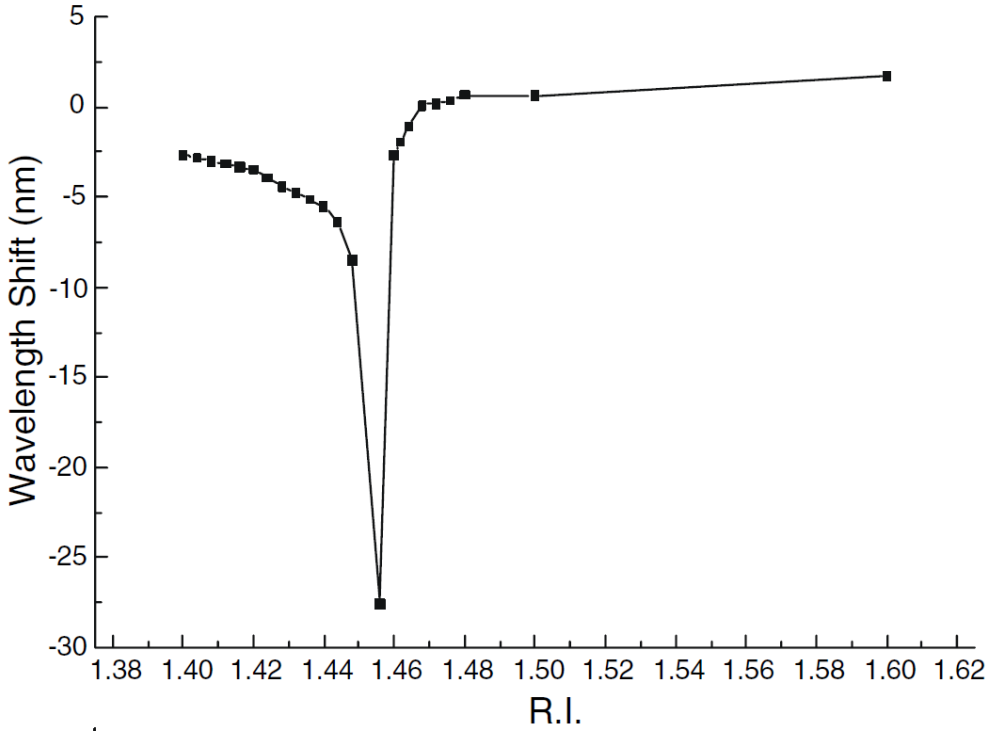

Figure 3.8: Spectral response as a function of external refractive index for an attenuation band of an LPG with period 400 μm. Taken from [11]

This sensitivity to fluctuations in surrounding refractive index has been widely exploited in the literature to demonstrate sensors for determining liquid-level [27], antifreeze concentration [28] and xylene/heptane ratios [29].

3.4.4 Coating deposition on LPGs

The ability of LPGs to respond to refractive index variations from changes in concentrations has allowed these devices to be exploited as chemical sensors [30, 31, 32] (see Section 3.4.3). However, these sensors are not chemical specific, as such, observed changes in refractive index could be induced by sources other than that of the target substance. Additionally, these devices are also limited to solutions with a refractive index lower than that of the cladding (as can be noted by the minimal wavelength shift for $RI > 1.458$ in Fig. 3.8). Nevertheless, it is possible to overcome these restrictions through the deposition of a coating to the cladding of the LPG.

The application of a thin-film overlay to the surface of an LPG causes a shift in central wavelengths of the resonance features [33]. If the coating possess a refractive index greater than that of the cladding, as the thickness of the deposition increases and reaches a certain dimension, cladding modes will begin to be guided by the

overlay material [34]. At this mode transition region, cladding modes undergo a reorganisation with a rapid change in modal effective indices where higher order modes adopt the effective index of the adjoining lower order mode (Fig. 3.9) [35]. This transformation in modal effective indices equates to a rapid change in the central wavelength of each attenuation band. At this point, the effective refractive index of the overlay contains a large imaginary part, reducing the coupling efficiency between core and cladding modes and causing the resonance features to disappear. Increasing the overlay thickness past this region completes the modal reorganisation, re-establishing coupling efficiency and restoring extinction losses in the resonance features [18, 35]. Therefore, to produce a sensor with the greatest sensitivity to changes in the surrounding medium, an appropriate coating thickness which lies in the mode transition region should be selected.

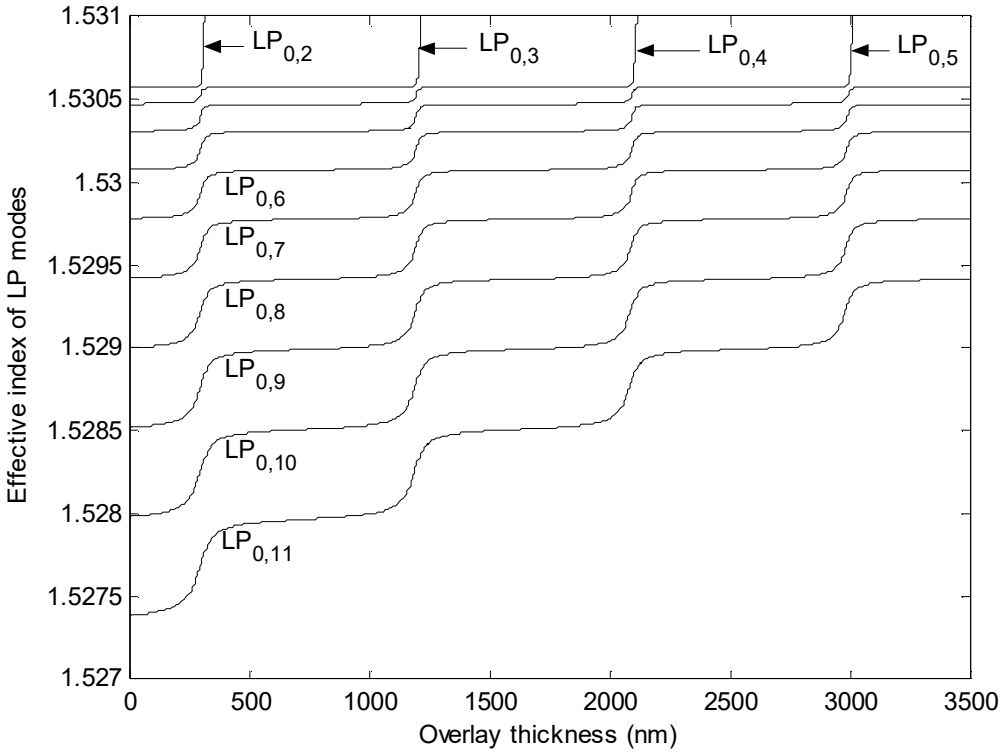

Figure 3.9: The effect of overlay thickness on effective indices of LP modes. Taken from [18]

Coated LPGs have been used extensively for chemical and biological sensors [31, 32, 36, 37] where the overlay has been applied to improve sensitivity and selectivity for the measurand of interest. Typically, coatings can be categorised into either chemical-specific or non-specific coatings.

Non-specific coatings do not react with a particular analyte but rather increase the sensitivity of the LPG through utilisation of the mode transition region. This

scheme has the advantage that the overlays generally do not require refreshing or become poisoned over time through extended exposure or contamination. However, non-specific coatings do not offer selectivity, consequently, an observed response in the device may be due to a competing factor or a combination of factors. Passively coated LPGs have been utilised to augment the distinction between pure gaseous nitrogen and CO_2 [38]. Besides chemical sensing, non-specific coatings may also be used to package an LPG in order to provide temperature insensitivity [24].

Chemical-specific coatings, unlike their non-specific counterparts, provide selectivity in addition to increased sensitivity. Typically, the deposition aims to interact explicitly with the target molecule, often through chemical binding, mediating a refractive index change in the coating. Similar to non-specific coatings, chemical-specific coatings can also tailored to an appropriate thickness to allow access to the sensitive mode transition region [39]. Although an increased selectivity can be gained through the use of chemical-specific coatings, they are, however, prone to a diminishing response and may require refreshing to maintain their initial sensitivity [32]. Furthermore, despite improved selectivity in comparison to LPGs with non-specific coatings, achieving complete specificity for the target molecule with an chemical-specific coating is difficult. Using LPGs with a specific coating, it has been possible to detect concentrations of ammonia to 0.14 ppm [32], chloroform to 5 ppm [30] and toluene to $\sim$100 ppm [31].

3.4.5 Summary of sensitivity characteristics

The sensitivity of LPGs to physical parameters derives from the dependence of the phase matching expression on the changes in the grating's period and the fibre's optical properties. Although LPGs are innately sensitive to all of these environmental parameters, it is possible to dramatically reduce the response of individual parameters through careful grating selection and fibre choice. Furthermore, an LPG's surrounding refractive index sensitivity can be tailored to a specific analyte by applying a coating that demonstrates an affinity for this specie. By applying a CO_2 sensitive coating to an LPG that has been carefully designed, the sensor devised here will demonstrate CO_2 selectivity yet possess insensitivity to additional interfering parameters (e.g. temperature, strain).

3.5 Fabrication techniques

The creation of an LPG requires a refractive index change in the core of the fibre which is predominantly achieved through photo-induction. Other techniques can also be used to form LPGs that involve altering the intrinsic properties of the glass itself. The following section will outline the numerous approaches used to fabricated LPGs and methods of post-treatment with particular emphasis on UV photo-induced techniques due to it pertinence throughout this thesis.

3.5.1 Physical perturbation

Physical deformation of an optical fibre is produced through the use of electrical-arc discharge [40], femtosecond laser exposure [41], irradiation by a CO_2 laser [42] or mechanical manipulation [43]. The subsequent section will provide a brief description of these fabrication processes and discuss the refractive index change mechanism.

CO_2 laser

The use of a CO_2 laser to fabricate in-fibre gratings in standard glass fibre was first proposed by Davis *et al.* [42]. It facilitates the fabrication of LPGs in the majority of fibre types including photonic crystal and photonic band-gap fibres without the need for photosensitive- or hydrogen loaded-fibre (see Section 3.5.2), although the latter has been found to enhance the writing sensitivity with this technique [42]. A conventional CO_2 laser fabrication system is illustrated in Fig. 3.10, where the LPG is created by focussing the beam onto the optical fibre, heating the desired location, and moving the fibre perpendicular to the incident beam to achieve the desired period and grating length. To ensure only the appropriate fibre sections are irradiated, a computer controlled shutter mechanism is used to block the CO_2 laser output during fibre translation.

LPGs fabricated using a CO_2 laser produce the required refractive index modulation via localised modifications to the structural properties of the glass, namely, the relaxation of residual stress (stress originally produced during the manufacture of the fibre) and the densification of the glass [44]. To solely create a refractive index variation, the laser is configured such that the fibre receives short pulse lengths (<450 ms) at a low power (<5 W) [45]. The type and magnitude of the index profile modulation is determined by the composition of the fibre. The refractive index change induced in a Ge-doped fibre is predominantly caused by residual stress relief,

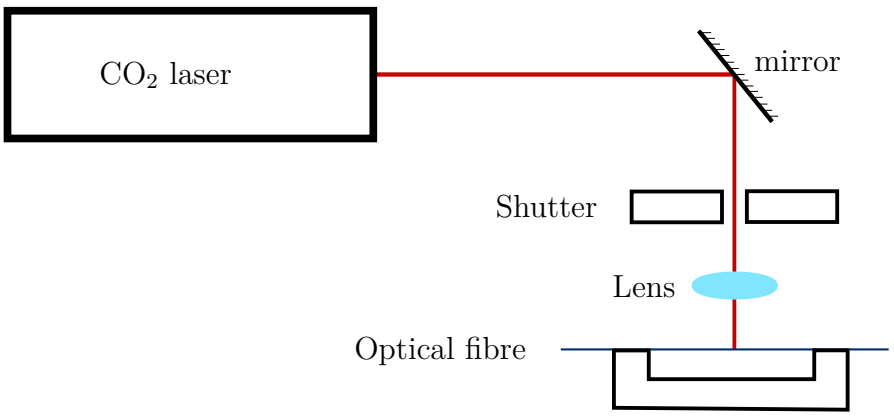

Figure 3.10: A standard arrangement for the fabrication of fibre gratings using a CO_2 laser. Adapted from [44]

producing a decrease in refractive index, while CO_2 laser irradiation of a B-doped fibre induces a positive refractive index change resulting from glass densification [44]. In addition to refractive index modulation, LPGs fabricated using a CO_2 laser can also be created by implementing a geometric taper (Fig. 3.11) via increasing the beam power (5 - 10 W) and applying a slight tension to the fibre [46]. In either scheme, the refractive index modulation occurs in both the core and cladding of the fibre [45].

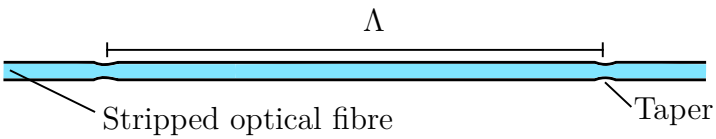

Figure 3.11: Illustration of a typical tapered LPG. The periodic geometric perturbations enhance the refractive index change, augmenting phase matching

A number of fabrication parameters associated with LPGs produced via CO_2 irradiation can influence the quality and reproducibility of the grating. The symmetry of the fibre alteration (i.e. whether the entire circumference of the fibre is exposed to the beam) influences transmission spectra of LPGs, where gratings fabricated with axial symmetry display cleaner spectra with lower insertion losses than asymmetrically produced LPGs [47]. Additionally, controlled heating of the optical fibre is essential to prevent the formation of internal bubbles (over-heating) or applying excessive stress on the fibre (under-heating) [48]. Finally, the vibration of the fibre during the periodic translation can cause inhomogeneous heating as the fibre shifts in and out of the CO_2 laser beam's focal point [44]. Due to these issues, more elaborate fabrication systems than depicted in Fig. 3.10 have been developed. Variations to the standard fabrication system include, the use of a scanning mirror to produce

uniform temperature along the heating zone [48], and a reflector positioned directly behind the fibre to produce a more axially uniform modulation [47].

The greatest advantage offered by LPG sensors produced via CO_2 laser irradiation is their exceptional high temperature stability. This means they are ideally suited as temperature sensors, particularly for operating at high temperatures ($\sim 900°C$) [49] where gratings fabricated using UV exposure are not appropriate.

Electric-arc discharge

Electric-arc discharge predominantly forms LPGs through the rapid heating and cooling of the glass inducing a density alteration, thus a refractive index change [40]. The bare fibre is positioned between two electrodes while held under constant axial tension (Fig. 3.12). The discharge locally heats the fibre for a short duration (200 ms - 2 s) before the fibre is translated by the desired period. This process is repeated until the required length is achieved. This method can also be used to fabricate tapered LPGs (Fig. 3.11).

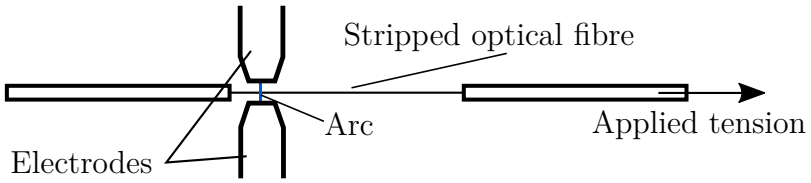

Figure 3.12: Typical arrangement for the fabrication of LPGs using electric-arc discharge

Similar to LPGs produced using a CO_2 laser, electric-arc discharge creates LPGs by locally heating the fibre, allowing the fabrication of LPGs in specialised fibres (PCF, band-gap fibre) and that display high thermal stability [50]. Additionally, this method does not require expensive lasing equipment [40]. However, the asymmetric structure changes induced by the arc can vary with every discharge making it difficult to manufacture LPGs with reproducible characteristics [51].

Femtosecond laser

Femtosecond lasers utilise a similar method to CO_2 lasers where upon exposure to the short laser pulses a densificiation in the glass produces the desired refractive modulation [41]. Generally, the femtosecond laser operates in the infrared region, where the short pulses are focussed onto the fibre, locally heating it to above $500°C$. The thermal effects used to induce the refractive index shift display high

thermal stability up to the fabrication temperature. The temperature sensitivity of a femtosecond laser fabricated LPG with a period of 435 μm was demonstrated to be $\sim$30 pm$\cdot^{\circ}C$ [52], far less than an LPG written using UV irradiation (125 pm$\cdot^{\circ}C$) at a similar period (400 μm) [53]. This difference in temperature sensitivity derives from the fact the refractive index change caused by a femtosecond laser is predominately produced from glass densification rather than an electron transfer induced during UV irradiation (see Section 3.5.2) [52].

Mechanical deformation

The fabrication of LPGs using laser-based techniques involves a large initial investment in equipment before gratings can be produced. As LPGs are formed using relatively large periods, in comparison to FBGs, it is possible to produce a refractive index change mechanically. This can be accomplished by taking advantage of the optical fibre's photoelastic effect by pressing it between a flat surface and a corrugated plate with a set periodicity. In addition to the ease of fabrication, this technique also produces cleaner, lower loss spectra when the plastic jacket is not removed, speculated to be caused by a reduction in micro-bending, in addition to reducing the devices vulnerability to fractures. LPGs induced through mechanical deformation are reversible, as once the perturbation is removed the spectrum returns to its unaltered state [43].

3.5.2 UV Photo-induction

The most common method of manufacturing LPGs is through the use of UV irradiation. Here, unlike LPGs fabricated through physical manipulation, only the core experiences a refractive index change. For gratings to be fabricated using UV, the optical fibre must be photosensitive, which can be achieved by either pre-treating with hydrogen or using a fibre composed of high concentrations of photosensitive dopants. The Ge doping of optical fibre naturally increases the refractive index of the core and introduces photosensitivity through intrinsic defects (Ge-Si wrong bonds) in the glass structure which promote absorption bands at UV wavelengths [54]. The pretreatment of optical fibre using hydrogen, termed hydrogen loading, can vastly improve photosensitivity and has been performed by diffusing hydrogen molecules into the fibre at various temperatures (20 - 145 $^{\circ}C$) and pressures (1 - 200 atm) for 2 - 14 days depending on the magnitude of the parameters (where elevated temperature/pressures enhance the diffusion rate) [55, 56, 57]. The permanent

refractive index change occurs when the hydrogen loaded fibre is exposed to UV or intense heat, causing the dissolved hydrogen to react with Ge sites in the core allowing structural changes (thus a refractive index change) to transpire at every exposed Ge site. The primary mechanism for the increase in refractive index is the formation of Si-OH and GeH groups at normal Si-O-Ge sites [15]. Interestingly, it has been noted that the reaction of hydrogen with Ge sites may in fact continue for up to 2 h post UV exposure, causing a slight red shift in the resonance features [58].

Although hydrogen loading dramatically improves photosensitivity and allows gratings to be written in standard telecommunication fibre, it is also possible to fabricate UV induced gratings in B-Ge codoped fibre without the need for hydrogen diffusion. The addition of boron reduces the refractive index of the glass. This allows for the incorporation of a greater concentration Ge while still maintaining a low core-cladding index difference [15], thus, the greater proportion of Ge promotes an increase in Ge-Si defects [54]. However, B-doped fibre produces additional loses at 1550 nm of 120 dB·km^{-1} in PS1250/1500 (Fibercore) in comparison to 30 dB·km^{-1} at 780 nm in PS750, (Fibercore) and therefore may not be suitable for every application.

Fabrication methods by UV irradiation

The simplest method to produce a UV induced LPG is to use an amplitude mask. The mask is comprised of a fine comb-like structure usually manufactured with chrome-plated silica or laser prepared metal foil [11]. This structure dictates the duty cycle and period of the intended LPG and is located between the UV source and the fibre. Generally, a cylindrical lens is used to produce a line focus orientated in the same plane as the optical fibre. The UV laser irradiates the mask, creating multiple periods simultaneously in a single exposure [59]. The use of an amplitude mask allows for quick and repeatable fabrication of LPGs, ideal for batch production.

Another method for producing LPGs is to build up the the index modulation in a point-by-point fashion. This cumulative technique operates by irradiating a section of the fibre, translating it equal to the LPG's period, and repeating this process until the desired grating length has been achieved. While the amplitude mask predetermines the duty cycle, in the point-by-point method, the UV beam is focused through an adjustable aperture to produce the desired duty cycle. Although a slower process than use of an amplitude mask, the point-by-point technique provides greater flexibility in fabrication parameters adjustments (period, duty cycle) and allows the manufacture of more complicated LPG designs (chirped, phase-shifted) [59].

In both techniques, the amplitude of the refractive index change is determined by

the exposure time each period experiences. Nevertheless, variations in temperature, humidity, irradiation source power and fibre batches can dramatically affect the reproducibility of LPGs written using a single exposure [53]. An alternative technique to the single exposure point-by-point scheme is to repeatedly irradiate each section for a short period of time [59]. Termed the overwrite method, each period is exposed for a short interval (∼5 s), where, once the desired length has been fabricated, the translation stage is returned to its initial position and the process repeated until the required refractive index change has been attained. It was demonstrated that this method improved the repeatability of the production of LPGs and can be utilised to tune gratings such that they possess resonance features at specific wavelengths. This fabrication approach was developed during this project and is discussed in greater detail in Chapter 5.

3.5.3 Post-fabrication treatment

Post fabrication treatments are predominantly used to either stabilise the transmission resonance features to a particular environmental factor, or to fine-tune their wavelength to a specific value. The following section outlines the more common methods used for post-fabrication adjustments.

Annealing

The annealing of a fibre post UV-fabrication serves to stabilise the LPG's optical properties by [1]: 1) outgassing an excess of hydrogen from the core which would otherwise influence its refractive index, thus resonance features' wavelength; 2) providing thermal stability over a long period of time through the removal of unstable UV-created sites which would degrade slowly over time. The conditions needed to anneal an LPG depends on the fibre type, the intended operating temperature and the desired stability [1]. During the annealing process hydrogen initially diffuses quickly from the cladding, altering the differential refractive index between the core and cladding, causing a large wavelength shift in transmission features to occur. This is followed by a slower rate of diffusion from the fibre's core, resulting in the resonance bands returning to their original wavelengths [15]. Typically, annealing is conducted above $150°C$ for up to 42 h, where greater temperatures require less annealing time [1, 58, 60]. Although annealing causes complete removal of hydrogen from within the fibre and allows the immediate use of thermally stable devices, non-reacted hydrogen will naturally diffuse out of the fibre within 20 days of removal from the hydrogen

rich environment [58]. A detailed description of the 4 stage diffusion process can be found in [61]. The annealing process causes a permanent alteration in the LPG's sensitivity [9].

Etching

The ability to tune the central wavelengths of resonance bands post fabrication allows specific transmission spectra to be obtained (i.e. a particular attenuation feature at an exact wavelength). As the phase matching condition (Equation 3.3) is dependant on the physical properties of the cladding (refractive index, radius), it is possible to alter the resonance wavelength through modifying the cladding radius. Reducing the radius can be accomplished by etching the LPG with hydrofluoric acid in a controlled manner [62]. The removal of cladding results in resonance features experiencing a red shift where higher-order modes display a faster rate of change [63].

UV Trimming

In addition to etching, the central wavelengths of resonance features can be altered through the application of UV trimming. This technique involves exposing the LPG to a uniform UV irradiation dose until the required spectrum is achieved [64]. The effect of UV trimming differs depending on the process utilised to introduce photosensitivity in the fibre. In hydrogen-loaded fibre, the regions previously exposed to UV irradiation during fabrication display enhanced photosensitivity in comparison to unexposed sections [65]. This difference in photosensitivity is then exploited during the trimming process, where a uniform dose of UV irradiation increases the amplitude of the index modulation in the exposed regions but not in the non-exposed portions [65]. However, in fibre doped with high concentrations of Ge (non-hydrogen loaded), uniformly exposing the LPG to UV irradiation has been speculated to increase the average index of the fibre, causing a wavelength alteration but, unlike hydrogen-loaded fibre, also degradation in attenuation of the resonance features [59].

3.5.4 Summary of fabrication techniques

The fabrication of LPGs can be achieved through a number of physical techniques, each offering unique advantages (ability to create custom LPGs, temperature stability, creation of reversible gratings) and disadvantages (initial cost of equipment, grating fragility). Nevertheless, LPGs utilised in this thesis will be fabricated via UV

irradiation since this method offers the flexibility to fabricate bespoke sensors and that the Centre for Engineering Photonics is in possession of a UV system. Additionally, the use of annealing post-fabrication will allow temperature sensitivity to be assessed in LPGs, essential for accurate sensor characterisation.

3.6 Variations to the LPG design

The increasing attention that LPGs have attracted over the past few decades has naturally led to the development of variations in the basic design and fabrication techniques. Therefore, the following section outlines some of the common LPG variations.

3.6.1 LPGs at the phase matching turning point

The sensitivity of LPGs to physical perturbations has been shown theoretically and experimentally [26] to be improved by operating at the so-called phase matching turning point (PMTP), or turn around point. All cladding modes exhibit a turning point, however, the PMTPs for lower-order modes are at larger wavelengths, generally out of the wavelength range for standard interrogation techniques. Higher-order-modes on the other hand possess PMTPs that can be clearly observed using a CCD spectrometer [53] or an optical spectrum analyser (OSA) [66] and are accessible through fabricating LPGs with shorter periods (<250 μm) [67]. Near the PMTP it is possible for light to couple to the same cladding mode at two wavelengths producing dual attenuation bands [68]. Fabricating an LPG with a cladding mode accessing the PMTP requires careful consideration of the period, therefore phase matching curves (see Fig. 3.5) are essential in initially identifying an appropriate period.

Although a cladding mode displays its greatest sensitivity at the PMTP (i.e. where $\frac{d\lambda}{d\Lambda} = \infty$) [26], from a sensing perspective, it is problematic to track external mediated changes in an attenuation band operating in this region. For example, a decrease in surrounding refractive index will produce a reduction in intensity of the resonance band, whereas an increase in this parameter will cause the band to shift in wavelength, splitting into two distinct features (Fig. 3.13). Monitoring just one dependent variable (intensity or wavelength) is not appropriate in resolving the parameter change for an LPG operating at the PMTP, consequently, assessment of both variables is required. However, this is impractical, particularly considering intensity is liable to fluctuations through light source power variations and connection losses [19]. It is therefore

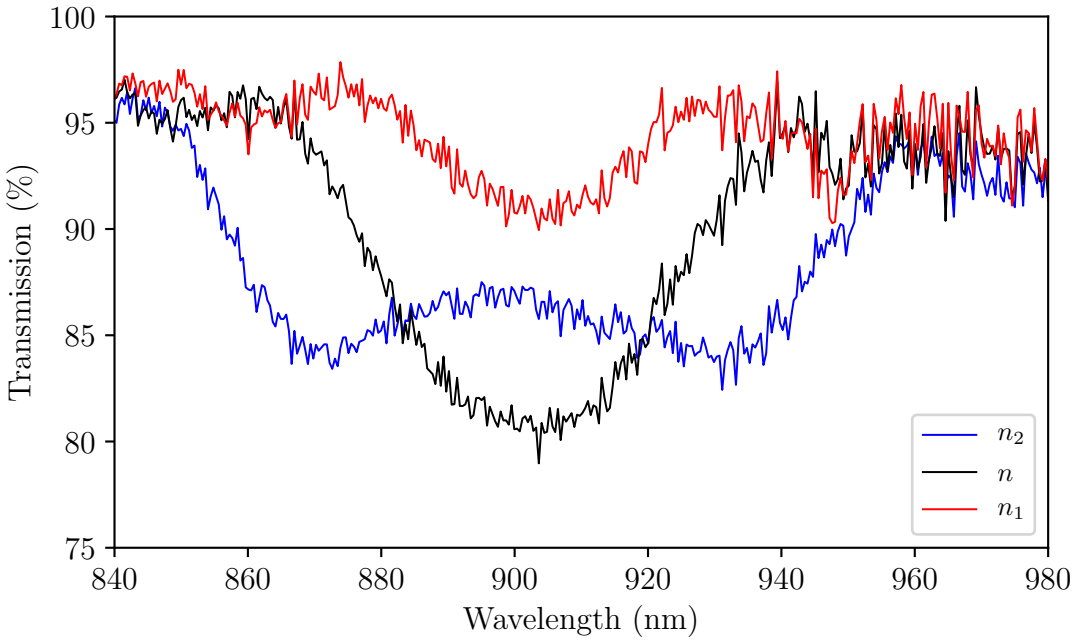

Figure 3.13: The spectra of an LPG operating at the PMTP in different refractive indices where $n_1 < n < n_2$. A decrease in refractive index produces a reduction in intensity (n_1) while an increase causes two distinct resonance bands (n_2).

preferential to utilise an LPG near the PMTP that exhibits dual resonance, thus allowing wavelength analysis to be exclusively employed.

The use of LPGs exploiting the PMTP to optimise sensitivity has been widely implemented in the literature for spectral filtering [69] and in particularly chemical sensing [32, 36, 70]. The increase in sensitivity achieved through the utilisation of the PMTP can be seen in two separate articles developing LPG kerosene sensors. The standard LPG resulted in a sensitivity of 0.6 nm·%$^{-1}$ change in kerosene concentration [71], where an LPG operating at the PMTP demonstrated a sensitivity of 0.949 nm·%$^{-1}$ [70]. Although LPGs operating at the PMTP offer increased sensitivity, they are also more susceptible to external parameters such as temperature [72], therefore to maintain the sensitivity improvement (without loss to poor signal-to-noise ratio) competing variables need to be closely controlled.

3.6.2 Cascaded LPGs

Fabricating a pair of identical LPGs in series along the same fibre (Fig. 3.14), termed cascaded LPGs, has been explored for the use in sensor applications. Cascaded LPGs form an in-fibre Mach-Zehnder interferometer producing a channelled spectrum pattern for each attenuation band (Fig. 3.15). The narrow bandwidth of the interference

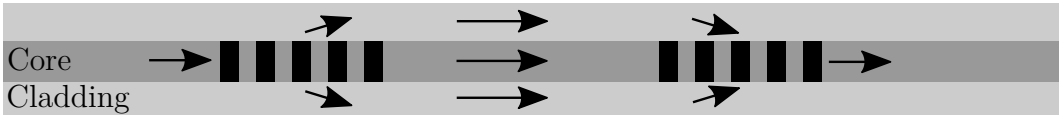

Figure 3.14: Principle of operation for a cascaded LPG. Adapted from [11]

fringes is fine enough that a resolution greater than a standard LPG is achievable [11]. Cascaded LPGs operate by coupling the incident light to cladding modes at the first grating, in the same manner as a standard LPG. Light continues to propagate in the core and cladding towards the second grating in the non-modulated section. Upon reaching the second grating, energy from cladding modes is coupled back into the core. The disparity between the cladding's refractive index and the core's produces a phase shift between the light in the cladding and core. Upon coupling back into the core, the phase shifted light interacts with light already propagating in this region producing interference features [73]. Varying the distance between the two LPGs causes a change in frequency of the interference fringes within the resonance bands, where a greater separation increases the number of visible peaks [74].

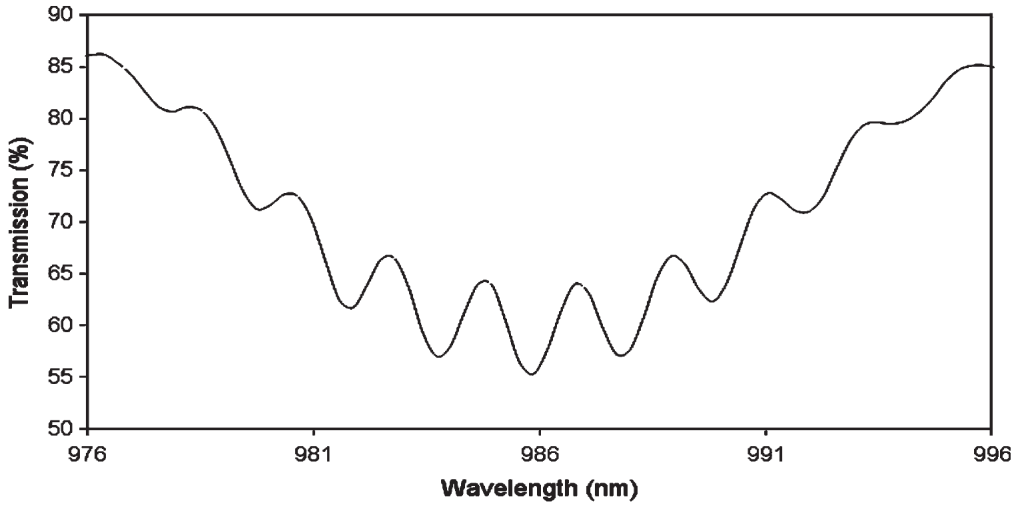

Figure 3.15: A single attenuation band with a channelled spectrum for a cascaded LPG with a 90 cm separation. Taken from [73]

Utilisation of thin-film overlays is particularly useful in improving the selectivity of LPGs to specific analytes of interest (see Section 3.4.4), as such, the response of cascaded LPGs has been investigated following the application of nanoscale overlays. Data presented by James and colleagues [75] demonstrated that coating the entire device (both LPGs and the separation gap) with a thin-film overlay possessing a refractive index of 1.57 caused a wavelength shift in the attenuation band and a

phase change in the fringe pattern. The authors also showed that deposition of the material onto the gap that separates the gratings caused a change in the phase of the channelled spectrum as a function of coating thickness but the central wavelength of the resonance band remained unchanged. This method has allowed cascaded LPGs to be used as a chemical sensor in the detection of ammonia gas [76]. Cascaded LPGs have also been utilised for multi-parameter sensing, distinguishing between temperature and refractive index [77] and for bend sensing [78].

3.6.3 Phase-shifted LPGs

Typically, a uniform LPG is fabricated with a consistent structure that possesses a phase-shift of 2π, described as the period of the grating. However, phase shifted LPGs disrupt this structure in one or more places by introducing an additional shift that deviates from this regular arrangement (Fig. 3.16) [79]. The addition of the phase shift causes the light coupled into the cladding from the sections either side of the phase-shift to interfere with each other resulting in an alteration to the structure of the resonance features (Fig. 3.17) [80].

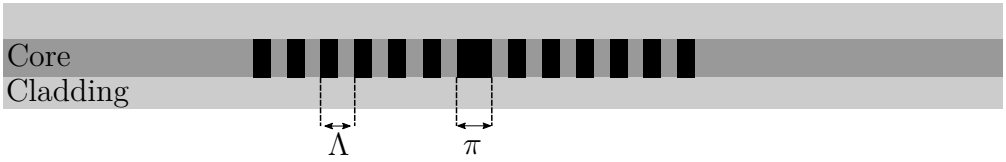

Figure 3.16: Illustration of a phase-shifted LPG possessing a single central phase shift, π. Adapted from [12]

This principle can be extended further by incorporating multiple phase-shifts to a single grating in order to produce a transmission spectrum with sharp, narrow attenuation bands. Although, this technique introduces side-lobes into the transmission spectra, it is possible to suppress these features through the application of length apodisation (e.g. spacing the phase-shifts along the grating in a Gaussian distribution) [79]. It has been suggested that the narrow attenuation bands possessed by this type of grating lend themselves to high-resolution measurements since it is possible to resolve smaller wavelength shifts [12].

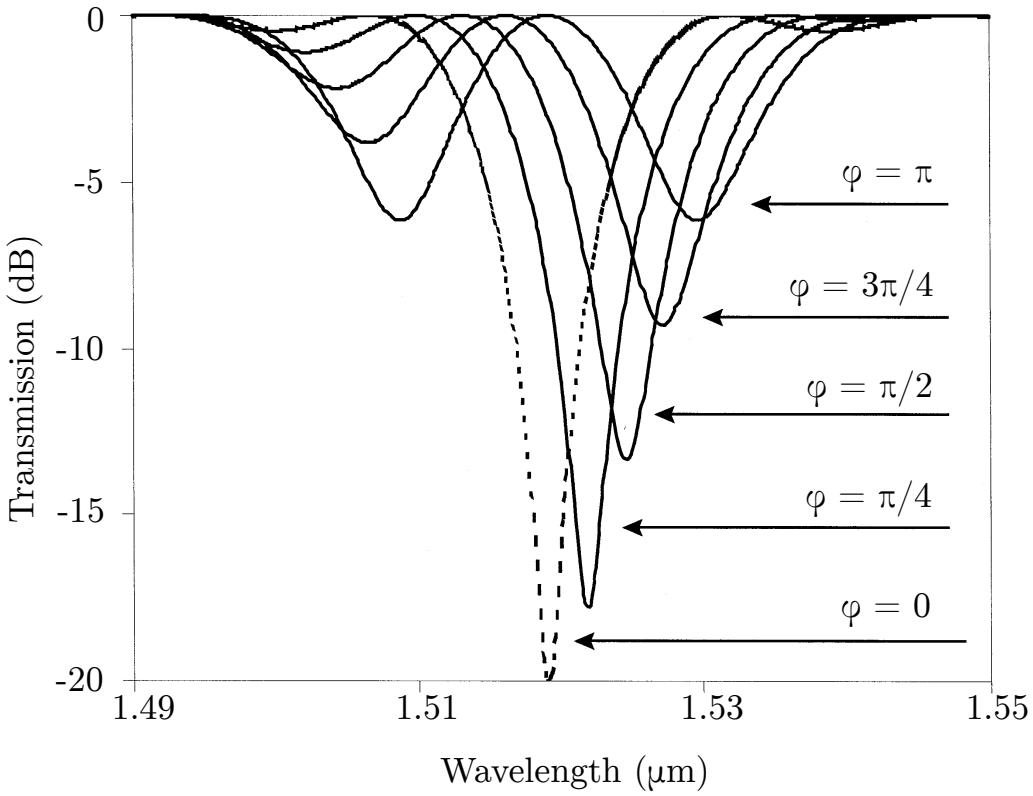

Figure 3.17: Transmission spectra of phase-shifted LPGs with phase shifts of $\phi = 0$ to π. Adapted from [80]

3.6.4 Summary of LPG design variations

Since their initial inception in 1996, the basic design of LPGs has been adapted in order to manipulate the transmission spectrum with the aim to optimise measurement resolution and improve sensitivity. Utilising LPGs that operate at the PMTP will maximise the CO_2 sensor's sensitivity.

3.7 Multi-parameter sensing using LPGs

Monitoring multiple parameters simultaneously allows interfering factors such as temperature to be assessed and compensated for. Although optical fibres are well suited for multiplexing, where it is possible to fabricate up to 30 FBGs on a single array [81], LPGs are difficult to multiplex due the requirement of multiple sources and corresponding interrogating units [82]. However, as has been alluded to through the discussion of LPGs sensitivity (Section 3.4), it is possible to design an LPG sensor in such a way that discrimination between two or more separate measurands is achievable. This can be accomplished through the generation of resonance features

which are insensitive to one parameter, multiplexing numerous in-series LPG elements in a single fibre and demodulating the resulting signal, or utilising features of higher order harmonics.

3.7.1 Insensitive resonance features

Fabrication of an LPG that displays an insensitive resonance band can be produced via the use of an appropriate choice of period and fibre composition. This scheme was adopted by Bhatia *et al.* [83] to distinguish strain in temperature variations, where the temperature insensitive attenuation band (1.8 pm·°C^{-1}) was identified at 1141.5 nm using an LPG written in Corning Flexcor fibre with a period of 40 μm produced a strain resolution of -21.44 nm·%ϵ^{-1}. The authors repeated this for a strain insensitivity band (-0.4 nm·%ϵ^{-1}) in a separate fibre using a period of 340 μm providing a temperature resolution of 0.8 °C. The insensitivity of the bands derives from the ability to couple to specific cladding modes which display a reduced contribution from a fibre parameter. In the case of the temperature insensitive resonance feature, the band is associated with a cladding mode that has a reduced material contribution [83]. LPGs with a resonance band which displayed temperature insensitivity yet responded to strain and bending have also been manufactured using PCF [25]. The temperature insensitivity displayed by PCF-based LPGs derives from the reduction in material contributions since the core in PCF is surrounded with air-holes rather than silica as is the case with standard fibre. Although this technique provides a simple method for discriminating between two parameters, it does restrict the device to specific fibre composition and operating wavelengths.

3.7.2 In-series gratings

Rather than relying on the features produced from a single LPG element, it has been previously shown that it is possible to multiplex LPGs in-series and discriminate measurement changes from each element [73]. Two different pairs of identical cascaded LPGs with a physical separation of 90 mm in the first pair, a 30 mm separation for the second pair and a 1 m gap between the pairs, were fabricated in hydrogen loaded fibre. A 30 mm section of the fibre separating each LPG in a cascaded pair was placed in a refractive index oil, where the oil's refractive index was controlled via thermoelectric heaters. Applying a Fourier transform to the obtained spectrum allowed the phase shift of the two cascaded LPG pairs to be resolved by considering the real and imaginary parts of their associated frequencies. Since

variations in environmental parameters induce changes in the interference fringes of cascaded LPGs, it was possible to distinguish which LPG pair underwent the temperature mediated refractive index change by monitoring the phase variations in the channelled spectrum. Determination of changes in different LPGs does not necessarily require extensive signal processing. Hromadka *et al.* [84] fabricated a single optical fibre with three separate gratings in-series but with different periods in order to differentiate between relative humidity, temperature and volatile organic compounds. The authors multiplexed three LPGs with periods that differed only by 0.1 μm in order to produce a spectrum with multiple resonance bands near the PMTP, each coated with a different thin-film overlay in order to provide selectivity for one measurand of interest. However, very careful design was required to ensure large changes in a particular attenuation band do not coalesce with local features in order to avoid the use of elaborate signal processing techniques.

3.7.3 Hybrid systems

Combining both LPGs and FBGs onto a single fibre is another scheme in which multi-parameter sensing has been accomplished to discriminate between strain and temperature [21]. Typically, this type of array consists of an LPG proceeded by an FBG in-series (Fig. 3.18). The use of a hybrid LPG/FBG configuration has

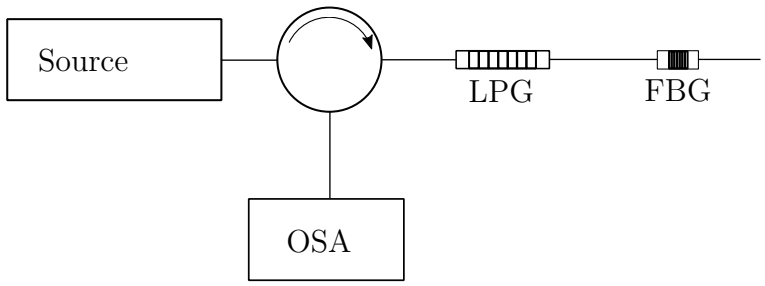

Figure 3.18: Typical configuration for a hybrid multi-parameter system where a circulator is used to distribute reflected signals to an interrogator. Adapted from [85]

been exploited to detect simultaneous changes in surrounding refractive index and temperature [85]. In this case, only the LPG displays sensitivity to variations in ambient refractive index (producing an intensity change in the counter-propagating signal) while both the LPG and FBG respond to temperature fluctuations. Using both wavelength changes and shifts in amplitude of the reflected signal, it is possible to distinguish between temperature and refractive index. This system has also been applied to distinguish variations in strain or temperature [21].

3.7.4 Differential shift in multiple bands

Rather than relying on a completely insensitive feature, it is possible to discern axial strain and temperature using a single LPG element through differential shifts in multiple resonance bands [22]. Fabricating an LPG with $\Lambda = 280$ μm in hydrogen loaded Corning SMF-28, two resonance bands at 1607.9 and 1332.9 nm were selected where the latter feature displayed negligible thermal cross sensitivity. Using an OSA to interrogate the fibre, the authors were able to achieve minimum detectable strain and temperature changes of 30 $\mu\epsilon$ and 0.6 °C respectively. An interesting method for creating resonance bands with different sensitivities is through the use of higher order harmonics. Different order harmonics displayed differing sensitivities allowing the discrimination between temperature and strain to be deduced to a resolution of 0.7°C and 25 $\mu\epsilon$ via 1^{st} and 2^{nd} ordered resonance features [14]. This technique is explored further in Chapter 6.

3.8 Summary and conclusions

A concise review of LPG operational theory, characterisation and fabrication has been outlined. It is clear that with use of the transfer matrix method to model phase matching curves it is possible to estimate the transmission spectrum through period selection, facilitating the design of LPGs. The origins of an LPGs response to physical parameters and methods in which these effects have been exploited for sensing capabilities has been discussed. Additionally, common techniques used to fabricate LPGs (Table 3.2) and variations of the uniform grating design have been presented. Finally, an overview of the schemes used to perform multi-parameter sensing with LPGs was summarised.

It is clear from a review of the literature that an LPG-based CO_2 sensor would require a coating that possesses an affinity for this analyte in order to selectively utilise the inherent surrounding refractive index sensitivity of these in-fibre gratings. This is investigated further in Chapter 4. Furthermore, through the use of UV irradiation, the fabrication of LPGs for the CO_2 sensor can be tailored such that sensitivity is maximised (by employing LPGs operating at the PMTP, explored in Chapter 5) and competing environmental effects discriminated between (use of higher order attenuation bands in the transmission spectrum, discussed in Chapter 6).

Table 3.2: Summary table of LPG fabrication techniques. Abbreviations: Advantage (+), Disadvantage (−)

Technique	**Mechanism of refractive index change**	**Notes**
CO_2 laser irradiation	Densification of glass	(+) Possible to fabricate LPGs in non-standard fibre (+) Ability to create tapered LPGs (+) Inherent thermal stability
Electrical discharge	Densification of glass	(+) Possible to fabricate LPGs in non-standard fibre (+) Inherent thermal stability (+) Ability to create tapered LPGs (−) Difficult to reproduce LPGs with the same characteristics
Femtosecond laser irradiation	Densification of glass	(+) Possible to fabricate LPGs in non-standard fibre (+) Inherent thermal stability
Mechanical deformation	Alters fibre's photoelastic properties	(+) Minimal financial investment required (+) Produces temporary LPG structure (−) Nominal practical applications
UV irradiation	Formation of Si-Ge structures	(+) Amplitude mask may be used (+) Only the core experiences refractive index change (+) Ability to tailor LPG structure through cumulative UV exposure

3.9 References

[1] A. M. Vengsarkar, P. J. Lemaire, J. B. Judkins, V. Bhatia, T. Erdogan, and J. E. Sipe. Long-period fiber gratings as band-rejection filters. *Journal of Lightwave Technology*, 14(1):58–65, 1996.

[2] B. Eggleton, R. Slusher, J. Judkins, J. Stark, and A. Vengsarkar. All-optical switching in long-period fiber gratings. *Optics Letters*, 22(12):883–885, 1997.

[3] A. Yariv. *Optical Electronics*. Saunders College Publishing, London, UK, 1991.

[4] E. Hecht. *Optics*. Addison Wesley, London, 4th ed., 2002.

[5] B. E. A. Saleh and M. C. Teich. *Fundamentals of Photonics*. John Wiley & Sons, Inc, Chichester, UK, 1st ed., 1991.

[6] C. C. Davis. *Lasers and Electro-Optics*. Cambridge University Press, Cambridge, UK, 2nd ed., 2014.

[7] V. Bhatia and A. M. Vengsarkar. Optical fiber long-period grating sensors. *Optics Letters*, 21(9):692–694, 1996.

[8] Y. Koyamada. Numerical analysis of core-mode to radiation-mode coupling in long-period fiber gratings. *IEEE Photonics Technology Letters*, 13(4):308–310, 2001.

[9] S. J. Buggy. *Composite material process monitoring using optical fibre grating sensors*. Ph.D. thesis, Cranfield University, 2008.

[10] H. L. Dobb. *Fibre gratings in novel optical fibres for applications in sensing*. Ph.D. thesis, Aston University, 2007.

[11] S. W. James and R. P. Tatam. Optical fibre long-period grating sensors: characteristics and application. *Measurement Science and Technology*, 14(5):R49–61, 2003.

[12] R. Y. N. Wong. *Advanced fibre optic long period grating sensors; design, fabrication and sensing*. Ph.D. thesis, Cranfield University, 2014.

[13] T. Erdogan. Cladding-mode resonances in short-and long-period fiber grating filters. *Journal of the Optical Society of America A*, 14(8):1760–1773, 1997.

[14] T. Allsop, L. Zhang, D. J. Webb, and I. Bennion. Discrimination between strain and temperature effects using first and second-order diffraction from a long-period grating. *Optics Communications*, 211(1-6):103–108, 2002.

[15] Y. Kashyap. *Fiber Bragg Gratings*. Academic Press, London, UK, 1st ed., 1999.

[16] D. Gloge. Weakly guiding fibers. *Applied Optics*, 10(10):2252–2258, 1971.

[17] E. Anemogiannis, E. N. Glytsis, and T. K. Gaylord. Transmission characteristics of long-period fiber gratings having arbitrary azimuthal/radial refractive index variations. *Journal of Lightwave Technology*, 21(1):218–227, 2003.

[18] I. Del Villar, I. R. Matias, F. J. Arregui, and P. Lalanne. Optimization of sensitivity in long period fiber gratings with overlay deposition. *Optics Express*, 13(1):56–69, 2005.

[19] S. Khaliq. *Fibre optic long period fibre gratings for sensing applications*. Ph.D. thesis, Cranfield University, 2003.

[20] C. L. Zhao, L. Xiao, J. Ju, M. S. Demokan, and W. Jin. Strain and temperature characteristics of a long period grating written in a photonic crystal fiber and its application as a temperature-insensitive strain sensor. *Journal of Lightwave Technology*, 26(2):220–227, 2008.

[21] H. Patrick, G. Williams, A. Kersey, J. Pedrazzani, and A. Vengsarkar. Hybrid fiber Bragg grating/long period fiber grating sensor for strain/temperature discrimination. *IEEE Photonics Technology Letters*, 8(9):1223–1225, 1996.

[22] V. Bhatia, D. Campbell, R. O. Claus, and A. M. Vengsarkar. Simultaneous strain and temperature measurement with long-period gratings. *Optics Letters*, 22(9):648–650, 1997.

[23] X. Shu, T. Allsop, B. Gwandu, L. Zhang, and I. Bennion. High-temperature sensitivity of long-period gratings in B-Ge codoped fiber. *IEEE Photonics Technology Letters*, 13(8):818–820, 2001.

[24] J.-N. Jang, S. Y. Kim, S.-W. Kim, and M.-S. Kim. Temperature insensitive long-period fibre gratings. *Electronics Letters*, 35(24):2134–2136, 1999.

[25] H. Dobb, K. Kalli, and D. J. Webb. Temperature-insensitive long period grating sensors in photonic crystal fibre. *Electronics Letters*, 40(11):657–658, 2004.

[26] X. Shu, L. Zhang, and I. Bennion. Sensitivity characteristics of long-period fiber gratings. *Journal of Lightwave Technology*, 20(2):255–266, 2002.

[27] S. Khaliq, S. W. James, and R. P. Tatam. Fiber-optic liquid-level sensor using a long-period grating. *Optics Letters*, 26(16):1224–1226, 2001.

[28] H. J. Patrick, A. D. Kersey, and F. Bucholtz. Analysis of the response of long period fiber gratings to external index of refraction. *Journal of Lightwave Technology*, 16(9):1606, 1998.

[29] T. Allsop, L. Zhang, and I. Bennion. Detection of organic aromatic compounds in paraffin by a long-period fiber grating optical sensor with optimized sensitivity. *Optics Communications*, 191(3-6):181–190, 2001.

[30] A. Cusano, A. Iadicicco, P. Pilla, L. Contessa, S. Campopiano, A. Cutolo, M. Giordano, and G. Guerra. Coated long-period fiber gratings as high-sensitivity optochemical sensors. *Journal of Lightwave Technology*, 24(4):1776–1786, 2006.

[31] M. Partridge, R. Wong, S. W. James, F. Davis, S. P. Higson, and R. P. Tatam. Long period grating based toluene sensor for use with water contamination. *Sensors and Actuators B: Chemical*, 203(1):621–625, 2014.

[32] S. Korposh, R. Selyanchyn, W. Yasukochi, S.-W. Lee, S. W. James, and R. P. Tatam. Optical fibre long period grating with a nanoporous coating formed from silica nanoparticles for ammonia sensing in water. *Materials Chemistry and Physics*, 133(2-3):784–792, 2012.

[33] N. D. Rees, S. W. James, R. P. Tatam, and G. J. Ashwell. Optical fiber long-period gratings with Langmuir–Blodgett thin-film overlays. *Optics Letters*, 27(9):686–688, 2002.

[34] I. Del Villar, I. R. Matias, and F. J. Arregui. Enhancement of sensitivity in long-period fiber gratings with deposition of low-refractive-index materials. *Optics Letters*, 30(18):2363–2365, 2005.

[35] S. W. James, C. S. Cheung, and R. P. Tatam. Experimental observations on the response of 1st and 2nd order fibre optic long period grating coupling bands to the deposition of nanostructured coatings. *Optics Express*, 15(20):13096–13107, 2007.

[36] S. M. Topliss, S. W. James, F. Davis, S. P. Higson, and R. P. Tatam. Optical fibre long period grating based selective vapour sensing of volatile organic compounds. *Sensors and Actuators B: Chemical*, 143(2):629–634, 2010.

[37] S. M. Tripathi, W. J. Bock, P. Mikulic, R. Chinnappan, A. Ng, M. Tolba, and M. Zourob. Long period grating based biosensor for the detection of Escherichia coli bacteria. *Biosensors and Bioelectronics*, 35(1):308–312, 2012.

[38] L. Melo, G. Burton, B. Davies, D. Risk, and P. Wild. Highly sensitive coated long period grating sensor for CO2 detection at atmospheric pressure. *Sensors and Actuators B: Chemical*, 202(1):294–300, 2014.

[39] S. Korposh, S. W. James, S.-W. Lee, S. Topliss, S. C. Cheung, W. J. Batty, and R. P. Tatam. Fiber optic long period grating sensors with a nanoassembled mesoporous film of SiO2 nanoparticles. *Optics Express*, 18(12):13227–13238, 2010.

[40] G. Rego, O. Okhotnikov, E. Dianov, and V. Sulimov. High-temperature stability of long-period fiber gratings produced using an electric arc. *Journal of Lightwave Technology*, 19(10):1574–1579, 2001.

[41] Y. Kondo, K. Nouchi, T. Mitsuyu, M. Watanabe, P. G. Kazansky, and K. Hirao. Fabrication of long-period fiber gratings by focused irradiation of infrared femtosecond laser pulses. *Optics letters*, 24(10):646–648, 1999.

[42] D. Davis, T. Gaylord, E. Glytsis, S. Kosinski, S. Mettler, and A. Vengsarkar. Long-period fibre grating fabrication with focused CO2 laser pulses. *Electronics Letters*, 34(3):302–303, 1998.

[43] S. Savin, M. Digonnet, G. Kino, and H. Shaw. Tunable mechanically induced long-period fiber gratings. *Optics Letters*, 25(10):710–712, 2000.

[44] Y. Wang. Review of long period fiber gratings written by CO2 laser. *Journal of Applied Physics*, 108(8):11, 2010.

[45] K. Mullaney. *The fabrication of micro-tapered optical fibres for sensing applications*. Ph.D. thesis, Cranfield University, 2016.

[46] D. C. Alves, J. M. Coelho, M. Nespereira, F. Monteiro, M. Abreu, and J. Rebordão. Automation methodology for the development of LPFG using CO2 laser radiation. In *8th Iberoamerican Optics Meeting and 11th Latin American Meeting on Optics, Lasers, and Applications*, vol. 8785, p. 87854X. International Society for Optics and Photonics, 2013.

[47] V. Grubsky and J. Feinberg. Fabrication of axially symmetric long-period gratings with a carbon dioxide laser. *IEEE Photonics Technology Letters*, 18(21):2296–2298, 2006.

[48] F. Bayle and J.-P. Meunier. Efficient fabrication of fused-fiber biconical taper structures by a scanned CO2 laser beam technique. *Applied Optics*, 44(30):6402–6411, 2005.

[49] Y. Zhu, P. Shum, H.-W. Bay, M. Yan, X. Yu, J. Hu, J. Hao, and C. Lu. Strain-Insensitive and High-Temperature Long-Period Gratings Inscribed in Photonic Crystal Fiber. In *Optical Fiber Communication Conference and Exposition and The National Fiber Optic Engineers Conference*, pp. 367–369. Optical Society of America, 2005.

[50] A. K. Debowska, M. Smietana, P. Mikulic, and W. J. Bock. High temperature nano-coated electric-arc-induced long-period gratings working at the dispersion turning point for refractive index sensing. *Japanese Journal of Applied Physics*, 53(8S2):1 – 5, 2014.

[51] S.-Y. Tan, Y.-T. Yong, S.-C. Lee, and F. Abd Rahman. Review on an arc-induced long-period fiber grating and its sensor applications. *Journal of Electromagnetic Waves and Applications*, 29(6):703–726, 2015.

[52] F. Ahmed, H.-E. Joe, B.-K. Min, and M. B. Jun. Characterization of refractive index change and fabrication of long period gratings in pure silica fiber by femtosecond laser radiation. *Optics and Laser Technology*, 74:119–124, 2015.

[53] R. Y. Wong, E. Chehura, S. E. Staines, S. W. James, and R. P. Tatam. Fabrication of fiber optic long period gratings operating at the phase matching turning point using an ultraviolet laser. *Applied Optics*, 53(21):4669–4674, 2014.

[54] M. Sceats, G. Atkins, and S. Poole. Photolytic index changes in optical fibers. *Annual Review of Materials Science*, 23(1):381–410, 1993.

[55] P. J. Lemaire. Reliability of optical fibers exposed to hydrogen: prediction of long-term loss increases. *Optical Engineering*, 30(6):780–790, 1991.

[56] P. J. Lemaire, R. Atkins, V. Mizrahi, and W. Reed. High pressure H2 loading as a technique for achieving ultrahigh UV photosensitivity and thermal sensitivity in GeO2 doped optical fibres. *Electronics Letters*, 29(13):1191–1193, 1993.

[57] R. Atkins, P. Lemaire, T. Erdogan, and V. Mizrahi. Mechanisms of enhanced UV photosensitivity via hydrogen loading in germanosilicate glasses. *Electronics Letters*, 29(14):1234–1235, 1993.

[58] L. Qin, Z.-X. Wei, Q.-Y. Wang, H.-P. Li, Y.-S. Zhang, and D.-S. Gao. Abnormal shift of center wavelength in annealing long period gratings. *Chinese Physics Letters*, 17(1):28, 2000.

[59] M. Partridge, S. W. James, J. H. Barrington, and R. P. Tatam. Overwrite fabrication and tuning of long period gratings. *Optics Express*, 24(20):22345–22356, 2016.

[60] T. Libish, M. Bobby, J. Linesh, S. Mathew, P. Biswas, S. Bandyopadhyay, K. Dasgupta, and P. Radhakrishnan. The effect of annealing and temperature on transmission spectra of long period gratings written in hydrogen loaded standard single mode fiber. *Optik-International Journal for Light and Electron Optics*, 124(20):4345–4348, 2013.

[61] K. Fujita, Y. Masuda, K. Nakayama, M. Ando, K. Sakamoto, J.-p. Mohri, M. Yamauchi, M. Kimura, Y. Mizutani, S. Kimura, *et al.* Dynamic evolution of the spectrum of long-period fiber Bragg gratings fabricated from hydrogen-loaded optical fiber by ultraviolet laser irradiation. *Applied Optics*, 44(33):7032–7038, 2005.

[62] K. Zhou, H. Liu, and X. Hu. Tuning the resonant wavelength of long period fiber gratings by etching the fiber's cladding. *Optics Communications*, 197(4):295 – 299, 2001.

[63] S. Kim, Y. Jeong, S. Kim, J. Kwon, N. Park, and B. Lee. Control of the characteristics of a long-period grating by cladding etching. *Applied Optics*, 39(13):2038–2042, 2000.

[64] M. Harumoto, M. Shigehara, and H. Suganuma. Gain-flattening filter using long-period fiber gratings. *Journal of Lightwave Technology*, 20(6):1027, 2002.

[65] F. Abrishamian and K. Morishita. Broadening adjustable range on post-fabrication resonance wavelength trimming of long-period fiber gratings and the mechanisms of resonance wavelength shifts. *IEICE Transactions on Electronics*, 94(4):641–647, 2011.

[66] P. Biswas, N. Basumallick, S. Bandyopadhyay, K. Dasgupta, A. Ghosh, and S. Bandyopadhyay. Sensitivity enhancement of turn-around-point long period gratings by tuning initial coupling condition. *IEEE Sensors Journal*, 15(2):1240–1245, 2015.

[67] M. Gambhir and S. Gupta. Review of turn around point long period fiber gratings. *Journal of Sensor Technology*, 5(4):81–89, 2015.

[68] X. Shu, X. Zhu, Q. Wang, S. Jiang, W. Shi, Z. Huang, and D. Huang. Dual resonant peaks of LP15 cladding mode in long-period gratings. *Electronic Letters*, 35(8):649–651, 1999.

[69] H. Chen and Z. Gu. Filtering characteristics of film-coated long-period fiber gratings operating at the phase-matching turning point. *Optik-International Journal for Light and Electron Optics*, 125(20):6003–6009, 2014.

[70] S. Kher, S. Chaubey, J. Kishore, and S. M. Oak. Detection of fuel adulteration with high sensitivity using turnaround point long period fiber gratings in B/Ge doped fibers. *IEEE Sensors Journal*, 13(11):4482–4486, 2013.

[71] V. Mishra, S. C. Jain, N. Singh, G. Poddar, and P. Kapur. Fuel adulteration detection using long period fiber grating sensor technology. *Journal of Scientific and Industrial Research*, 46(2):106–110, 2008.

[72] R. M. Carter, R. R. Maier, P. Biswas, N. Basumallick, S. Bandyopadhyay, B. J. Jones, S. McCulloch, and J. S. Barton. Experimental difficulties with LPG sensors operating close to the phase turning points. *Journal of Lightwave Technology*, 34(17):3999–4004, 2016.

[73] R. P. Murphy, S. W. James, and R. P. Tatam. Multiplexing of fiber-optic long-period grating-based interferometric sensors. *Journal of Lightwave Technology*, 25(3):825–829, 2007.

[74] L. Zhang, Y. Liu, L. Everall, J. A. R. Williams, and I. Bennion. Design and realization of long-period grating devices in conventional and high birefringence fibers and their novel applications as fiber-optic load sensors. *IEEE Journal of Selected Topics in Quantum Electronics*, 5(5):1373–1378, 1999.

[75] S. W. James, I. Ishaq, G. J. Ashwell, and R. P. Tatam. Cascaded long-period gratings with nanostructured coatings. *Optics Letters*, 30(17):2197–2199, 2005.

[76] S. W. James, S. Korposh, S.-W. Lee, and R. P. Tatam. A long period grating-based chemical sensor insensitive to the influence of interfering parameters. *Optics Express*, 22(7):8012–8023, 2014.

[77] B. A. Gwandu, X. Shu, T. D. Allsop, W. Zhang, L. Zhang, D. Webb, and I. Bennion. Simultaneous refractive index and temperature measurement using

a cascaded long-period grating device. In *Sensors, 2002. Proceedings of IEEE*, vol. 2, pp. 1032–1035. IEEE, 2002.

[78] B. H. Lee and J. Nishii. Bending sensitivity of in-series long-period fiber gratings. *Optics Letters*, 23(20):1624–1626, 1998.

[79] S. M. Topliss. *Optical fibre long period grating sensors with nanostructured coatings*. Ph.D. thesis, Cranfield University, 2011.

[80] Y. Liu, J. Williams, L. Zhang, and I. Bennion. Phase shifted and cascaded long-period fiber gratings. *Optics communications*, 164(1-3):27–31, 1999.

[81] A. Rogers. Distributed optical-fibre sensing. *Measurement Science and Technology*, 10(8):R75–R99, 1999.

[82] T. Allsop, T. Earthrowl, R. Reeves, D. J. Webb, and I. Bennion. The interrogation and multiplexing of long period grating curvature sensors using a Bragg grating based, derivative spectroscopy technique. *Measurement Science and Technology*, 15(1):44, 2003.

[83] V. Bhatia, D. K. Campbell, D. Sherr, T. D'Alberto, N. Zabaronick, G. A. Ten Eyck, K. A. Murphy, and R. O. Claus. Temperature-insensitive and strain-insensitive long-period grating sensors for smart structures. *Optical Engineering*, 36(7):1872–1877, 1997.

[84] J. Hromadka, S. Korposh, M. C. Partridge, S. W. James, F. Davis, D. Crump, and R. P. Tatam. Multi-parameter measurements using optical fibre long period gratings for indoor air quality monitoring. *Sensors and Actuators B: Chemical*, 244(1):217–225, 2017.

[85] D. A. C. Enriquez, A. R. da Cruz, and M. T. M. R. Giraldi. Hybrid FBG-LPG sensor for surrounding refractive index and temperature simultaneous discrimination. *Optics and Laser Technology*, 44(4):981 – 986, 2012.

Chapter 4

Optical fibre coating for CO_2 detection

As discussed in Section 3.4.4, the deposition of a coating material onto the surface of an LPG can improve the grating's sensitivity and selectivity to an analyte of interest. Within the context of this thesis, it is thus necessary to identify a suitable coating material for the development of the CO_2 sensor. For this project, the deposition material firstly must show an affinity for CO_2 at atmospheric pressure and temperatures. Secondly, it is necessary that the coating is hydrophobic in order to avoid humidity cross-sensitivity since human breath is saturated with water. Finally, to ensure the CO_2 sensor can be reusable and suitable in a practical situation, the deposition material must demonstrate a reversible change with CO_2 that does not require the use of high temperatures or pressures.

This chapter outlines techniques that may be used to apply materials to the surface of optical fibre. Additionally, groups of coating materials that display an affinity for CO_2 are outlined and a description of the mechanisms via which they interact with CO_2 and other pertinent cross-sensitive species is provided.

4.1 Optical fibre coating techniques

There are numerous methods that can be used to deposit a chemical or biological deposition onto a substrate's surface. One of the most common techniques used to apply a thin-film to a substrate is spin-coating. Essentially, the substrate is covered in an excess of aqueous material, spun to a pre-set velocity in order to remove unwanted material and to create a homogeneous thickness across the surface prior to

a final evaporation stage [1]. Although this mature technique produces homogeneous coatings and allows control of coating thickness by selection of the appropriate spin velocity, this procedure would not be suitable for optical fibres due to their cylindrical geometry.

Generally, optical fibres are coated via dip-coating, the Langmuir-Blodgett technique (LB), electrostatic self-assembly (ESA) or sol-gel deposition. As these techniques have all been utilised in the production of LPG sensors [2, 3, 4, 5], it is therefore pertinent that a detailed description of the basic procedure and characteristics of each process is provided in the subsequent sections.

4.1.1 Dip-coating

The simplicity, ease-of-use and minimal material wastage provided by dip-coating has caused it to be one of the most popular coating techniques [6]. The substrate is lowered into the coating solution and withdrawn vertically at a constant speed, leaving a layer of material on its surface as it is removed. Typically, the desired coating material is dissolved or suspended in a solvent (usually alcohols for their fast evaporation and low surface tension) so that as the substrate is withdrawn from the bulk-solution, the solvent evaporates. Dip-coating can be used to deposit polymers, metallic nano-particles, biomolecules or solid-films from a sol (a colloidal suspension of solid particles in solution) [7, 6].

On initial inspection the technique seems trivial. However, a more detailed examination reveals the complexity of competing forces involved in film formation, and consequently methods via which these parameters may be exploited for controllable deposition. As the substrate is withdrawn from the solution reservoir, liquid is drawn along behind which splits into two, with the outer layer returning to the bulk solution. The remaining inner layer adheres to the substrate surface, experiencing evaporation, viscous drag (from material draining back into the reservoir) and capillary flow deposition (Fig. 4.1). Interestingly, the relationship between withdrawal speed and thickness takes the form of a parabola where, at intermediate speeds (0.2 - 0.8 mm·s^{-1}), competing regimes are balanced and a minimum thickness can be obtained. The relationship between deposition thickness and competing regimes can be expressed by [8],

$$h_0 = k_i\left(\frac{E}{S_w u} + D u^{\frac{2}{3}}\right), \tag{4.1}$$

where h_0 is the deposition thickness (in mm), k_i is the solution composition constant (i.e. the solution components maintain their initial composition ratio), E is the

rate at which the solution undergoes evaporation, u is the withdrawal speed, S_w the substrate width and D is the solution's physical-chemical characteristics. The numerous driving forces outlined above, which govern deposition, are dependent on processing (withdrawal speed, atmospheric temperature, and humidity) and chemical (solvent choice and solution concentration) conditions. Therefore, to produce repeatable coatings, these critical parameters must be managed [8].

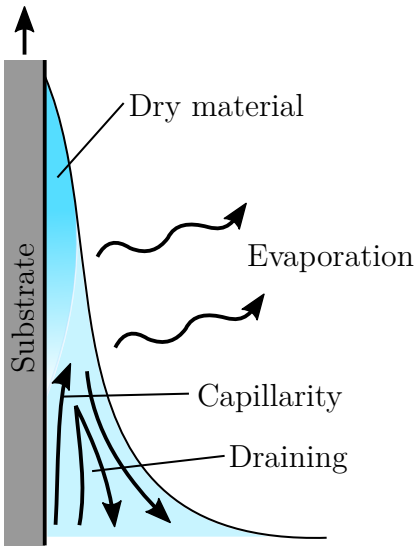

Figure 4.1: Mechanism by which thin-films are formed during the dip-coating technique [8]

Despite the potential for controlled deposition, dip-coating does possess a number of drawbacks. When using highly viscous or dilute solutions it is difficult to prepare ultra thin (<20 nm) and ultra-thick (>1000 nm) coatings in a controlled fashion. Furthermore, when using a porous substrate the coating is liable to infiltrate the structure, potentially altering the deposition properties. Finally, without careful control of atmospheric conditions, the coating is liable to crack, resulting from tensile stress experienced by the deposited coating during evaporation [6].

The use of dip-coating is exploited in Chapter 7 during the fabrication of the LPG-based CO_2 sensor.

4.1.2 Electrostatic self-assembly

The construction of multi-composite films on a surface can be achieved using the ESA technique. This simple procedure involves alternate submersion of the substrate in a cationic and an anionic solution (solutions can also be polymeric or colloidal) with a wash step in between each immersion (Fig. 4.2). Repeating this process allows

for a multi-layered film to be constructed on the substrate. Furthermore, composite coatings can be created by substituting either of the solutions with different molecules of the same charge, demonstrating the adaptability this technique offers [9].

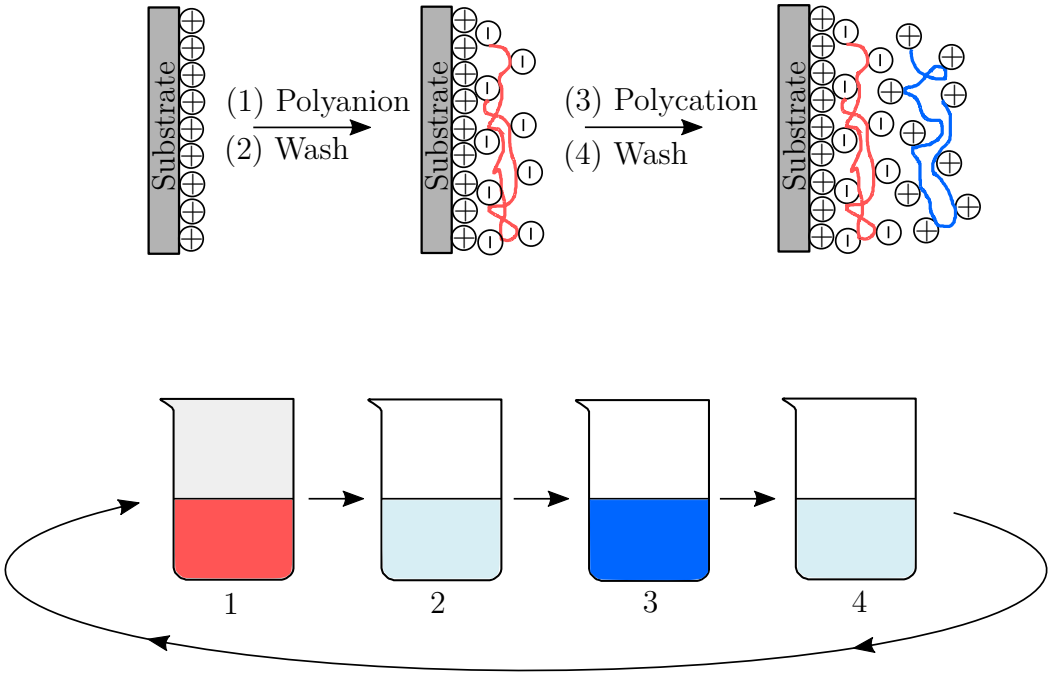

Figure 4.2: Simplified ESA concept. Charged substrate is immersed in the polyanion (1) and polycation (3) with wash steps (2)(4) in between. Repeating this process allows for multi-layers to be applied [9]

Preparation of the substrate requires it to be cleaned and a surface charge applied in order to provide a suitable foundation for subsequent deposition. Once immersed in the appropriate solution, the electrostatic attraction between the substrate and oppositely charged molecules forms the first layer. The surplus of molecules in solution are repelled from the similarly charged, newly formed coating, therefore limiting each deposition phase to a single self-regulating layer [10]. Following an intermediary washing step (necessary to remove excess non-attached molecules) the substrate is then dipped into the second solution of opposite charge. This process is repeated until the required coating thickness is achieved. The assembled deposition can be defined by $(A/B)_X$ where A and B are the two coating materials and X is the number of bilayers. Although the processing parameters are fairly broad, greater control over the layer's structure can be acquired by adjusting reaction conditions such as ionic solution concentration, adsorption times, pH and temperature [9]. Using this general approach it is possible to coat nearly all substrate surfaces, regardless of shape or size, so long as they are accessible to the ionic solutions [9]. Indeed, ESA

has been utilised frequently to apply chemical depositions to LPGs [11, 12, 13, 14] and is employed in Chapter 7.

One drawback of this technique is that it is not possible to deposit a coating thicker than one molecular layer using just a single material. Also, the coating/air layer of the deposited coating tends to be rough and requires post-treatment processes (salt solution washes) in order to remove the surface irregularities [10].

4.1.3 Langmuir-Blodgett

LB coating allows the controlled deposition of a material mono-layer onto to the surface of a vertically-dipped substrate using an LB trough. To achieve this, a thin layer of material, typically amphiphilic, is spread onto a water sub-phase, where the dispersed mono-layer orientates itself so that the hydrophilic heads interact with the water's surface and the hydrophobic tails are arranged away from the water. Upon compression of the surface area using the LB trough's moveable barriers, a condensed mono-layer, termed a Langmuir film, is formed. As the substrate is withdrawn through the sub-phase, the meniscus pushes the film onto the substrate's surface (Fig. 4.3). In order to create a homogenous, repeatable coating, the LB isotherm (a curve representing surface area against pressure for a single temperature) of each material must be deduced to allow the ideal surface pressure to be determined [15, 16].

Formation of a mono-layer coating is achieved by withdrawing the substrate through the surface of the Langmuir film once. By repeating the process of inserting and withdrawing the coated substrate through the film, it is possible to build up multiple layers, one molecule thick, at a time. Furthermore, by using two separate troughs with two different materials, it is possible to deposit a composite layer onto the substrate. The LB coating will typically take the form of one of three key structures which is determined by the nature and structure of the amphiphilic material. The most common of the LB structures is the Y-type, in which adjacent layers pack tail-to-tail and head-to-head. Less frequently witnessed layer organisations are X- and Z-types. Here, the substrate is only coated on either insertion or withdrawal creating head-to-tail layering (Fig. 4.4) [16].

For repeatable deposition to occur, both the substrate and LB trough must be carefully cleaned to remove dust and chemical residue [17]. One drawback of the LB coating technique is that during multi-layering any defect in the LB film or substrate surface will be amplified as each subsequent mono-layer is deposited [16].

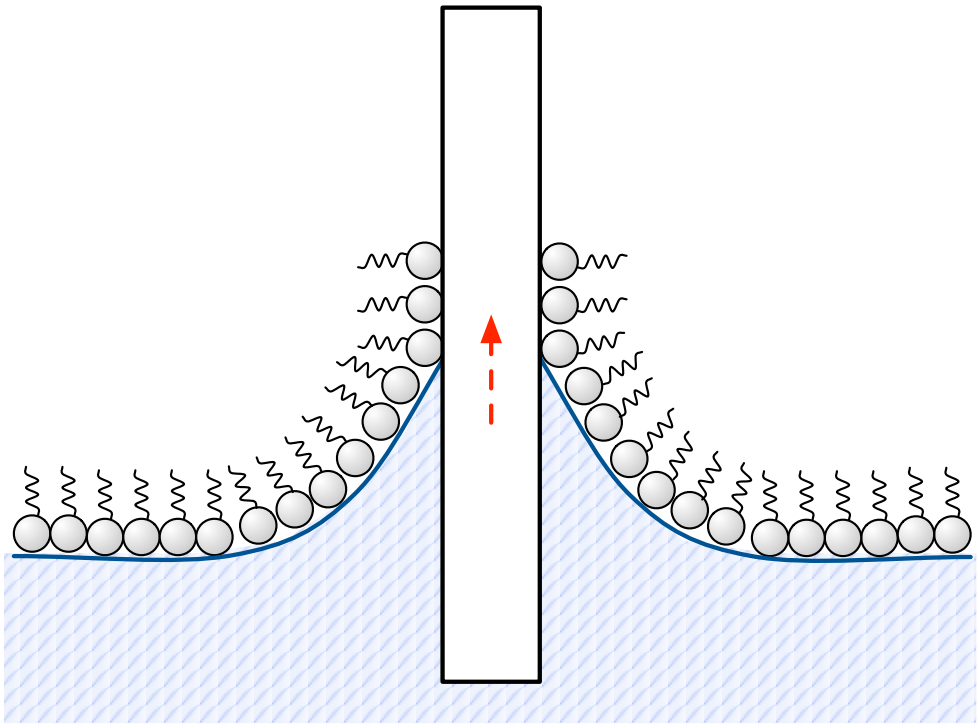

Figure 4.3: Mechanism of mono-layer coating using LB deposition where the amphiphilic material is uniformly orientated on the water sub-phase allowing a mono-layer film to form as the substrate is withdrawn. Taken from [16]

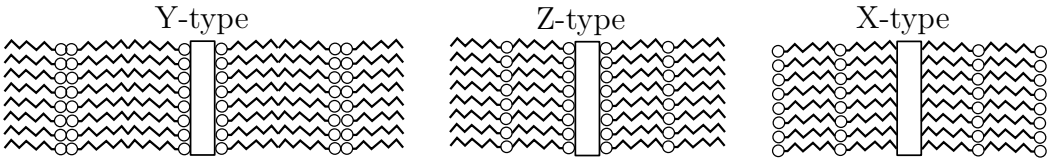

Figure 4.4: Three main layering structures in LB deposition. Hydrophilic heads and hydrophobic tails of amphiphilic material are depicted [17]

Another disadvantage of this technique is the requirement that the coating material's molecular structure must be amphiphilic [15].

4.1.4 Sol-gel

The sol-gel process can be described as the chemical action of forming a gel through the condensation/hydrolysis of an inorganic or metal organic pre-cursor sol [18]. The final product is a nanoporous material with high homogeneity and purity which can be tailored via judicial selection of sol reagents and reaction conditions. Typically, the sol-gel process consists of four stages: 1) preparation of the pre-cursor sol; 2) gelling of the sol; 3) drying, producing a low density xerogel or aerogel; and, if

required, 4) densification via high thermal treatment. The optional latter step allows the removal of the gel's porous structure, creating a density similar to that of fused silica [7].

Silica alkoxydes are popular pre-cursors in sol-gel research, where tetramethoxysilane and tetraethoxysilane are commonly studied examples. A general chemical formulation for silica alkoxydes during the sol-gel process can be described by the following [19],

$$\mathrm{Si(OR)_4} + (4-x)\mathrm{H_2O} \longrightarrow \mathrm{SiO}_x\,(\mathrm{OH})_{4-2x} + 4\,\mathrm{ROH}, \qquad \text{(C 4.1)}$$

where R represents an alkyl group. The sol pre-cursor undergoes hydrolysis (C 4.2) and condensation (C 4.3) reactions, gradually increasing in viscosity through polymerisation and forming a stable, interconnected porous gel.

$$\equiv\mathrm{Si{-}OR} + \mathrm{H_2O} \longrightarrow \equiv\mathrm{Si{-}OH} + \mathrm{ROH} \qquad \text{(C 4.2)}$$

$$\equiv\mathrm{Si{-}OH} + \mathrm{HO{-}Si}\equiv \longrightarrow \equiv\text{Si-O-Si}\equiv + \mathrm{ROH}. \qquad \text{(C 4.3)}$$

The gel is removed from solution and either dried at room temperature in order to obtain a xerogel or dried under supercritcal conditions using an autoclave to form an aerogel [20]. Characteristics of the gel (porosity, refractive index, surface area) can depend on process parameters such as, pre-cursor, pH, temperature, catalyst concentrations and drying method [20]. Furthermore, sol-gels are able to immobilise various organic and biological species within their matrices through simple modification of the polymerisation step [19].

Sol-gels have gained considerable interest for their ability to form thin-films via dip-coating or spin-coating [20]. These techniques have enabled the development of optical sensors with sol-gel coatings that contain chemical and biological recognising elements that absorb, fluoresce or luminesce in the presence of target species [21, 19, 22]. Thin-film sol-gels present mechanical resistance and exhibit response times under 2 min [19]. However, the thin-film's properties (thickness, volume fraction of solvent at solidification point) must be carefully considered to ensure cracking does not occur during the drying stage [20].

4.1.5 Summary of fibre coating techniques

Many coating techniques have been utilised to apply a functional material to the cladding of an optical fibre. The applicability of each technique is highly dependant

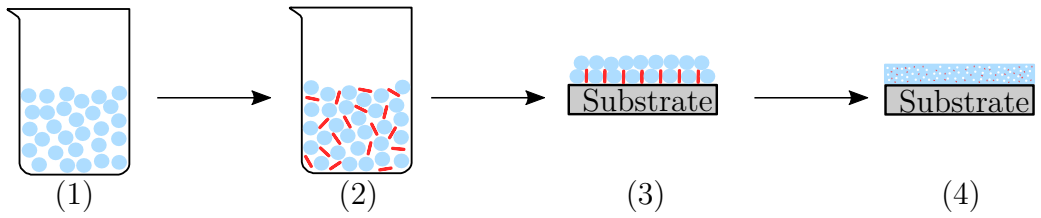

Figure 4.5: General overview of the formation of a sol-gel. Following mixing of the sol (1) with the addition of the chemical recognising groups (2), the substrate is coated with the gel (3) prior to drying to form the final xerogel coating

on the physical and chemical characteristics of the coating material. Nevertheless, some materials could be deposited onto an optical using a number of the methods outlined. It is these cases where equipment requirements and method complexities will need to be carefully considered.

4.2 Materials with a CO_2 affinity

CO_2 is a nonpolar, triatomic molecule comprised of two carbon-oxygen bonds arranged linearly around a central atomic carbon. This central atom is prone to nucleophilic attacks whereas the oxygen atoms tend to suffer from electrophilic encounters [23]. The most common CO_2 complex is formed through a strong covalent bond with Lewis acidic carbon atom of the CO_2 molecule and a Lewis base donor atom (e.g. formation of carbamate groups) [23]. Weaker interactions with CO_2 can be formed by inclusion complexes where the CO_2 molecule is adsorbed into 'holes' of porous structures without drastically altering the molecular arrangement. The ability to constrain CO_2 through the formation of weakly bound complexes is highly advantageous for material regeneration as these bonds require far less aggressive (high temperature and pressures) and energy-intense techniques to return the material to its original state [23]. The subsequent sections describe a selection of materials that demonstrate an affinity for CO_2, detailing their interaction mechanisms and key attributes with regards to an application in sensing.

4.2.1 Alkanoamines

Alkanoamines, such as monoethanolamine, diethanolamine and methyldiethanolamine, have been used extensively in the carbon sequestering industry in an attempt to mitigate global warming through the uptake of CO_2 [24]. They are generally in aqueous form in a 30 - 40 wt% amine in water [25]. Structurally, these alkanoamines

contain primary (-NH_2), secondary (-NH) and tertiary (-N-) amines groups which interact with CO_2. In the presence of anhydrous CO_2, amines can absorb 0.5 mol of CO_2/mol of amine [26].

The mechanism for CO_2 absorption in primary amines involves the formation of carbamate through zwitterionic intermediates. Initially, the central carbon atom on the CO_2 molecule undergoes nucleophillic attack from the lone electron pair present on the amine group to form the zwitterion. The zwitterion is deprotonated by a free base, typically another amine or H_2O in an aqueous amine environment, to form carbamate (Fig. 4.6). This mechanism is pertinent also for secondary amines where the NH_2 is replaced by NH [25, 27].

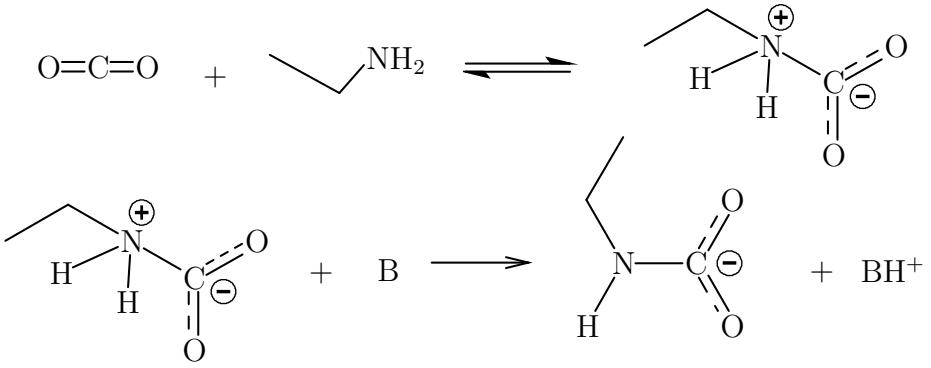

Figure 4.6: Mechanism for the reaction of primary amines with CO_2, where *B* is a free base [25]

Tertiary amines do no directly react with CO_2 but initially catalyse the formation of bicarbonate which subsequently forms an ionic association with the amine (Fig. 4.7). It is clear from Fig. 4.7 that tertiary amines are not able to react with CO_2 in dry air and require the presence of water. While this reaction can also occur in primary and secondary amines in the presence of water, however, the scheme outlined in Fig. 4.6 has a higher rate constant [25, 24].

Although alkanoamines display an affinity for CO_2 they become degraded through oxidation and carbamate polymerisation [24]. Degradation of alkanoamines can also occur through reactions with sulphur dioxide via the formation of sulfurous acid. This lowers the pH of the solution through proton release, ultimately disrupting the CO_2 absorption capabilities of the solution [28]. Furthermore, regeneration of alkanoamines requires large amounts of energy, the majority of which is used to heat H_2O in the aqueous solution [25]. Nevertheless, alkanoamines can be immobilised onto solid supports, producing a material which minimises some of the drawbacks aqueous alkanoamines suffer from yet still maintaining CO_2 affinity. Many of the materials discussed below incorporate amine functionalised groups to increase CO_2

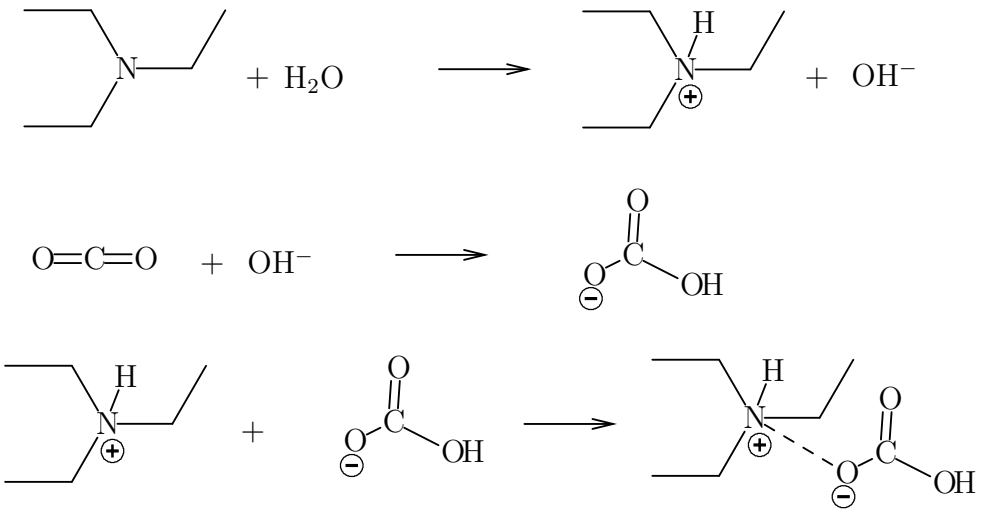

Figure 4.7: Reaction of tertiary amines with CO_2 through the initial catalysis of bicarbonate [25]

specificity.

4.2.2 Ordered mesoporous silica

Highly porous with a large surface area, ordered mesoporous silica (OMS) is an amorphous material which facilitates rapid gas diffusion. Since the first reported OMS family, M41S, numerous others have been created following their applications in catalysis, adsorption and separation processes [29]. Their structures can vary from hexagonal cylinders to cubic porous networks with pore sizes ranging from 2 - 30 nm [29]. OMS synthesis involves assembling the OMS through micelle-templating, followed by hydrothermal treatment to obtain the silcate and finally template removal via thermal or extraction techniques [30]. Although modifications to the basic synthesis process can provide different surface adaptations, without functionalisation, pure silica surfaces display poor CO_2 adsorption due to weak interactions between residual hydroxyl groups and CO_2 molecules [30, 29]. However, the large pores and hydroxyl groups of OMS makes them an ideal candidate for aminosilane functionalisation.

Functionalisation of OMS changes its porous properties, typically filling the volume. However, despite the reduction in pore volume, modification of the silcate with aminosilanes and amino-functional polymers dramatically improve CO_2 uptake. Work by Xu *et al.* [31] investigated the effect of polyethyleneimine (PEI) modification of the OMS MCM-41 on CO_2 adsorption capacity. The addition of the polyamine (50 wt% PEI loading) caused the CO_2 capacity to rise from 8.6 to 112 $mg{\cdot}g^{-1}$ of

adsorbent pre- and post-modification respectively. Many studies [32, 33, 34] have seen similar dramatic improvements in CO_2 uptake following the addition of amine containing molecules. Interestingly, the addition of humidity was noted to augment the uptake of CO_2 in OMS [32, 33, 34]. Enhancement in CO_2 capacity following exposure to a dry gas stream by the addition of amine groups is mechanistically the same as outlined in Section 4.2.1. The addition of water vapour allows further CO_2 to be adsorbed past that witnessed in a dry stream but at a substantially slower rate through the formation of bicarbonate groups. However, despite the increase in CO_2 capacity provided by the addition of moisture, the presence of water at elevated temperatures (100°C) causes severe degradation in the OMS structure via hydrolysis of Si-O-Si bonds [30].

Regeneration of amine functionalised OMS is generally achieved by temperature swing adsorption or temperature vacuum swing adsorption [35], this involves increasing the temperature or temperature and pressure in order to decrease the quantity of adsorbed gas. The effectiveness of each method depends on the adsorption temperature, where at ambient adsorption conditions (25°C) a vaccum swing technique provided better working capacity [35].

4.2.3 Zeolites

Zeolites are aluminosilicates which can be found naturally (natrolite) or synthesised artificially, where typically the latter is used commercially providing a uniform and pure product. There are numerous zeolite species classified by their structure and the ratio of Si/Al. Thermally stable, these porous crystalline structures are comprised of interlinked tetrahedral silicon tetraoxide and aluminate (AlO_4) via oxygen atoms. These frameworks possess open cavities in the form of channels and cages which molecules penetrate (e.g. Na^+, K+, Ca^{2+}, Mg^{2+}) balancing the overall negative charge created by the aluminosilcate structure [29]. Zeolites can be synthesised onto the surface of optical fibres, where they have been used in sensing applications [36, 37]. In terms of CO_2 uptake, adsorption capacities for standard zeolites such as 13X and 4A are in the range of 160 and 130 $mg{\cdot}g^{-1}$ adsorbent at room temperature and pressure [38]. A number of factors affect the CO_2 adsorption capacity of zeolites, pertaining to both the crystalline composition and the properties of the adsorbing gas.

Pore size can influence the adsorption capacity and rate of CO_2 uptake. Zeolites with small sized pores show the highest adsorption density for low pressures due to energetically favourable locations for the penetrating gas to occupy, ultimately

avoiding CO_2-CO_2 interaction. However, at high pressures the opposite is true, where large pores demonstrate the greatest uptake. The molecular interactions which hinder CO_2 adsorption at low pressures are not an issue, thus zeolites with larger pores allow CO_2 molecules to reside in the central regions of the pores, encouraging greater packing [39].

The adsorption behaviour of zeolites is also determined by the residing cation specie. The cation influences the electric field inside the pores, in addition to the available pore volume. The exchangeable cation acts as an acid site while the framework bound oxygen provides a basic site [40]. At standard pressure (1 bar), a decrease in CO_2 capacity is observed with increasing cation size, therefore cations with smaller radii (thus greater charge density), such as Li^+, display a higher capacity for CO_2 than larger, less charge dense cations [40]. Furthermore, an increased number of cations located in the zeolite structure provides more interaction sites, and therefore an increase in interactions with CO_2 molecules [39]. Cations also play a role in chemical adsorption where these metal ions act as catalysts in the formation of monodentate carbonate at the Al-Si bridging oxygen atom (Fig. 4.8). However, there is evidence that this group is thermally very stable, and heating to 700°C does not remove them from the zeolite framework, therefore blocking some surface cations [41].

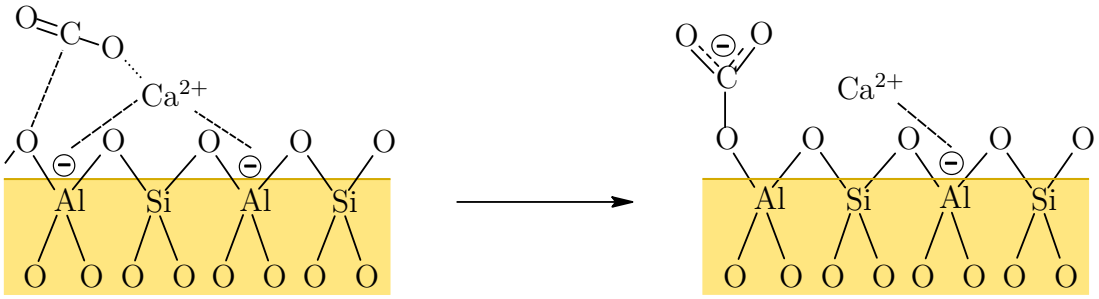

Figure 4.8: Chemical adsorption of CO_2 on a zeolite structure. The Ca^{2+} polarises the CO_2 molecule subsequently attacking the Al-Si bridging oxygen, breaking the Al-O bond finally forming a stable monodentate carbonate [39]

Another aspect of zeolite composition which effects CO_2 uptake is the ratio of Si/Al. It has been shown that decreasing the Si/Al ratio from 60 to 15 caused the CO_2 capacity to improve from 1.279 to 1.869 of $mmol^{-1}$ $CO_2 \cdot g^{-1}$ in zeolite ZSM-5 [42]. The authors suggested that this increase in CO_2 adsorption was due to a smaller Si/Al ratio produced by stronger electrostatic fields inside the pores (due to a higher framework basicity mediated via a greater Al^{3+} content), with a more pronounced effect on molecules with a strong, permanent quadrupole. It is this permanent quadrupole present in CO_2 molecules that allows selective adsorption to take occur,

preferentially interacting with cation sites over competing molecules (e.g. N_2) with lesser quadrupole moments [39].

The performance of zeolites can be improved via the integration of organic-amine groups into the porous structure. Chatti *et al.* [38] demonstrated that by loading the zeolite 13X with the amine monoethanolamine it was possible to improve CO_2 uptake by approximately 30% at 75°C. This result has also been confirmed in other zeolitic structures (Y-type zeolites) with the amine tetraethylenepentamine [43]. In addition to improved adsorption capacity, amines also improve the selectivity for CO_2 over N_2 and methane [44]. Mechanistically, the confined amine groups react with CO_2 via the same scheme as alkanoamines, outlined in Section 4.2.1. Furthermore, the regeneration in amine-impregnated zeolites is less energy intense as the moeities are suspended on a solid structure rather than being dissolved in an aqueous solution.

The presence of humidity has been shown to inhibit CO_2 adsorption in zeolites. The high polarity of water causes it to preferentially interact with the exchangeable cations in place of CO_2, reducing the strength of the electric field and limiting uptake [45].

4.2.4 Metal organic frameworks

Metal organic frameworks are crystalline porous organic molecules which display large pore volumes and high internal surface areas. Constructed of metal-containing units (secondary building units (SBUs)) linked with organic ligands, MOFs form well-defined two or three-dimensional network structures capable of organic modification (Fig. 4.9) [46]. Pores can be structured in channels, cages or a combination of both, influencing the adsorption capabilities. The ability to interchange the SBUs and organic ligands has led to the preparation of thousands of MOF structures [48]. With careful selection of SBUs, the original properties displayed by these units can be maintained and exhibited by the final product [46]. In addition to directly synthesising MOFs with desirable traits, these crystalline structures may also be modified post-synthetically, allowing the addition of groups which may otherwise interfere with the formation of the framework if added during direct synthesis. This is achieved by incorporating functional moieties (i.e. amines) using organic transformations, enhancing the structures reactivity to particular molecules [49].

The CO_2 adsorption capacity of MOFs is greatly affected by porosity parameters (surface area, pore size and volume) [50]. Increased surface area and pore volume has been recognised to increase adsorption capacity [47]. Enhancement of these porosity

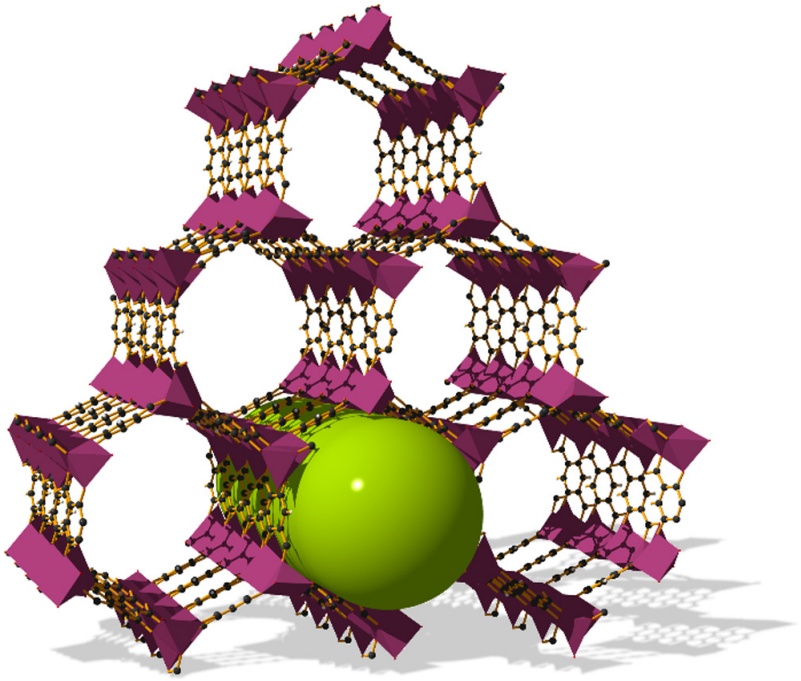

Figure 4.9: The structure of Mg-MOF-74 highlighting the porous channel (green rod). Mg, purple polyhedra; C, black; O, red; H, light grey. Taken from [47]

parameters in homogeneous MOFs can be achieved through the increase in pore size (0.8 - 2.0 nm), which leads to an improvement in CO_2 uptake at medium to high pressures (<50 bar) [47]. In addition to increased pore size, MOFs which possess high-densities of adsorption sites (e.g. exposed metal cations) also demonstrate excellent adsorption properties. At low pressures (<1.2 bar), CO_2 uptake is dictated by chemical features displayed by the framework, thus MOFs with functionalised pores performed the best [50]. Although MOFs with an increase in both surface area and pore volume may improve adsorption capacity, these crystalline structures lack specificity for CO_2 [47].

Two distinct mechanisms have been proposed for governing selectivity in MOFs. Firstly, size/shape-based selectivity, where the pore-size permits certain sized molecular diameters to diffuse into the MOF. However, this regime is limited to a few examples [51] as the majority of MOFs demonstrate large surface areas and adsorption capacity therefore possessing large pore openings permitting molecules larger than CO_2 into the framework. An alternate mechanism that regulates selectivity in MOFs is the variation in affinity for different components of the pore surface experienced by the gas mixture. Physisorptive adsorption relies on the polarisation or charge distribution of the target gas to preferentially interact with pore surface of the MOF over other competing molecules. This can be tailored by installing highly charged groups or metal cations directly to the MOF [52, 50].

Selectivity in MOFs can also be regulated through chemical interactions between functionalised groups attached to the pore's surface and the target gas, resulting in far greater selectivity than physisorptive adsorption alone [50]. Using post-synthetic treatments, MOFs have been functionalised with nucleophillic amine groups to improve CO_2 selectivity. The mechanism of action between a grafted amine moiety and CO_2 is the same as noted with alkanoamines outlined in Section 4.2.1. Post-synthetic amine-functionalised MOFs have been achieved using PEI [53] and ethylenediamine [54]. In addition to improved CO_2 affinity, the MOFs functionalised with amine groups also demonstrated a reduction in N_2 uptake through reductions in pore size resulting from the pore modification [50]

Although MOFs have the potential to become ideal CO_2 sensitive coatings, they do however have limitations. MOFs are susceptible to interactions with water, where typically the metal-ligand bond is most vulnerable to hydrolysis, leading to a loss in structure [55]. However, recent efforts have demonstrated that incorporation of a surfactant may aid reducing water mediated disturbances [56].

Despite the advantages displayed by MOFs for CO_2 adsorption, there is a limited number of CO_2 sensing devices which utilise these crystalline structures [57]. This lack of interest for exploiting MOFs as CO_2 sensors may be due to the difficulty in identifying an appropriate sensing technique that can recognise the CO_2 mediated change experienced by the MOF.

4.2.5 Ionic liquids

Ionic liquids are molten salts that are almost exclusively comprised of ions and which possess a melting point below 100°C, often below room temperature [58]. These molten salts are receiving ever increasing attention in the scientific community due to a number of attractive properties, including negligible vapour pressure, stability to thermal and electrochemical variations, and the ability to be tailored for specific functional needs via alterations to the anion/cation combination (examples of commonly used anions and cations can be see in Fig. 4.10) [59]. Although the first ionic liquid, ethanolammonium nitrate, was reported in 1888 with a melting point of 52-55°C [60], progress was subsequently slow until an eruption of interest was witnessed between 1998 - 2000 for their potential as a clean chemical alternative to widely utilised organic solvents which are environmentally hazardous [59].The concept of tailoring ionic liquids as solvents for specific molecules has provided a useful technique for separating individual gases from a mixture. This ability has been used to separate hydrogen [61] and remove sulphur dioxide from a simulated

gas flue [62]. Indeed, the capture of CO_2 by ionic liquids has attracted a lot of attention for its potential use in atmospheric carbon sequestering as a technique to offset global warming. Dissolution of CO_2 is achieved through either physical or chemical absorption.

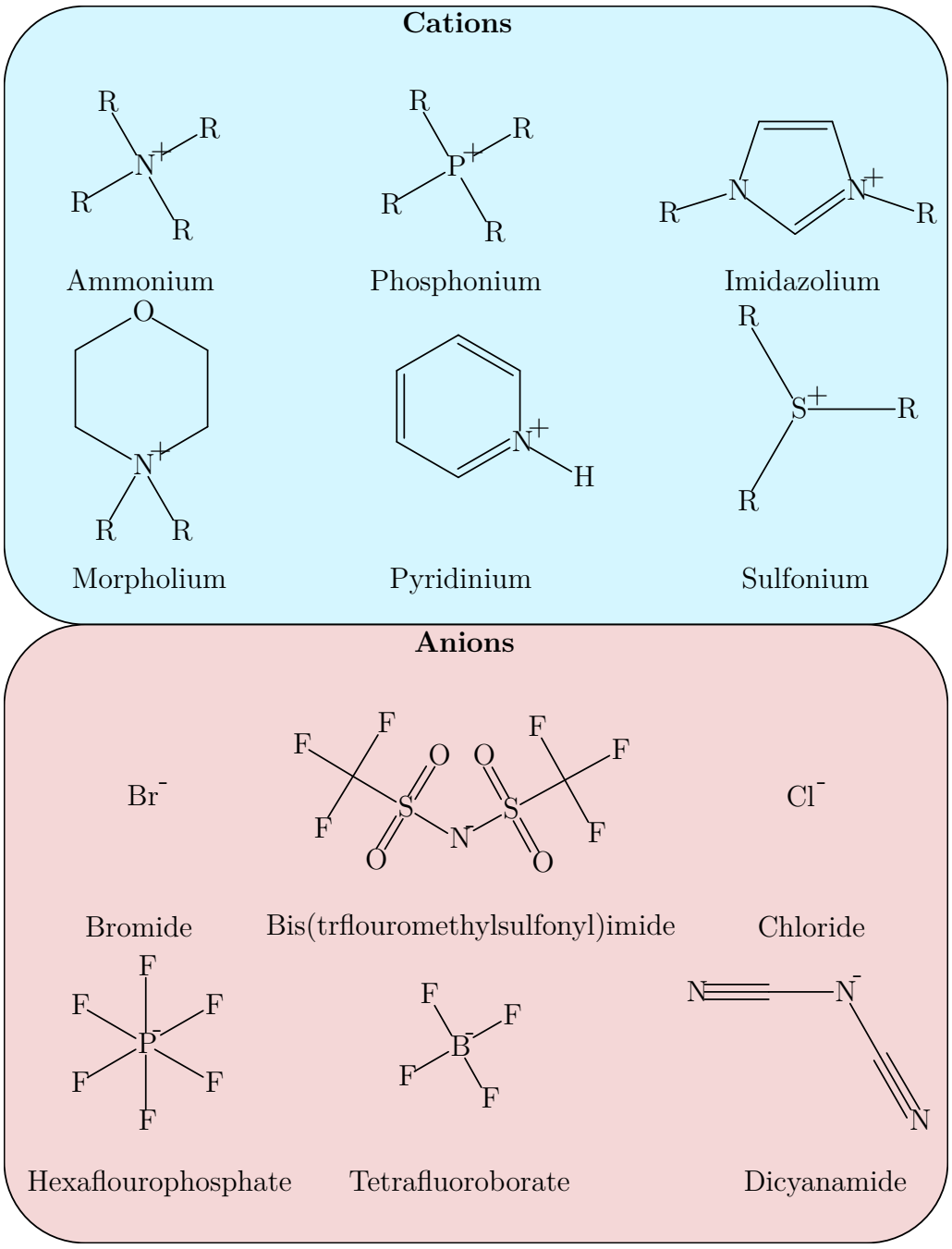

Figure 4.10: Chemical structure of common anions and cations of ionic liquids [63]

Synthesis

Only in the last decade have many of the common ionic liquids become commercially available. However, they are still relatively expensive to purchase. Typically, they tend to be synthesised in-house, and with the number of ionic liquids increasing the variety of methods in which to produce them has grown.

Many of the common ionic liquids are synthesised in a two-staged process. Initially, the cation is prepared by alkylation using an appropriate pre-cursor or halogenoalkane. Secondly, the desired anion is then exchanged with the unwanted halide anion via anion metathesis or by treating the halide salt with a Lewis acid [64]. The synthesis of 1-methyl-3-ethylimidazolium bis(trifluoromethylsulfonyl)imide is demonstrated in Fig. 4.11.

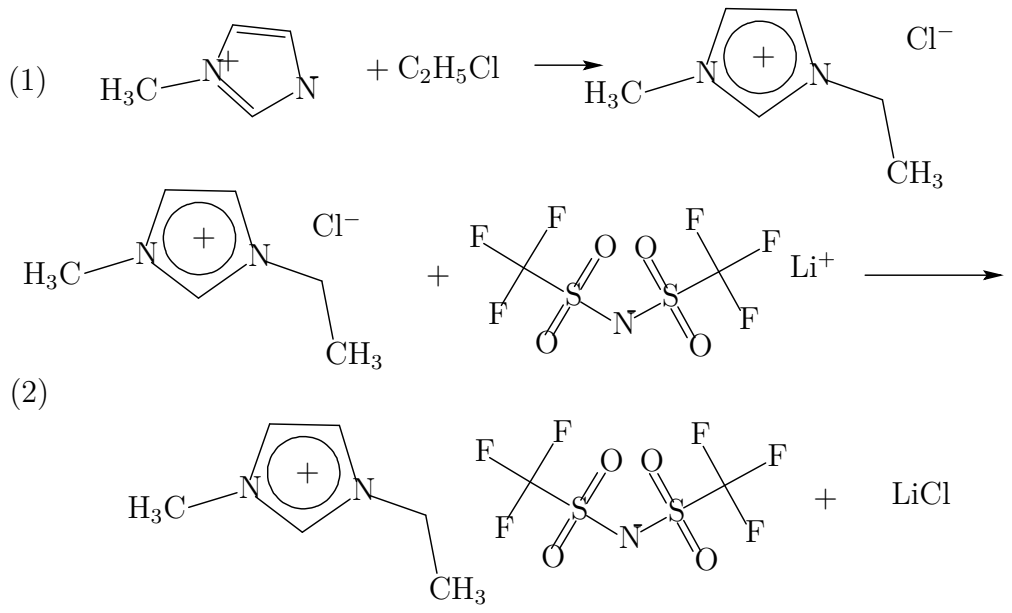

Figure 4.11: Synthesis of 1-methyl-3-ethylimidazolium bis(trifluoromethylsulfonyl)imide via alkylation (1) and anion metathesis (2)

Numerous ionic liquids can be synthesised with this scheme via the use of various organic salts and inorganic anion sources. However, the undesired halide salt can taint the ionic liquid product even following purification steps. Consequently, akyl-sulfates have been used in place of halogenalkanes as alkylating agents [65]. The main aim of all anion-exchange reactions is to produce an ionic liquid uncontaminated with undesired cations or anions.

Physical absorption of CO_2

Physical absorption of CO_2 does not require additional functional groups to be attached to the ionic liquid, therefore effective absorption is primarily dictated by temperature and pressure [66]. Typically, conventional ionic liquids (relying on physical absorption mechanisms) show excellent CO_2 capacity at high pressures (>10 bar) but diminished absorption in ambient conditions [67, 63]. While many ionic liquids have been assessed for their CO_2 solubility (ammonium-, phosphonium-, pyridinium-based), imidazolium-based ionic liquids have demonstrated a remarkable propensity to absorb CO_2 [68]. It is thought that the anion plays a dominant role in defining the CO_2 absorption ability of the ionic liquid. Two ionic liquids with the same cation (1-alkyl-3-methylimidazolium) but with different anions (tetrafluoroborate (BF_4), hexaflourophosphate (PF_6) were subjected to high pressure CO_2, to investigate the quantity of absorption [69]. Their results demonstrated a 40% difference in CO_2 absorption between the two ionic liquids, where it was speculated that CO_2 molecules organised themselves strongly around the anion. This idea was extended further to assess a range of anions for their capacity to dissolve CO_2 [70]. The anions were paired with the cation 1-butyl-3-methylimidazolium (Bmim) to produce the following order of increasing CO_2 solubility: nitrate < dicyanamide < methylsulfate < [BF_4] < [PF_6] < triflate < bis(trifluoromethylsulfonyl)imide ([Tf_2N]) < methide. It was suggested that this observed interaction of CO_2 with the anion could in part be due to acid/base interplay. This theory was also proposed by Kazarian and colleagues [69], where the results implied that [BF_4] and [PF_6] were acting as weak Lewis bases towards the CO_2. Furthermore, ionic liquids that contained fluorinated anions inclined to show a larger CO_2 solubility compared with non-fluorinated counterparts [71]. Interestingly, the same study also showed that fluorinated cations did not significantly improve CO_2 solubility.

Nevertheless, CO_2-anion interactions can not be the only mechanism that influences CO_2 absorption, as the solubility in ionic liquids comprised of [BF_4] is less than that in [Tf_2N] [69], which is unexpected as [BF_4] is a stronger Lewis base [72]. Thus it has been suggested that the free volume between the ions may have an effect on CO_2 absorption. Molecular dynamics simulation studies have investigated the size and structural variations of these cavities when the ionic liquid is exposed to CO_2. It has been shown that the fundamental structure of the ionic liquid was not altered upon the addition of CO_2, which was attributed to strong Coulombic forces governing the solvents structure [68]. However, the formation of solvent cages, often witnessed in standard solvent-solute interactions, in ionic liquids minimally

disrupts the overall ion organisation after CO_2 absorption, confirmed by the negligible changes in the radial distribution functions (i.e. the change in molecular density as a function of radius) [66]. Further simulation work has examined the role of cation-anion interactions and their effect on CO_2 solubility. Klahn and Seduraman [66] demonstrated that a reduction in ionic cohesion induced larger distances between the cations and anions enabling greater CO_2 insertion. These local cavities were considered a consequence of ionic size. As such, large, bulky cation-anion pairs like 1-hexyl-3-methylimidazolium ([C_6mim]) [Tf_2N] presented more empty space between ions and greater CO_2 absorption than more compact configurations seen in [Bmim][PF_6] (Fig. 4.12). Nevertheless, the pre-formed cavities are not adequately

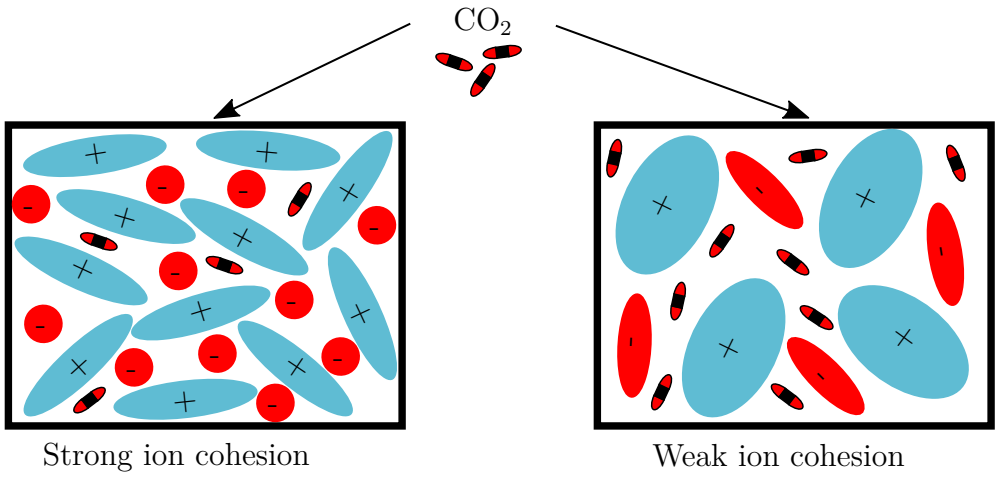

Figure 4.12: Strong cohesion between cations (aqua) and anions (red) reduces the size and number of spaces between molecules diminishing the ability for CO_2 absorption, whereas larger, less cohesive cation-anion pairs possess more cavities. Adapted from [66]

sized to accommodate a complete CO_2 molecule, suggesting that the ionic liquid undergoes small, localised ion expansion without disrupting the overall configuration [66]. The proposed cavity theory as a mechanism for CO_2 absorption explains the dependence of anion selection seen by Aki et al [70] as methide was the largest anion assessed and would demonstrate the greatest stearic repulsion.

While data has indicated that the cation does not play an important role in CO_2 affinity, research from Aki *et al.* [70] showed that the length of the alkyl chain found on the imidazolium ring does affect the solubility of CO_2. The authors tested CO_2 solubility in [Tf_2N] with 1-n-3-methylimidazolium for n = butyl, hexyl, and octyl. The results demonstrated that solubility increased with a greater alkyl chain length. Further alterations of the imidazolium ring have also been assessed for their effect on CO_2 solubility. Methyl group substitution of the protic hydrogen at the C2 position did not alter the solubility of CO_2 at pressures up to 13 bar [68].

However, for pressures exceeding 100 bar, removal of the protic hydrogen negatively affected CO_2 absorption [70]. Although an effect of CO_2 solubility has been noted through imidazolium-based cation modifications, these influences are only secondary compared with anion selection which dominates CO_2 absorption [70, 68, 72].

As previously mentioned, physio-chemical properties of ionic liquids can be modulated simply through appropriate anion/cation selection, influencing CO_2 absorption. However, in addition to effects of CO_2 dissolution, the anion and cation pair also determine the ionic liquid's hydrophilicty. Similar to CO_2 absorption, the anion has been found to play a more significant role [73]. Halide-, nitrate-, methyl-, and sulfonate-based anions aid water miscibility while $[PF_6]$ and $[Tf_2N]$ resist mixing with water [74]. Anions with a high charge density in a small volume (e.g. $[BF_4]$) form anion-water-anion hydrogen bond complexes [75] since water exhibits preferential interaction with anions as they are competitively smaller than cations and present greater surface charges [76]. These interactions would indicate that the primary mechanism for water miscibility in ionic liquids is electrostatics.

Although not a significant contributor to ionic liquid hydrophilicty, the physio-chemical nature of the cation can also influence the miscibility of water in ionic liquids. Experimental [77] and molecular simulation data [78] have demonstrated that an increased alkyl chain length on the imidazolium ring deceases the mutual solubilities between water and ionic liquid. The hydrophobicity caused by the greater alkyl chain length has been shown not to be caused by interference with hydrogen bonds formed between anions and water, thus not to interrupt the primary mechanism of water miscibility. Nevertheless, it has been suggested that the increase in alkyl chain length decreases the space around the imidazolium ring, which is relatively polar in comparison to alkyl chains, reducing water solubility of the ionic liquid [79]. The same study also indicated that an increase in alkyl side chain length up to 6 carbons significantly reduced water solubility for each additional CH_2 group for $[C_n\text{mim}][Tf_2N]$. However, further CH_2 groups did not demonstrate such dramatic decreases in water miscibility.

Physical CO_2 absorption in ionic liquids greatly depends on the cavities found between the cation and anion. In order to maximise these spaces, and thus CO_2 absorption, the ions should be large to increase inter-ionic repulsive interactions, reducing ion density and increasing regions of unoccupied space.

Chemical absorption of CO_2

In chemical absorption, CO_2 reacts with the ionic liquid generally offering greater solubility than ionic liquids which operate via pure physical absorption. Typically, these molten salts are tailored to a specific purpose via the introduction of a functional group. Termed task-specific, these ionic liquids have been applied to CO_2 absorption through the integration of functional groups such as amines, acetates and cyanates [66, 64].

The addition of a primary amine moeity to an imidazolium based ionic liquid demonstrated a 7.4% mass increase following a 3 h exposure to dry CO_2 at 1 atm which far exceeds the 0.088% shown by a similar structured conventional ionic liquid. Additionally, the task-specific ionic liquid was able to maintain the same absorption efficiency following 5 regeneration cycles [80]. This work has led to the development of further amine-functionalised ionic liquids [81], which have been applied to prototype CO_2 gas separation membrane technologies [82, 83]. Operationally, task-specific ionic liquids sequester CO_2 in a similar mechanism to standard alkanoamines (Section 4.2.1).

Although task-specific ionic liquids designed for CO_2 absorption outperform their standard counterparts, they do however require prolonged periods ($\sim$3 h) at temperatures in excess of 100°C while under vacuum to regenerate their absorption efficiency [80].

Ionogels

Although ionic liquids demonstrate the ability to absorb CO_2, these materials are naturally in the liquid phase at room temperature, and as such, would not adhere to the optical fibre in an organised structure. The ability to immobilise ionic liquids while maintaining their desired properties has been accomplished through the formation of ionic liquid gels, or ionogels.

Ionogels can be formed by inorganic, organic or a hybrid organic-inorganic synthesis [84]. Using the former category, single-walled carbon nanotubes were ground with various imidazolium based ionic liquids to form a gelatinous material which can be moulded into a desired shape yet retain ion-conductivity [85]. Additionally, ionic liquids have also been immobilised within carbon nanotubes producing ionic liquid crystals with a melting point of 200°C [86]. Although these techniques can stabilise ionic liquids, processing them with carbon nanotubes is a difficult method. For further detail on inorganic and hybrid ionogels see reference [84].

The formation of organic ionogels through the addition of low molecular-weight organic gelators (LMOGs) has allowed the simple production of physically stable, room temperature gels. Low loading of these small molecules can gel large volumes of liquid via physical bonding such as van der Waals forces, π-π bond stacking and hydrogen bonding [87]. Kimizuka and colleagues [88] were able to create ionogels through heating and cooling amolose with imidizolium based ionic liquids to form a stable ionogel at room temperature. Utilising this approach, Voss *et al.* [89] fabricated an ionogel for gas separation using the ionic liquid [C_6mim][Tf_2N] (which has demonstrated CO_2 affinity) and the LMOG 12-hydroxystearic acid (known for its ability to gel nonpolar solvents). The ionogel exhibited comparable levels to pure [C_6mim][Tf_2N] in CO_2 solubility (2.68 and 2.1 $cm^3 \cdot atm \cdot ml^{-1}$ respectively). The addition of LMOG to the ionic liquid created a stable soft gel that did not flow (under gravity) and could be thermally reversed. Organic ionogels are formed via percolation of the LMOG through the ionic liquid, subsequently immobilising the molten salt via formation of a fibrous, non-covalent network structure [90]. Although this technique provides a stable gel, mild elevations in temperature ($\sim$70°C) cause a gel-to-sol transition to occur thus limiting the real-world applications of this method.

4.2.6 Summary of CO_2 sensitive materials

The sole use of alkanoamines is not feasible for this project since they are in liquid phase and require the input of large amounts of energy to regenerate. Nevertheless, these amine-rich chemicals are easily acquirable commercially and can be immobilised onto solid supports (e.g. OMS) in order to provide a viable option for the fibre-based CO_2 sensor. In addition, non-aqueous polyamines could also be incorporated as part of an ESA derived coating. However, OMS, zeolites, and MOFs all suffer from humidity mediated CO_2 absorption inhibition, reducing their suitability as the LPG coating material for the CO_2 sensor here. Ionics liquids have the potential to be an ideal coating material as they possess the ability to absorb CO_2 yet display hydrophobic properties and can be stabilised through the formation of ionogels. The greatest drawback regarding their suitability for this project is whether ionic liquids will display a refractive index change following the uptake of CO_2.

4.3 Summary and conclusion

Descriptions of the 4 major optical fibre coating techniques have been outlined in Section 4.1. A review of potential CO_2 sensitive materials have also been discussed

in Section 4.2, where a concise summary of the main attributes of these materials are presented in Table 4.1. Following this review, it is clear that ionic liquids possess many qualities desirable in the coating material of a CO_2 sensor (CO_2 solubility, adaptable secondary properties, capable of being regenerated, able to form a stable gel structure). Therefore, the ionic liquid 1-hexyl-3-methylimidazolium bis(trifluoromethylsulfonyl)imide ($[C_6mim][Tf_2N]$) was chosen as the CO_2 sensitive material for the LPG-based CO_2 sensor based on the aforementioned attributes, its hydrophobic nature, and that it is commercial available (since the Centre for Engineering Photonics does not have access to the necessary equipment required to synthesis ionic liquids).

Table 4.1: Comparison of CO_2 sensitive materials for potential use as a fibre coating. Abbreviations: Metal organic frameworks (MOFs), Advantage (+), Disadvantage (−)

Material	**Notes**
Alkanoamines	(+) Minimal preparation required (−) High temperatures and/or vacuum for regeneration (−) Not suitable in aqueous form for fibre coating
Mesoporous silica	(+) CO_2 uptake enhanced by the presence of water (−) Naturally presents low CO_2 adsorption capacity - must be augmented with CO_2 functional groups (−) Structural degradation in humidity at elevated temperatures (100°C)
Zeolites	(+) High thermal stability (∼700°C) (+) Favourable CO_2 adsorption kinetics at ambient temperatures and pressures (0 - 100°C, 0.1 - 1.0 bar) (−) CO_2 uptake inhibited in the presence of water
MOFs	(+) Properties (pore size, pore volume, metal ion) can be tailored for specific requirements (+) Excellent CO_2 adsorption at high pressures (−) Framework susceptible to hydrolysis
Ionic liquids	(+) Large CO_2 absorption capacity at high pressures (+) Properties of liquid (hydrophobicity, CO_2 affinity) can be easily adapted through different ion combinations (+) May present hydrophobicity and CO_2 affinity simultaneously without post-treatment (+) Formation of stable matrix possible while maintaining initial properties (−) Conventional ionic liquids show low CO_2 solubility (∼0.4 wt%) at ambient temperatures and pressures (−) Synthesis requires equipment not available in the Centre for Engineering Photonics laboratories

4.4 References

[1] N. Sahu, B. Parija, and S. Panigrahi. Fundamental understanding and modeling of spin coating process: A review. *Indian Journal of Physics*, 83(4):493–502, 2009.

[2] T. Venugopalan, T. L. Yeo, T. Sun, and K. T. Grattan. LPG-based PVA coated sensor for relative humidity measurement. *IEEE Sensors Journal*, 8(7):1093–1098, 2008.

[3] M. Partridge, R. Wong, S. W. James, F. Davis, S. P. Higson, and R. P. Tatam. Long period grating based toluene sensor for use with water contamination. *Sensors and Actuators B: Chemical*, 203(1):621–625, 2014.

[4] S. Korposh, R. Selyanchyn, W. Yasukochi, S.-W. Lee, S. W. James, and R. P. Tatam. Optical fibre long period grating with a nanoporous coating formed from silica nanoparticles for ammonia sensing in water. *Materials Chemistry and Physics*, 133(2-3):784–792, 2012.

[5] P. Biswas, F. Chiavaioli, S. Jana, S. Bandyopadhyay, N. Basumallick, A. Giannetti, S. Tombelli, S. Bera, A. Mallick, F. Baldini, and C. Trono. Manufacturing and optimization of sol-gel-based TiO2-SiO2 thin Films as high refractive index overlays for long period grating-based biosensing. In *2016 4th International Conference on Photonics, Optics and Laser Technology*, pp. 1–7. 2016.

[6] D. Grosso. How to exploit the full potential of the dip-coating process to better control film formation. *Journal of Materials Chemistry*, 21(43):17033–17038, 2011.

[7] L. L. Hench and J. K. West. The sol-gel process. *Chemical Reviews*, 90(1):33–72, 1990.

[8] M. Faustini, B. Louis, P. A. Albouy, M. Kuemmel, and D. Grosso. Preparation of sol- gel films by dip-coating in extreme conditions. *The Journal of Physical Chemistry C*, 114(17):7637–7645, 2010.

[9] G. Decher. *Polyelectrolyte Multilayers: An overview*, chap. 1, pp. 1–46. Wiley-Blackwell, 2003.

[10] G. Decher. Fuzzy nanoassemblies: toward layered polymeric multicomposites. *Science*, 277(5330):1232–1237, 1997.

[11] I. Del Villar, M. Achaerandio, I. R. Matías, and F. J. Arregui. Deposition of overlays by electrostatic self-assembly in long-period fiber gratings. *Optics Letters*, 30(7):720–722, 2005.

[12] S. Korposh, S. W. James, S.-W. Lee, S. Topliss, S. C. Cheung, W. J. Batty, and R. P. Tatam. Fiber optic long period grating sensors with a nanoassembled mesoporous film of SiO2 nanoparticles. *Optics Express*, 18(12):13227–13238, 2010.

[13] S. Korposh, S.-W. Lee, S. W. James, and R. P. Tatam. Refractive index sensitivity of fibre-optic long period gratings coated with SiO2 nanoparticle mesoporous thin films. *Measurement Science and Technology*, 22(7):1–10, 2011.

[14] J. Hromadka, B. Tokay, R. Correia, S. P. Morgan, and S. Korposh. Carbon dioxide measurements using long period grating optical fibre sensor coated with metal organic framework HKUST-1. *Sensors and Actuators B: Chemical*, 255(1):2483–2494, 2018.

[15] S. M. Topliss. *Optical fibre long period grating sensors with nanostructured coatings*. Ph.D. thesis, Cranfield University, 2011.

[16] M. Partridge. *Fibre-optic sensors with molecular coatings*. Ph.D. thesis, Cranfield University, 2012.

[17] S. W. James and R. P. Tatam. Fibre optic sensors with nano-structured coatings. *Journal of Optics A: Pure and Applied Optics*, 8(7):S430–S444, 2006.

[18] C. J. Brinker. *Chemical Solution Deposition of Functional Oxide Thin Films*, chap. 10, pp. 233–261. Springer, 2013.

[19] P. C. Jerónimo, A. N. Araújo, and M. C. B. Montenegro. Optical sensors and biosensors based on sol–gel films. *Talanta*, 72(1):13–27, 2007.

[20] C. J. Brinker and G. W. Scherer. *Sol-Gel Science*. Academic Press inc., London, UK, 1st ed., 1990.

[21] B. D. MacCraith, C. M. McDonagh, G. O'Keeffe, E. T. Keyes, J. G. Vos, B. O'Kelly, and J. F. McGilp. Fibre optic oxygen sensor based on fluorescence quenching of evanescent-wave excited ruthenium complexes in sol–gel derived porous coatings. *Analyst*, 118(4):385–388, 1993.

[22] M. Attia, H. Zoulghena, and M. Abdel-Mottaleb. A new nano-optical sensor thin film cadmium sulfide doped in sol–gel matrix for assessment of α-amylase activity in human saliva. *Analyst*, 139(4):793–800, 2013.

[23] L. J. Murphy, K. N. Robertson, R. A. Kemp, H. M. Tuononen, and J. A. Clyburne. Structurally simple complexes of CO2. *Chemical Communications*, 51(19):3942–3956, 2015.

[24] C.-H. Yu, C.-H. Huang, C.-S. Tan, *et al.* A review of CO2 capture by absorption and adsorption. *Aerosol Air Quality Research*, 12(5):745–769, 2012.

[25] S. Choi, J. H. Drese, and C. W. Jones. Adsorbent materials for carbon dioxide capture from large anthropogenic point sources. *ChemSusChem*, 2(9):796–854, 2009.

[26] G. Sartori and D. W. Savage. Sterically hindered amines for carbon dioxide removal from gases. *Industrial and Engineering Chemistry Fundamentals*, 22(2):239–249, 1983.

[27] Y. G. Ko, S. S. Shin, and U. S. Choi. Primary, secondary, and tertiary amines for CO2 capture: Designing for mesoporous CO2 adsorbents. *Journal of Colloid and Interface Science*, 361(2):594–602, 2011.

[28] Y. Beyad, R. Burns, G. Puxty, and M. Maeder. The role of SO2 in the chemistry of amine-based CO2 capture in PCC. *Energy Procedia*, 37(1):1262–1266, 2013.

[29] N. Gargiulo, F. Pepe, and D. Caputo. CO2 adsorption by functionalized nanoporous materials: a review. *Journal of Nanoscience and Nanotechnology*, 14(2):1811–1822, 2014.

[30] T.-L. Chew, A. L. Ahmad, and S. Bhatia. Ordered mesoporous silica (OMS) as an adsorbent and membrane for separation of carbon dioxide (CO2). *Advances in Colloid and Interface Science*, 153(1-2):43–57, 2010.

[31] X. Xu, C. Song, J. M. Andresen, B. G. Miller, and A. W. Scaroni. Preparation and characterization of novel CO2 'molecular basket' adsorbents based on polymer-modified mesoporous molecular sieve MCM-41. *Microporous and Mesoporous Materials*, 62(1-2):29–45, 2003.

[32] G. P. Knowles, J. V. Graham, S. W. Delaney, and A. L. Chaffee. Aminopropyl-functionalized mesoporous silicas as CO2 adsorbents. *Fuel Processing Technology*, 86(14-15):1435–1448, 2005.

[33] R. Serna-Guerrero, E. Dana, and A. Sayari. New insights into the interactions of CO2 with amine-functionalized silica. *Industrial and Engineering Chemistry Research*, 47(23):9406–9412, 2008.

[34] S. Liu, Q. Shen, Y. Cao, L. Gan, Z. Wang, M. L. Steigerwald, and X. Guo. Chemical functionalization of single-walled carbon nanotube field-effect transistors as switches and sensors. *Coordination Chemistry Reviews*, 254(9-10):1101–1116, 2010.

[35] R. Serna-Guerrero, Y. Belmabkhout, and A. Sayari. Triamine-grafted pore-expanded mesoporous silica for CO 2 capture: effect of moisture and adsorbent regeneration strategies. *Adsorption*, 16(6):567–575, 2010.

[36] N. Liu, J. Hui, C. Sun, J. Dong, L. Zhang, and H. Xiao. Nanoporous zeolite thin film-based fiber intrinsic Fabry-Perot interferometric sensor for detection of dissolved organics in water. *Sensors*, 6(8):835–847, 2006.

[37] J. Zhang, X. Tang, J. Dong, T. Wei, and H. Xiao. Zeolite thin film-coated long period fiber grating sensor for measuring trace chemical. *Optics Express*, 16(11):8317–8323, 2008.

[38] R. Chatti, A. K. Bansiwal, J. A. Thote, V. Kumar, P. Jadhav, S. K. Lokhande, R. B. Biniwale, N. K. Labhsetwar, and S. S. Rayalu. Amine loaded zeolites for carbon dioxide capture: Amine loading and adsorption studies. *Microporous and Mesoporous Materials*, 121(1-3):84–89, 2009.

[39] D. Bonenfant, M. Kharoune, P. Niquette, M. Mimeault, and R. Hausler. Advances in principal factors influencing carbon dioxide adsorption on zeolites. *Science and Technology of Advanced Materials*, 9(1):013007, 2008.

[40] K. S. Walton, M. B. Abney, and M. D. LeVan. CO2 adsorption in Y and X zeolites modified by alkali metal cation exchange. *Microporous and Mesoporous Materials*, 91(1-3):78–84, 2006.

[41] C. Angell and M. Howell. Infrared spectroscopic investigations of zeolites and adsorbed molecules. Part V. Carbon dioxide. *Canadian Journal of Chemistry*, 47(20):3831–3836, 1969.

[42] G. Calleja, J. Pau, and J. Calles. Pure and multicomponent adsorption equilibrium of carbon dioxide, ethylene, and propane on ZSM-5 zeolites with different Si/Al ratios. *Journal of Chemical and Engineering Data*, 43(6):994–1003, 1998.

[43] F. Su, C. Lu, S.-C. Kuo, and W. Zeng. Adsorption of CO2 on amine-functionalized Y-type zeolites. *Energy and Fuels*, 24(2):1441–1448, 2010.

[44] X. Xu, X. Zhao, L. Sun, and X. Liu. Adsorption separation of carbon dioxide, methane and nitrogen on monoethanol amine modified β-zeolite. *Journal of Natural Gas Chemistry*, 18(2):167–172, 2009.

[45] F. Brandani and D. M. Ruthven. The effect of water on the adsorption of CO2 and C3H8 on type X zeolites. *Industrial and Engineering Chemistry Research*, 43(26):8339–8344, 2004.

[46] J. L. Rowsell and O. M. Yaghi. Metal–organic frameworks: a new class of porous materials. *Microporous and Mesoporous Materials*, 73(1-2):3–14, 2004.

[47] Y. Belmabkhout, V. Guillerm, and M. Eddaoudi. Low concentration CO2 capture using physical adsorbents: Are metal–organic frameworks becoming the new benchmark materials? *Chemical Engineering Journal*, 296(1):386–397, 2016.

[48] H. Furukawa, K. E. Cordova, M. O'Keeffe, and O. M. Yaghi. The chemistry and applications of metal-organic frameworks. *Science*, 341(6149):1–12, 2013.

[49] Z. Wang and S. M. Cohen. Postsynthetic covalent modification of a neutral metal-organic framework. *Journal of the American Chemical Society*, 129(41):12368–12369, 2007.

[50] K. Sumida, D. L. Rogow, J. A. Mason, T. M. McDonald, E. D. Bloch, Z. R. Herm, T.-H. Bae, and J. R. Long. Carbon dioxide capture in metal–organic frameworks. *Chemical Reviews*, 112(2):724–781, 2012.

[51] M. Dinca and J. R. Long. Strong H2 binding and selective gas adsorption within the microporous coordination solid Mg3(O2C-C10H6-CO2)3. *Journal of the American Chemical Society*, 127(26):9376–9377, 2005.

[52] J.-R. Li, R. J. Kuppler, and H.-C. Zhou. Selective gas adsorption and separation in metal–organic frameworks. *Chemical Society Reviews*, 38(5):1477–1504, 2009.

[53] Y. Lin, H. Lin, H. Wang, Y. Suo, B. Li, C. Kong, and L. Chen. Enhanced selective CO2 adsorption on polyamine/MIL-101 (Cr) composites. *Journal of Materials Chemistry A*, 2(35):14658–14665, 2014.

[54] A. Demessence, D. M. D'Alessandro, M. L. Foo, and J. R. Long. Strong CO2 binding in a water-stable, triazolate-bridged metal- organic framework

functionalized with ethylenediamine. *Journal of the American Chemical Society*, 131(25):8784–8786, 2009.

[55] L. Huang, H. Wang, J. Chen, Z. Wang, J. Sun, D. Zhao, and Y. Yan. Synthesis, morphology control, and properties of porous metal–organic coordination polymers. *Microporous and Mesoporous Materials*, 58(2):105–114, 2003.

[56] C. A. Fernandez, S. K. Nune, H. V. Annapureddy, L. X. Dang, B. P. McGrail, F. Zheng, E. Polikarpov, D. L. King, C. Freeman, and K. P. Brooks. Hydrophobic and moisture-stable metal–organic frameworks. *Dalton Transactions*, 44(30):13490–13497, 2015.

[57] J. Hromadka, B. Tokay, S. W. James, and S. Korposh. Metal-organic framework thin films on a surface of optical fibre long period grating for chemical sensing. In *Optical Fiber Sensors Conference (OFS), 2017 25th*, pp. 1–4. IEEE, 2017.

[58] M. Cvjetko Bubalo, S. Vidović, I. Radojčić Redovniković, and S. Jokić. Green solvents for green technologies. *Journal of Chemical Technology and Biotechnology*, 90(9):1631–1639, 2015.

[59] M. Freemantle. *An Introduction to Ionic Liquids*. The Royal Society of Chemistry, Cambridge, UK, 1st ed., 2009.

[60] T. L. Greaves and C. J. Drummond. Protic ionic liquids: properties and applications. *Chemical Reviews*, 108(1):206–237, 2008.

[61] J. Kumełan, Á. Pérez-Salado Kamps, D. Tuma, and G. Maurer. Solubility of H2 in the ionic liquid [hmim][Tf2N]. *Journal of Chemical and Engineering Data*, 51(4):1364–1367, 2006.

[62] W. Wu, B. Han, H. Gao, Z. Liu, T. Jiang, and J. Huang. Desulfurization of flue gas: SO2 absorption by an ionic liquid. *Angewandte Chemie International Edition*, 43(18):2415–2417, 2004.

[63] J. Huang and T. Rüther. Why are ionic liquids attractive for CO2 absorption? An overview. *Australian Journal of Chemistry*, 62(4):298–308, 2009.

[64] E. I. Privalova, P. Mäki-Arvela, D. Y. Murzin, and J.-P. Mikkola. Capturing CO2: conventional versus ionic-liquid based technologies. *Russian Chemical Reviews*, 81(5):435–457, 2012.

[65] J. D. Holbrey, W. M. Reichert, R. P. Swatloski, G. A. Broker, W. R. Pitner, K. R. Seddon, and R. D. Rogers. Efficient, halide free synthesis of new, low cost

ionic liquids: 1, 3-dialkylimidazolium salts containing methyl-and ethyl-sulfate anions. *Green Chemistry*, 4(5):407–413, 2002.

[66] M. Klahn and A. Seduraman. What determines CO2 solubility in ionic liquids? A molecular simulation study. *The Journal of Physical Chemistry B*, 119(31):10066–10078, 2015.

[67] D. W. Kim, Y. Zhang, K. L. Cooper, and A. Wang. In-fiber reflection mode interferometer based on a long-period grating for external refractive-index measurement. *Applied Optics*, 44(26):5368–5373, 2005.

[68] C. Cadena, J. L. Anthony, J. K. Shah, T. I. Morrow, J. F. Brennecke, and E. J. Maginn. Why is CO2 so soluble in imidazolium-based ionic liquids? *Journal of the American Chemical Society*, 126(16):5300–5308, 2004.

[69] S. G. Kazarian, B. J. Briscoe, and T. Welton. Combining ionic liquids and supercritical fluids: in situ ATR-IR study of CO2 dissolved in two ionic liquids at high pressures. *Chemical Communications*, 0(1):2047–2048, 2000.

[70] S. N. Aki, B. R. Mellein, E. M. Saurer, and J. F. Brennecke. High-pressure phase behavior of carbon dioxide with imidazolium-based ionic liquids. *The Journal of Physical Chemistry B*, 108(52):20355–20365, 2004.

[71] M. J. Muldoon, S. N. Aki, J. L. Anderson, J. K. Dixon, and J. F. Brennecke. Improving carbon dioxide solubility in ionic liquids. *The Journal of Physical Chemistry B*, 111(30):9001–9009, 2007.

[72] R. Babarao, S. Dai, and D.-e. Jiang. Understanding the high solubility of CO2 in an ionic liquid with the tetracyanoborate anion. *The Journal of Physical Chemistry B*, 115(32):9789–9794, 2011.

[73] M. G. Freire, L. M. Santos, A. M. Fernandes, J. A. Coutinho, and I. M. Marrucho. An overview of the mutual solubilities of water–imidazolium-based ionic liquids systems. *Fluid Phase Equilibria*, 261(1-2):449–454, 2007.

[74] F. Di Francesco, N. Calisi, M. Creatini, B. Melai, P. Salvo, and C. Chiappe. Water sorption by anhydrous ionic liquids. *Green Chemistry*, 13(7):1712–1717, 2011.

[75] Y. Danten, M. Cabaco, and M. Besnard. Interaction of water highly diluted in 1-alkyl-3-methyl imidazolium ionic liquids with the PF6- and BF4- anions. *The Journal of Physical Chemistry A*, 113(12):2873–2889, 2009.

[76] M. Klahn, C. Stuber, A. Seduraman, and P. Wu. What determines the miscibility of ionic liquids with water? Identification of the underlying factors to enable a straightforward prediction. *The Journal of Physical Chemistry B*, 114(8):2856–2868, 2010.

[77] M. G. Freire, P. J. Carvalho, R. L. Gardas, I. M. Marrucho, L. M. Santos, and J. A. Coutinho. Mutual solubilities of water and the [Cnmim][Tf2N] hydrophobic ionic liquids. *The Journal of Physical Chemistry B*, 112(6):1604–1610, 2008.

[78] S. Feng and G. A. Voth. Molecular dynamics simulations of imidazolium-based ionic liquid/water mixtures: Alkyl side chain length and anion effects. *Fluid Phase Equilibria*, 294(1-2):148–156, 2010.

[79] K. A. Kurnia, C. M. Neves, M. G. Freire, L. M. Santos, and J. A. Coutinho. Comprehensive study on the impact of the cation alkyl side chain length on the solubility of water in ionic liquids. *Journal of Molecular Liquids*, 210(1):264–271, 2015.

[80] E. D. Bates, R. D. Mayton, I. Ntai, and J. H. Davis. CO2 capture by a task-specific ionic liquid. *Journal of the American Chemical Society*, 124(6):926–927, 2002.

[81] B. F. Goodrich, J. C. de la Fuente, B. E. Gurkan, Z. K. Lopez, E. A. Price, Y. Huang, and J. F. Brennecke. Effect of water and temperature on absorption of CO2 by amine-functionalized anion-tethered ionic liquids. *The Journal of Physical Chemistry B*, 115(29):9140–9150, 2011.

[82] S. Hanioka, T. Maruyama, T. Sotani, M. Teramoto, H. Matsuyama, K. Nakashima, M. Hanaki, F. Kubota, and M. Goto. CO2 separation facilitated by task-specific ionic liquids using a supported liquid membrane. *Journal of Membrane Science*, 314(1-2):1–4, 2008.

[83] C. Myers, H. Pennline, D. Luebke, J. Ilconich, J. K. Dixon, E. J. Maginn, and J. F. Brennecke. High temperature separation of carbon dioxide/hydrogen mixtures using facilitated supported ionic liquid membranes. *Journal of Membrane Science*, 322(1):28–31, 2008.

[84] J. Le Bideau, L. Viau, and A. Vioux. Ionogels, ionic liquid based hybrid materials. *Chemical Society Reviews*, 40(2):907–925, 2011.

[85] T. Fukushima, A. Kosaka, Y. Ishimura, T. Yamamoto, T. Takigawa, N. Ishii, and T. Aida. Molecular ordering of organic molten salts triggered by single-walled carbon nanotubes. *Science*, 300(5628):2072–2074, 2003.

[86] S. Chen, G. Wu, M. Sha, and S. Huang. Transition of ionic liquid [bmim][PF6] from liquid to high-melting-point crystal when confined in multiwalled carbon nanotubes. *Journal of the American Chemical Society*, 129(9):2416–2417, 2007.

[87] P. T. Nguyen, B. A. Voss, E. F. Wiesenauer, D. L. Gin, and R. D. Noble. Physically gelled room-temperature ionic liquid-based composite membranes for CO2/N2 separation: Effect of composition and thickness on membrane properties and performance. *Industrial and Engineering Chemistry Research*, 52(26):8812–8821, 2012.

[88] N. Kimizuka and T. Nakashima. Spontaneous self-assembly of glycolipid bilayer membranes in sugar-philic ionic liquids and formation of ionogels. *Langmuir*, 17(22):6759–6761, 2001.

[89] B. A. Voss, J. E. Bara, D. L. Gin, and R. D. Noble. Physically gelled ionic liquids: Solid membrane materials with liquidlike CO2 gas transport. *Chemistry of Materials*, 21(14):3027–3029, 2009.

[90] K. Hanabusa, H. Fukui, M. Suzuki, and H. Shirai. Specialist gelator for ionic liquids. *Langmuir*, 21(23):10383–10390, 2005.

Chapter 5

Fabrication of LPGs at the phase matching turning point

The fabrication of the LPGs used throughout this work was accomplished via the point-by-point method using UV irradiation. As discussed in Section 3.5.2, this particular manufacturing scheme provides flexibility in the choice of LPG fabrication parameters, and is ideally suited for tailoring the periodicity to the requirements of a particular application without the need for numerous amplitude masks. The Engineering Photonics centre within Cranfield University uses the overwrite variation of the point-by-point fabrication technique [1]. This technique is based on the index modulation amplitude dependence of the phase matching in LPGs and allows features of the LPG transmission spectra to be tuned to desired wavelengths. Although the overwrite technique was conceived and preliminarily functional prior to the start of this project, part of the work presented in this thesis was concerned with validation and optimisation of the implementation of this process and therefore, a full description of the fabrication system and working principle is provided.

LPG-based sensors typically desire the grating to possess the greatest sensitivity possible to a particular measurand (LP mode dependant), which is often achieved by exploiting the PMTP. Nevertheless, this requires preliminary numerical modelling to identiofy a suitable period and a fabrication system that reliably produces LPGs. It is therefore necessary that the repeatability of the overwrite system is assessed. Additionally, accurate numerical modelling of specialist fibres is difficult (see Section 3.3), therefore an investigation into an empirically derived method for designing LPGs for the use as sensors would aid future fabrication of these in-fibre devices in this project.

The first section of the chapter summarises the overwrite method. This includes

a description of the working principle, the components utilised in the fabrication system and a brief outline of the software used to control the procedure. The second section presents data from a study of the repeatability of LPGs manufactured using the overwrite method and highlights the ability this technique provides for tailoring LPG spectra. The final section demonstrates a novel application of the overwrite method in which the wavelengths and period at which the PMTPs of a number of cladding modes are accessed have been experimentally determined.

5.1 The overwrite method

A diagrammatic representation of the LPG fabrication system can be seen in Fig. 5.1. A photosensitive fibre with a plastic jacket free section is attached to an aluminium

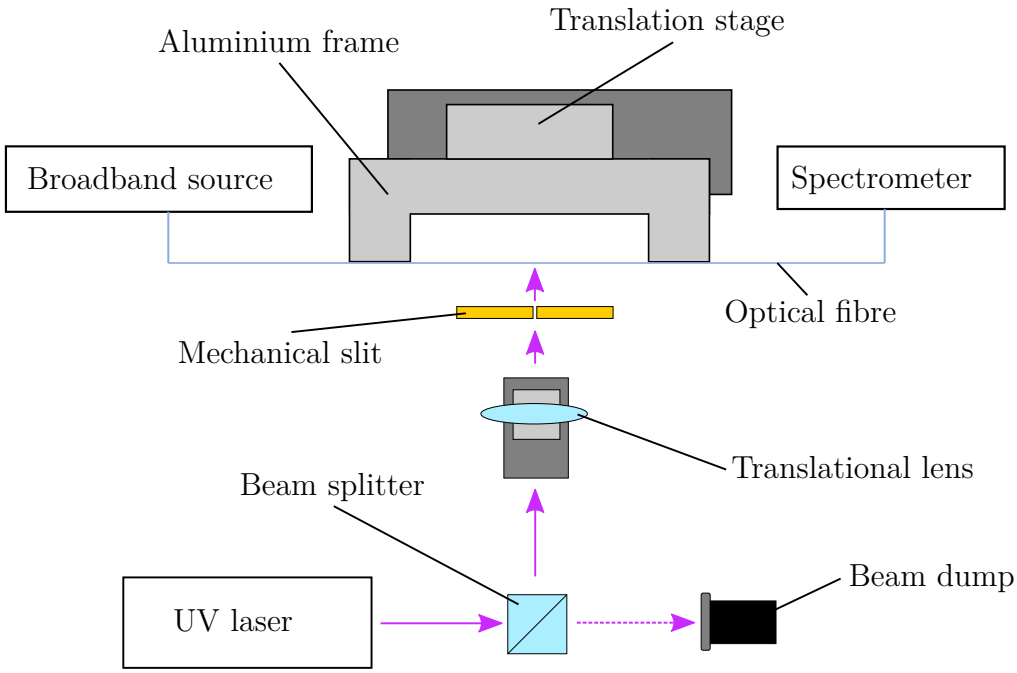

Figure 5.1: Layout of the LPG fabrication system

fibre holder in v-grooves by means of small magnetic strips. The fibre is interrogated throughout the fabrication procedure via the use of a fibre-coupled broadband source (LS-1, Ocean Optics) and a CCD spectrometer (S2000, Ocean Optics) with a detection range of 550 - 1100 nm and a resolution of 0.36 nm. The aluminium frame is attached to a translation stage (M150.11, PI), control of which allows selection of

the grating period. The stage has a motion range of 49 mm at a resolution of 25 nm. The secured fibre is positioned directly behind (∼1 mm) an in-house manufactured mechanical slit which governs the irradiation duty cycle. The mechanical slit is comprised of two copper plates that are forced apart in unison by a tapered dowel in order to create the desired aperture. The slit was initially made of steel plates, however, during preliminary work, it was observed that these suffered severe UV ablation damage and were therefore replaced with copper which possess a greater UV ablation threshold [2]. The dowel's movement was controlled by a translation stage (M110.1DG, PI) which possessed a resolution of 7 nm and a maximum travel distance of 5 mm. UV irradiation was produced by a 10 Hz frequency quadrupled Nd:YAG laser operating at 266 nm (Quanta-Ray, Spectra Physics), where the output was guided to the fibre via a 50:50 beam splitter (Melles Griot) followed by a translatable bi-convex focussing lens with a 100 mm focal length (LB4941, Thorlabs) in order to govern the power density experienced by the fibre.

Unlike the standard point-by-point scheme, where each period is subjected to its total UV irradiation in one exposure (detailed in Section 3.5.2), the overwrite method builds up the UV mediated refractive index change over a number of repeat cycles. Initially, a section of the fibre experiences a short burst (generally 5 s) of UV irradiation prior to the fibre being translated orthogonally to the incident beam by a distance equal to the required period. This is repeated until the desired grating length has been achieved, where upon completion, the translation stage is returned to its starting location and the process is repeated until the transmission features are located at the desired wavelengths. For each exposure, the mechanical slit is opened for the elected irradiation time and closed during fibre translation, thus ensuring that only the intended portion of the fibre receives UV radiation. This procedure has the advantage that the LPG resonance bands' wavelengths and attenuation magnitudes can be finely tuned by varying the number of irradiation cycles and exposure time the fibre experiences. Nevertheless, the overwrite method is more time consuming than the standard point-by-point technique due to the additional translation stage movement accrued via the method's cyclic nature (typically around 2 h longer).

The overwrite method exploits the relationship between attenuation bands' central wavelengths and core index modulation amplitude. The phase matching expression (Equation 3.3) can be modified to consider this influence [3],

$$\lambda_{(x)} = \frac{(n_{core} + \delta n_{core} - n_{clad(x)} - \delta n_{clad})\Lambda}{N} \tag{5.1}$$

where δn_{core} and δn_{clad} refer to the average index modulation over the entire grating

length for the core and cladding respectively. δn_{clad} is assumed to be zero throughout the fabrication process due the lack of photosensitive dopants present in the cladding. As δn is dependent on the UV dose, control of resonance band wavelength can be tuned by varying the number of short UV exposures or by altering the intensity of the pulses the grating is subjected to [3].

During this work, the LPG fabrication system was partially automated with both the slit and translation stage controlled via a custom designed LabView program, where a flowchart demonstrating the operating principle for the fabrication of a uniform period LPG can be seen in Fig. 5.2. To monitor the evolution of the LPGs transmission spectrum during fabrication, the spectrometer was also linked to the LabView program, providing a live feed of the transmission spectra and the ability to save the spectrum following each fabrication cycle.

5.2 Repeatability of overwrite fabrication system

As with any manufacturing process, the ability to reliably create a product is an important aspect. Minimisation of device-to-device variability in the LPG fabrication system allows for greater automation and provides a method of consistently producing gratings with specific resonance band wavelengths and attenuation intensity. It was therefore essential that the repeatability of the current LPG system was determined.

5.2.1 Method

To assess the repeatability of the overwrite method, 3 LPGs of 40 mm length and a nominal period of 174 μm with a 50% duty cycle were fabricated in B-Ge co-doped photosensitive optical fibre (PS750, Fibercore) on different days using 6 overwrite cycles and a UV exposure time of 5 s (where exposure time signifies the duration of UV irradiation applied to fibre at each period). To prepare the fibre for LPG fabrication, a 45±2 mm section of the protective plastic jacket was mechanically removed from a 2 m length of optical fibre using fibre strippers (JIC 375, Jonard Tools). This length of grating (40 mm) was used throughout the thesis as it offers a compromise between maximising the depth of attenuation features by using a longer grating (see Equation 3.4) yet maintaining enough protective jacket to minimise fibre fragility. The newly exposed cladding surface was wiped with lens tissue saturated in isopropyl alcohol (IPA). Finally, both ends of the fibre were cleaved using a FKII cleaver (PK Technology) and inserted into bare fibre adaptors with SMA connectors

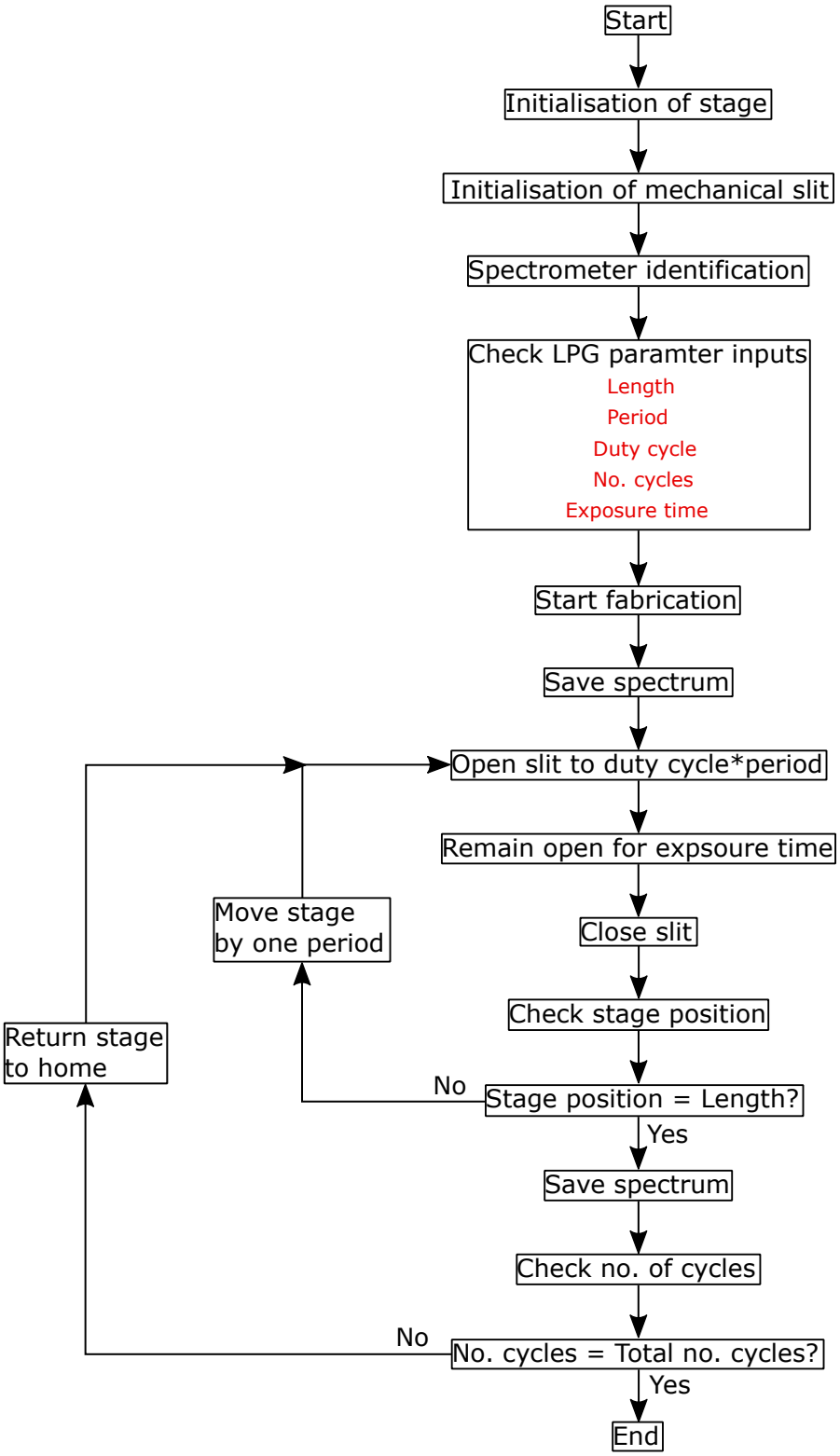

Figure 5.2: Flowchart of the program used to fabricate LPGs using the overwrite method

(F-AM-SMA, Newport) for attachment to the broadband source and spectrometer. The Nd:YAG laser was allowed to stabilise (generally taking ∼1 h) before the power

was measured via a laser power meter (AN/2, Ophir) located after the beam splitter. Stability of the laser is necessary to ensure a pseudo-Gaussian beam distribution and thus a steady power output. Typically, a power of 220 mW (at a wavelength of 266 nm) was achieved which fluctuated by ±10 mW during the fabrication process. The power reading was used to inform the position of the translational lens in order to obtain an approximate power density of 14 mW·mm^{-2} onto the fibre. Higher power densities have been found to negatively affect the fibre's mechanical strength, increasing its susceptibility to breakages [4]. Throughout the fabrication process, the laboratory environment was maintained at 20±2°C via air conditioning.

In order to compensate for wavelength and intensity variations derived through fibre coupling efficiencies, spectral data for each LPG was normalised to its related baseline spectrum (pre-irradiation) by $(I_F(\lambda)/I_B(\lambda)) \times 100$ where $I_F(\lambda)$ and $I_B(\lambda)$ are the final (cycle 6) and baseline spectra associated intensities respectively. The central wavelengths and intensities of attenuation bands were determined using Spectrum Interrogation Routine software [5]. This peak tracking software functions by fitting a quadratic polynomial to sequential data points in order to identify the peaks in the spectrum. Once identified, the algorithm predicts the location of the peak in the next spectrum based on the position of the previous peaks of a particular feature. If the peak is within 5% of the predicted location, this value is then associated with this feature, resulting in a list of positions (in this case a wavelengths) for every feature within the set of spectra.

5.2.2 Results and discussion

A plot showing the 3 LPG spectra fabricated is presented in Fig. 5.3. It is clear from an initial inspection of Fig. 5.3 that the attenuation bands of LP_{10} - LP_{14} demonstrate similar central wavelengths for all the fabricated LPGs. However, as the LP mode number increases, the variability in central wavelengths between each LPG also increases. Quantitatively, this equates to a maximum wavelength difference of 0.71 nm and 4.11 nm for attenuation bands LP_{09} and LP_{14}, respectively. This result is not unexpected as resonance bands coupling to LP modes nearer to their PMTP demonstrate greater sensitivity to changes in the phase matching condition, induced in the core during fabrication, than modes operating away from the PMTP [6]. Furthermore, these wavelength deviations are also likely to be caused by temperature fluctuations in the laboratory environment. Wong *et al.* [6] demonstrated that changes in temperature produce dramatic alterations in attenuation band characteristics, where a temperature variation of 5°C produced

a 28.7% extinction change in LP_{19} which was operating at the PMTP. Since the laboratory temperature was maintained to 20±2°C and LPGs fabricated in B-Ge codoped fibre possess temperature sensitivities up to 2.75 nm·C^{-1} [7], it is feasible that the differences in central wavelength of the attenuation feature associated with LP_{14} was induced purely by temperature. Therefore, the reliability of the fabrication process would be improved by minimising temperature fluctuations. This could be achieved by containing the system in an insulated enclosure (as described in [6]) or via utilisation of an enclosure that possesses a temperature control feedback system.

In comparison to the single exposure technique, the overwrite method provides greater repeatability, where LPGs produced using the same fabrication parameters (period, grating length, duty cycle) possessed attenuation features associated with LP_{14} that differed by 4.11 nm (Fig. 5.3) whereas the single exposure technique produced gratings with resonance features that varied by 10 nm [1].

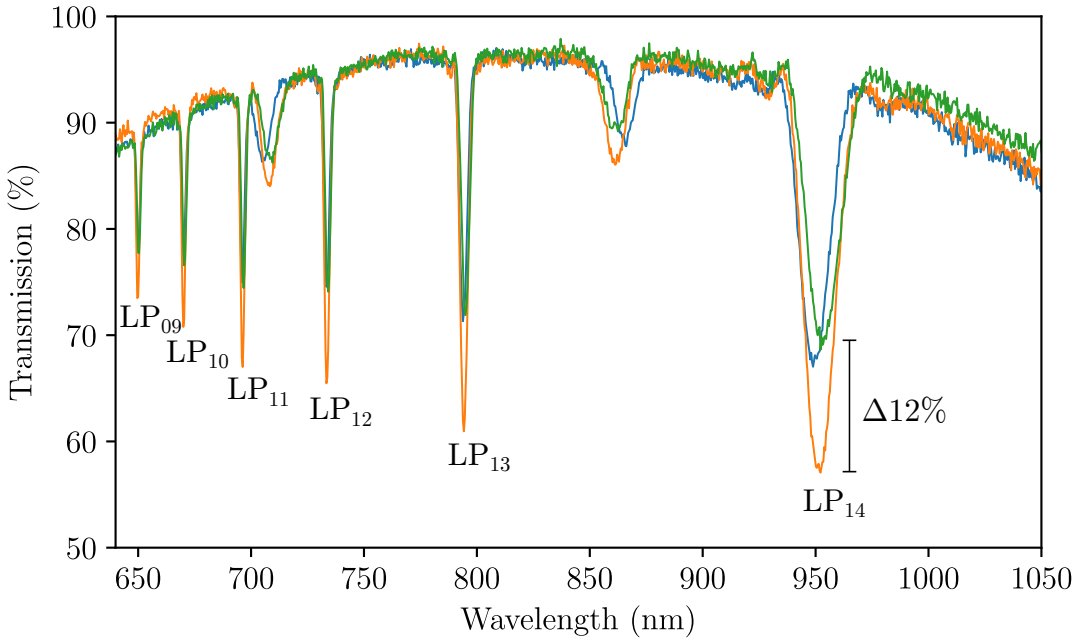

Figure 5.3: Transmission spectra of three 40 mm long LPGs fabricated on separate days all with a period of 174 μm

Although the resonance bands are aligned closely in wavelength, there is a large discrepancy in attenuation, where, for LP_{14}, an intensity difference of 12% can be seen. This variation is conceivably due to laser power fluctuation during the fabrication process and slight disparity in fibre dopant concentrations. It should be noted that all 3 fabricated LPGs contain smaller attenuation bands located at ∼710 and ∼860 nm. These bands correspond to 2^{nd} order coupling between core

and cladding modes, which will be discussed in greater detail in Chapter 6 and to a lesser extent, the following section.

While the data presented in Fig. 5.3 shows the overwrite method can be used to reliably create LPGs with the same period, the real strength of this scheme is the ability to produce LPGs with repeatable spectral characteristics by stopping the fabrication process once an attenuation band has achieved the desired wavelength. This can be seen in Fig. 5.4, where two LPGs with periods of 113.0 and 113.2 μm have dual attenuation bands corresponding to LP_{19} at the same central wavelengths (within 0.4 nm of each other). This has been achieved by exposing the LPG with

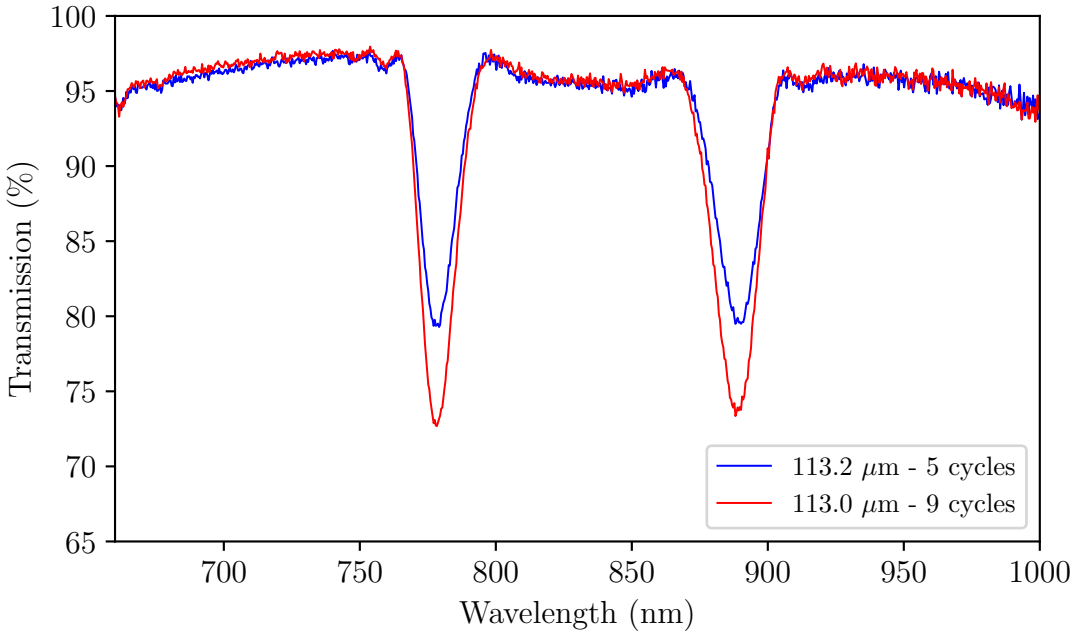

Figure 5.4: Transmission spectra of two 40 mm long LPGs with periods of 113.0 and 113.2 μm that have been fabricated using the overwrite method such that the attenuation bands corresponding to LP_{19} have identical wavelengths

the shorter period (113.0 μm) to a greater number of exposure cycles (9), thereby increasing the average index modulation resulting in a resonance wavelength shift (Equation 5.1). It can also be seen in Fig. 5.4 that the increased number of irradiation cycles experienced by the LPG with a period of 113.0 μm produced resonance features with greater attenuation in comparison to the LPG that received 5 cycles (113.0 μm). Again, this disparity is produced from the larger average index modulation experienced by the LPG with a period of 113.2 μm (Equation 3.4).

Generally, LPGs are defined by their length, period and, occasionally, their duty cycle. However, the data presented in Fig. 5.4 demonstrates that the amplitude of the index modulation is also a key parameter in defining LPGs and can be exploited to fabricate

gratings that possess resonance features at desired wavelengths. Furthermore, by selecting a shorter period than required to produce attenuation features at specific wavelengths and increasing the number of exposure cycles, it is possible to obtain an LPG with resonance bands at greater depths yet are still located at the appropriate wavelengths (as can been seen in Fig. 5.4). This is of particular use for LPGs that require thick coatings (e.g. for chemical sensing) that would otherwise cause a complete loss in attenuation of the resonance bands. Additionally, this fabrication method allows LPGs to be reliably produced regardless of temperature fluctuations since the process is terminated once the transmission features posses the desired wavelength and not following a set number of cycles.

5.3 Experimental determination of phase matching turning points

Many LPG sensing applications require the in-fibre element to function at its greatest sensitivity within the detectable range of an interrogation unit. This is often attained by fabricating an LPG which possesses a mode operating at its PMTP (see Section 3.6.1), where the appropriate period required for this to occur is chosen based upon numerical modelling (see Section 3.3.1). However, data on the fibre's parameters (core and cladding refractive indices/radii) are not known with sufficient accuracy for precise attenuation band wavelength prediction, thus, numerical models are not always accurate and do not necessarily portray all the spectral features present. The technique proposed in this section aims to alleviate these issues through the combination of a reliable LPG fabrication system and a novel method for representing the subsequently manufactured LPGs spectra. It was therefore the aim of this experiment to demonstrate this method by identifying all the PMTPs that can be accessed using PS750 when the period is varied in the range of 100 - 200 μm.

5.3.1 Method

In order to identify an appropriate period to initiate fabrication, phase matching curves were generated using the method outlined in Section 3.3 and utilised as a guide. The preparation of the optical fibres and the pre-fabrication procedures utilised were described in Section 5.2.1. To identify the PMTP for each LP mode, an LPG was fabricated with a period equal to that mode's turning point as displayed in Fig. 3.5.

The resulting transmission spectrum was subsequently used to inform the period of the next LPG by either determining the difference in wavelength between the dual resonance bands of the LP mode in question, or, in the case for larger periods where the attenuation band of the dual resonance with a longer wavelength was located outside the spectrometer's wavelength range, the width of the remaining attenuation band was used (where a wider attenuation band or shorter wavelength difference indicated closer proximity to the PMTP). Once the period had been identified at which the PMTP could be observed, the process was repeated for each LP mode shown in Fig. 3.5 resulting in the manufacture of 67 LPGs, each fabricated with a 50% duty cycle using 6 cycles of 5 s exposure time. LP modes were identified using numerically modelled phase matching curves.

5.3.2 Results and discussion

All experimental transmission spectra of the fabricated LPGs were combined and subsequently processed into a single intensity plot (Fig. 5.5). To aid comparisons between the modelled and empirical data in Fig. 5.5, the theoretical phase matching curves presented in Fig. 3.5 have been superimposed over the experimental data.

The resonance features in Fig. 5.5 (the red bands) demonstrate a similar form to the theoretical phase matching curves which both show that 8 turning points are present within the 100 - 200 μm range. Additionally, the gradient of the resonance bands in Fig. 5.5 decreases with increasing LP mode number, which is in agreement with the theoretical model. Nevertheless, it is clear that there is a discrepancy between the experimental data and numerical model regarding the periodicity at which PMTPs can be observed and the wavelength at which these features are apparent. According to the numerical model, a period of 194 μm will produce an LPG that couples to the turning point of LP_{13}, however, the experimental data shows that in fact a period of 197 μm is required to couple to the PMTP of the aforementioned cladding mode. This difference to the theoretical model in determining the periodicity which governs the coupling to PMTPs can be noted for all turning points displayed in Fig. 5.5. Furthermore, there is a stark difference in the evolution of the phase matching curves between the theoretical and empirical data. For example, the gradient of the curve associated with LP_{16} is dramatically steeper in the experimental data in comparison to its theoretical counterpart, resulting in large deviations in period selection towards the fibre's cut-off wavelength ($\Delta 8$ μm at 700 nm). This is of particular importance when designing LPGs that will receive a coating, since the grating is fabricated with resonance features operating away from the PMTP in order have attenuation bands

functioning at this highly sensitive region post-deposition.

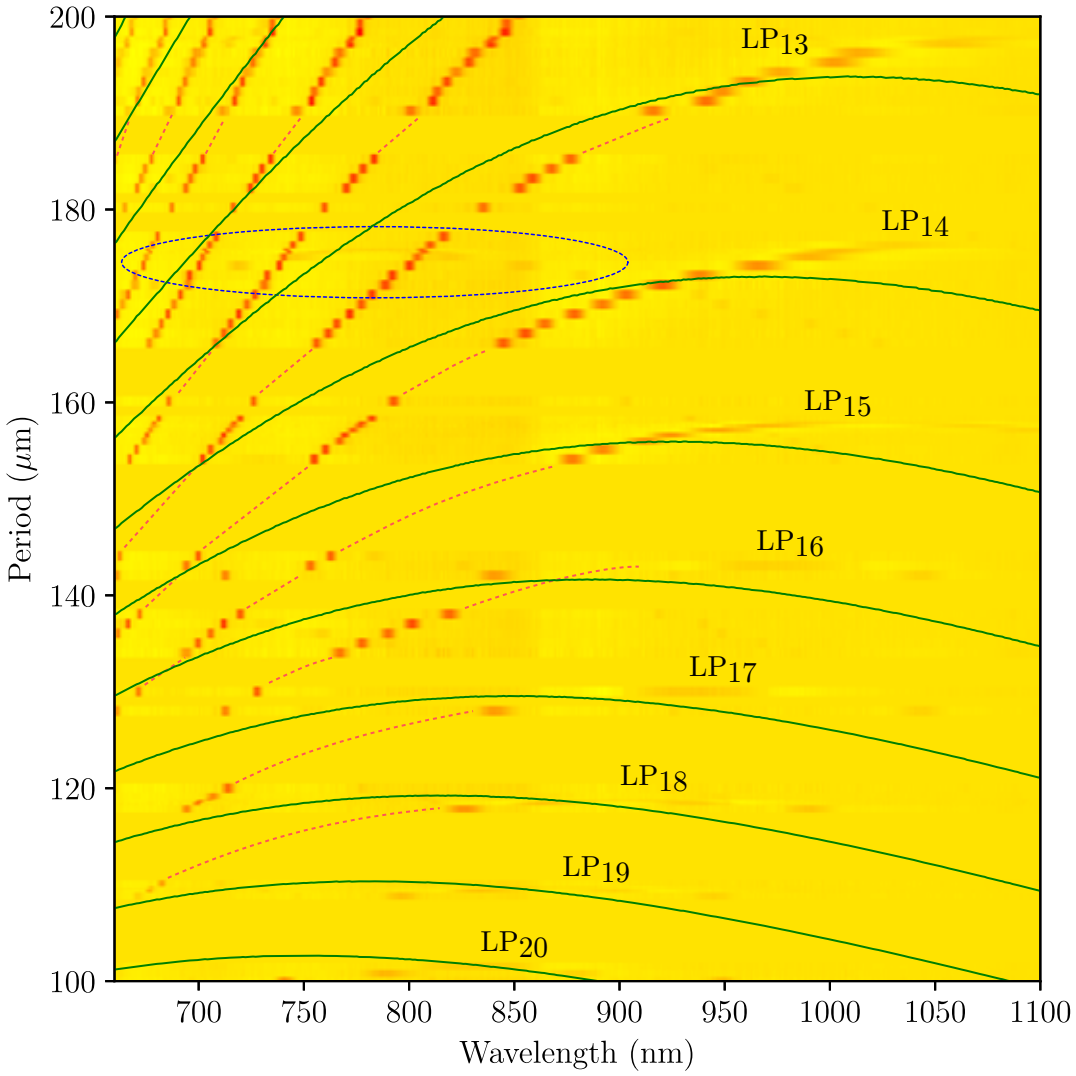

Figure 5.5: Intensity plot illustrating resonance bands operating at the PMTP for LPGs with periods between 100 - 200 μm. Numerically modelled data has been overlaid (green lines). The highlighted area indicates the presence of a PMTP associated with higher order coupling. Dotted lines are visual aids only. Yellow and red represent 100% and 74% transmission respectively

There are a number of explanations for the differences noted between the experimental data and the numerically derived phase matching curves. The fabrication of LPGs near the PMTP are highly sensitive to changes in grating period, where a difference of 0.6 μm can result in a 45 nm change in the separation of dual attenuation bands [6]. Since the resonance wavelength of an LPG is highly dependant on period, the linear relationship described in Equation 3.3 implies that it is also extremely sensitive to changes to the refractive index of the core and cladding when operating at the PMTP. This can be seen in the modelled data of Fig. 5.6, where a 1×10^{-4}

change in the core's refractive index changes the period at which to couple to the PMTP of LP_{14} by 3 μm. Unlike standard optical fibre (e.g. SMF28), the core and cladding refractive indices of PS750 are not well known and, from experience, can vary from batch-to-batch (fabricating LPGs in different fibre batches using the same fabrication parameters resulted in different spectra). This makes it difficult to obtain suitable values for the refractive index of the core and cladding required for accurate numerical modelling without employing additional techniques, such as refracted near-field [8], to determine the refractive index profile of the fibre. Furthermore, variations in temperature during the fabrication process and the degree of strain applied to the optical fibre when attaching it to the aluminium fibre holder may have also contributed to the disparity between the results presented in Fig. 5.5.

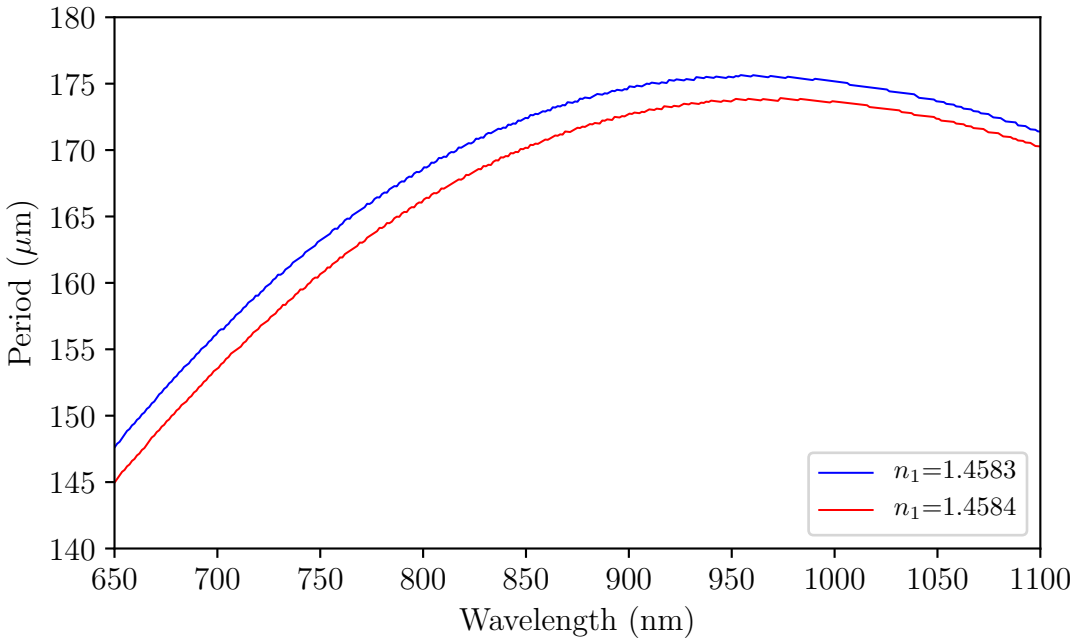

Figure 5.6: Two phase matching curves for LP_{14} calculated using refractive index values for n_1 that vary by only 1×10^{-4}

The process of presenting the sequentially fabricated LPGs transmission spectra as intensity plots not only allows for fast recognition of PMTPs but also provides advantages for designing coated LPG sensors. The technique of applying a coating to an LPG to improve the sensitivity and selectivity to a particular chemical analyte is commonly used (see Section 3.4.4), where it is often desired that the LPG displays spectral features that operate at the PMTP or the mode transition region following deposition to maximise the device's sensitivity [9]. To achieve this, an LPG is fabricated using a period with an offset in order to compensate for spectral shifts

induced through the application of a coating. An efficient method to select this initial period is to employ numerical modelling. Nevertheless, the thickness and refractive index of the coating are not always known with the required precision for accurate modelling to be conducted and therefore the period must be estimated. Since Fig. 5.5 displays the evolution of the resonance features, it is possible to use transmission spectra data displayed in this manner to select a suitable period prior to coating. Furthermore, once the data in Fig. 5.5 has been obtained, it can be adapted for variations in different optical fibre batches by fabricating an LPG in the new fibre using the same fabrication parameters thus, by using the difference between the original spectrum and the newly manufactured LPG, the intensity plot can be translated accordingly.

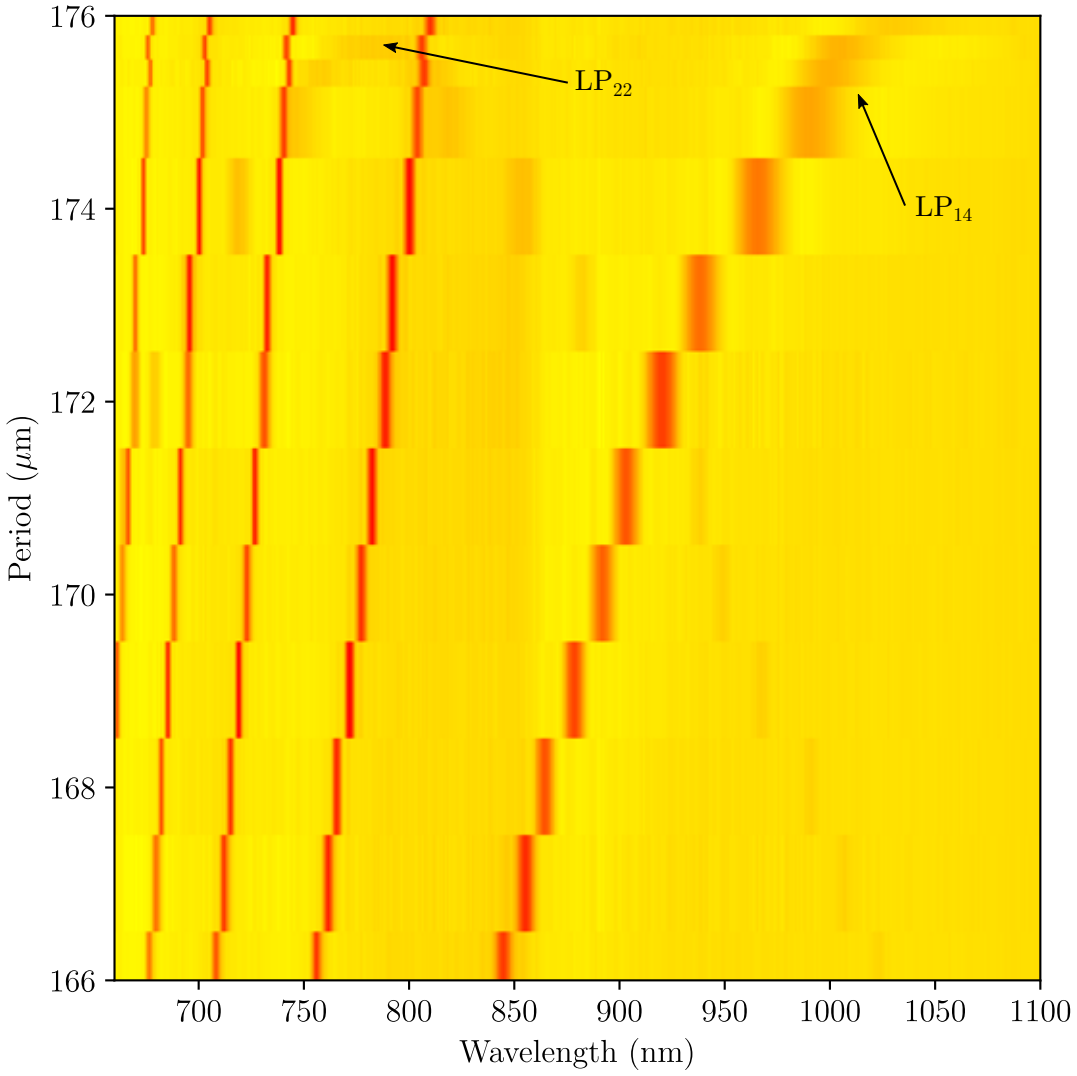

Figure 5.7: Intensity plot of 2^{nd} order PMTP formation. Yellow and red represent 100 and 82% transmission respectively

In addition to the aforementioned advantageous provided by mapping sequential LPG transmission spectra as an intensity plot, it also provides an insight into additional spectral features. A closer inspection of Fig. 5.5 reveals that another, less distinct attenuation band can be observed for periods of 166 - 176 μm (Fig. 5.7). It is speculated that this feature is associated with higher order coupling. By generating phase matching curves to include 2^{nd} order diffraction (Fig. 5.8), a clear comparison can be made between Fig. 5.7 and Fig. 5.8. However, similar to the 1^{st} order (or fundamental) resonance features, a difference in feature location and associated period between the theoretical model and the experimental data also exists.

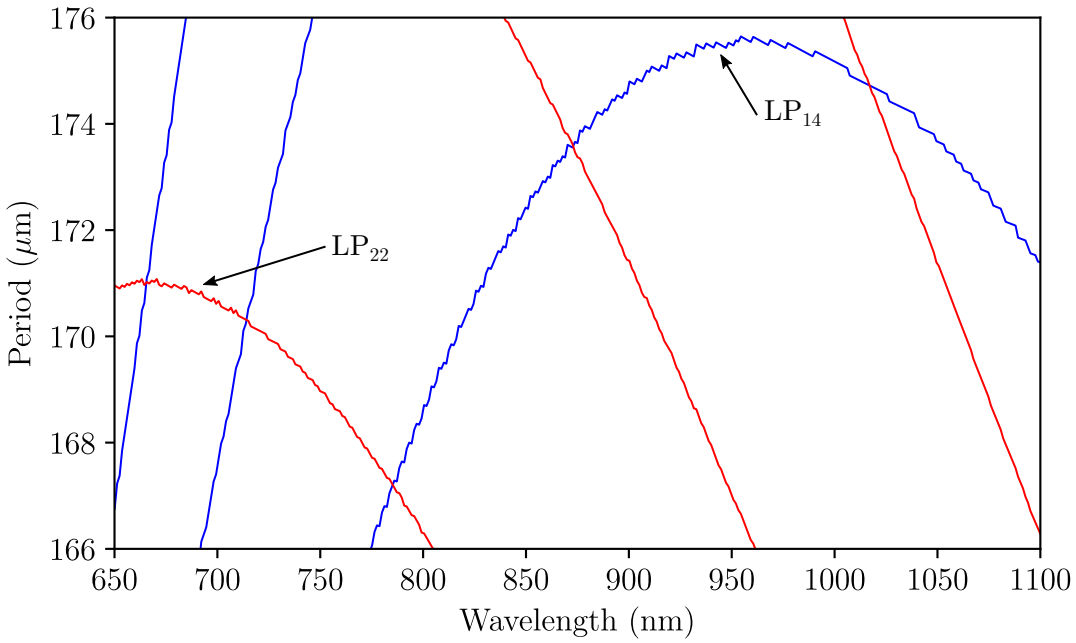

Figure 5.8: Numerically modelled phase matching curves for periods of 167 - 176 μm depicting both 1^{st} (blue) and 2^{nd} (red) order diffraction

The dual attenuation bands of the 2^{nd} feature can be seen drawing closer together in wavelength as the pitch increases, where upon reaching a period of 175.55 μm, the resonance bands coalesce at the PMTP, centred around ~785 nm (Fig. 5.7). In contrast to previous work [10], the 2^{nd} order resonance bands possess diminished attenuation in comparison to features associated with fundamental diffraction, demonstrating less efficient coupling to their associated cladding modes. As depicted in Fig. 5.8, the 2^{nd} order attenuation band is produced by coupling to LP_{22}, which is of higher order than the mode related to the nearest 1^{st} order resonance feature (LP_{14}). Higher order LP modes demonstrate greater sensitivity to surrounding refractive index perturbations [11], therefore by utilising higher order diffraction, it is possible to couple to these

sensitivity enhanced modes at periods which produce features visible in the operating range of a CCD spectrometer.

As discussed in Section 3.7, LPGs are able to perform multi-parameter sensing through monitoring wavelength shifts in resonance bands associated with different LP modes. One method for attaining this was proposed by Allsop *et al.* [10], where the authors used higher order diffraction features in order to obtain the differential behaviour required to distinguish between two measurands. Although multi-parameter sensing was achieved, it could be possible to augment this technique by improving sensitivity through coupling both 1^{st} and 2^{nd} order resonance features at the PMTP. In Fig. 5.7, it can be seen that fabricating an LPG with a period of 175.5 μm, it would be possible to couple the PMTP of the 2^{nd} order feature (LP_{22}) and near the PMTP of the 1^{st} order band (LP_{14}). By utilising the sensitive PMTP, sensitivity to physical parameters (temperature, strain, refractive index) would be enhanced.

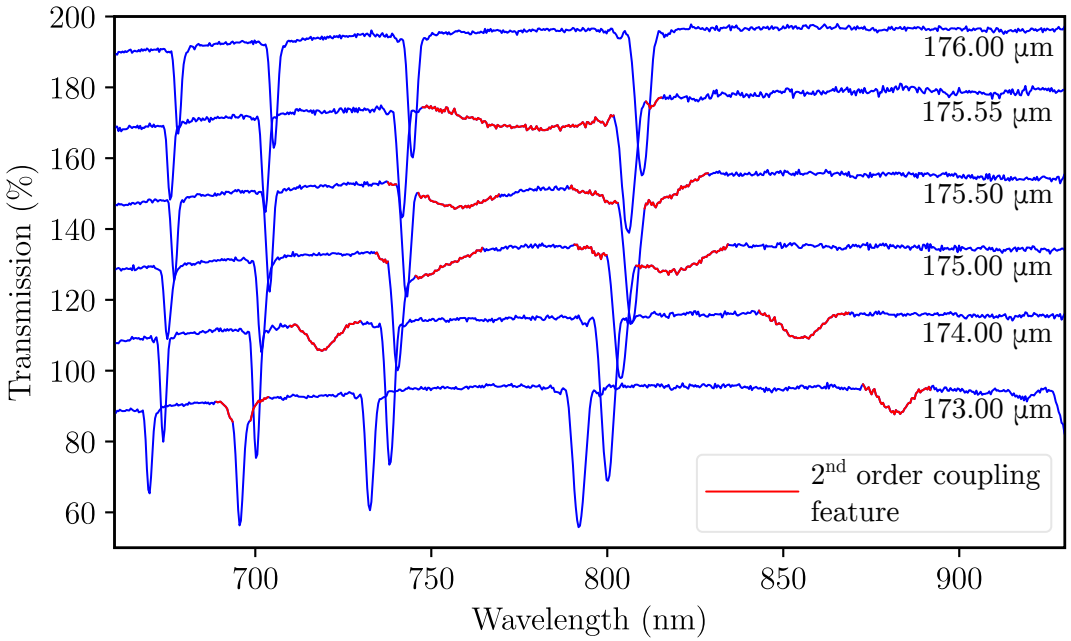

Figure 5.9: Offset transmission spectra for LPGs with periods 173 - 176 μm demonstrating the evolution of the PMTP for a 2^{nd} order feature (highlighted in red) associated with LP_{22}

However, it should be stated that wavelength tracking of 2^{nd} order attenuation bands required for sensing has some additional problems. Fig. 5.9 shows the evolution of the 2^{nd} order attenuation band as it forms the PMTP. At 175 μm, the 2^{nd} order feature coalesces with the 1^{st} order attenuation band (~810 nm), thus potentially creating difficulty in tracking the exact wavelength of the 2^{nd} order band. One simple

solution would be to fabricate the LPG in such a way that the feature remains between other bands for its entire sensing range thus avoiding the issue completely. A more complex approach would be to monitor both wavelength and intensity of the visible features. The merging of two resonance bands produces an attenuation change, therefore, by monitoring the relative intensities prior to coalescing, inference of the 2^{nd} order feature's wavelength could be accomplished. Nevertheless, the former method is a suitable approach for sensing situations in which small wavelength shifts occur.

5.4 Summary and conclusion

The fabrication of LPGs using the overwrite method has been demonstrated to be a repeatable process, where in Section 5.2 gratings written using identical parameters (period, duty cycle etc.) with a set number of UV exposure cycles produced LPGs with attenuation features that were within ∼4 nm of each other. Furthermore, by employing the overwrite method, it is possible to create two LPGs with different periods but that possess attenuation features with near-identical central wavelengths (within 0.4 nm) by utilising a different number of irradiation cycles. Using this method will allow LPGs to be fabricated with attenuation bands at specific wavelengths, which will be essential for optimising the grating during the development of the CO_2 sensor. This will be paramount in creating a functional device since the application of a coating material can severely alter the wavelength of the attenuation features in the transmission spectrum and therefore the sensitivity of the CO_2 sensor (see Section 3.4.4 for details on the effect of applying a coating material to the surface of an LPG).

The fabrication system has been implemented in a novel method for identifying the period required to produce LPGs with features operating at the PMTP. The disparity between the empirical and modelled data described in Section 5.3.2 highlights that numerical modelling is not an appropriate substitute for identifying the period of LPGs (required for obtaining a transmission spectrum with specific spectral features) in non-standard optical fibre (i.e. PS750). Therefore, Fig. 5.5 can be used as a look-up table in order to determine the period of the LPG prior to the fabrication of any future gratings required for the CO_2 sensor, therefore minimising the requirement for additional UV exposure cycles, ensuring the fabrication process is more efficient. Additionally, by presenting the transmission spectra of LPGs with sequential periods in an intensity plot, the identification of 2^{nd} order attenuation bands has been

achieved. The PMTP of this higher order resonance feature was determined to be accessible for LPGs with periods of 175.55 μm. Interestingly, using this period, it is possible to obtain two distinct resonance features at different coupling orders that operate near the PMTP. Since previous work has shown multi-parameter sensing is achievable through the use of 1^{st} and 2^{nd} order attenuation features [10], by utilising an LPG with a 175.55 μm period, the features associated with different coupling orders operating at the PMTP may enhance the sensitivity of a multi-parameter LPG sensor. Since LPGs possess inherent sensitivity to other external parameters (i.e. temperature, strain), the use these features in the LPG-based CO_2 sensor to compensate for these cross-sensitivities would be desirable, as such, this area is explored further in the following chapter.

5.5 References

[1] M. Partridge, S. W. James, J. H. Barrington, and R. P. Tatam. Overwrite fabrication and tuning of long period gratings. *Optics Express*, 24(20):22345–22356, 2016.

[2] P. Mannion, J. Magee, E. Coyne, and G. M. O'Connor. Ablation thresholds in ultrafast laser micromachining of common metals in air. In *Opto-Ireland 2002: Optics and Photonics Technologies and Applications*, vol. 4876, pp. 470–479. International Society for Optics and Photonics, 2003.

[3] T. W. MacDougall, S. Pilevar, C. W. Haggans, and M. A. Jackson. Generalized expression for the growth of long period gratings. *IEEE Photonics Technology Letters*, 10(10):1449–1451, 1998.

[4] R. Y. N. Wong. *Advanced fibre optic long period grating sensors; design, fabrication and sensing*. Ph.D. thesis, Cranfield University, 2014.

[5] M. Partridge. Spectral processing software. Retrieved 23rd April 2017. https://github.com/MCeeP/SIR.

[6] R. Y. Wong, E. Chehura, S. E. Staines, S. W. James, and R. P. Tatam. Fabrication of fiber optic long period gratings operating at the phase matching turning point using an ultraviolet laser. *Applied Optics*, 53(21):4669–4674, 2014.

[7] S. W. James and R. P. Tatam. Optical fibre long-period grating sensors: characteristics and application. *Measurement Science and Technology*, 14(5):R49–61, 2003.

[8] A. El Sayed, S. Pilz, M. Ryser, and V. Romano. Two-dimensional refractive index profiling of optical fibers by modified refractive near-field technique. In *Micro-Structured and Specialty Optical Fibres IV*, vol. 9886, pp. 1–8. International Society for Optics and Photonics, 2016.

[9] M. Partridge, R. Wong, S. W. James, F. Davis, S. P. Higson, and R. P. Tatam. Long period grating based toluene sensor for use with water contamination. *Sensors and Actuators B: Chemical*, 203(1):621–625, 2014.

[10] T. Allsop, L. Zhang, D. J. Webb, and I. Bennion. Discrimination between strain and temperature effects using first and second-order diffraction from a long-period grating. *Optics Communications*, 211(1-6):103–108, 2002.

[11] V. Bhatia and A. M. Vengsarkar. Optical fiber long-period grating sensors. *Optics Letters*, 21(9):692–694, 1996.

Chapter 6

Generation and characterisation of 2^{nd} order resonance bands

In Chapter 5, LPGs with 2^{nd} order resonance features operating at the PMTP were observed. Higher order attenuation bands have been noted previously [1, 2] and have been considered a hindrance through the production of undesired spectral features [3]. Nevertheless, the fabrication parameters required to reliably produce higher order coupling are not fully understood, where this information is not found in the literature. Therefore, this chapter determines the key fabrication parameters that govern the formation of 2^{nd} order resonance.

The generation of 2^{nd} order attenuation bands operating at the PMTP has the potential to improve the sensitivity of multi-parameter sensing schemes which utilise these features [1]. Previous LPG-based chemical sensors (kerosene) have shown a 40% improvement in device sensitivity when using attenuation bands at the PMTP [4] in comparison to resonance features which were not at the PMTP [5]. Additionally, the 1^{st} and 2^{nd} order resonance features utilised in [1] for multi-parameter sensing were interrogated over a large bandwidth (1000 nm) using an OSA. The results presented in Section 5.3 indicate that it is possible to obtain an LPG spectrum with both 1^{st} and 2^{nd} order coupling features within the detection range of a CCD spectrometer (650 - 1000 nm). As LPG sensors are typically used in the detection of temperature, strain or surrounding refractive index (or a combination of these), it was therefore pertinent to characterise the sensitivity of an LPG that possessed both 1^{st} and 2^{nd} order resonance features at the PMTP to these measurands and assess the ability of the LPG to discriminate between independent physical parameters during simultaneous measurement.

This chapter initially concerns the fabrication parameters required to reliably produce

an LPG that couple to higher order harmonics. This knowledge is then used to fabricate an LPG which possessed both 1^{st} and 2^{nd} order spectral features operating near the PMTP within the detectable range of a CCD spectrometer in order to theoretically assess the ability to perform multi-parameter sensing with these features. The response of the bands to temperature, strain and surrounding refractive index are subsequently analysed. Finally, using the characterisation data, the LPG is assessed theoretically for its capability in multi-parameter sensing using a range of numerical methods.

6.1 Generation of 2^{nd} order resonance bands

The fabrication of LPGs by UV exposure, whether using an amplitude mask or the point-by-point method, produces an irradiation pattern that closely resembles a square-wave [3]. The width of this square-wave is dictated by the duty cycle of the LPG as a percentage of the grating's periodicity. Generally, LPGs cited in the literature use a duty cycle of 50% as this proportion of irradiation, although rarely stated, provides the greatest coupling strength to the fundamental harmonic of the period [6]. However, there has been minimal research conducted on optimising coupling to 2^{nd} order harmonics in LPGs.

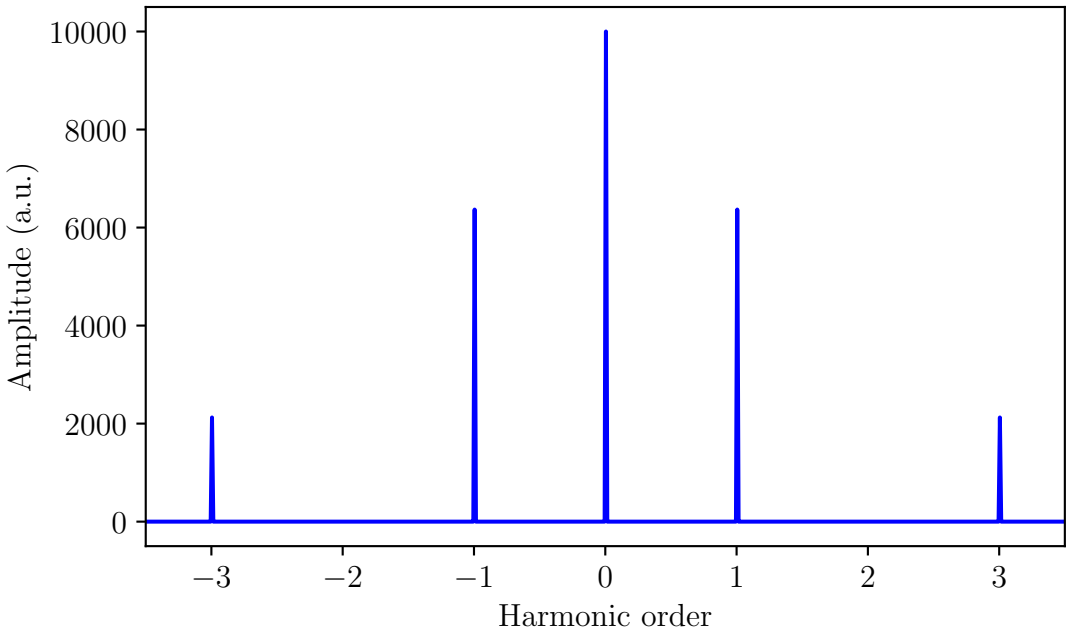

Figure 6.1: Harmonic content of sqaure-wave with a 50% duty cycle through the application of a discrete Fourier transform

To establish the harmonic content and coupling strength of a square-wave fabricated LPG with a 50% duty cycle, a discrete Fourier transform was applied to this wave form (Fig. 6.1) using a Python script (see Appendix B).

It is clear from Fig. 6.1 that a 50% duty cycle square wave does not have 2^{nd} order harmonic Fourier components, thus, as experimentally confirmed by Wong *et al.* [6] for this duty cycle, 1^{st} order coupling features of an LPG's transmission spectrum exhibit the highest coupling efficiency with no evidence of 2^{nd} order coupling. The lack of 2^{nd} order harmonics present in a square-wave with a 50% duty cycle indicates that duty cycle plays a profound effect in the generation of 2^{nd} order coupling. Nevertheless, there is currently no literature assessing the effect of varying the duty cycle on the characteristics of LPGs. In order to further understand the effects duty cycle has on harmonic coupling efficiency from an LPG, a Fourier transform was applied to a square wave with duty cycles varying from 0 - 100%. The results were subsequently analysed and displayed in Fig. 6.2 such that the intensities of 1^{st}, 2^{nd}, 3^{rd} and 4^{th} order harmonics are plotted as a function of duty cycle (see Appendix C for the Python script).

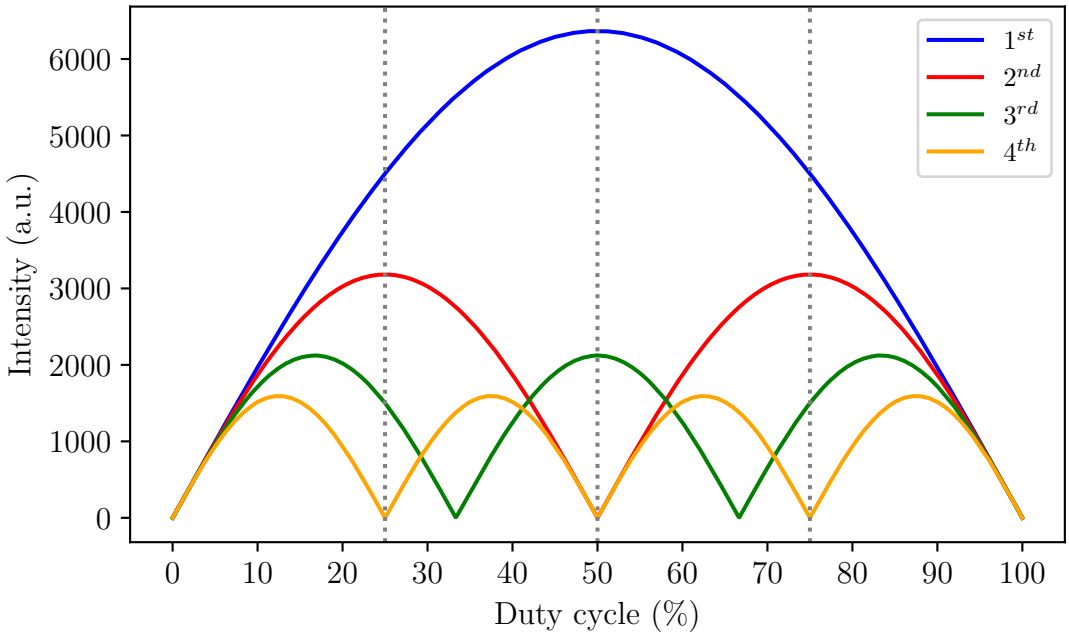

Figure 6.2: Intensity of the 1^{st}, 2^{nd}, 3^{rd} and 4^{th} order harmonics present in a square wave plotted as a function of duty cycle. The vertical dotted lines act as a guide for the eye

The data presented in Fig. 6.2 shows that 1^{st} order harmonics in a square wave possess their greatest amplitude at a 50% duty cycle. Additionally, it can also be seen in Fig. 6.2 that the maximum amplitude of 2^{nd} order harmonics was observed

at duty cycles of either 25% or 75%. Furthermore, there is a marked decrease in amplitude as the harmonic order increases, where, even at duty cycles that optimise the intensity of 3^{rd} order harmonics (17%, 50% and 83%), the amplitude of these features is less than that of 1^{st} and 2^{nd} order harmonics at their respective optimal duty cycles.

It is expected that the harmonic order of attenuation features displayed by LPGs fabricated using a square wave irradiation pattern will exhibit a similar dependency on duty cycle as outlined in Fig. 6.2. Furthermore, the extinction strength of the resonance features in LPGs will also correspond to the amplitude of the harmonic order. For example, the greatest attenuation in 1^{st} order attenuation bands of an LPG would be expected at a 50% duty cycle as depicted in Fig. 6.2. Therefore, in order to experimentally confirm this theory, an LPG which possessed a range of duty cycles (0 - 100%) was fabricated.

6.1.1 Experimental procedure

The fabrication system used to produce the LPGs utilised in this experiment possessed the same layout as detailed in Fig. 5.1, however, a number of the components were updated. Firstly, the Spectra Physics source was replaced by a frequency-quadrupled Nd:YAG laser operating at 266 nm (10 Hz repetition rate and 10 ns pulse width, 450 TRLi, Litron Ltd). The new laser provided improved beam quality, greater power output control, and required less maintenance thereby reducing the amount of time the system was off-line. Secondly, to maximise the power of UV irradiation, a reflector (Thor Labs) was substituted in place of the beam splitter. Finally, the copper plates used in the mechanical slit were replaced by ceramic plates (Macor™, RS). The data presented in Section 5.3 showed that an LPG with a designated duty cycle of 50% fabricated with the system incorporating the copper slit exhibited both 1^{st} and 2^{nd} order resonance features. Inspection of the copper plates used in the mechanical slit indicated levels of UV mediated ablation forming a small opening at the edge of the plate. These slight gaps in the copper edge permitted more of the fibre to be exposed to UV thus inadvertently increasing the duty cycle. Since Macor™ceramics possess a greater pulsed laser ablation threshold than copper [7], it was therefore decided that by replacing the copper slits with ceramic, this UV mediated ablation would be eradicated. The range of slit width provided by the new ceramic plates was 1 - 1000 μm.

To efficiently produce transmission spectra of LPGs with a range of duty cycles from 0 - 100%, a single 40 mm long LPG with a period of 380 μm was fabricated. This period

was selected based on generated phase matching curves (see Section 3.3.1), which showed that 1^{st} and 2^{nd} order coupling features are visible within the wavelength range of a CCD spectrometer. The LPG was written initially with a 5% duty cycle using the overwrite method [8]. Following the 10^{th} fabrication cycle, the translation stage was returned to the initial position minus a length equivalent to that of 5% of the period (19 μm). The addition of an offset allowed an LPG with a duty cycle equivalent to 10% to be subsequently fabricated in the same section of optical fibre (Fig. 6.3). This offset was added cumulatively following every 10^{th} fabrication cycle, until an LPG with a 100% duty cycle was manufactured. The transmission spectrum was recorded following each fabrication cycle, producing a total of 10 spectra for 5% increment in the duty cycle.

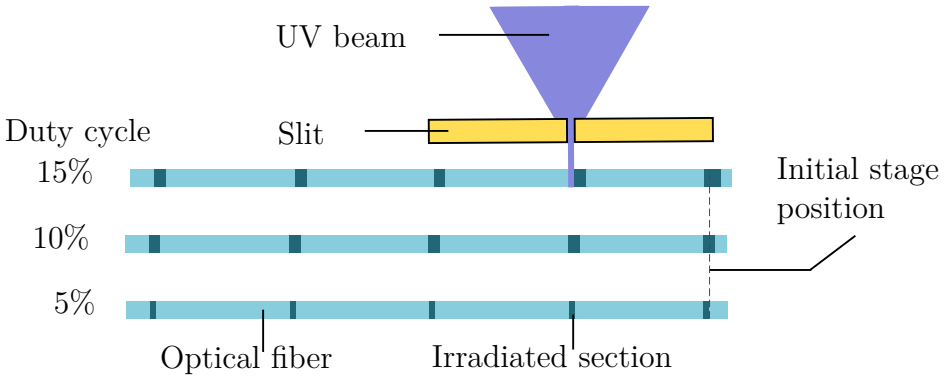

Figure 6.3: Diagrammatic representation of the fabrication method used to create the single LPG. The initial stage position is labelled to highlight the shift in stage position required to produce spectra pertaining to 0 - 100% duty cycles with a single fibre

6.1.2 Results and discussion

The intensity plot presented in Fig. 6.4 shows the evolution of attenuation bands in the transmission spectrum of the LPG as the duty cycle varied from 0 - 100%. Although a total of 10 spectra were obtained for each duty cycle increment, only the final spectrum from the last fabrication cycle was used in the generation of the figure.

The resonance bands visible continuously between duty cycles of 5 - 90% correspond to 1^{st} order coupling to cladding modes LP_2 - LP_8, which correlate well with the 1^{st} order harmonics seen in the modelled data (Fig. 6.2) where the 1^{st} order attenuation band intensity varies with duty cycle. Additionally, both the experimental results and the theoretical data show that the greatest attenuation of the 1^{st} order resonance

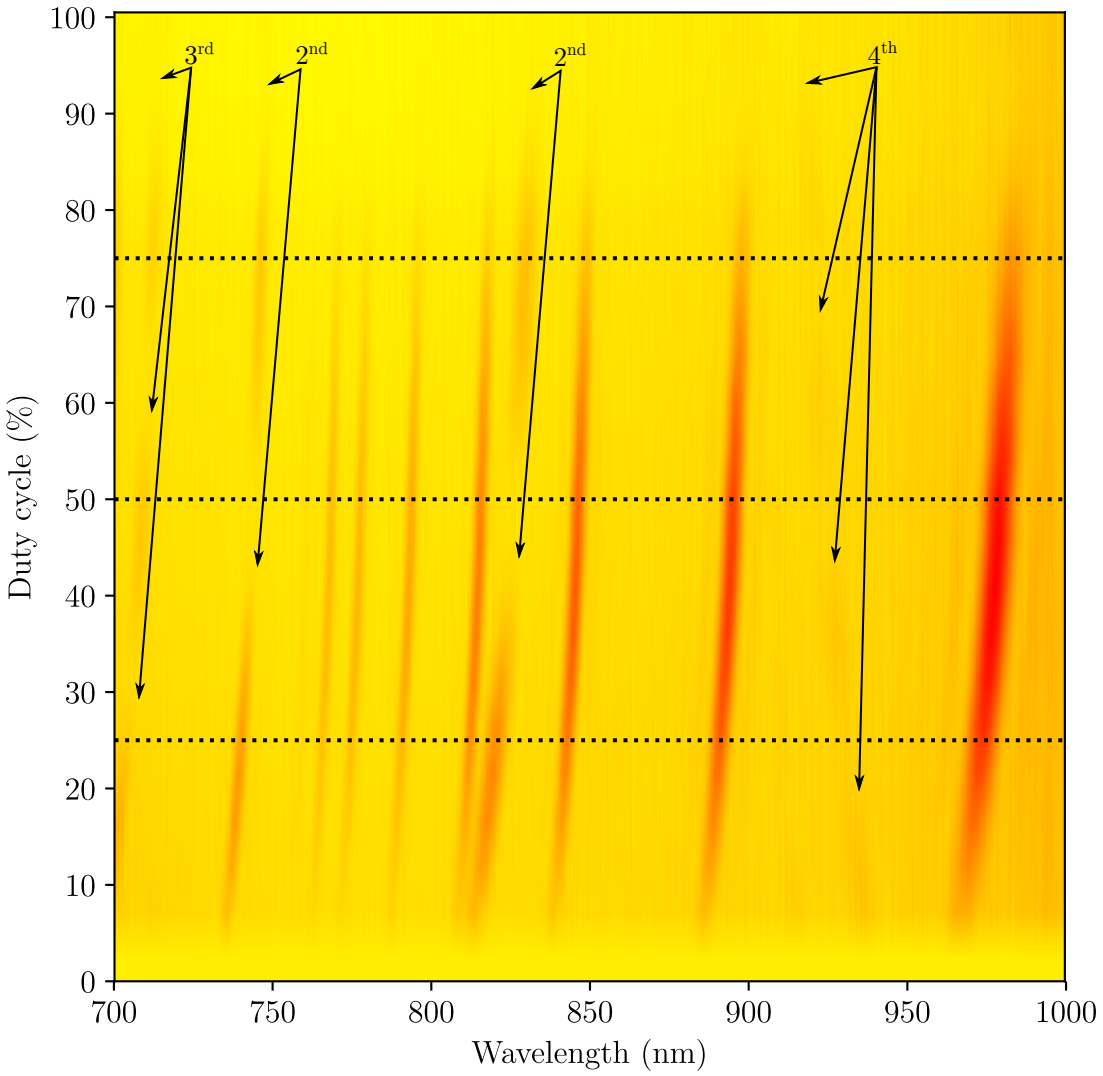

Figure 6.4: Intensity plot depicting the relationship between transmission and wavelength for 0 - 100% duty cycles for a 40 mm long LPG fabricated with a period of 380 μm. The 2^{nd}, 3^{rd} and, 4^{th} order coupling features have been identified, any other resonance bands are considered 1^{st} order. Red and yellow correspond to 75% and 100% transmission, respectively

bands is achieved by the selection of a 50% duty cycle.

In addition to the 1^{st} order attenuation bands, less intense features are also notable at wavelengths of 740 nm and 810 nm. These 2^{nd} order harmonics are generated optimally when a duty cycle of 25% or 75% is selected. The contribution of the 2^{nd} order harmonic coupling diminishes around a duty cycle of 50%. This result is mirrored in the Fourier analysis (Fig. 6.2) where, at 25% and 75% duty cycles, even ordered harmonics provide their greatest contribution to the formation of the square wave but diminish at a 50% duty cycle.

It is also possible to discern 3^{rd} and 4^{th} order attenuation bands in Fig. 6.4, visible at

wavelengths of 700 and 940 nm, respectively. The duty cycles at which these features are present in Fig. 6.4 is reflected in Fig. 6.2. While these features are observable, the strength of the attenuation bands would make them difficult to track during sensor operation. The absence of resonance bands corresponding to harmonics greater than 4^{th} order in the transmission spectrum of the LPG is due to the diminished amplitude of the higher order harmonics in the Fourier series of the square wave. In order to observe these attenuation bands, a greater cumulative exposure period than was utilized here would be required.

It can also be seen from Fig. 6.4 that the central wavelengths of the attenuation

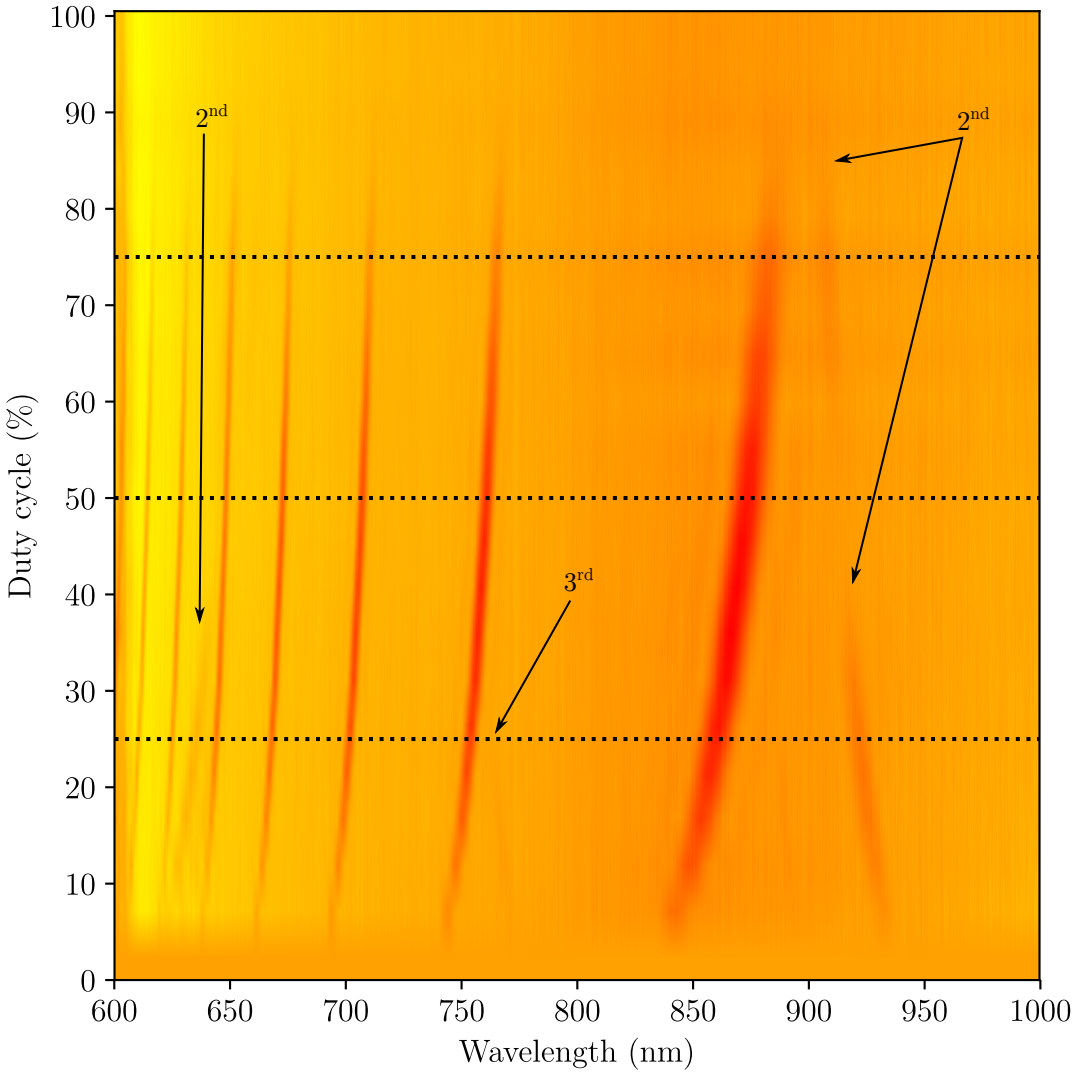

Figure 6.5: Intensity plot depicting the relationship between transmission and wavelength for 0 - 100% duty cycles for a 40 mm long LPG fabricated with a period of 175 μm. The 2^{nd} and 3^{rd} order coupling features have been identified, any other resonance bands are considered 1^{st} order. Red and yellow correspond to 85% and 100% transmission, respectively

bands experience a wavelength shift throughout the fabrication procedure. This is due to the attenuation band's central wavelength being influenced by the total amplitude of the refractive index change (see Section 5.1) where, in this case, the cumulative UV exposure is created from each cycle.

Confirmation that the experimental technique employed here operated as intended was achieved by extending the UV exposure to include a 100% duty cycle, such that the entire 40 mm length experienced a uniform exposure and thus the resonance bands would be expected to be absent from the resulting transmission spectrum. This result can be clearly observed in Fig. 6.4.

Another LPG with a period of 175 μm was fabricated using the same procedures outlined in Section 6.1.1 (with the 5% duty cycle was equal to 8.75 μm) in order to confirm the results in an LPG with resonance features operating near the PMTP, therefore more pertinent to sensor design.

The attenuation features displayed in Fig. 6.5 display a similar behaviour to the LPG fabricated with a 380 μm period (Fig. 6.4), where the 1^{st} order coupling features are visible for duty cycles of 5-90% and 2^{nd} order coupling features are not prominent for a duty cycle of 50%. However, as the LPG was fabricated with a shorter period (175 μm), 4^{th} order coupling features are not present in the intensity plot of Fig. 6.5.

Since LPG transmission data is not used practically as intensity plots, a comparison of the transmission spectra of the LPG with a 25% and a 50% duty cycle can be seen in Fig. 6.6. The lack of a 2^{nd} order feature in an LPG with a 50% duty cycle (Fig. 6.6b) is apparent when compared to a grating fabricated with a 25% duty cycle (Fig. 6.6a), where the 2^{nd} order attenuation band has a central wavelength of 635 nm.

Although a 2^{nd} order harmonic resonance band is evident in Fig. 6.6a, there is a clear disparity in extinction between 1^{st} and 2^{nd} order features, where the attenuation of the 1^{st} order resonance bands is at least 2 times greater than that of the 2^{nd} order. Again, this result correlates well with the data presented in Fig. 6.2 which shows that contributions from harmonics to generate a square wave decrease as the order increases. This reduction in intensity however furthers the difficulty of identifying 2^{nd} order attenuation bands in the transmission spectrum. Therefore, appropriate selection of duty cycle (i.e. 25%) to ensure optimal coupling is essential for designing LPGs that require 2^{nd} order resonance bands.

It should be noted that there is a 5% offset in both Fig. 6.4 and Fig. 6.5, where the greatest intensity of the 1^{st} and 2^{nd} order coupling features are shown to be at 45% and 20% (rather than 50% and 25% as expected), respectively. This may be caused

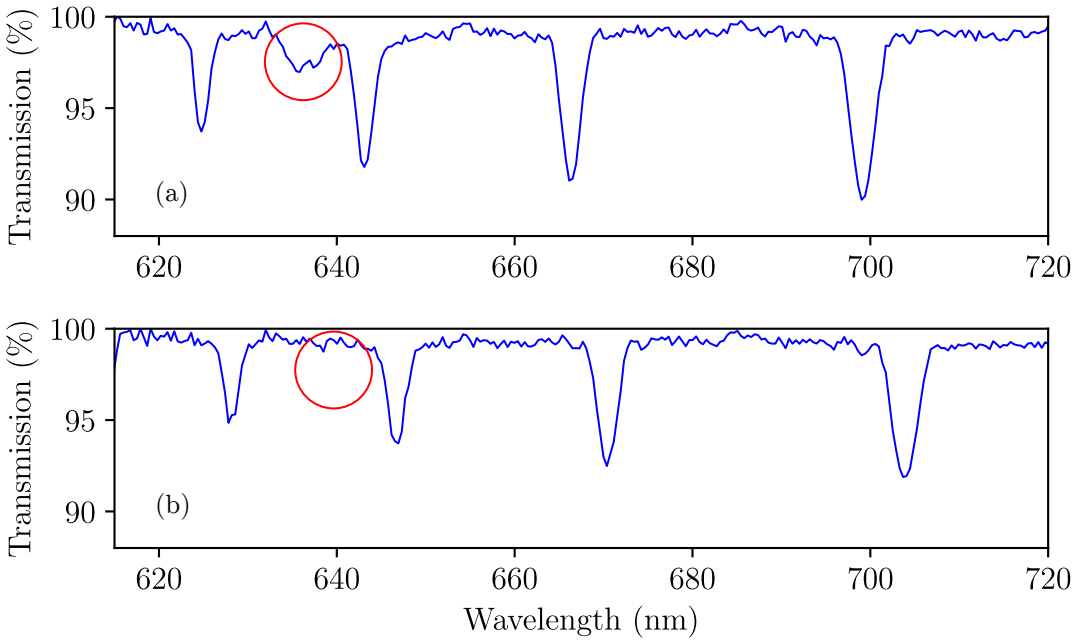

Figure 6.6: Transmission spectra comparing 25% (a) and 50% (b) duty cycles. The highlighted region indicates where the 2^{nd} order feature is visible for a 25% duty cycle and where it is missing for a 50% duty cycle

by errors in the mechanical slit aperture. For example, the LPG fabricated with a 380 μm period required a mechanical slit aperture of 19 μm for a 5% duty cycle. However, even ± 1 μm error would create an LPG with either a 95% or 105% duty cycle following the final cycle in the fabrication process described in Section 6.1.1. This error is introduced into the system through the calibration of the slit, which involves measuring the width of the aperture using light microscopy at different translation stage distances and producing a calibration curve. In standard LPG fabrication, this error would not significantly influence the final spectrum, however, since the method adopted here is a cumulative process, small errors in aperture width can severely affect the behaviour of the transmission features. One alteration that could be made to the fabrication system to improve the reliability of the aperture mechanism would be to incorporate a shutter mechanism between the UV beam and the mechanical slit. The shutter would be open during the irradiation cycle and be moved into place during fibre translation to block the incident beam. This would allow the aperture to be set to a precise width and would therefore not need to be opened and closed during the fabrication process thus ensuring the desired irradiation length.

6.2 Characterisation of 2^{nd} order resonance

The use of 2^{nd} order resonance features for multi-parameter sensing has been achieved over a large wavelength range (∼1000 nm) through use of an OSA [1]. However, data presented in Section 5.3 shows that it is possible to fabricate an LPG which possesses attenuation bands that operate near the PMTP for both 1^{st} and 2^{nd} order within the detectable wavelength range of a CCD spectrometer by using optical fibre with a short cut-off wavelength (630 nm). Through utilising both of these attenuation bands simultaneously, multi-parameter sensing could be accomplished via the use of a relativity cheap (in comparison to an OSA) CCD spectrometer yet exploit resonance bands operating at the highly sensitive PMTP. Therefore, to assess the sensitivity of the 1^{st} and 2^{nd} order coupling features operating at the PMTP, the response of these features to temperature, strain and surrounding refractive index were characterised. Additionally, 1^{st} order attenuation bands not operating at the PMTP were also monitored throughout the characterisation tests in order to provide a comparison.

6.2.1 Experimental methods

A 40 mm long LPG with a period of 181.5 μm and a 25% duty cycle was written in PS750 optical fibre using 8 cycles with 5 s dwell time via the method described in Section 5.4. This period was selected as the LPG spectrum contained both 1^{st} and 2^{nd} order attenuation bands that were operating near their PMTP within the detectable range of a CCD spectrometer (Fig. 6.7). The sensitivity of these features was assessed by monitoring the relative wavelength shift in response to each physical parameter. For all characterisation experiments, the LPG was interrogated using a fibre-coupled broadband light source (LS-1, Ocean Optics) and a CCD spectrometer (S2000, Ocean Optics), where the former was allowed to warm-up for 40 min before data acquisition. This was deemed the minimum amount of time required for the light source to reach a stabilised power output. Prior to testing, the LPG underwent annealing by placing it in a laboratory oven (VTM7004, Votsch) set to 100°C for 3 h in order to stabilise the grating. All characterisation tests were performed a total of 3 times. Attenuation band tracking was determined using SIR software [9]. The following sections outline the experimental procedures used to assess sensitivities to strain, temperature, and surrounding refractive index.

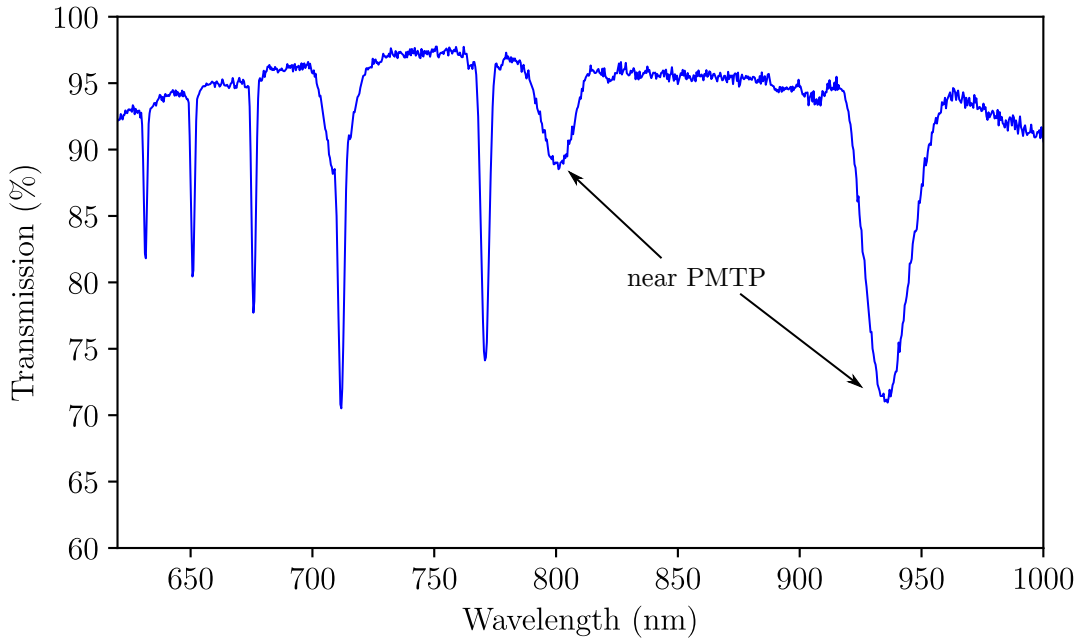

Figure 6.7: Transmission spectrum of a 40 mm long LPG with a period of 181.5 μm and a 25% duty cycle. The two features indicated are 1^{st} (∼930 nm) and 2^{nd} (∼805 nm) order attenuation bands operating near their respective PMTPs

Strain

The application of axial strain was achieved by clamping one side of the LPG to an optical bench edge while the LPG was suspending vertically. Masses ranging from 200 - 386 g were attached to the optical fibre on the other side of the grating using a custom designed mass-applicator (Fig. 6.8). This range of masses were determined following preliminary work where the application of masses greater than this caused the mass-applicator to slip, therefore not applying the anticipated axial strain. Strain, ϵ, experienced by the LPG was calculated by [10],

$$\epsilon = \frac{mg}{GA_f} \tag{6.1}$$

where m is the applied mass, g is gravitational acceleration, 9.81 m·s^{-2}, G is Young's modulus of silica glass, 73.1 GPa and A_f is the cross-sectional area of the optical fibre. Confirmation that the LPG did not experience a permanent physical change following each trial was confirmed by the transmission spectral features returning to values obtained prior to strain assessment. The temperature was maintained at 20.5±1°C throughout the experiment.

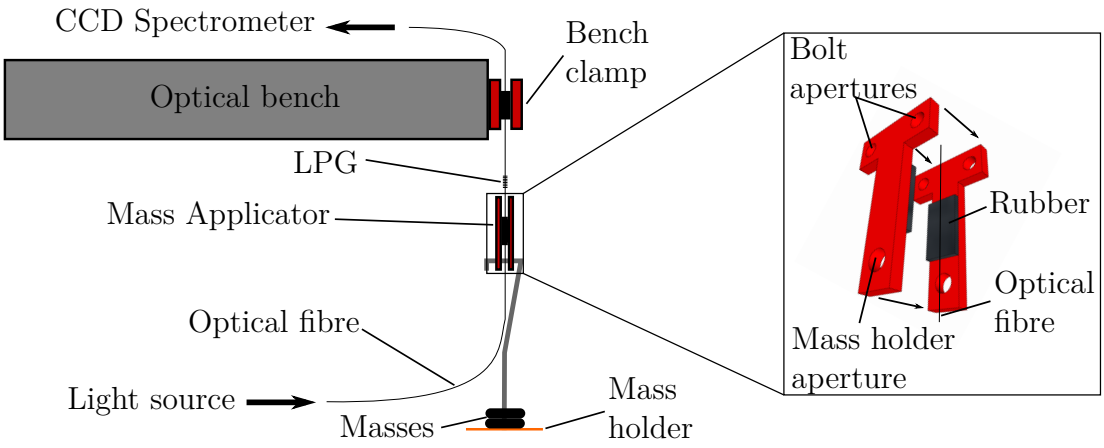

Figure 6.8: Experimental setup for strain measurements. Inset image depicts the 3D printed custom designed mass applicator (dimensions = 70 x 40 x 15 mm)

Temperature

To investigate the LPGs sensitivity to temperature, the grating was attached to an aluminium fibre holder (to maintain tension) and placed inside a digitally controlled oven (VTM7004, Votsch). The ends of the optical were fed through an access port and attached to the spectrometer and light source situated outside the oven (Fig. 6.9). Readings were collected in 10°C increments from 25 - 95°C. To ensure data was collected at the desired temperature, oven stability was characterised and it was deemed that at least 30 min were required for the temperature to plateau following a newly set temperature. However, it should be noted that the aluminium frame will experience thermal expansion as the temperature is increased, thus altering the tension on the LPG. The strain induced by this effect would equal 1.68 $\mu\epsilon$ at 95°C (see Appendix D for the calculation), equating to a significant wavelength change of 3.6 nm (using a typical LPG sensitivity of 2.2 pm$\cdot\mu\epsilon^{-1}$ [11]). It will therefore be necessary to compensate the temperature characterisation results prior to numerically assessing the LPG for multi-parameter capabilities.

Surrounding refractive index

The practical characterisation of the refractive index sensitivity of an LPG, whether this is performed using index matching oils or solutions of materials with varying concentrations (e.g. ethanol solutions [12]), is typically labour intensive, often requiring the manual preparation of the LPG by removing the previous solution, cleaning off any residue and drying the fibre for every sample point in the procedure [10]. It was therefore decided that the use of an automated approach would be more

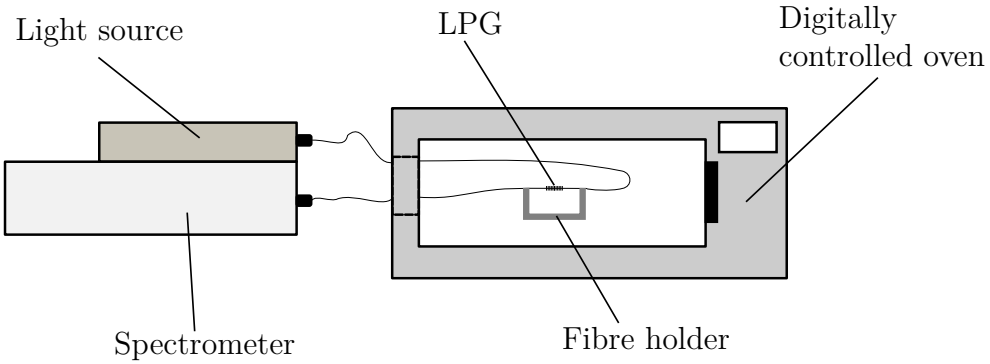

Figure 6.9: Experimental setup for temperature characterisation

time efficient. Sucrose solution was used as the test medium to assess the refractive index sensitivity of the LPG as this has been successfully employed previously [13, 12]. Additionally, unlike index matching oils, sucrose solutions are cheaper and can be diluted by water, thus allowing a greater number of sample points to be obtained.

Initially, a bulk sucrose solution was prepared (ACS reagent grade, Sigma Aldrich) and the concentration confirmed through the use of an automatic refractometer with a functioning wavelength of 589 nm and a resolution of 0.0001 nD operating at 20±0.05°C (Abbemat 200, Anton Paar). A prototype of the refractive index sensitivity characterisation system was created where by the bulk sucrose solution was incrementally added to a trough of deionised water by expelling a set volume of solution from a syringe controlled by a translation stage. This automated procedure allowed small increases in sucrose concentration (thus refractive index) in the trough to be achieved and permitted the LPG to be immersed in the solution continually without the need for fibre preparation between each dose. However, the incremental movement produced from the stage caused lateral motion in the syringe plunger. As a result, the desired volume was not dispensed, inducing variations in the resulting sucrose concentrations. To improve this, a diaphragm lab dosing-pump (Simdos 02, KNF) was substituted in place of the translation stage driven syringe as shown in Fig. 6.10.

To assess the accuracy and reliability of the system, the trough was partially filled with 20 ml of deionised water, which was measured using a high accuracy balance (GA200D, OHAUS) and the subsequent result converted into volume using a density of 0.998 g·ml^{-1} [14]. The dosing pump was programmed to deliver 8 cycles of 52.35% (w/w) bulk sucrose solution in 2 ml doses with a 2 min pause between each dose to allow the solution in the trough to become homogeneous via magnetic stirring. The temperature was controlled using the hot plate stirrer's RTD probe (VWR) and was

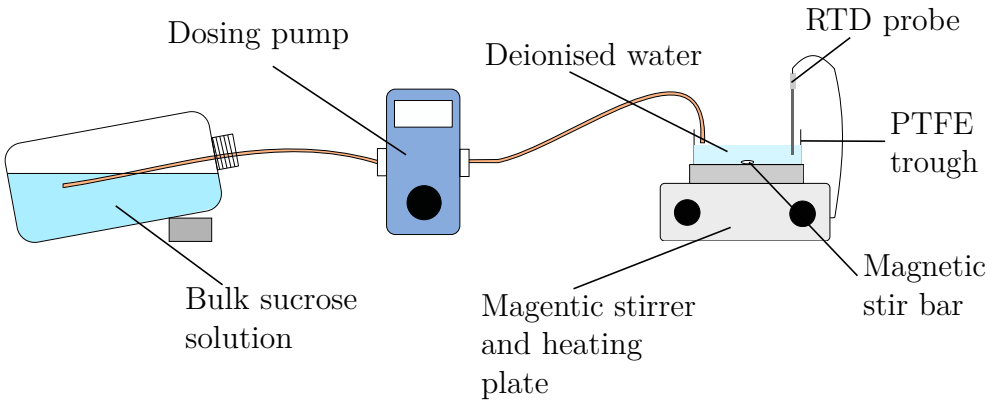

Figure 6.10: Experimental setup for automated refractive index testing

set to 20±0.5°C. The dosing pump was calibrated to the viscosity of the bulk sucrose solution. Following the 2 min pause of each dose, 60 μl was taken from the testing trough, assessed for its sucrose concentration using the automatic refractometer and, subsequently compared with expected concentrations, $C_{exp}(\%)$, calculated using the following expression,

$$C_{exp}(\%) = \left(\frac{V_{dose} C_{bulk}}{V_{wt} + V_{dose} - V_{samp}} \right) \times 100, \tag{6.2}$$

where C_{bulk} is the fractional bulk sucrose concentration, V_{wt}(ml) is the initial volume of deionised water, V_{dose}(ml) is the dose cumulative volume and, V_{samp}(ml) is the test sample cumulative volume. V_{samp} is needed to compensate for the volume removed from each dose for sucrose concentration validation. The procedure was repeated for a total of 4 tests.

The accuracy of the refractive index sensitivity characterisation system can be noted in Fig. 6.11. A good correlation can be seen between the calculated concentrations and measured values, demonstrating an r^2 value of 0.9999. The largest mean difference from the calculated values was 0.32% for a sucrose concentration of 30.54% which equates to 0.00042 in refractive index units (RIU). This result is only slightly less accurate than index matching oils of the same range (1.300 - 1.395, Series AAA, Cargille) which display a stated accuracy of ±0.00020 RIU. To assess the reliability of the refractive index sensitivity characterisation system, 95% confidence intervals were calculated for each sucrose dose and plotted as error bars in Fig. 6.11. Due to the small sample size for each dose ($n = 3$), an adapted formula for the confidence intervals, CI, was used [15],

$$CI = \bar{x} \pm (t_{n-1} \times SE), \tag{6.3}$$

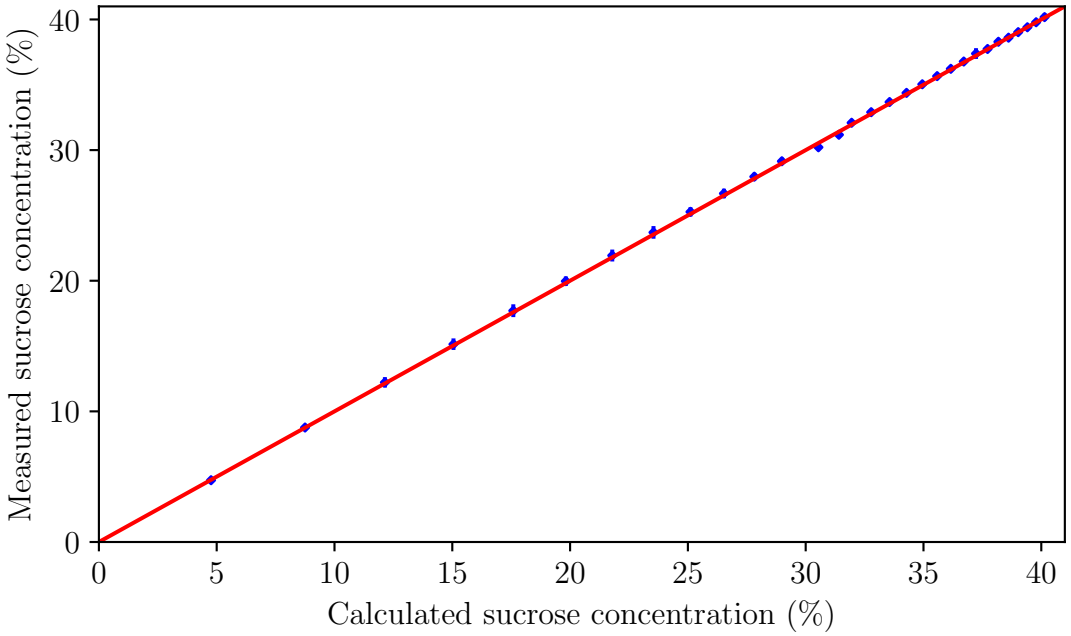

Figure 6.11: Correlation between calculated sucrose concentrations and measured values. The red line depicts perfect accuracy to act as a guide. Error bars that depict 95% confidence intervals are smaller than the points

where $\bar{x}$ is the mean dose%, t_{n-1} is the two-tailed t-value (in this case 4.30, obtained from critical t-value tables with a probability of 0.05 [15]) and SE is the standard error of the mean. From Fig. 6.11 it can be seen that the confidence intervals are small, indicating that error of the system was low.

This aforementioned system was used to evaluate the surrounding refractive index sensitivity of the LPG. Using the same concentration of bulk sucrose solution (52.35% (w/w)) and dose volume (2 ml), the device was exposed to sucrose concentrations ranging from 0 - 40.14% (corresponding to 1.333 - 1.399 RIU) dispensed in 30 cycles. The sucrose concentration range was calculated using Equation 6.1 with the V_{samp} term removed. Prior to the addition of sucrose, the LPG was immersed in the 20 ml deionised water for 20 min in order to stabilise the spectrum before baseline data was obtained. Subsequent spectra were automatically collected for all concentration points in the last 10 s of the 2 min pause between doses.

6.2.2 Results and discussion

The temperature sensitivity of attenuation bands associated with LP_{09} - LP_{14} and LP_{22} can be seen in Fig. 6.12. The wavelength shift experienced by the resonance bands displayed a linear response for the assessed temperature range. This temper-

ature sensitivity experienced by LPGs is produced by the expansion/contraction of the waveguide, not only changing the gratings period but also causing the effective refractive index to alter, resulting in a resonance wavelength shift (see Section 3.4).

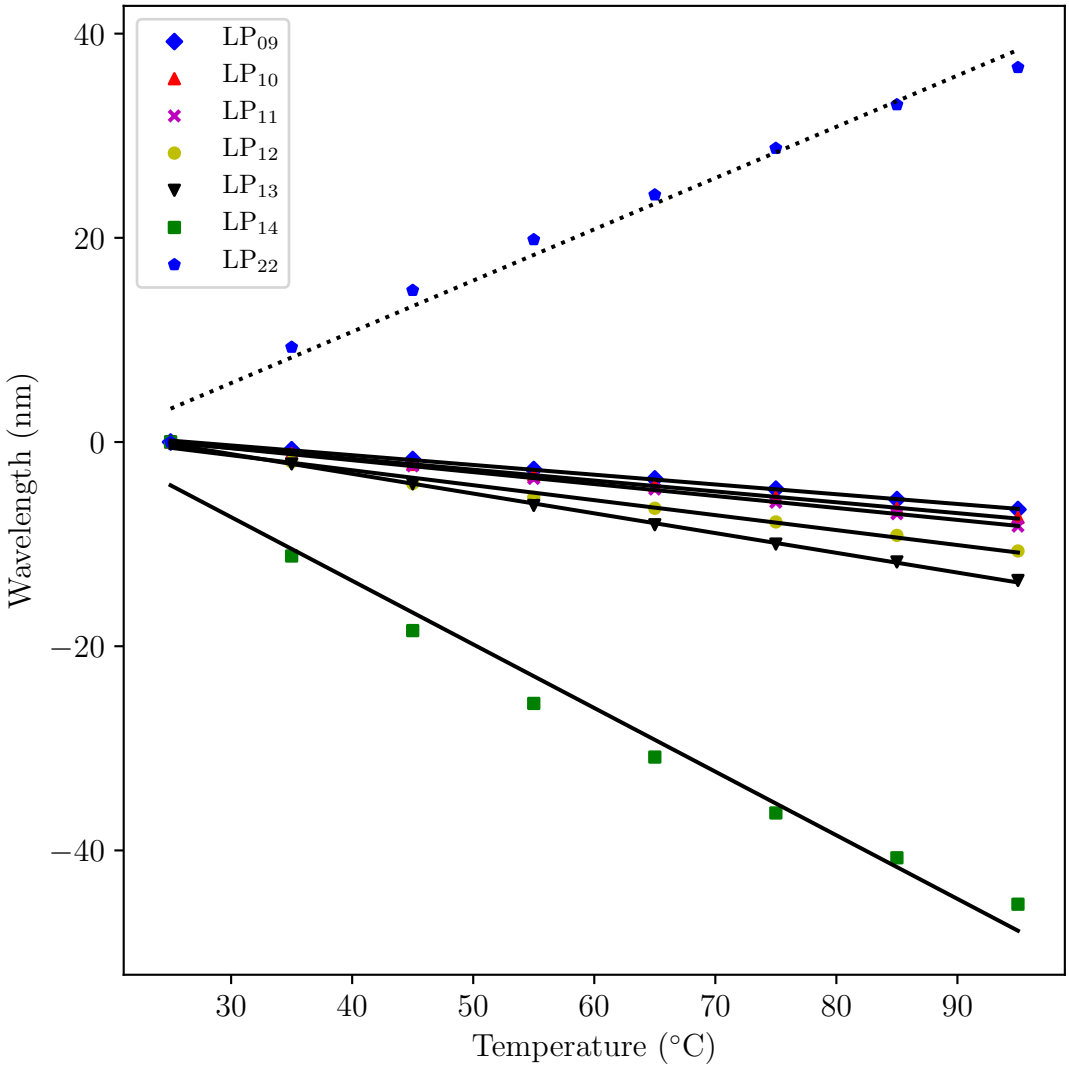

Figure 6.12: Wavelength shift of attenuation bands corresponding to coupling to LP_{09} - LP_{14} and LP_{22} to changes in temperature 25 - 95°C for an LPG displaying both 1^{st} and 2^{nd} order coupling near the PMTP. Method of least squares was used to calculate the linear fit in order to provide resonance band sensitivity (dotted line represents 2^{nd} order coupling). Error bars depicting the standard deviation (SD) are smaller than the points

As expected, attenuation bands corresponding to higher order modes displayed greater sensitivity to variations in temperature, as established by their larger gradients. Additionally, the two attenuation bands associated with modes operating near their PMTP (LP_{14} and LP_{22}) demonstrated larger responses to an increase in temperature compared with resonance bands functioning in a normal region. The difference in

shift direction demonstrated by the 1^{st} and 2^{nd} order resonance bands is caused by the features operating near the PMTP, where in this case the 1^{st} order attenuation feature experiencing a blue shift (a negative wavelength shift) and the 2^{nd} order resonance band undergoing a red shift (a positive wavelength shift) are tracked. The 2^{nd} order attenuation band (LP_{22}) displayed a sensitivity of 0.502 nm·°C^{-1} which was slightly less in magnitude than -0.623 nm·°C^{-1} shown by the 1^{st} order band (LP_{14}). These values are greater than data presented [1], where the sensitivities for the 1^{st} and 2^{nd} order attenuation bands to temperature are -0.509 and -0.251 nm·°C^{-1} respectively. The improved sensitivity witnessed in the present work is due to the features operating near the PMTP. However, it should be noted that the attenuation band monitored in [1] was associated with a lower order cladding mode (LP_{08}) than the features tracked here, thus the difference seen in sensitivity could be partly due to the use of attenuation bands corresponding to higher order modes which have been demonstrated to be more sensitive to temperature [16]. Similar to [1], 1^{st} order coupling showed higher sensitivity to temperature than 2^{nd} order coupling.

Akin to the results noted in Fig. 6.12, the wavelength shifts mediated through the application of axial strain also demonstrate a linear response (Fig. 6.13). Furthermore, both of the resonance features associated with modes operating at the PMTP also presented greater sensitivity to axial strain than bands not coupled near the PMTP. Although small variations in wavelength shift can be observed for attenuation bands corresponding to modes LP_{09} - LP_{12} in Fig. 6.13, these changes are below the resolution of the spectrometer (0.36 nm) thus indicating that these features demonstrate minimal sensitivity to axial strain. This response to axial strain seen in LPGs is largely produced by the elongation of the grating, which increases its periodicity inducing a resonance wavelength shift.

Comparing strain sensitivity between the 1^{st} and 2^{nd} order features operating near the PMTP, it can be seen that the 2^{nd} order (-3.185 nm·mϵ^{-1}) presented greater sensitivity than the 1^{st} order feature (2.815 nm·mϵ^{-1}). Again, similar to the temperature characterisation, the 1^{st} and 2^{nd} order features monitored here demonstrated higher sensitivity to axial strain than that presented in [1] (1.46 and 0.647 nm·mϵ^{-1}).

The surrounding refractive index characterisation is presented in Fig. 6.14. The inherent sensitivity displayed by LPGs to refractive index changes in the surrounding medium the fibre are produced by the dependence of the cladding modes' effective indices on perturbations of the refractive index of the local environment [16]. Greater sensitivity was witnessed as the mode order to which the resonance features

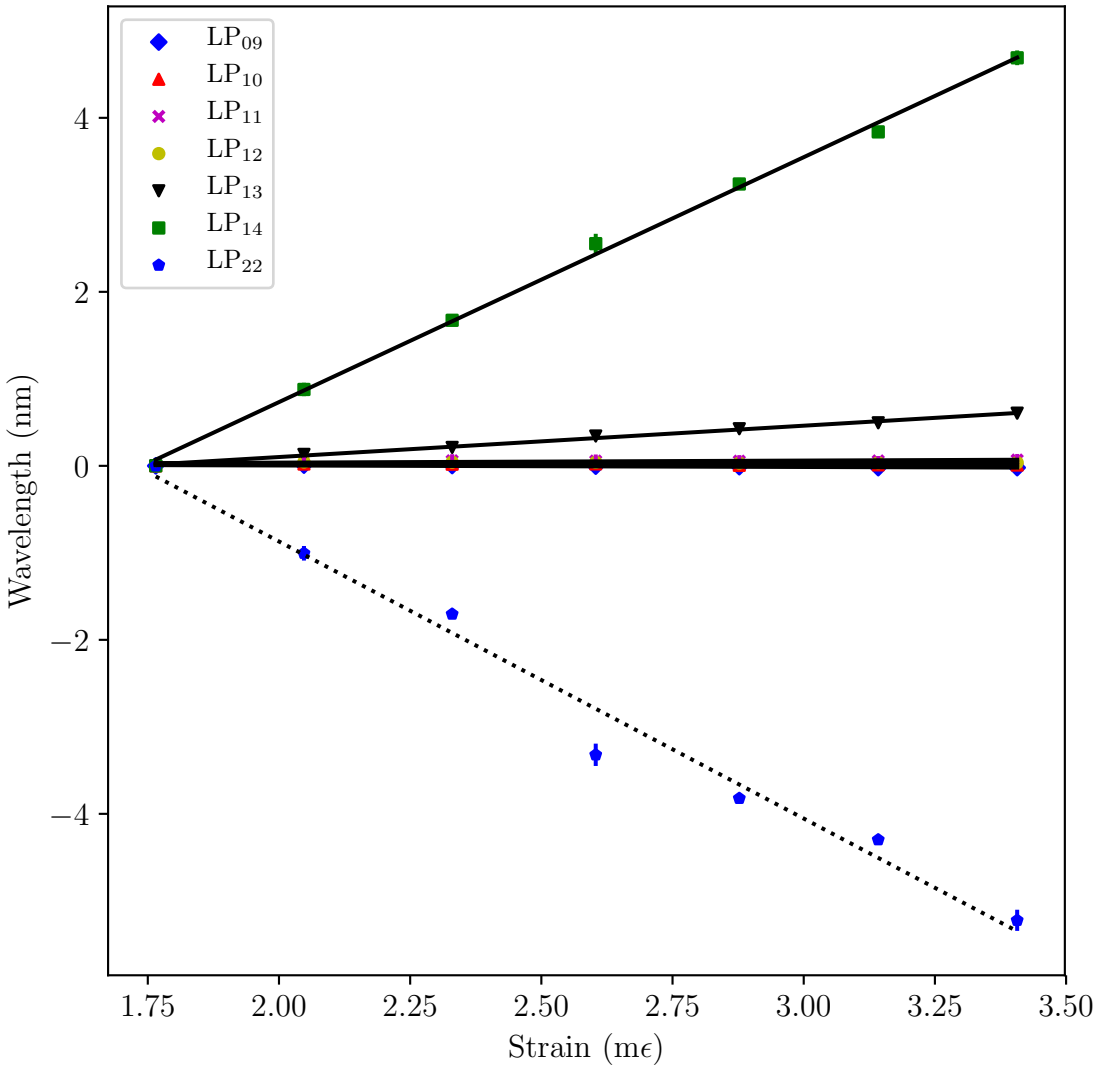

Figure 6.13: Wavelength shift of attenuation bands corresponding to coupling to LP_{09} - LP_{14} and LP_{22} to changes in strain 1.76 - 3.40 $\mu\epsilon$ for an LPG displaying both 1^{st} and 2^{nd} order coupling near the PMTP. Method of least squares was used to calculate the linear fit in order to provide resonance band sensitivity (dotted line represents 2^{nd} order coupling). Errors bar are SD

coupled increased. Indeed, for a 40% change in sucrose concentration (0.07 RIU) the attenuation bands associated with lower order modes (LP_{09} - LP_{12}) displayed a negligible wavelength shift. The higher order modes (LP_{13}, LP_{14}, LP_{22}) show a non-linear relationship between sucrose concentration and wavelength shift as the surrounding refractive index approaches that of the cladding, which is in agreement with previous work [10]. The 2^{nd} order attenuation band (LP_{22}) showed a maximum wavelength shift of 13.51 nm, larger than the 10.80 nm shift displayed by the 1^{st} order feature (LP_{14}) for a sucrose concentration of 40.14%.

No previous studies have investigated 2^{nd} order coupling in response to surrounding

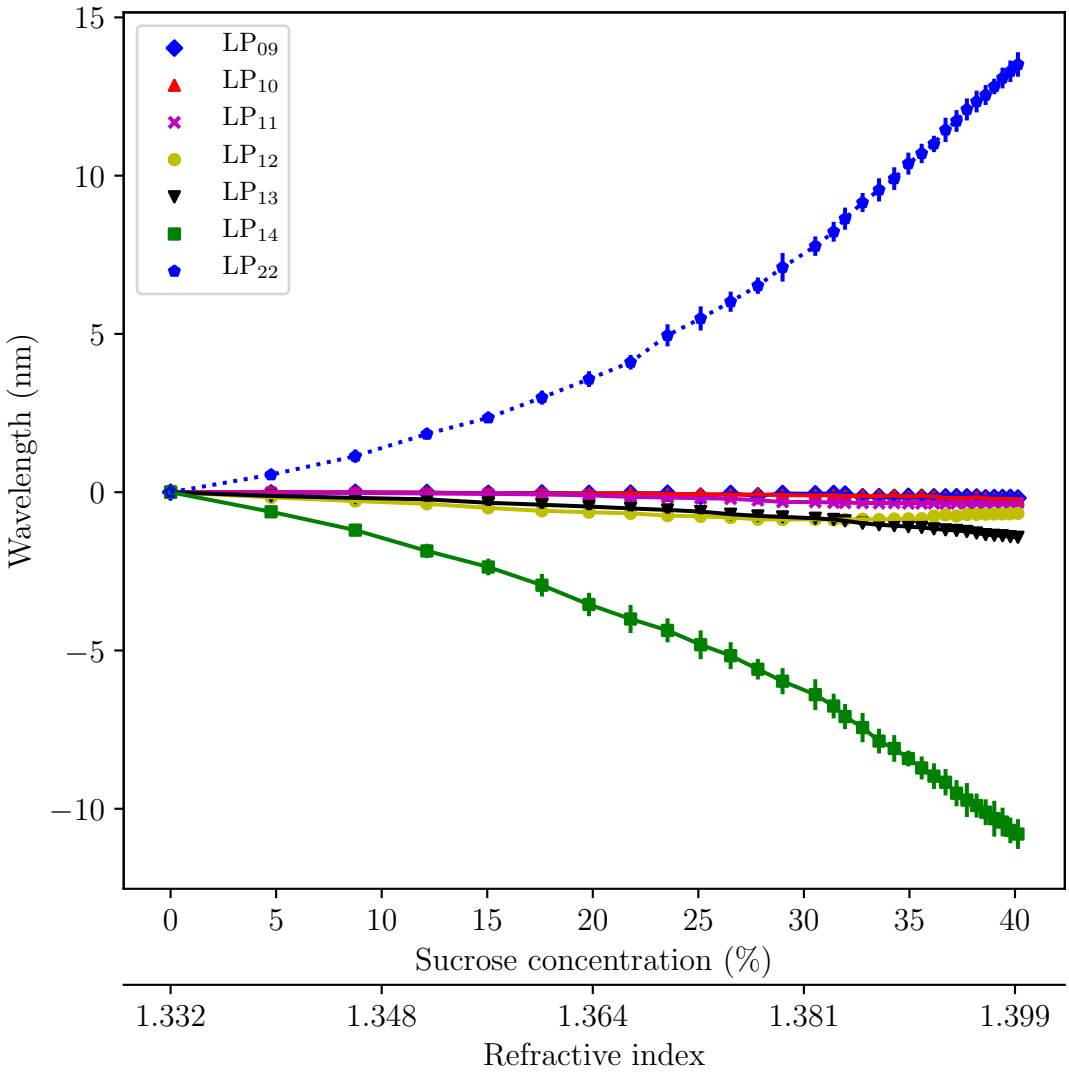

Figure 6.14: Wavelength shift of attenuation bands corresponding to coupling to LP_{09} - LP_{14} and LP_{22} to changes in sucrose solution concentration 0 - 40.14% for an LPG displaying both 1^{st} and 2^{nd} order coupling near the PMTP. The lines are visual aids only, where the dotted line signifies 2^{nd} order coupling. Error bars are SD

refractive index changes. However, comparing its sensitivity to LPGs with fundamental resonance bands tuned to the PMTP, it can be seen that the device presented here does not display an equivalent performance (Δ2.35 nm for LP_{22} from the LPG characterised here compared to Δ29 nm for a refractive index range of 1.335 - 1.360) [17]. This reduction in sensitivity arises from the requirement to select a period that allows coupling to both 1^{st} and 2^{nd} order resonance bands that are detectable within the wavelength range of a CCD spectrometer (550 - 1000 nm) in addition to ensuring 2^{nd} order features are distinct from their 1^{st} order counterparts. Thus, by optimising the phase matching condition to allow 1^{st} order coupling to a cladding

mode that is operating at the PMTP (increasing the sensitivity of the corresponding attenuation band) results in 2^{nd} order coupling to a cladding mode that is further from the PMTP (therefore the resonance feature displays less sensitivity).

It should be noted that the left and right bands associated with a cladding mode operating near the PMTP (dual resonance phenomenon) will present slightly different sensitivities to the same measurand change. This is caused by the asymmetry of the phase matching curves around the PMTP [18], where the right handed band located at the longer wavelength shows a larger response to variations in environmental parameters (temperature, strain, refractive index) [18, 10]. However, due to restrictions imparted by the wavelength range of the CCD spectrometer in the present work, it was not possible to compare the corresponding bands for both the 1^{st} and 2^{nd} order features.

Through the fabrication of LPGs with a 25% duty cycle and an appropriate period it is possible to produce gratings that possess resonance bands of both 1^{st} and 2^{nd} order that operate near their associated PMTP in the spectral range of a CCD spectrometer. This allows an LPG to possess two attenuation features that demonstrate enhanced sensitivity corresponding to different cladding modes within the detectable wavelength range of a CCD spectrometer.

6.3 Feasibility of multi-parameter sensing using 2^{nd} order resonance in LPGs

In the previous section, an LPG with both 1^{st} and 2^{nd} order attenuation bands operating near the PMTP was characterised for temperature, strain and surrounding refractive index. However, as mentioned in Section 6.2.1 the additional strain applied to the LPG via the thermal expansion of the aluminium frame during temperature characterisation would induce a significant wavelength shift. Therefore, the temperature coefficients calculated in Section 6.2.2 for the resonance features LP_{14} and LP_{22} have been appropriately modified (using the calculation presented in Appendix D) for the following numerical analysis. Since this fabricated device displays 1^{st} and 2^{nd} order features with enhanced sensitivity in comparison to [1], it is therefore expected that a greater performance in multi-parameter sensing could be obtained using the sensor characterised here.

6.3.1 Qualitative analysis

Simultaneous measurement of two measurands using the LPG presented here can be achieved by exploiting the differing responses of the 1^{st} and 2^{nd} order attenuation bands to the perturbations seen in Section 6.2.2. This change in central wavelength experienced by the resonance features, $\Delta\lambda_i$, to variations in two environmental parameters, A and B, can be given by,

$$\Delta\lambda_i = K_{iA}A + K_{iB}B, \tag{6.4}$$

where K_{iA} and K_{iB} are the environmental parameter coefficients ($K_{iA} = \partial\lambda_i/\partial A$ and $K_{iB} = \partial\lambda_i/\partial B$) for resonance feature i which was obtained using linear regression. It is possible to independently determine the parameters A and B by expressing Equation 6.4 in matrix form to describe both 1^{st} and 2^{nd} order bands (Equation 6.5) and performing an inverse matrix operation.

$$\begin{pmatrix}\Delta\lambda_1\\ \Delta\lambda_2\end{pmatrix} = \begin{pmatrix}K_{1A} & K_{1B}\\ K_{2A} & K_{2B}\end{pmatrix}\begin{pmatrix}A\\ B\end{pmatrix}. \tag{6.5}$$

Errors obtained through inaccurate determination of λ_i and imperfect estimation of the matrix coefficients can lead to significant errors in solutions to the simultaneous equations [19]. Therefore, in order to assess the stability of a linear system to matrix element perturbations, the matrix condition number, C_n, is often employed to assess sensor performance [20, 21, 22]. It is calculated using [23],

$$C_n = \|\mathbf{K}\|\left\|\mathbf{K}^{-1}\right\|, \tag{6.6}$$

where $\|\mathbf{K}\|$ and $\|\mathbf{K}^{-1}\|$ are the norm and the inverse norm of matrix $\mathbf{K}$, respectively. This value provides a qualitative estimation of the sensor's behaviour, where an optimum device would attain unity. Typical condition numbers for wavelength dependent sensors discriminating between temperature and strain, such as FBGs and LPGs are 39.4 [22] and 76.9 [1] (calculated using the sensitivity coefficients presented in the papers) respectively.

To qualitatively assess the performance of the LPG characterised in Section 6.2.2 for multi-parameter sensing using 1^{st} and 2^{nd} order features, condition numbers were calculated using the sensitivity coefficients presented in Table 6.1 for discrimination between temperature-strain, temperature-surrounding refractive index and, surrounding refractive index-strain. The values presented in Table 6.1 were derived from linear regression analysis (using least squares method) conducted in the generation of

Fig. 6.12 and Fig. 6.13 for temperature and strain characterisation respectively. As this calculation assumes that the measurands have a linear relationship with respect to wavelength shift, the coefficients pertaining to the surrounding refractive index sensitivity were calculated using the final 12 values (34.95 - 40.14%) as this region displayed a linear correlation.

Table 6.1: Calculated sensitivity coefficients ± standard error for 1^{st} (LP_{14}) and 2^{nd} (LP_{22}) order resonance in response to independent changes in temperature, strain and surrounding refractive index

Parameter	**Sensitivity coefficients**	
	LP_{14}	**LP_{22}**
Temperature (nm·°C^{-1})	-0.570±0.039	0.449±0.028
Strain (nm·mϵ^{-1})	2.815±0.057	-3.185±0.202
Surrounding refractive index (nm·%$^{-1}$)	-0.463±0.005	0.614±0.006

It can be seen from Table 6.2 that the condition number for temperature-strain is lower than 76.9, obtained from a similar LPG scheme presented in [1]. Furthermore, this number is comparable to values obtained by FBGs using the dual-wavelength technique (38.6 [24], 39.4 [22]). The simultaneous measurement of temperature-surrounding refractive index using a single LPG element has not been performed before. Previously, this measurement has been conducted using a number of in-series LPGs [25] or via use of a hybrid FBG-LPG system [26]. However, it is clear from the small condition number that independent recovery of these two meaurands would contain minimal errors, therefore allow accurate values to be obtained. Surrounding refractive index-strain was included for completeness as this simultaneous measurement has minimal practical value, thus no literature exists in LPGs for these two meaurands, although work has been conducted on discriminating all three physical parameters in tapered and etched FBGs [27, 28]. The condition numbers detailed in Table 6.2 demonstrates that it is possible to perform multi-parameter sensing utilising the LPG characterised here which uses 1^{st} and 2^{nd} order resonance bands near the PMTP.

Table 6.2: Condition numbers calculated for the discrimination of three simultaneous parameters using 1^{st} and 2^{nd} order attenuation bands

Discrimination Parameters	**Condition number**
Temperature-strain	33.7
Temperature-surrounding refractive index	7.7
Surrounding refractive index-strain	73.5

Nevertheless, although commonly used [20, 21], the condition number does not necessarily indicate that the sensor will be able to accurately discriminate between two simultaneous measurands. This estimate provides a means to compare the maximum errors in a system with other devices [22], however, a comparison of sensors with condition numbers from 3 - 300 were all found be broadly comparable in performance [20]. Furthermore, it is not possible to distinguish the contribution of each environmental parameter within this error [20]. In order to provide a more detailed discussion regarding the suitability of the LPG presented here, calculations formulated by Jin *et al.* [20] were employed, allowing a quantitative analysis of the LPG's ability to separate environmental parameters to be conducted.

6.3.2 Quantitative analysis

The errors calculated using the analysis technique presented in [20] are dependent upon the wavelength determination precision, the uncertainties accrued through linear coefficient calculations and on the environmental parameter values. Similar to previous work [22, 29], these formulations will be used to quantify: cumulative errors associated with determining wavelength, cumulative matrix element generated errors and, non-cumulative errors obtained by both matrix elements and wavelength measurement precision. While the cumulative errors provide the worse possible case, the non-cumulative errors are more representative by accounting for the direction of the individual terms [22].

The general formulation is based upon the condition that both transfer matrix, $\mathbf{K}$, and wavelength determination, $\boldsymbol{\lambda}$, contain errors such that,

$$\boldsymbol{\lambda} = \lambda_T + \delta\lambda, \tag{6.7}$$

$$\mathbf{K} = K_0 + \delta K, \tag{6.8}$$

where λ_T and $\delta\lambda$ represent the true value and errors in $\boldsymbol{\lambda}$ respectively, while K_T and δK depict the true value and errors in $\mathbf{K}$.

To assess the $\boldsymbol{\lambda}$-errors only, the errors within $\mathbf{K}$ are neglected, allowing the following formulations to be implemented,

$$|\delta A| = \frac{|K_{2B}||\delta\lambda_1| + |K_{1B}||\delta\lambda_2|}{|\Delta|}, \tag{6.9}$$

$$|\delta B| = \frac{|K_{2A}||\delta\lambda_1| + |K_{1A}||\delta\lambda_2|}{|\Delta|}, \tag{6.10}$$

where K_{iA} and K_{iB} maintain the same definition as described in Section 6.3.1 and $\Delta = K_{1A}K_{2B} - K_{2A}K_{1B}$ is the determinant of $\mathbf{K}$ and δ_{iA} and δ_{iB} are the standard error of the matrix coefficient for attenuation band i and environmental parameters A and B, respectively. To consider the case where matrix dominated errors are significant, the measured wavelength errors are assumed to be negligible, leading to the expressions

$$|\delta A| = \frac{(|K_{1A}K_{2B}\delta_{1A}| + |K_{1B}K_{2A}\delta_{2A}|)|A| + |K_{1B}K_{2B}|(|\delta_{1B}| + |\delta_{2B}|)|B|}{|\Delta|}, \tag{6.11}$$

$$|\delta B| = \frac{(|K_{1B}K_{2A}\delta_{1B}| + |K_{1A}K_{2B}\delta_{2B}|)|B| + |K_{1A}K_{2A}|(|\delta_{1A}| + |\delta_{2A}|)|A|}{|\Delta|}, \tag{6.12}$$

Finally, to calculate the theoretical resolution of the sensor by combining both $\boldsymbol{\lambda}$-error and $\mathbf{K}$-error the subsequent equations were used

$$\begin{aligned} A =& \frac{1}{\Delta(\Delta + \Delta^*)}((K_{2B}\delta\lambda_1 - K_{1B}\delta\lambda_2)\Delta + (K_{2B}\delta_{2B}\lambda_1 - K_{1B}\delta_{1B}\lambda_2)\Delta + \\ & (K_{2B}\delta_{2B}\delta\lambda_1 - K_{1B}\delta_{1B}\delta\lambda_2)\Delta - (K_{2B}\lambda_1 - K_{1B}\lambda_2)\Delta^*), \end{aligned} \tag{6.13}$$

$$\begin{aligned} B =& \frac{1}{\Delta(\Delta + \Delta^*)}((K_{2A}\delta\lambda_1 - K_{1A}\delta\lambda_2)\Delta + (K_{2A}\delta_{2A}\lambda_1 - K_{1A}\delta_{1A}\lambda_2)\Delta + \\ & (K_{2A}\delta_{2A}\delta\lambda_1 - K_{1A}\delta_{1A}\delta\lambda_2)\Delta - (K_{2A}\lambda_1 - K_{1A}\lambda_2)\Delta^*), \end{aligned} \tag{6.14}$$

where

$$\Delta^* = K_{1A}K_{2B}(\delta_{1A} + \delta_{2B} + \delta_{1A}\delta_{2B}) - K_{1B}K_{2A}(\delta_{1B} + \delta_{2A} + \delta_{1B}\delta_{2A}), \tag{6.15}$$

$\lambda_i = AK_{iA} + BK_{iB}$ is the combined wavelength shift of attenuation band i in response to environmental parameters A and B and $\delta\lambda_i$ is the wavelength measurement precision of attenuation band i. For all calculations, the latter was deemed to be 0.13 nm for both 1^{st} and 2^{nd} order resonance features (determined by the spectrometer's resolution). To quantify the maximum error in $\mathbf{K}$ and to establish the combined errors of $\boldsymbol{\lambda}$ and $\mathbf{K}$, temperature, strain and surrounding refractive index values of 25°C, 2.0 mϵ and 38.2% were used, respectively.

The data presented in Table 6.3 indicates that, although the device here demon-

Table 6.3: Error analysis using the quantitative method described in [20] for temperature-strain (Temp-str), temperature-surrounding refractive index (Temp-SRI) and surrounding refractive index-strain (SRI-str)

	Discrimination Parameter					
	Temp-str		Temp-SRI		SRI-str	
	T (°C)	ϵ (mϵ)	T (°C)	RI (%)	RI (%)	ϵ (mϵ)
$\boldsymbol{\lambda}$-error	1.42	0.24	0.98	0.93	0.55	3.04
$\mathbf{K}$-error	13.35	2.39	4.33	3.90	3.56	20.76
$\boldsymbol{\lambda}$ + $\mathbf{K}$-error	5.06	0.99	2.06	1.28	61.78	9.63

strated condition numbers equivalent to other sensing methods (Table 6.2), deeper quantitative analysis has shown that accurate multi-parameter sensing would not be achievable. Indeed, the resolution of the LPG for simultaneous measurement of temperature-strain is ±5.06°C and ±0.99 mϵ, and, when compared to other schemes discriminating between the same parameters, it can be seen that a single-element titled FBG was able to possess resolutions of ±1°C and ± 12 $\mu\epsilon$ following the same quantitative analysis [22], demonstrating a greater performance. Although the temperature resolution of the LPG presented here could potentially be suitable for distinguishing large temperature shifts, the strain resolution clearly shows an unacceptable degree of performance with minimal practical value.

By far the least erroneous resolution displayed by the LPG for discriminating between parameters can be seen for temperature-surrounding refractive index (Table 6.3). A temperature and sucrose concentration resolution of ±2.06°C and ±1.28% (±1.74 × 10^{-3} RIU) respectively could be acceptable in some cases, particularly if a large wavelength change is observable. However, it should be noted that these changes are only applicable over the range of 35 - 40% sucrose concentration due to the non-linear relationship outside of this region. Additionally, in the majority of chemical/biological LPG sensing applications where a small change in the refractive index of a functional coating occurs, this level of resolution would not be sufficient. The use of this LPG to discriminate between surrounding refractive index and strain would be impossible due the large errors noted for both of these parameters (Table 6.3).

Inspection of the $\boldsymbol{\lambda}$-error in Table 6.3 for all simultaneous parameters shows that, with the exception of the strain measurement in the surrounding refractive index-strain assessment, the cumulative errors for wavelength measurement precision demonstrate adequate levels of error. However, it is clear that the $\mathbf{K}$-error is significantly greater than $\boldsymbol{\lambda}$ induced errors. This error is derived from calculating the matrix elements which depend on the suitability of the linear fit. Thus any experimental error

accrued during data collection for each environmental parameter would influence this result. Therefore, the discrimination performance of the device could be improved through the use of more accurate experimental designs, producing data that allows an improved linear fit. Interestingly, the performance noted in Table 6.3 for $\boldsymbol{\lambda}$ + **K**-error follows a similar trend to the condition numbers calculated (Table 6.2) for the respective simultaneous measurements, where temperature-surrounding refractive index showed the lowest condition number and greatest discrimination accuracy, reinforcing the use of this value as a suitable estimator for comparison to other devices.

6.4 Summary and conclusion

Through altering the fabrication UV irradiation duty cycle, it is possible to access higher order harmonics using a single LPG. Although the use of 2^{nd} order coupling has been discussed previously [1, 2, 3], the fabrication parameters required to produce these harmonics had not previously been investigated. It was found that a 25% duty cycle produced LPGs that optimally coupled to these features.

Using this method, an LPG with both 1^{st} and 2^{nd} order attenuation bands operating near the PMTP within the detectable wavelength range of a CCD spectrometer was fabricated. The LPG was characterised for temperature, strain and surrounding refractive index, where the latter required the design and development of an automated refractive index testing rig. The LPG was then theoretically assessed for its ability to perform multi-parameter sensing by distinguishing between simultaneous parameters from the characterisation data through the use of condition number and quantitative analysis. Although the condition number showed that the LPG was suitable for multi-parameter sensing, the detailed quantitative analysis demonstrated that accurate discrimination between all assessed parameters would not be achievable in practice. This result is in disagreement with the majority of previous work that has examined the use of different resonance features of a single LPG for multi-parameter sensing [1, 30]. Nevertheless, the work presented here employed a more in-depth analytical approach than is generally used, ultimately suggesting that performing multi-parameter sensing in LPGs utilising different resonance bands with large variations in parameter sensitivities may not be a viable option.

In terms of the CO_2 sensor here, this result demonstrates that another scheme would be necessary (see Section 3.7 for alternatives) to distinguish between surrounding refractive index (mechanism for detecting CO_2) and other physical parameters LPGs

are innately sensitive to (e.g. temperature).

6.5 References

[1] T. Allsop, L. Zhang, D. J. Webb, and I. Bennion. Discrimination between strain and temperature effects using first and second-order diffraction from a long-period grating. *Optics Communications*, 211(1-6):103–108, 2002.

[2] S. W. James, C. S. Cheung, and R. P. Tatam. Experimental observations on the response of 1st and 2nd order fibre optic long period grating coupling bands to the deposition of nanostructured coatings. *Optics Express*, 15(20):13096–13107, 2007.

[3] V. Grubsky, A. Skorucak, D. Starodubov, and J. Feinberg. Fabrication of long-period fiber gratings with no harmonics. *IEEE Photonics Technology Letters*, 11(1):87–89, 1999.

[4] S. Kher, S. Chaubey, J. Kishore, and S. M. Oak. Detection of fuel adulteration with high sensitivity using turnaround point long period fiber gratings in B/Ge doped fibers. *IEEE Sensors Journal*, 13(11):4482–4486, 2013.

[5] V. Mishra, S. C. Jain, N. Singh, G. Poddar, and P. Kapur. Fuel adulteration detection using long period fiber grating sensor technology. *Journal of Scientific and Industrial Research*, 46(2):106–110, 2008.

[6] R. Y. Wong, E. Chehura, S. E. Staines, S. W. James, and R. P. Tatam. Fabrication of fiber optic long period gratings operating at the phase matching turning point using an ultraviolet laser. *Applied Optics*, 53(21):4669–4674, 2014.

[7] H. Schroeder, M. Hippler, P. Allenspacher, W. Riede, A. Ciapponi, A. B. Mateo, T. Ivanov, J. Alves, J. Piris, C. Heese, *et al.* Investigation of laser-induced ablation of ceramic materials for spaceborne applications. In *Laser-Induced Damage in Optical Materials 2016*, vol. 10014, p. 100141K. International Society for Optics and Photonics, 2016.

[8] M. Partridge, S. W. James, J. H. Barrington, and R. P. Tatam. Overwrite fabrication and tuning of long period gratings. *Optics Express*, 24(20):22345–22356, 2016.

[9] M. Partridge. Spectral processing software. Retrieved 23rd April 2017. https://github.com/MCeeP/SIR.

[10] R. Y. N. Wong. *Advanced fibre optic long period grating sensors; design, fabrication and sensing.* Ph.D. thesis, Cranfield University, 2014.

[11] S. W. James and R. P. Tatam. Optical fibre long-period grating sensors: characteristics and application. *Measurement Science and Technology*, 14(5):R49–61, 2003.

[12] S. Korposh, S.-W. Lee, S. W. James, and R. P. Tatam. Refractive index sensitivity of fibre-optic long period gratings coated with SiO2 nanoparticle mesoporous thin films. *Measurement Science and Technology*, 22(7):1–10, 2011.

[13] J.-F. Ding, A. P. Zhang, L.-Y. Shao, J.-H. Yan, and S. He. Fiber-taper seeded long-period grating pair as a highly sensitive refractive-index sensor. *IEEE Photonics Technology Letters*, 17(6):1247–1249, 2005.

[14] G. Kell. Precise representation of volume properties of water at one atmosphere. *Journal of Chemical and Engineering data*, 12(1):66–69, 1967.

[15] A. Field. *Discovering Statistics using SPSS*. SAGE Publications Ltd, London, UK, 3rd ed., 2009.

[16] V. Bhatia and A. M. Vengsarkar. Optical fiber long-period grating sensors. *Optics Letters*, 21(9):692–694, 1996.

[17] P. Biswas, N. Basumallick, S. Bandyopadhyay, K. Dasgupta, A. Ghosh, and S. Bandyopadhyay. Sensitivity enhancement of turn-around-point long period gratings by tuning initial coupling condition. *IEEE Sensors Journal*, 15(2):1240–1245, 2015.

[18] X. Shu, L. Zhang, and I. Bennion. Sensitivity characteristics of long-period fiber gratings. *Journal of Lightwave Technology*, 20(2):255–266, 2002.

[19] A. M. Vengsarkar, W. C. Michie, L. Jankovic, B. Culshaw, and R. O. Claus. Fiber-optic dual-technique sensor for simultaneous measurement of strain and temperature. *Journal of Lightwave Technology*, 12(1):170–177, 1994.

[20] W. Jin, W. C. Michie, G. Thursby, M. Konstantaki, and B. Culshaw. Geometric representation of errors in measurements of strain and temperature. *Optical Engineering*, 36(8):2272–2279, 1997.

[21] W. Jin, W. C. Michie, G. Thursby, M. Konstantaki, and B. Culshaw. Simultaneous measurement of strain and temperature: error analysis. *Optical Engineering*, 36(2):598–610, 1997.

[22] E. Chehura, S. W. James, and R. P. Tatam. Temperature and strain discrimination using a single tilted fibre Bragg grating. *Optics Communications*, 275(2):344–347, 2007.

[23] G. Strang. *Introduction to Linear Algebra*. Cambridge Press, Wellesley, US, 4th ed., 2009.

[24] O. Frazao and J. Santos. Simultaneous measurement of strain and temperature using a Bragg grating structure written in germanosilicate fibres. *Journal of Optics A: Pure and Applied Optics*, 6(6):553, 2004.

[25] J. Yan, A. P. Zhang, L. Y. Shao, J. F. Ding, and S. He. Simultaneous measurement of refractive index and temperature by using dual long period gratings with an etching process. *IEEE Sensors Journal*, 7(9):1360–1361, 2007.

[26] D. A. C. Enriquez, A. R. da Cruz, and M. T. M. R. Giraldi. Hybrid FBG-LPG sensor for surrounding refractive index and temperature simultaneous discrimination. *Optics and Laser Technology*, 44(4):981 – 986, 2012.

[27] S.-M. Lee, S. S. Saini, and M.-Y. Jeong. Simultaneous measurement of refractive index, temperature, and strain using etched-core fiber Bragg grating sensors. *IEEE Photonics Technology Letters*, 22(19):1431–1433, 2010.

[28] R. Oliveira, J. H. Osório, S. Aristilde, L. Bilro, R. N. Nogueira, and C. M. Cordeiro. Simultaneous measurement of strain, temperature and refractive index based on multimode interference, fiber tapering and fiber Bragg gratings. *Measurement Science and Technology*, 27(7):1–6, 2016.

[29] J.-L. Tang and J.-N. Wang. Error analysis and measurement uncertainty for a fiber grating strain-temperature sensor. *Sensors*, 10(7):6582–6593, 2010.

[30] V. Bhatia, D. Campbell, R. O. Claus, and A. M. Vengsarkar. Simultaneous strain and temperature measurement with long-period gratings. *Optics Letters*, 22(9):648–650, 1997.

Chapter 7

CO_2 sensing using LPGs

In this chapter, the development of a novel LPG-based CO_2 sensor is described. As outlined in Chapter 1, the CO_2 sensor is to be part of an ammonia breath sensor to provide a method for recognising exhaled breath that has been in contact with alveoli blood. The device therefore must possess a response time of <0.1 s and a detection range 0 - 15% with an accuracy of ±0.2%. In addition to these specifications, it is also necessary that the sensor displays a negligible response to humidity variations and is not sensitive to ammonia. To achieve this, LPGs fabricated via the overwrite method (see Section 5.1) are coated with a number of the CO_2 sensitive materials described in Section 4.2 and their responses characterised to 20% CO_2 and their cross-sensitivity to humidity. Here, particular emphasis is placed on the use of an ionic liquid based coating to produce the LPG sensor with the specificity and sensitivity to CO_2. The use of these materials has not been explored previously for CO_2 sensing with LPGs, where materials such as MOFs [1] and polystyrene (non-specific coating) [2] have been used instead. The physical CO_2 absorption mechanism exhibited by certain ionic liquids means that the regeneration step requires a less energy intensive process (lower temperatures, standard pressures), making these materials ideally suited as the CO_2 LPG sensitive coating.

Although the previous chapter explored LPGs with higher order coupling features with the aim of conducting multi-parameter sensing, the work in this chapter was focussed upon identifying whether these CO_2 sensitive materials are capable of eliciting a wavelength response in LPGs following exposure to CO_2 and not, at this stage, if competing environmental parameters (e.g. temperature) could be compensated for during sensor operation. Therefore, all LPGs utilised in this chapter were fabricated so that only 1^{st} order coupling features were present, thus ensuring attenuation bands associated with higher order coupling would not potentially interfere with

CO_2 mediated wavelength responses.

Initially, this chapter focuses on the detection of CO_2 via the use of an LPG coated with the commonly utilised alkanoamine, polyethylenimine (PEI). Following on from this, the ionic liquid 1-hexyl-3-methylimidazolium bis(trifluoromethylsulfonyl)imide ($[C_6mim][Tf_2N]$) was assessed for its suitability as a CO_2 sensitive coating material for an LPG sensor. The subsequent sections detail the novel coating procedure and fibre surface preparations necessary for applying the ionic liquid to an LPG. Finally, the $[C_6mim][Tf_2N]$ coated LPG was characterised for its response to CO_2, humidity and temperature.

7.1 PEI-based LPG CO_2 sensor

As discussed in Section 4.2.1, amines demonstrate excellent CO_2 absorption, so that materials which contain these functional groups have been used as the sensing layer on a number of CO_2 sensors [3, 4, 5]. A commonly used polyamine for CO_2 sensing and enhancement of adsorption is PEI [4, 5, 6, 7]. This polymer can be synthesised with a linear or branched structure, where its molecular arrangement effects which amine groups are present (primary, secondary, tertiary, see Section 4.2.1). Absorption of CO_2 produces a structural change through the formation of carbamate or bicarbonate depending on the amine group involved in the reaction [8]. Due to its polycationic nature, PEI has been applied to substrate surfaces via the use of ESA (see Section 4.1.2) with an appropriate polyanion counterpart [9, 10]. It was therefore proposed that, by using this coating technique, PEI could be applied to the surface of an LPG, and when exposed to gaseous CO_2, the aforementioned reaction would induce a refractive index change in the PEI-coating, producing a detectable resonance wavelength shift.

7.1.1 PEI coating procedure

A 40 mm long LPG operating at the PMTP was written in PS750 optical fibre with a period and duty cycle of 113.4 μm and 50%, respectively. It was fabricated via the procedure outlined in Section 5.1. The ESA method used to coat the LPG with PEI was based on previous work reported by Korposh *et al.* [11].

KOH pellets (Sigma Aldrich) were dissolved in deionised water (DirectQ, MilliPore) to produce a 0.1 M solution. Additionally, solutions of 5 $mg{\cdot}ml^{-1}$ branched PEI (Av. Mw: 25000, Sigma Aldrich) and 1% silica nano-particles (SiO_2) (40 - 50 nm

diameter, Nissan Chemicals) were prepared using deionised water. SiO_2 NP were selected as the polyanion due to their ability to create porous layers during ESA [11], which would aid CO_2 gas diffusion through the coating.

The LPG was attached to a CCD spectrometer (HR4000, Ocean Optics) with a resolution of 0.130 nm, and to a tungsten light source (LS-1, Ocean Optics) using bare fibre SMA connectors, where the latter was allowed to stabilise for 40 min prior to data collection. To ensure that the LPG remained taut throughout the experiment, the fibre was attached to an aluminium frame via PTFE thumb-screw tabs.

Initially, the LPG was immersed in 0.1 M KOH for 20 min to gently etch the fibre cladding in order to produce a negatively charged surface. Following cladding preparation, the aluminium frame was attached to a rotary dip-coater (ND-R, Nadetech) which was programmed to alternately immerse the LPG for 20 min into the PEI (polycation) and SiO_2 (polyanion) solutions to build up the LbL deposition. Before each immersion, the LPG was rinsed in deionised water to remove any unbound material. The fibre was left in air to dry for 5 min following each layer (polycation and polyanion) in order to obtain a spectrum. For brevity, each ESA layer will be expressed as $(A/B)_X$, where X is the number of bilayers and A and B are polycation and polyanion, respectively. A coating of $(PEI/SiO_2)_{10}$ was initially selected based, on previous report of ESA work with LPGs [12].

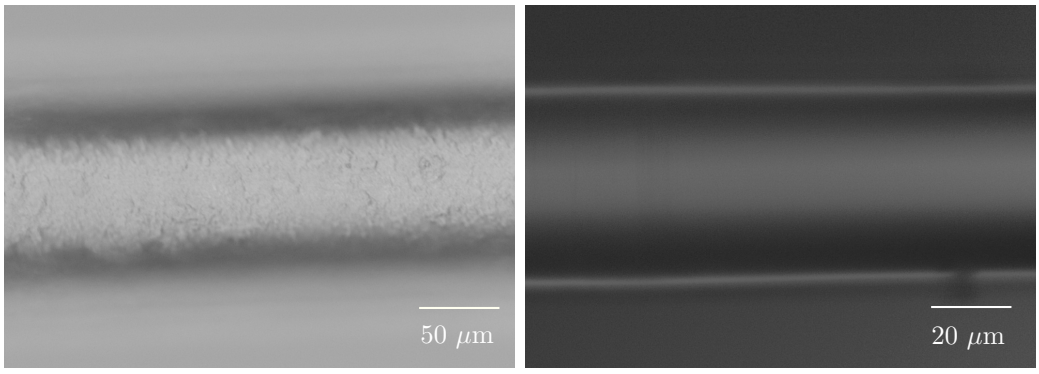

Figure 7.1: Light microscopy images of a $(PEI\text{-}SiO_2)_{10}$ coated fibre (a) with an image of a non-coated fibre (b) for comparison. Despite the greater magnification of (b), it is clear the optical fibre surface has no deposition

Confirmation of the $(PEI/SiO_2)_{10}$ deposition was achieved via the use of light microscopy (Fig. 7.1) and scanning electron microscopy (eSEM), where the latter determined its thickness to be 580 nm. Spectral changes are also induced by the coating process, where upon each new layer of (PEI/SiO_2) the attenuation

band operating at the PMTP develops towards the formation of dual resonance (Fig. 7.2). This alteration is induced by the change in the cladding mode's effective refractive index that is produced by the presence of a deposition layer. As the central wavelengths and intensities of the attenuation bands are dependent on both the refractive index and the thickness of the coating [13, 14], each additional layer of (PEI/SiO_2) applied to the LPG prompts a small wavelength shift. The magnitude of the shift is dependent on the modal order and in which region coupling has occurred (i.e. distinct from or at the PMTP), where the large change in intensity displayed by the LPG in Fig. 7.2 following the first initial layers is caused by the attenuation band operating at the sensitive PMTP. As further layers were deposited onto the LPG, its operation moved away from the PMTP, spectral changes became less pronounced as evidenced by the small wavelength change witnessed between $(PEI/SiO_2)_9$ and $(PEI/SiO_2)_{10}$.

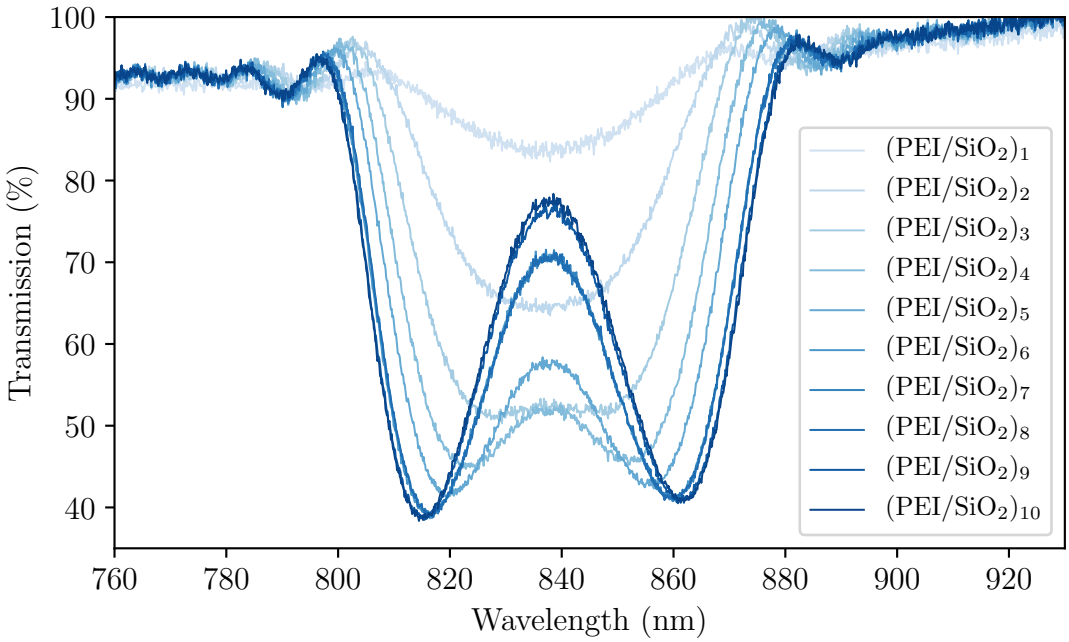

Figure 7.2: Spectra showing the evolution of the attenuation band associated with LP_{19} following each additional coating of PEI/SiO_2

7.1.2 CO_2 response of the PEI coated LPG

To assess the CO_2 response of the $(PEI/SiO_2)_{10}$ coated LPG, a cylindrical gas cell (with an internal volume of 113.4 ml) was modified to be able to incorporate an optical fibre. This was achieved by removing the glass windows and replacing them

with aluminium plates possessing a 3 mm hole in the centre to allow the optical fibre to be fed through. Nevertheless, small air gaps were present, particularly where the fibre was inserted, and these have been shown to allow atmospheric gas to diffuse into the cell and influence the test gas mixture [15]. To overcome this issue, Zakaria [15] ensured a positive pressure was maintained within the cell and all components sealed with wax. Although sealing the gas cell here with wax would ameliorate this issue, it would severely hinder removal of the data logger between tests and would be an excessive step considering the high concentration of CO_2 (20%) being used initially (unlike Zakaria [15] who was interested in ppm concentrations). Therefore, rather than sealing the modified gas cell, a positive pressure will be maintained during testing to minimise diffusion of atmospheric air.

A 40 mm long LPG was fabricated with a period of 113.8 μm and a 50% duty cycle via the method outlined in Section 5.1 and was coated with $(PEI/SiO_2)_{10}$ as described in Section 7.1.1. Using an aluminium frame located outside the gas cell, the LPG was positioned in the centre of the cell and held at constant tension. The grating was interrogated throughout the experiment via the same light source and spectrometer as detailed in Section 7.1.1 (Fig. 7.3). Using a mass flow controller and its associated ports (THPS-400, Teledyne Hastings Instruments), 200 ml·min^{-1} of synthetic air (SA)(20-22% O_2, 1 ppm CO_2, 2 ppm H_2O, BOC) was used to purge the gas cell for 15 min in order to remove moisture and to provide a standard environment in which to begin the experiment. Following the purge, the coated LPG was then exposed to 20% CO_2 (Scott Speciality Gases) for 60 min. Temperature and humidity were monitored for the duration of the experiment using a remote data logger (i-Button, Maxim Integrated), with a temperature and humidity resolution of $\pm$0.5 °C and $\pm$0.6 % respectively, which was placed inside the gas cell. The wavelengths of the attenuation bands were tracked using SIR software [16].

By monitoring the shorter-wavelength attenuation band associated with dual resonance of LP_{19}, the wavelength response of this attenuation band to 20% CO_2 was determined and presented in Fig. 7.4. A 3.3 nm wavelength shift was observed following the 60 min exposure to CO_2. However, during the experiment, a 22% decrease in humidity was also observed. The wavelength response observed could therefore be partially or fully induced by humidity variations thus the noted wavelength shifts can not be attributed to either parameter.

The sensitivity to humidity displayed by the PEI/SiO_2 coated LPG is speculated to derive from the SiO_2 layers of the coating [17]. The use of these nano-particles was intended to increase the porosity of the coating, consequently aiding the diffusion of

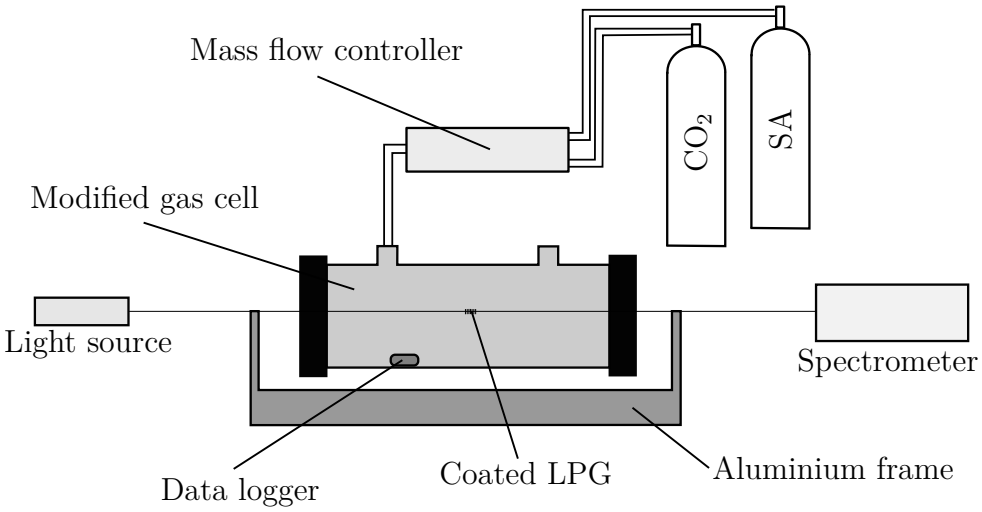

Figure 7.3: Experiential layout for testing CO_2 response of PEI/SiO_2 coated fibre, located inside a modified gas cell (100 x ⌀38 mm)

CO_2 molecules through the deposition. Nevertheless, SiO_2 nano-particles demonstrate a high affinity for water and have been implemented as the coating for an LPG humidity sensor [17]. It is therefore unclear whether the wavelength shift depicted in Fig. 7.4 is the product of humidity mediated effects, the exposure to CO_2, or a combination of both. In order to distinguish between these measurands, the use of a humidity generator (GenRH, Surface Measurement Systems) to control the moisture in the CO_2 in-flow was implemented.

The humidity generator was introduced into the experiential arrangement of Fig. 7.3 after the mass flow controller but before the in-flow of the modified gas cell. Humidity was controlled in the generator via the bubbling of gas through deionised water. Since CO_2 readily dissolves in water [18], CO_2 was allowed to flow through (500 cc·min^{-1}) the humidity generator system for 1 h in order to saturate the deionised water thus minimising water CO_2 absorption during the procedure.

To improve the sensitivity of the $(PEI/SiO_2)_{10}$ coated LPG sensor, a 40 mm long LPG was newly fabricated with a period of 114.0 μm and a 50% duty cycle. This period produced a sensor that operated nearer to the PMTP following $(PEI/SiO_2)_{10}$ deposition. The same fabrication, coating and experimental procedures were utilised as outlined previously, with the exception that the duration of the CO_2 exposure was decreased to 40 min since the wavelength response witnessed in Fig. 7.4 occurred well within this time period. The humidity generator was programmed with a humidity and temperature of 45% and 20.0°C, respectively.

The response of the $(PEI/SiO_2)_{10}$ coated LPG to CO_2 in a humidity stabilised gas

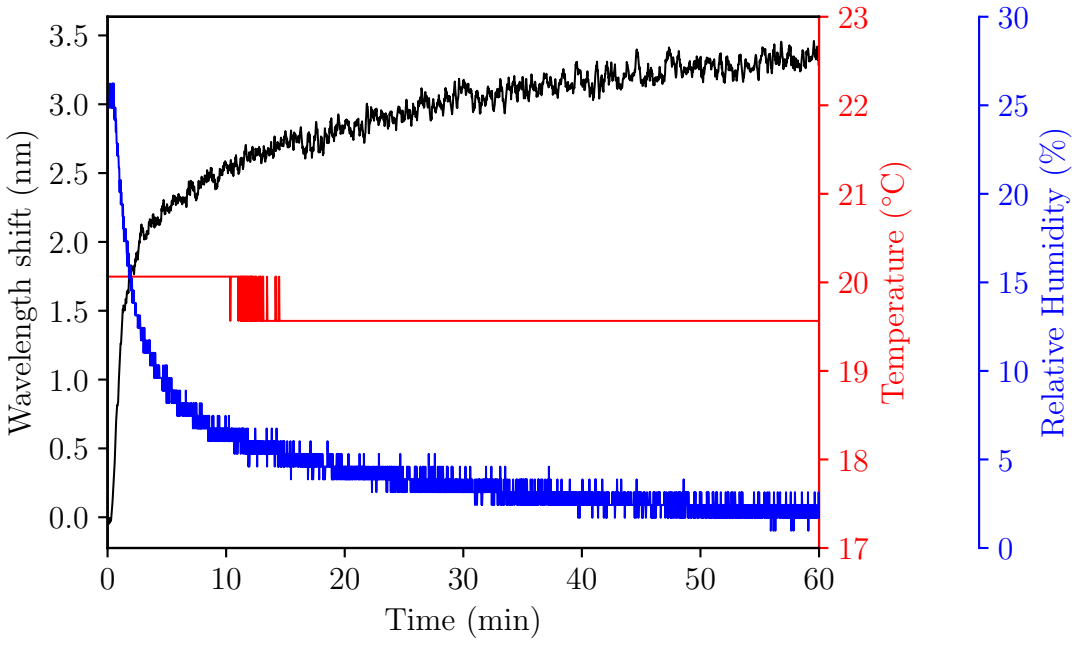

Figure 7.4: The response of $(PEI/SiO_2)_{10}$ coated LPG to 20% CO_2. Lines are associated with their y-axis based on like colours

flow can be seen in Fig. 7.5. Similar to the result presented in Fig. 7.4, the left-hand attenuation band corresponding to LP_{19} demonstrates a trend suggesting an inverse relationship with changes in humidity, where a 4% decrease in humidity initiated a 2 nm wavelength shift. This response demonstrates greater sensitivity than the $(PEI/SiO_2)_{10}$ coated LPG depicted in Fig. 7.4 due to the attenuation band operating closer to the PMTP.

It is interesting to note that at both 0 and 40 min the relative humidity is 46.5%. However, there is 0.5 nm wavelength shift discrepancy between the two time points. This difference in wavelength could be a result of a temperature induced response. Typically, LPGs with resonance features operating at the PMTP show temperature sensitivities in the region of 0.99 $nm{\cdot}°C^{-1}$ [19], since the temperature decreased by 1°C, it is conceivable that the 0.5 nm wavelength shift was caused by the change in temperature. It could also be speculated that this wavelength shift was a response to CO_2. The mechanism by which the PEI derived coating operates is based on the formation of carbamate through the reaction of CO_2 with the amine groups present in PEI [5] (see Section 4.2.1). The addition of the carbamate group to the coating would induce a refractive index change, ultimately inducing a resonance wavelength response. Although the aforementioned difference is most likely a CO_2 response, thus the PEI/SiO_2 coating was able to detect CO_2, the large humidity sensitivity

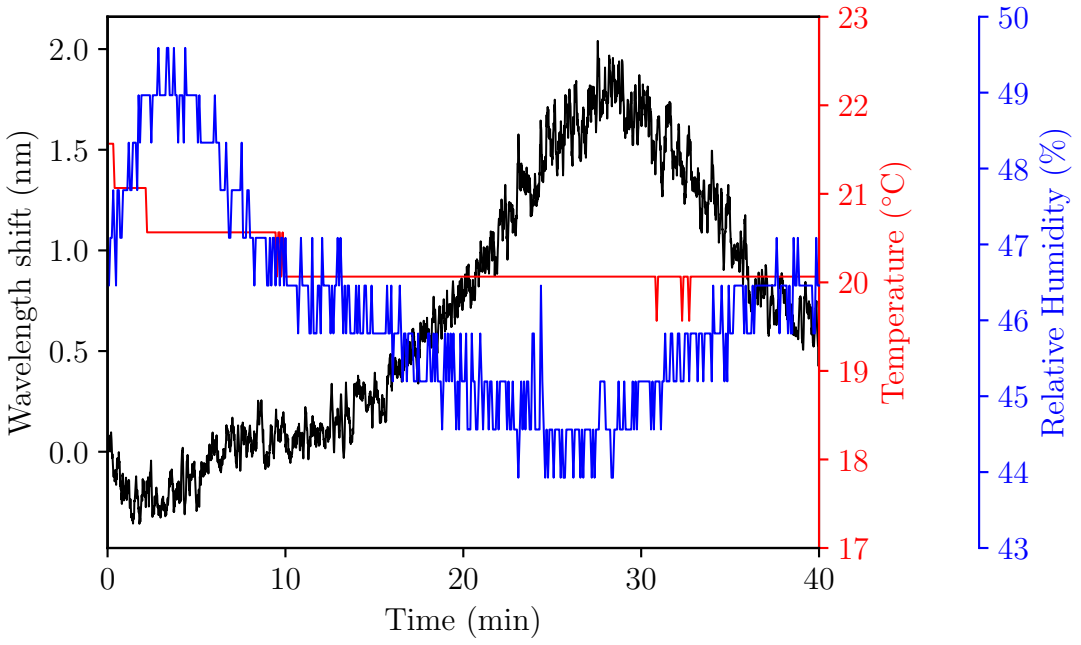

Figure 7.5: The response of $(PEI/SiO_2\ NP)_{10}$ coated LPG to 20% CO_2 while relative humidity is controlled. Lines are associated with their y-axis based on like colours

displayed by the deposition make it difficult to distinguish CO_2 mediated changes. In practise this means this deposition is unsuitable for an independant LPG CO_2 sensor. However, as described in [20], the CO_2 response could be resolved from humidity mediated effects by adding an additional grating that is dedicated to monitoring humidity.

7.2 The suitability of $[C_6mim][Tf_2N]$ as a CO_2 sensitive coating

Ionic liquids possess many of the qualities that are essential for the active coating of a CO_2 sensor; CO_2 absorption, hydrophobicity, and the ability to form a stable structure (see Section 4.2.5). However, as is clear from Sections 3.4.3 and 3.4.4, an LPG chemical sensor that employs a coating to enhance sensitivity and provide selectivity requires the deposition to experience a refractive index change in response to the measurand. Although ionic liquids are potentially ideal for the current project, no previous literature has investigated whether these materials demonstrate a refractive index change when exposed to CO_2, it is therefore essential that this parameter is evaluated before further work is conducted on ionic liquids.

7.2.1 CO_2 response of ionic liquids

The ionic liquid [C_6mim][Tf_2N] was selected based on its CO_2 absorption ability, hydrophobic nature and its capability to form an ionogel [21, 22, 23]. Furthermore, the commercial availability of [C_6mim][Tf_2N] was also an important factor due to the lack of available equipment required to synthesise and conduct essential post-manufacture purity assessments. The basic thermo-physical properties of [C_6mim][Tf_2N] can be seen in Table 7.1 .

Table 7.1: The thermo-physical properties of [C_6mim][Tf_2N] at 0.1 MPa; triple point (T_{Tr}), boiling point (T_B), density ($\boldsymbol{\rho}$) and, Henry's constant (H_C)

Ionic liquid	$\mathbf{T}_{Tr}$ (K)	$\mathbf{T}_B$ (K)	$\boldsymbol{\rho}$ (kg·m^{-3})	$\mathbf{H}_C$ (bar)
[C_6mim][Tf_2N]	272.13 [24]	897 [25]	1372.21[a] [26]	32.8[a] [27]

[a] measured at 298.15 K

To identify whether [C6mim][Tf_2N] displayed a refractive index change in response to CO_2, the ionic liquid was exposed to the gas for 16 h. CO_2 (20%) was bubbled through $\sim$ 5 ml of [C_6mim][Tf_2N] (purity >98.0%, TCI chemicals) at a flow rate of 5 ml·min^{-1}, where a small sample was removed pre- and post-CO_2 exposure for a refractive index measurement to be obtained via the use of an automatic refractometer with accuracy and resolution of $\pm 1 \times 10^{-4}$ RIU (Abbemat 200, Anton Paar). Using the in-built automatic Peltier control of the refractometer, the temperature of the sample well was maintained at 20±0.05°C.

Following the exposure to CO_2, [C_6mim][TF_2N] experienced a -3×10^{-4} RIU change from 1.43155±5 × 10 to 1.43125±5 × 10 (mean±SD). This alteration in refractive index is speculated to be caused by [C_6mim][Tf_2N] absorbing CO_2 molecules into the local cavities between the anions and cations. The uptake of CO_2 molecules into these inter-ionic spaces causes localised expansion while still maintaining the overall configuration of the liquid [28]. As the medium expands, the volume increases slightly, reducing the density thus causing the observed refractive index change.

This preliminary work showed that [C_6mim][Tf_2N] experienced a refractive index change following CO_2 exposure. Nevertheless, the noticeable difference in refractive index was small and close to the resolution displayed by the refractometer. As the refractive index change of the ionic liquid will need to be detected by an LPG, it was therefore decided that the experiment would be repeated using an LPG immersed in the ionic liquid to identify whether the refractive index alteration could also be observed by an in-fibre grating.

A 40 mm long LPG of 113.7 μm period with a 50% duty cycle was placed inside a PTFE trough that contained grooves at either end to allow the LPG to be fully submerged in the ionic liquid and be held under constant tension. The aforementioned procedure was used with the exception that the pre- and post-exposure samples were dispensed into the PTFE trough for assessment by the LPG, which was interrogated using a broadband light source (LS-1, Ocean Optics) and a CCD spectrometer (S2000, Ocean Optics) with resolution of 0.36 nm (Fig. 7.6). In addition to $[C_6mim][Tf_2N]$

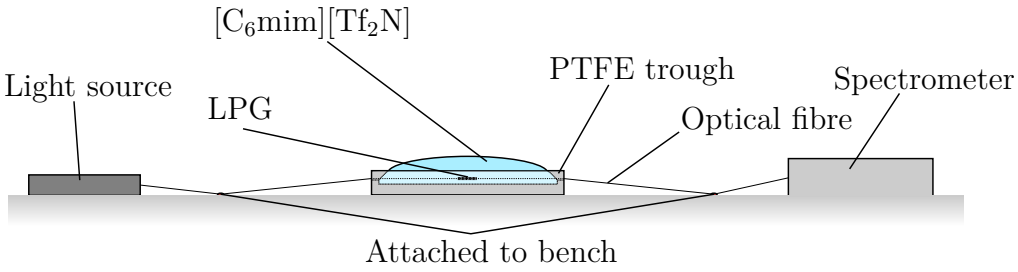

Figure 7.6: Experimental arrangement for assessing refractive index change in $[C_6mim][Tf_2N]$ following exposure to CO_2

being exposed to CO_2, the ionic liquid was also subjected to SA for the same period of time to act as a control sample. Once the initial wavelength had been obtained for a particular test, the fibre was not adjusted until the post-exposure measurement had been taken in order to ensure a consistent tension across the LPG. Both CO_2 and SA tests were repeated 3 times, where, following each measurement, the fibre was washed with propanone and IPA prior to being dried with compressed air (Hurricane, O2) until the baseline spectrum had been reacquired. Throughout the experimental period, the laboratory temperature was measured every 15 min using a data logger (i-Button, Maxim Integrated).

The left-hand attenuation band associated with LP_{19} operating at the PMTP (centred at ~810 nm in air) was used to assess whether a refractive index change in $[C_6mim][Tf_2N]$ was apparent. The average laboratory temperatures throughout the tests for responses to CO_2 and SA were 18.9±0.21 and 18.8±0.21°C respectively. Fig. 7.7 shows the measured wavelength of the attenuation band following immersion in $[C_6mim][Tf_2N]$ before and after the ionic liquid was subjected to either CO_2 or SA. An average red-shift of 1.22 nm was witnessed following exposure to CO_2 in comparison to a 3.33×10^{-4} nm change displayed following SA treatment. This shows that the refractive index change observed after CO_2 exposure was produced by CO_2 and not by another atmospheric air constituent such as Nitrogen or Oxygen (major constituents of SA). The difference in initial wavelength (Pre) between SA and CO_2 is 0.357 nm which is below the resolution of the spectrometer and therefore

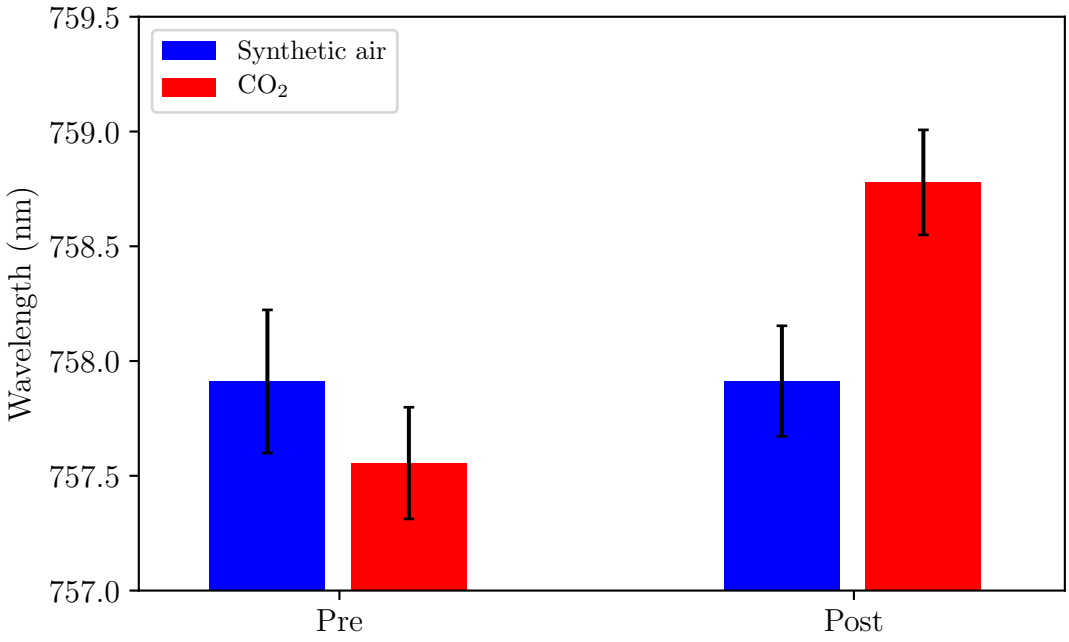

Figure 7.7: Wavelength of the attenuation band corresponding to LP_{19} from a 40 mm LPG with period 113.7 μm immersed in [C_6mim][Tf_2N] pre- and post- the ionic liquid being exposed to 16 h of CO_2 or SA. Error bars represent SD

can be considered negligible.

The 1.22 nm red-shift detected in the ionic liquid subjected to CO_2 indicates that there was a reduction in the surrounding refractive index. This supports the result in the previous experiment conducted using the automated refractometer where -3×10^{-4} RIU difference was also observed post-CO_2 exposure. Crucially, this outcome confirms that an LPG operating at or near the PMTP is able to detect the change in refractive index experienced by [C_6mim][Tf_2N] when subjected to 20% CO_2 for 16 h.

In order to inform the experimental procedures used later in this chapter, it was necessary to establish the response time of CO_2 absorption in [C_6mim][Tf_2N]. Using the same experimental procedure as previously described (Fig. 7.6), [C_6mim][Tf_2N] was exposed to 20% CO_2 for 15, 30, 60, 900, 1800, 3600, 7200 s (ranging from 15 s to 2 h) and the wavelength shift of a newly fabricated 40 mm long LPG with the same parameters (113.7 μm period and a 50% duty cycle) was assessed.

Inspection of the data presented in Fig. 7.8 demonstrates that an exposure time of 60 s is required for [C_6mim][Tf_2N] to absorb CO_2 that induces a measurable wavelength response. Exposure times greater than 30 s produced wavelength shifts that were significantly larger than the one noted at 15 and 30 s, where all the wavelengths

for these exposure times displayed a significant shift greater than error produced by the resolution of the spectrometer (0.36 nm). Nevertheless, the error bars depicted in Fig. 7.8 are derived from the spectrometer's resolution. However, the central wavelengths of these features were determined using the peak tracking software [29] that operates by fitting a polynomial function to the data points. By applying a curve fitting algorithm to the data, previous work has shown that it is possible to obtain sub-pixel resolution in the determination of peak identification [30]. Therefore, the error bars used in Fig. 7.8 depict the central wavelength of the attenuation features in a worst case scenario and, since a polynomial algorithm was applied here, it is highly likely that there is a more significant difference between the data points either side of 60 s. This result demonstrates that ionogel requires at least 60 s of CO_2 exposure to elicit a significant wavelength response.

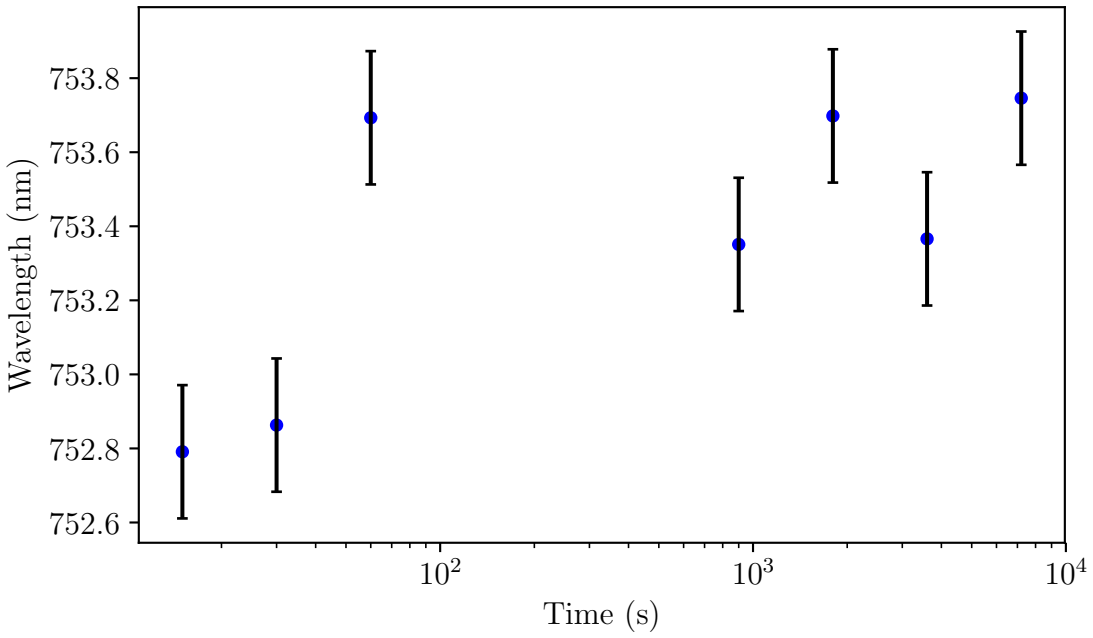

Figure 7.8: Wavelength of the attenuation band corresponding to LP_{19} from a 40 mm LPG with period 113.7 μm immersed in $[C_6mim][Tf_2N]$ which had been to subjected to varying CO_2 exposure times. Error bars represent the resolution of the spectrometer (0.36 nm)

7.2.2 Preparation of ionogel

Since $[C_6mim][Tf_2N]$ displays a refractive index change in response to CO_2, the next step was to develop a means to deposit the ionic liquid onto the surface of an optical fibre while preserving the its CO_2 absorption properties. Voss *et al.* [23] demonstrated that it was possible to produce an ionogel (see Section 4.2.5), through

the addition of a low molecular-weight organic gelator (LMOG), that possessed mechanical stability yet still offered CO_2 absorption performance similar to that of pure $[C_6mim][Tf_2N]$.

Based on the method outlined in [23], 6070 mg of $[C_6mim][Tf_2N]$ was added to 91 mg of 12-hydroxystearic acid (Sigma Aldrich) prior to being heated at ∼100°C until a homogeneous solution was obtained. Upon cooling, a 1.5% (w/w) LMOG loaded opaque gel was formed which, when inverted, did not flow (Fig. 7.9). This percentage has been shown to be the maximum LMOG loading possible before a bi-phasic product is produced that contains an ionic liquid rich phase and an LMOG saturated phase [23].

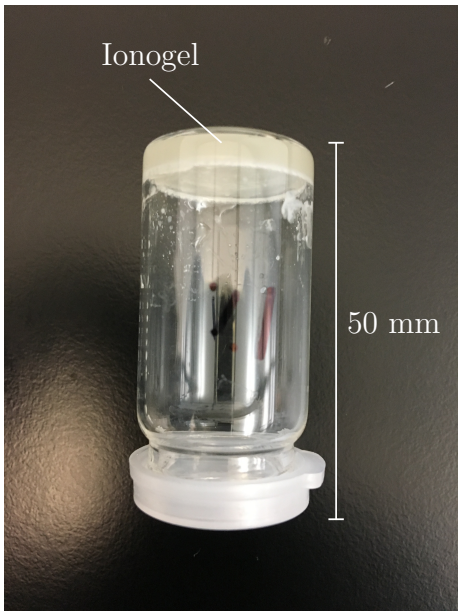

Figure 7.9: $[C_6mim][Tf_2N]$ ionogel formed via the addition of 12-hydroxystearic acid. Note the mechanical stability of the gel upon inversion

As the ionogel produced in [23] transits to a sol phase at ∼70°C, the ionogel produced here was also characterised for its sol-gel transition temperature. This was achieved by placing the vial of ionogel in a water bath, placed on a hotplate with an RTD probe (VWR), where the temperature was incrementally increased by 1°C starting initially at 65°C. The vial was held at each temperature for 10 min to allow the temperature to equilibrate in the ionogel. Once the time had elapsed, the inverted test tube method was applied in which the vial was inverted and assessed to determine whether the ionogel present flowed [31]. The temperature at which this occurred was considered to be the sol-gel transition temperature, where this value was deemed to be 74±0.5°C for the ionogel.

7.3 Ionogel fibre coatings

In order to apply the ionogel to the surface of the optical fibre, a coating system had to be designed and developed. The deposition method would utilise the ionogel's ability to transit between a liquid and a gel. Using a temperature above the ionogel's sol-gel transition point would allow the coating to be applied whilst in liquid phase, where upon cooling the ionogel deposited on the fibre would revert to the mechanically stable gel phase. A dip-coating based system (see Section 4.1.1) was considered to be the most suitable deposition method to exploit this attribute of the ionogel.

7.3.1 Development of coating system

The first prototype of the ionogel coating system can be seen in Fig. 7.10. The operating principle of the apparatus relied on the temperature gradient between the heated ionogel in the reservoir (controlled using the hotplate) and the surrounding environment. A j-piece shaped glass capillary tubing was used to guide the optical

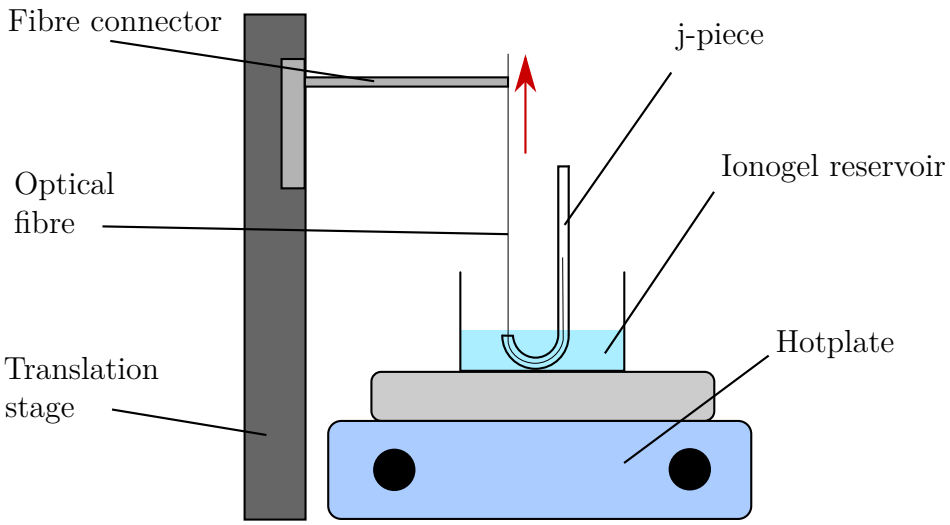

Figure 7.10: Diagrammatic representation of the initial prototype ionogel coating system. Arrow indicates withdrawal direction

fibre into the ionogel and ensure that it emerged perpendicular to the gel's surface. Attaching the fibre to a translation stage (M150.11, PI) allowing withdrawal speeds between 0 - 110.8 mm·min^{-1} to be obtained. Additionally, using a short j-piece ensured only minimal ionogel volumes (∼4 ml) were required for each coating, thus reducing the amounted wasted.

While this first coating system proved to be capable of depositing an ionogel onto the fibre's surface, it did suffer from a number of operational issues. The capillary

tube j-piece was created with the largest possible bend radius in an attempt to reduce fibre breakages. Nevertheless, the portion of the fibre which was stripped of the plastic jacket regularly fractured inside the bend of the j-piece (80% of the fibres tested). Secondly, the hotplate did not provide an accurate means by which to heat the ionogel reservoir, potentially influencing the coating thickness and quality. Finally, the layout of the system meant that a maximum 45 mm of fibre could be coated. Although this would suffice for the majority of LPGs utilised, a greater length would improve the flexibility of the coating system.

Following the issues identified in the initial coating system, the apparatus was re-designed. The updated version of the coating system operated by feeding the optical fibre into the bottom of a heated aluminium block, and withdrawing it perpendicular through the ionogel reservoir, avoiding excessive bending of the optical fibre (Fig. 7.11). This reservoir again was designed such that only a minimal quantity

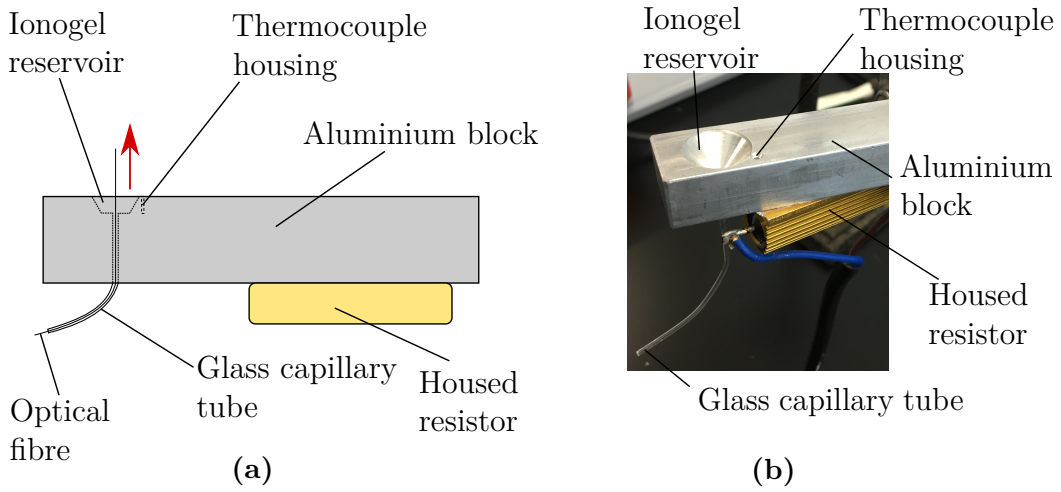

Figure 7.11: Diagram (a) and image (b) of the 2^{nd} prototype of the ionogel coating system. Arrow indicates withdrawal direction

of ionogel (∼1.5 ml) was required for coating. Additionally, the temperature control was improved through the use of a PID controller (Rex C100, Bermes) that operated a housed resistor. The feedback required for PID control was provided by a k-type thermocouple which was situated directly adjacent to the ionogel reservoir. Finally, the maximum coating distance was improved through integrating the coating apparatus with the dip-coater (ND-R, Nadetech), where this equipment replaced the translation stage as the mechanism controlling fibre withdrawal velocity.

Although the changes implemented to the system alleviated many of the issues encountered in the previous design, a number of new problems were identified following preliminary tests. These involved coating standard optical fibre (SMF-28) with a 40 mm portion of its plastic jacket removed to simulate an LPG inscribed

fibre. The ionogel temperature was nominally set to 80°C and a withdrawal speed of 30 mm·s^{-1} was used.

Firstly, the attachment of the glass capillary tube to the aluminium block was inherently weak. After a number of preliminary tests, the repeated force applied to tubing by the fibre being withdrawn through the apparatus caused fractures in the glass resulting in liquid ionogel leaking from the joint. More crucial however, was the irregular ionogel deposition noted following examination of the fibre (Fig. 7.12).

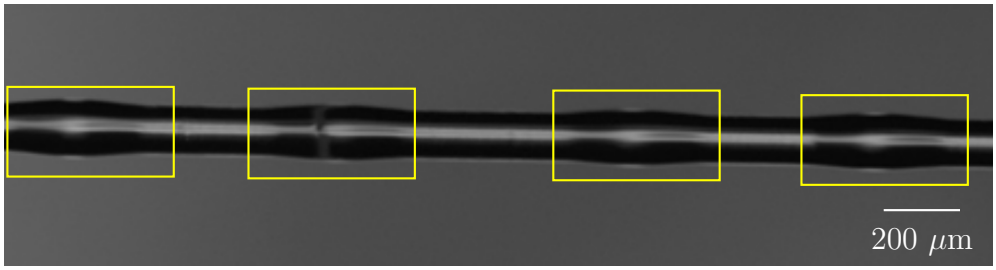

Figure 7.12: Light microscopy image of a ionogel coated optical fibre using the 2^{nd} coating system showing irregular features in the deposition (highlighted in yellow)

Closer inspection of the coating system during operation revealed that these deposition features are most likely produced by the glass capillary tube at the glass-aluminium interface. The adhesive used to attach the tube to the aluminium allows for slight movement (further enhanced by the fractures previously mentioned), such that once the optical fibre starts to be withdrawn through the system, the capillary tubing shifts slightly, absorbing the fibre's movement and reducing its speed, resulting in a change in the deposition parameters of this deposited coating thickness. Once the capillary tube had reached a certain point, it would recoil to its initial position, changing the deposition again. This action was repeated throughout the entire coating process causing the oscillatory deposition structures visible in Fig. 7.12.

Further refinements were implemented to the coating system to address the newly identified problems. Most importantly, the glass capillary tube was substituted for a stainless steel tube with a 500 μm lumen, which provided a non-fragile, stiffer structure in which to guide the optical fibre. Additionally, this tube also stopped the ionogel from flowing out of the reservoir. As the distal portion of the tube was of a lower temperature, the ionogel solidified, thus acting as a self-regulating plug that an optical fibre could pass through. In addition to the stainless steel tube, the large, single housed resistor was replaced by two smaller resistors which were positioned either side of the ionogel reservoir in order to reduce the heating-up time and to provide a more even heat distribution to the reservoir. The final version of

the coating system can be seen in Fig. 7.13. The system was able to maintain the ionogel reservoir temperature to ±0.5°C and, through use of the dip-coater, possessed withdrawal velocities ranging from 0.12 - 500 mm·min^{-1}. All ionogel coated fibres used in the remainder of this work were all produced using this coating system.

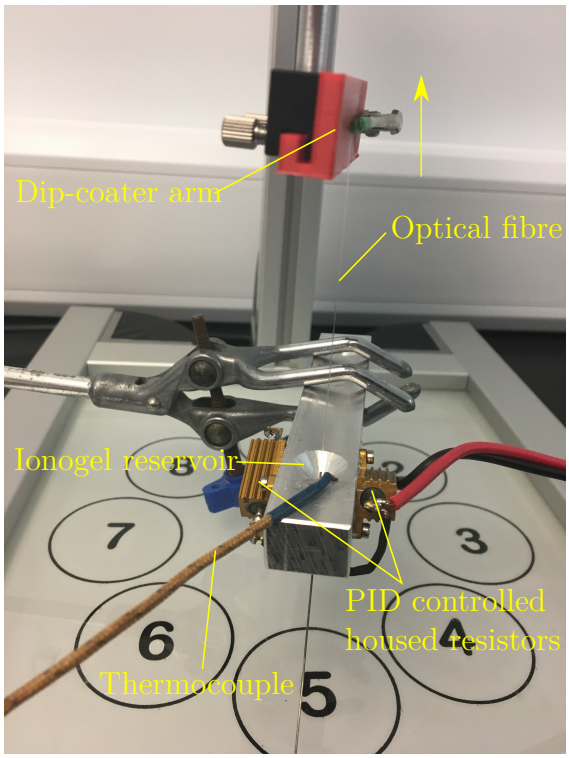

Figure 7.13: Image of the final coating system used to deposit ionogel. Arrows indicates direction of withdrawal

7.3.2 Ionogel surface characteristics

Visual inspection of the ionogel coating was performed in order to understand the surface morphology and to obtain an initial coating thickness measurement. Indeed, both of these coating parameters directly affect the sensitivity of an LPG sensor [32, 12]. Similar to the test fibres described in the previous section, lengths of PS750 fibre were coated with ionogel for environmental eSEM imaging.

Fibres were prepared for deposition by mechanically stripping 40 mm of the outer plastic jacket and cleaning the newly exposed cladding surface with an IPA saturated lens tissue in order to remove any dust or organic residue. A small piece of solid ionogel was placed inside the reservoir prior to the apparatus being heated to 80°C. This initial temperature was decided upon as it is higher than the ionogel's sol-gel transition temperature (74°C) and was found to ensure no gel re-solidified on the

liquid's surface. The fibre was subsequently fed through the stainless steel tube and attached to the dip-coater's arm which had been positioned to provide a coating distance of 50 mm. The ionogel was allowed to reach a temperature steady-state for 15 min.

Using a withdrawal speed of 30 mm·min^{-1} (which is centred within the range of speeds noted to produce a coating with minimal thickness in sol-gel dip-coating [33] (see Section 4.1.1)), the fibres were coated, and once finished, were removed carefully from the system ensuring that the fibre was not bent, which could damage the ionogel coating. Coated fibre samples for eSEM analysis were hand-cleaved in the centre of the ionogel coated section to allow both a thickness measurements (using the freshly produced fibre end-face) and surface images to be obtained.

Fig. 7.14 shows the surface of the ionogel coated fibre. A deposition can clearly be seen on the fibre's surface. However, the ionogel coating contains numerous small structures. Theses features may have been produced through surface contamination or potentially via the trapping of small air-bubbles below the coating.

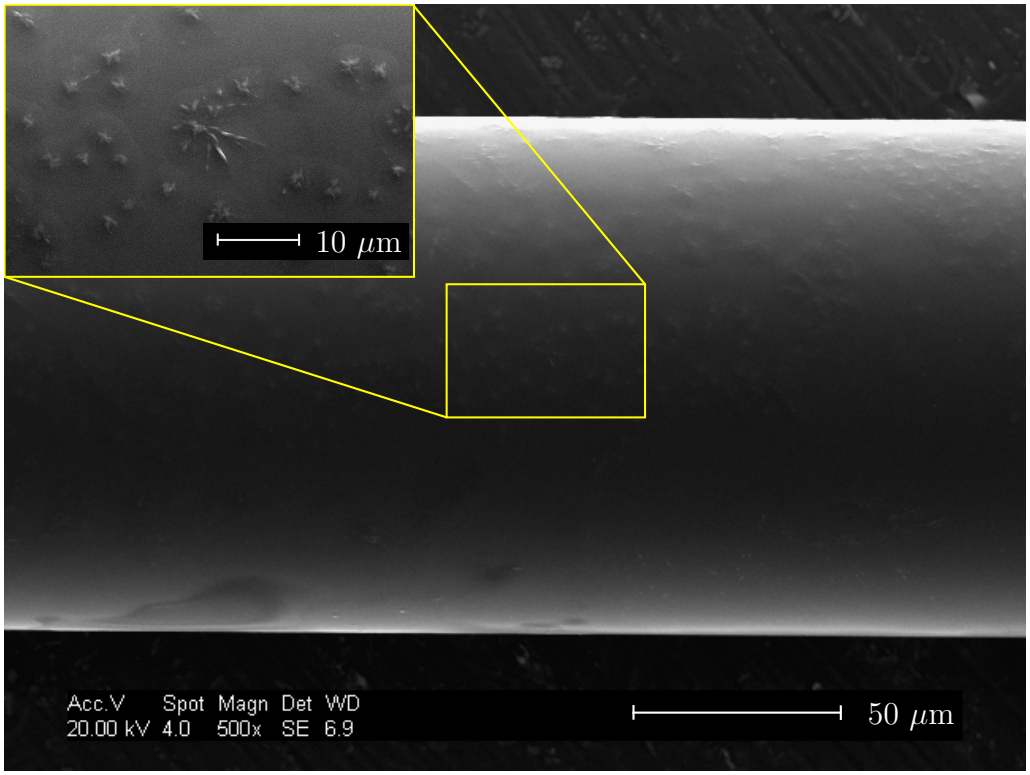

Figure 7.14: eSEM image of the ionogel coated fibre. Inset provides a more detailed view of the ionogel surface features

Inspection of Fig. 7.15 reveals that the ionogel coating possessed a thickness of ∼500 nm. This coating is relatively thick for a sensing layer for an optical fibre, where

typically coating thickness are in the region of 50 - 500 nm [34, 35, 1]. As discussed in Section 4.1.1, the speed with which the fibre is withdrawn from the coating solution effects the thickness of the deposition. The ionogel does not undergo evaporation, a factor that influences the deposition process of materials typically used in dip-coating [33], therefore withdrawal speed and ionogel viscosity are most likely the dominant players in determining the thickness of the ionogel coating.

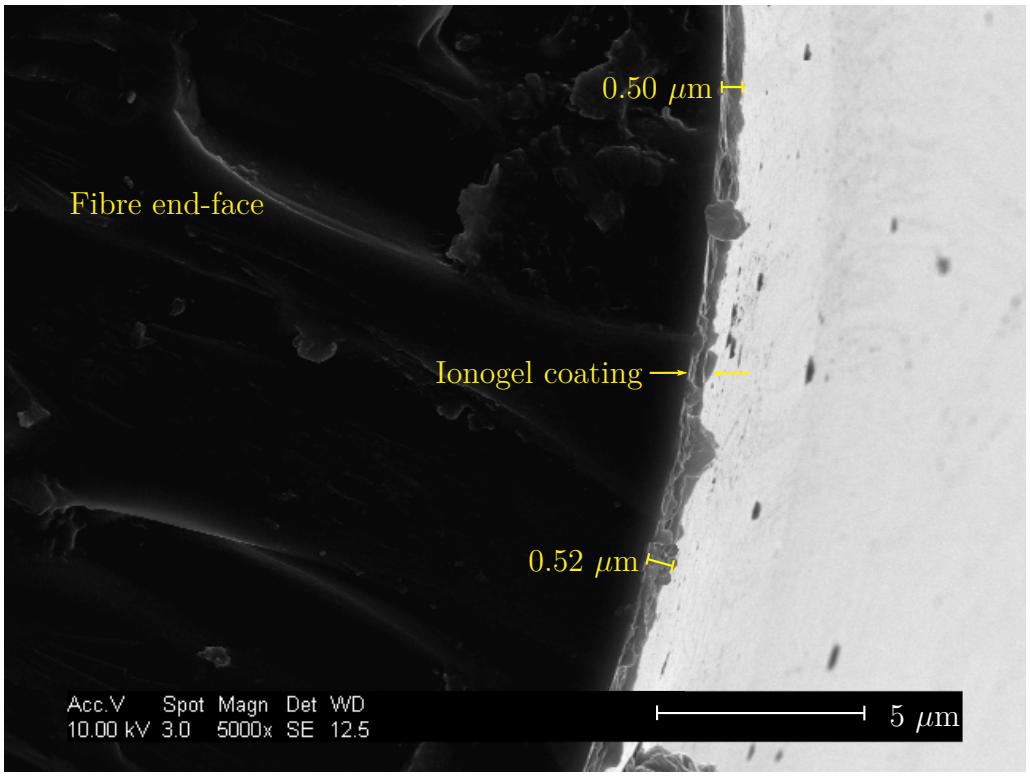

Figure 7.15: eSEM image of the ionogel coated fibre's end-face with coating thickness measurements defined

Fig. 7.14 and 7.15 shows a section of uniform ionogel coating. Nevertheless, inspection of another section of the coated fibre reveals that the deposition was inconsistent, with large portions of the cladding surface completely absent of the ionogel coating (Fig. 7.16). The contamination features ($\sim$40 μm in diameter) highlighted in Fig. 7.16 could potentially be caused by dust or pieces of solidified gel that are present on the surface of the ionogel in the reservoir when the fibre is withdrawn through the interface. Additionally, it can be seen from Fig. 7.16 that there are sections of the fibre with poorly deposited coating that appear to have contracted, forming a ridged surface. It is unclear whether these structures are caused via the rapid cooling of the ionogel coating or produced due to unsuitable fibre surface chemistry.

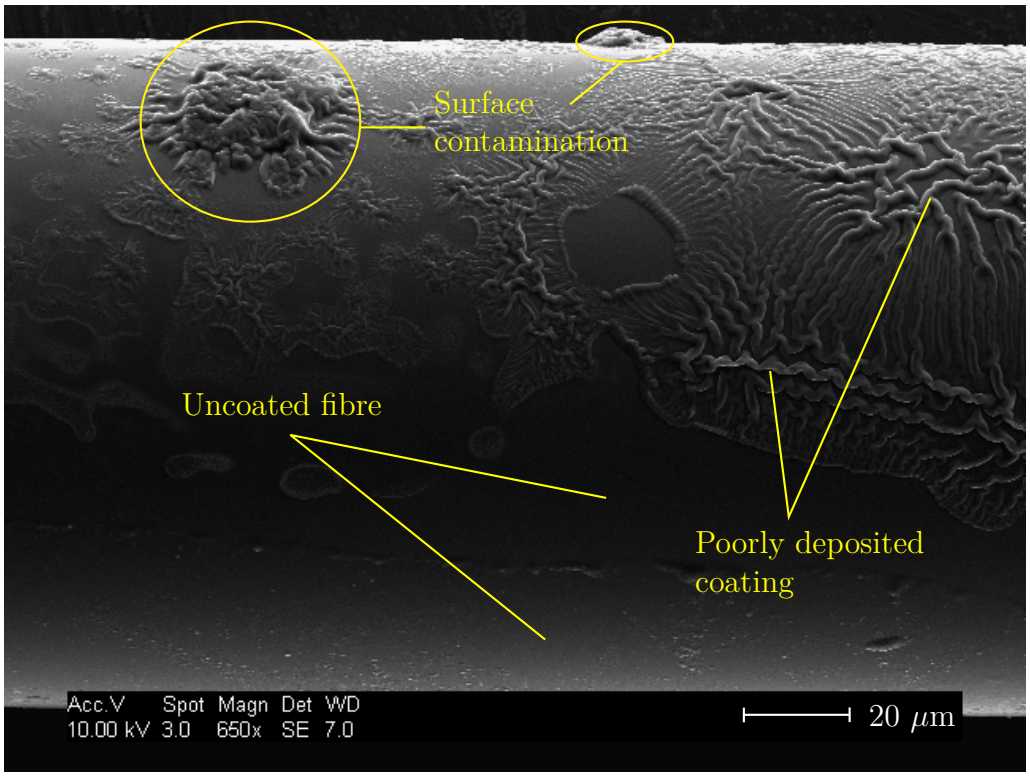

Figure 7.16: eSEM image of the ionogel coated fibre with various deposition issues identifying

7.4 Improving the ionogel coating

As mentioned in the previous section, the shrinking of the ionogel coating observed in Fig. 7.16 could be caused by the surface chemistry of the optical fibre. As the ionogel is hydrophobic in nature, poorly deposited features could be caused by the intermolecular forces of the ionogel and fibre surface repelling each other (analogous to standard oil-water interactions). Indeed, LB coatings of the saturated fatty acid ω-tricosenoic acid have been improved by treating the substrate with silane-based pre-treatment to form preliminary hydrophobic surface [36]. This form of surface treatment would minimise any repulsive inter-molecular forces between the ionogel and optical fibre, which are speculated to be partly responsible for the inhomogeneous deposition.

7.4.1 Silanisation

Silanisation is commonly employed to produce a hydrophobic glass surface [37, 38]. This is achieved by reacting silanisation agents such as (3-mercaptopropyl)triethoxysilane [37] or (3-Aminopropyl)trimethoxysilane (AMPS) [38] with activated glass (Fig. 7.17).

To confirm whether the pre-treatment procedure created a hydrophobic surface, glass slides were initially used instead of optical fibre to allow goniometric analysis to be performed. The glass surface must be cleaned thoroughly prior to any treatment to ensure reproducible silansiation results [37]. A number of glass cleaning methods have been reported in the literature, which combine various acids, bases, and solvents in order to remove surface contamination [37]. As the cleaning process will ultimately be applied to an optical fibre, which is inherently fragile, the cleaning method must not be overly aggressive and not weaken the fibre structure.

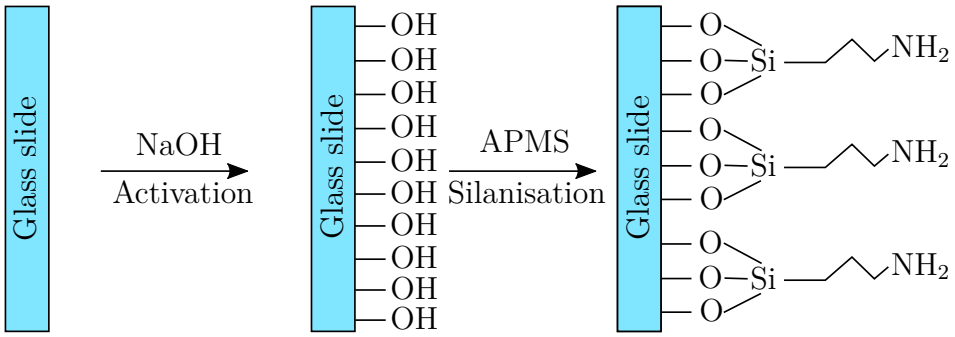

Figure 7.17: Process of silanating glass slides. Freshly cleaned glass is activated using NaOH to produce surface hydroxyl-groups, which react with AMPS to form the silanated glass slide

To assess whether the process would negatively affect the fibre structure, two successful cleaning methods outlined in [37] were tested on ten 50 mm lengths of plastic jacket-free PS750 optical fibre (5 for each method). These schemes included a 30 min incubation in either CH_3OH:HCl (1:1) solution (method 1) or piranha solution (H_2O_2:H_2SO_4; 1:2) (method 2). Following both schemes, the fibres were rinsed exhaustively with deionised water and allowed to fully air-dry. All reagents used to create the cleaning solutions were used in concentrated form and purchased from Sigma Aldrich.

It quickly became apparent that method 2 was unsuitable for cleaning optical fibres as 80% of the test pieces were found to be broken upon being withdrawn from the solution (in comparison to 0% witnessed in method 1). This level of damage would be unacceptable for processing LPGs, considering the fabrication time needed to produce a single grating (∼6 h). It was therefore decided that method 1 (CH_3OH:HCl) would be used to clean the glass slides in preparation for silanisation.

The protocol depicted in Fig. 7.17 was utilised to silanate glass slides (Blue Star) (which was adapted from [38]). Following the application of cleaning method 1, the slides were incubated in 1 M NaOH which was heated to 60°C. Upon reaching this temperature, the fibre was kept in the solution for a further 5 min. The glass slides

were removed from the NaOH and rinsed in 60°C deionised water to remove any excess base. Following a final wash with propanone, the slides were air dried in the fume hood and a solution of 2% (v/v) AMPS in anhydrous toluene (Sigma Aldrich) was produced. The AMPS solution was poured into a coplin jar containing the activated glass slides so that the silane completely covered the slides. The jar lid was replaced, sealed with parafilm (ensuring minimal solvent evaporation), and left to incubate for 24 h to ensure complete binding of the silane. Finally, the slides were rinsed with propanone and left to dry in the fume hood.

7.4.2 Contact angle assessment

To confirm that the silanisation protocol created a hydrophobic glass surface, the prepared slides were analysed by measuring the static contact angle between a sessile water droplet and the glass surface using optical tensiometery. This technique is often employed to evaluate a surface's wetting ability, where the contact angle is acquired by applying tangential lines along the liquid-gas and liquid-solid interfaces (Fig. 7.18) [39]. Small contact angles indicate that the test surface possesses high wettability (<90°) while the converse is true for larger angles (>90°). Super-hydrophobic surfaces demonstrate water contact angles in the region of 150° [39]. Although a number of other techniques are available to assess contact angles (Captive Bubble Method, Wilhelmy Balance Method), the simplicity and convenience provided by optical tensiometery makes it ideal for this experiment.

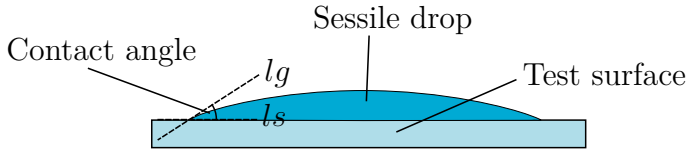

Figure 7.18: Illustration of contact angle assessment of a water sessile drop. As indicated by the small contact angle, the surface is displaying hydrophilic properties. *lg* and *ls* indicate liquid-gas and liquid-solid interfaces respectively

An optical tensiometer (Theta Lite, Attension) was used to measure the contact angle on 8 glass slides that had been silanated as described in Section 7.4.1. To provide a control comparison, 8 glass slides that had been cleaned using CH_3OH:HCl (see Section 7.4.1) but not silanated were also assessed. Typically, glass surfaces which are contaminate free are highly hydrophilic, thus possessing low water contact angles [40].

The slides were placed on the optical tensiometer's stage and a 2 μl deionised water

droplet was dispensed onto the glass surface via a micro-syringe pipette (Fig. 7.19). During this process, the camera recorded the formation of the drop (at 6 fps) as it was placed onto the glass slide over a 3 s period. For each frame, the optical tensiometer software automatically calculated a mean contact angle (by fitting the Young-Laplace equation around the drop) from angles obtained at the left and right side of the drop. The contact angle used for each drop was produced by averaging the final 6 mean values provided by the software. Every slide was tested with 6 drops and a mean contact angle calculated.

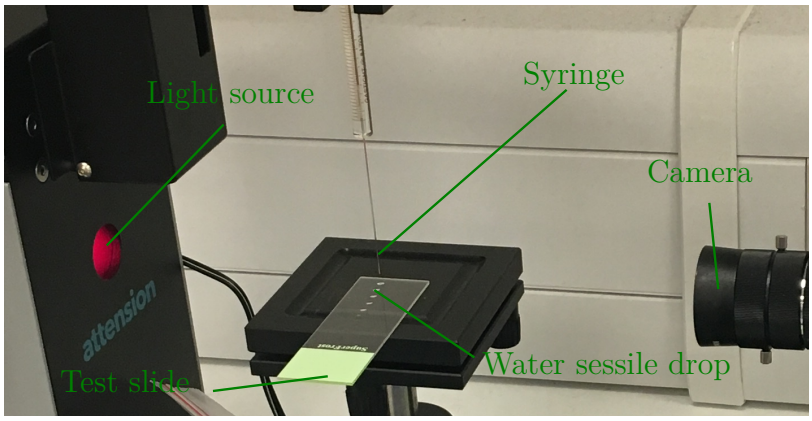

Figure 7.19: Image of the Optical Tensiometer setup. As the water sessile drop is placed onto the slide, the camera records the process for contact angle analysis to be conducted

The results from the contact angle analysis can be seen in Fig. 7.20. It is clear that all the glass slides that experienced silanation displayed greater contact angles than those that were just cleaned (control). This result is reflected in the inset of Fig. 7.20 where the average contact angle (±SD) for the silananted slides is 59.75±2.39° compared with 32.25±2.28° for the control slides. The difference in contact angle demonstrates that the surface of the silanated slides are more hydrophobic than the slides that only experienced the cleaning protocol. The average contact angle noted by the silanated slides is of a similar magnitude to previous literature [37], although the authors of this work used (3-mercaptopropyl)triethoxysilane as the silanating reagent.

However, comparing the mean contact angle of the control slides with contact angles noted in the paper from which the cleaning method was obtained [37], it can be seen that the angles observed here are significantly larger. This indicates that the glass surface is not as clean as the ones reported by Cras and colleagues [37]. One reason for this could be due the fact that the authors in [37] dried the samples with pure Nitrogen in a glove box whereas the glass slides reported here were left to dry in a fume hood, thus open to contamination from particles circulating in the laboratory

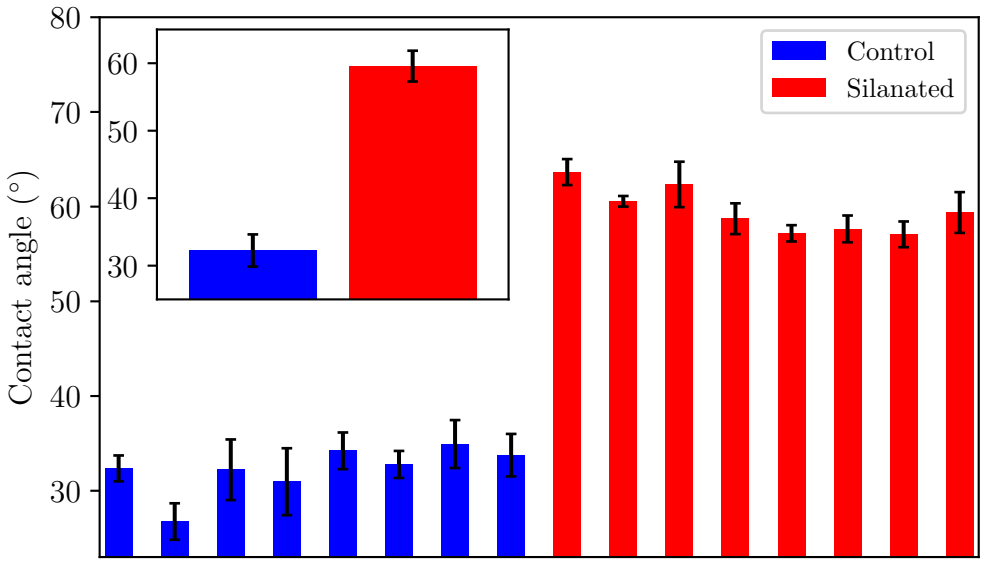

Figure 7.20: Comparison between mean contact angles for silanated (AMPS) and control (CH_3OH:HCl cleaned) treated glass slides. Inset shows the mean contact angle for all slides of a particular treatment. Error bars in both cases represent SD

air. Nevertheless, when comparing the mean contact angle of the control samples (32.25±2.28°) with the contact angle of a glass slide freshly withdrawn from a new box of slides (48.92±0.68°), the reduction in angle following cleaning would suggest that process did improve the cleanliness of the surface.

The results presented in Fig. 7.20 demonstrate that the silanation method not only fixed the AMPS onto the glass slides but also that this deposition presented hydrophobic tendencies. Since the silanation method was successful on glass slides, the next step was to confirm that this could be translated to optical fibres.

Utilising the same procedures as mentioned previously (see Section 7.4.1), optical fibres were cleaned and silanated. However, as optical tensiometry can not be performed on an optical fibre (physically too small), a qualitative colorimetric confirmation process was adopted. Since AMPS contains primary amine groups ($-NH_2$), it is possible to observe an orange colour change when these groups are exposed to 2,4,6-trinitrobenzene sulfonic acid (TNBSA). Therefore, using an adapted procedure outlined in [41] that uses TNBSA for amine detection, the silanated optical fibres were assessed for the presence of primary amine groups (and by extension the presence of silanation).

Once the silanated fibres had dried, a solution of 2% (v/v) TNBSA in deionised

water was then heated to 37°C. The fibres were incubated in the solution for 10 min. To ensure the colour change was induced by the AMPS deposition and not via the cleaning process, a control fibre which had been cleaned but not silanated was also incubated in the TNBSA solution to act as a control.

Qualitative confirmation that the silanation process described in Section 7.4.1 could be translated to optical fibres can be seen in Fig. 7.21, where the primary amines present on the AMPS-silanated fibre have reacted with the TNBSA to form the orange chromogenic product. This change was not observed on the control fibre which had only received the cleaning procedure. Variations in the depth of colour displayed by the AMPS-treated fibre would indicate that the silanation process was not consistent along the fibre. Nonetheless, the entire section of the fibre treated with AMPS did react with TNBSA showing that silanation occurred over the intended region. The TNBSA treated fibre was also wiped with a lens tissue saturated with IPA to qualitatively assess whether the silanated deposition could endure physical manipulation. Following 3 passes (up and down) with the lens tissue, the orange product was still visible thus suggesting that a silanated fibre could be coated with ionogel, have the deposition removed using IPA saturated lens tissue, and still possess a silanated surface in preparation for further coating.

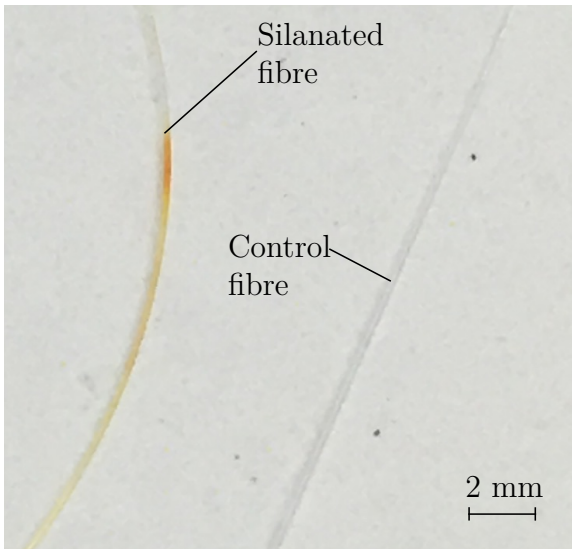

Figure 7.21: Qualitative confirmation of the presence of AMPS on optical fibres where the silanated fibre clearly shows an orange derivative which is not observable on the control fibre

It should be noted that contact angle of fibre-like structures can be inferred using the Wilhelmy Balance method [39], however this process requires the use of a sensitive tensiometer which was not available during this project. Nevertheless, the data portrayed in Fig. 7.20 along with the image depicted in Fig. 7.21 present substantial

evidence for the occurrence of silanation on optical fibres and that this deposition creates a hydrophobic surface.

7.4.3 Ionogel coating following fibre pretreatment

The results from the previous sections have shown that it is possible to silanate the surface of a silica optical fibre with AMPS and that a silica surface treated with this aminosilane presents hydrophobic properties. It was therefore necessary to utilise this pretreatment for ionogel coated fibres and determine whether an improvement in coating quality could be identified.

Short lengths of PS750 optical fibre had a 40 mm section of plastic jacket removed and the newly revealed surface was silanated using the procedure described in Section 7.4.1. The coating parameters (ionogel temperature and withdrawal speed) used in Section 7.3.2 were also adopted here to provide a fair comparison with the results outlined in that section. Again, similarly to the method adopted in Section 7.3.2, the coated fibres were hand-cleaved in the centre of the ionogel coating to allow thickness measurements and surface characteristics to be obtained by eSEM analysis.

An eSEM image of the fibre's surface is shown in Fig. 7.22. Pretreatment of the fibre with AMPS prior to coating has improved the ionogel surface. In comparison to Fig. 7.14, the coating is more homogeneous showing fewer surface features and abnormalities. The noted improvement is speculated to be caused by augmenting the ionogel's wetting ability, increasing the adhesive forces between the fibre's surface and ionogel. Although improved, the coating is not perfect, where there are still noticeable defects present on the ionogel's surface.

An inspection of Fig. 7.23 reveals that the coating thickness is of a similar magnitude to that seen prior to silanisation treatment (Fig. 7.15). This is expected as the silanisation fibre pretreatment would improve the coating's homogeneity but not effect its thickness.

7.4.4 Withdrawal speed effect on ionogel coating thickness

Since the silanisation pretreatment allowed a more reliable ionogel coating to be applied to an optical fibre, an investigation into the effect of withdrawal speed on coating thickness was undertaken. Typically, coating thickness is influenced by the substrate's withdrawal speed in a standard dip-coating procedure, where the material

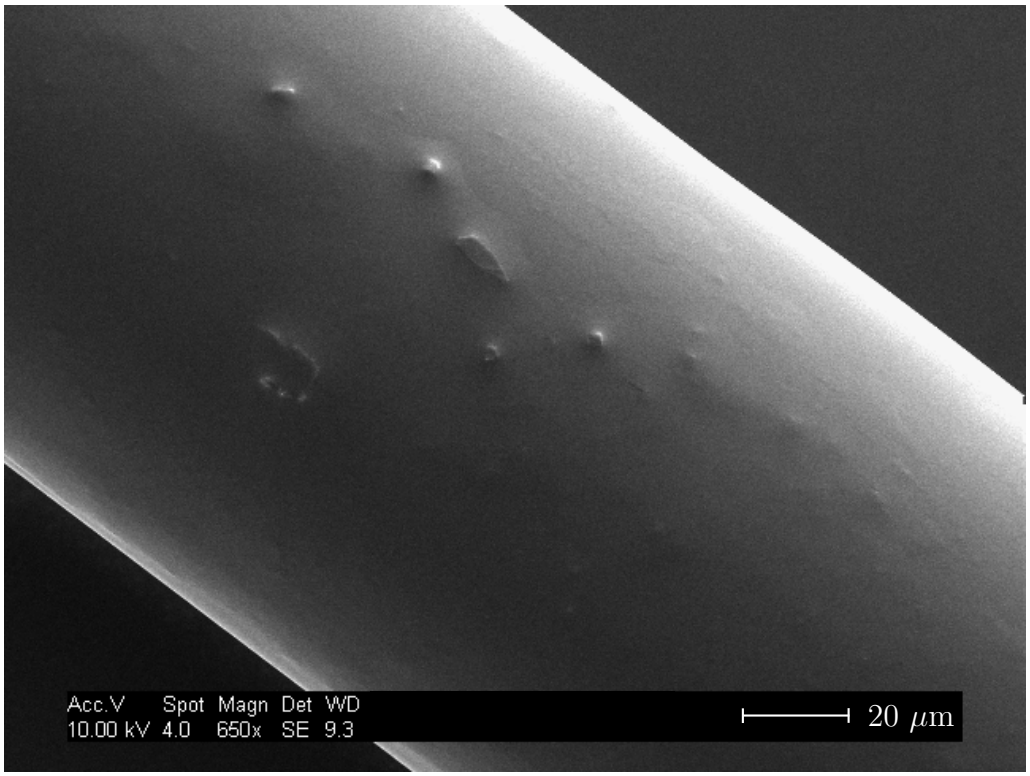

Figure 7.22: eSEM image of an ionogel coated fibre which had been pretreated with the silane AMPS

to be applied is dissolved in a solvent e.g. sol-gel (see Section 4.1.1). However, the process used here is slightly different. The ionogel is not dispersed in a solvent but maintained in liquid form via an elevated temperature. The ionogel solidifies once removed from the heat source. Although suspected, it is unclear whether the withdrawal speed of the optical fibre influences the coating thickness.

Since LPGs demonstrate a wavelength shift in response to variations in coating thickness [42, 11], it was decided that these in-fibre gratings would be used to asses the effect of withdrawal speed on ionogel coating thickness. A 40 mm long LPG of period 109.2 μm and a duty cycle of 50% was fabricated as outlined in Section 5.1 and silanated as previously described (Section 7.4.1). The LPG was interrogated with a LS-1 tungsten light source (Ocean Optics) and a CCD spectrometer with a resolution of 0.13 nm (HR4000, Ocean Optics). A new batch of 1.5% (w/w) LMOG ionogel was produced (transition temperature of 74°C) and placed into the ionogel reservoir where it was heated to 80°C. A baseline spectrum was obtained. The end of the fibre coupled to the light source was then removed and subsequently fed through the ionogel reservoir into the stainless steel tube before being attached to the dip-coater arm. Removing the light-source coupled fibre-end rather than the spectrometer fibre-end ensured that spectral artefacts (intensity change, skewed spectrum), observable

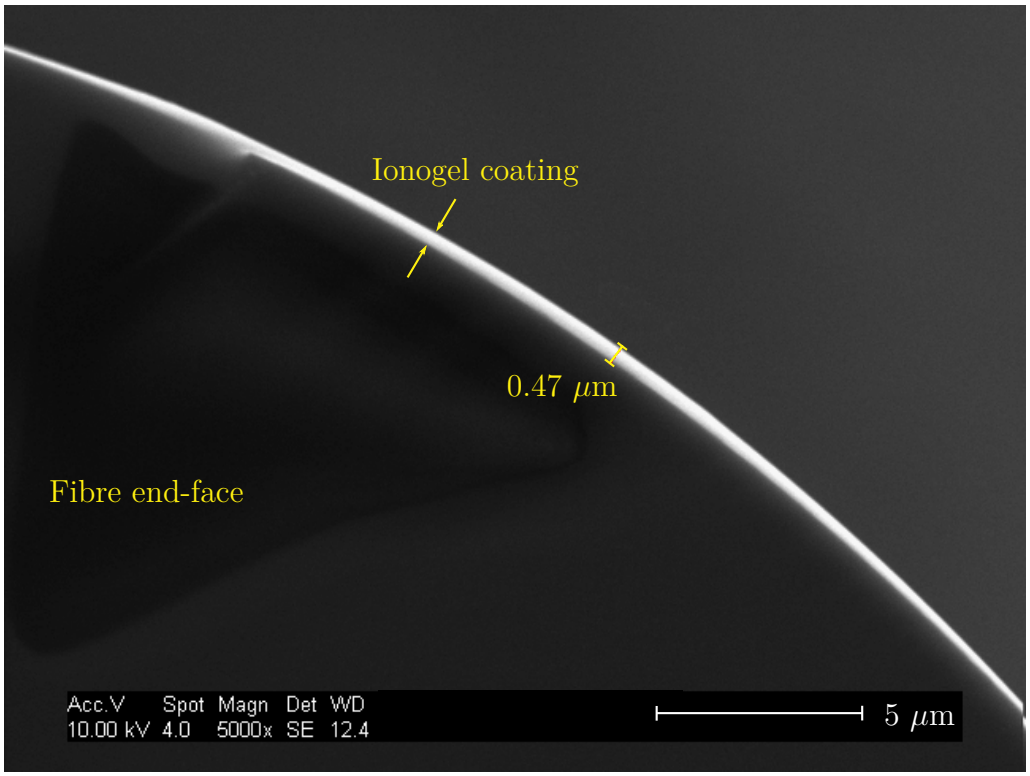

Figure 7.23: eSEM image of an ionogel coated fibre's end-face with coating thickness measurements defined

when re-coupling a fibre to a spectrometer, were kept to a minimum. The LPG was coated using withdrawal speeds of 18, 30, 100, 200, 300 mm·min^{-1}. After coating, the fibre was removed from the apparatus and attached to an aluminium frame to maintain tension across the grating. Prior to obtaining a spectrum, the fibre-end was re-cleaved before being coupled to the light source. Between each deposition, the ionogel coating was removed using IPA saturated lens tissue and the fibre was wiped until the transmission spectrum had returned to baseline indicating that the ionogel had been completely removed. Coating depositions at each withdrawal speed were repeated for a total of 3 times. The attenuation band central wavelengths were identified using SIR software [29].

The resonance band corresponding to LP_{19} was initially operating at the PMTP. Upon coating, the change in phase matching condition was such that dual resonance bands were formed. The left-hand (blue shifted) attenuation band was monitored for coating mediated wavelength changes. This response can be seen in Fig. 7.24. An increasing withdrawal speed produced a greater wavelength shift from the attenuation band. A larger shift implies that the thickness of the coating increased (on the assumption that the refractive index remains constant) [42] with faster withdrawal speeds. This result is in agreement with previous literature on dip-coating [43],

where the relationship between withdrawal speed and coating thickness takes the form of a parabola, with velocity values further from the vertex producing thicker coatings. It should be noted that the dependence of wavelength on coating thickness shows a non-linearity [42, 44], which is further compounded by operating near the PMTP. As a result, the data presented in Fig. 7.24 provides a qualitative view on the relationship between withdrawal speed and ionogel coating thickness.

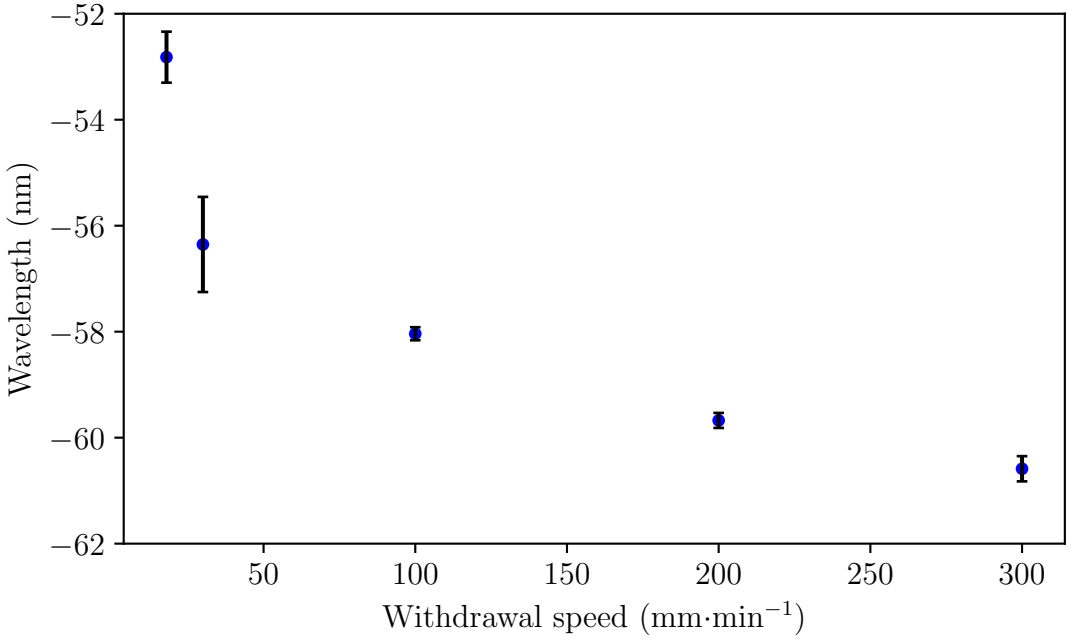

Figure 7.24: Wavelength response of attenuation band corresponding to LP_{19} to the deposition of an ionogel using different withdrawal speeds. Error bars represent SD

The coating thickness for standard sol-gel dip-coating can be estimated using Equation 4.1, which considers both draining and capillarity regimes (see Section 4.1.1). This expression is unsuitable for the ionogel coating described here since the gel does not experience evaporation, thus capillarity effects do not influence the deposition thickness. Eliminating the irrelevant terms and expanding D, the coating thickness can be estimated by [33],

$$h_0 = \frac{0.94\eta_g^{2/3}}{\gamma_g(\rho_g g)^{1/2}} u^{2/3}, \tag{7.1}$$

where η_g, γ_g, and ρ_g are viscosity, the surface tension and density of the ionogel, respectively, while g is gravitational acceleration. Equation 7.1 describes the draining regime only, indicating an inverse linear relationship between withdrawal speed and coating thickness. However, this description does not explain fully the non-linear correlation noted in Fig. 7.24. Nevertheless, Equation 7.1 does not take into account

the cooling effect of the ionogel as it is withdrawn from the reservoir. The gel's viscosity would change as it cools, most likely influencing the thickness of the ionogel coating. Therefore, further work is required to fully understand the mechanisms that govern the coating thickness and to adapt Equation 7.1 to take into account the solidification of the ionogel during the coating process.

7.5 Characterisation of LPG CO_2 ionogel sensor

Sections 7.2.1 and 7.4.3 have confirmed that the ionic liquid $[C_6mim][Tf_2N]$ absorbs CO_2 and that it is possible to coat an optical fibre with an ionogel of this ionic liquid. It is therefore necessary to establish whether an LPG coated with ionogel will be able to detect CO_2 and whether the response is reversible.

7.5.1 Ionogel CO_2 response

A 40 mm long LPG of period 113.5 μm with a 50% duty cycle was fabricated as described in Section 5.1. This period was selected to ensure the grating was operating past the PMTP of LP_{19}, such that, once coated, the LPG would display dual resonance band corresponding to this cladding mode. The LPG was silanated as described in Section 7.4.1 and coated with ionogel using a withdrawal speed of 30 mm·min^{-1}. The coating was assessed under a light microscope before progressing further in order to confirm deposition. Using the same experimental layout depicted in Fig. 7.6, but with the addition of the humidity generator as described in Section 7.1.2, the ionogel coated LPG was inserted into the modified gas cell along with a data logger (i-button, Maxim Integrated) to monitor temperature and humidity at an acquisition interval of 20 s. Throughout the experiment the coated LPG was interrogated using a broadband light source (LS-1, Ocean Optics) and a CCD spectrometer (HR4000, Ocean Optics) with a resolution of 0.13 nm. The humidity generator was set to produce a flow rate of 400 cc·min^{-1} with 50% RH and 20°C. The modified gas cell was flushed with SA for 25 min to ensure a consistent temperature and humidity. Following the preliminary cell preparation, the SA was turned off and the LPG was exposed to 20% CO_2 for 25 min. The attenuation band's central wavelength was tracked using SIR software [29] and associated data was processed with a moving average function (window size of 10).

The response of the ionogel coated LPG to 20% CO_2 is presented in Fig. 7.25. The attenuation band displayed an 8.3 nm wavelength shift which took approximately 90

s to occur. In comparison to previous literature, the wavelength shift noted here is far greater than that reported by Melo *et al.* [2] who observed a 0.134 nm shift to 100% CO_2 using an LPG with a passive coating (polystyrene) operating at the mode transition region. However, Hromadka *et al.* [45] demonstrated a MOF (HKUST-1) coated LPG which showed a 10.58 nm shift in response to 4% CO_2 showing a larger wavelength change to a lower CO_2 concentration than the response presented in Fig. 7.25. Although it is not possible to definitively compare the response time of the ionogel coated LPG described here with the aforementioned literature, as this datum was not explicitly disclosed in the articles, estimations based on graph interpretations show that all 3 devices have response times between 1-2 min.

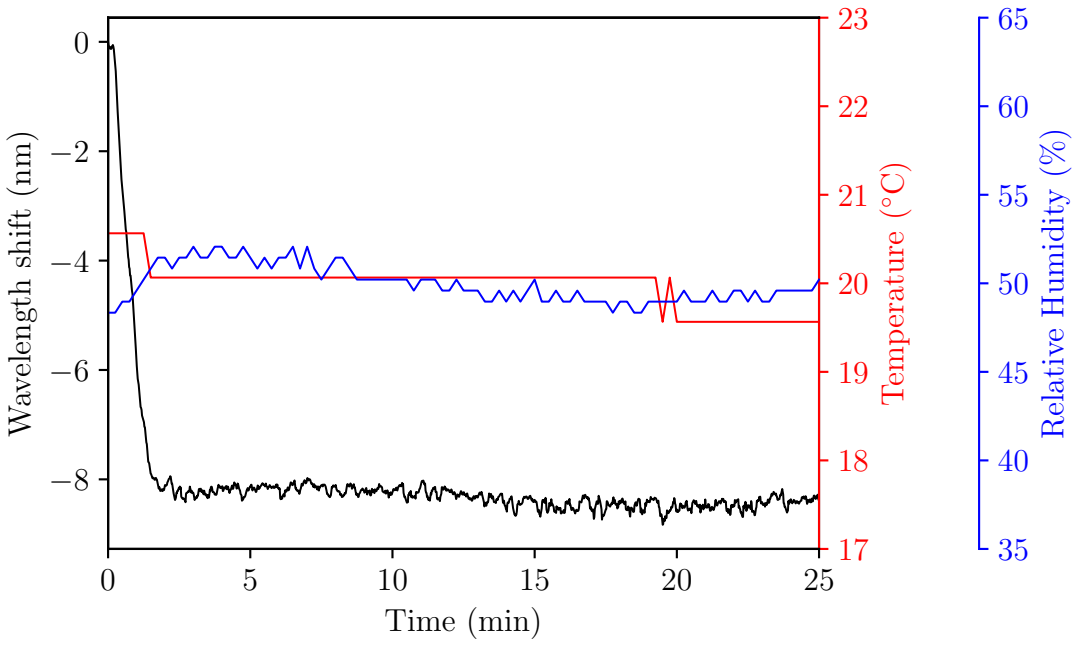

Figure 7.25: Wavelength response of attenuation band corresponding to LP_{19} from an LPG coated with $[C_6mim][Tf_2N]$ ionogel when exposed to 20% CO_2. Temperature and relative humidity are also shown in order to provide a clear comparison. Lines are associated with their y-axis based on like colours

To ensure this change was CO_2 mediated and not due to an external parameter, relative humidity and temperature were plotted in conjunction with the wavelength shift to identify if any correlation existed between these measurands (Fig. 7.25). A small change in both temperature (0.5°C) and relative humidity (∼3%) can be noted at a similar time to the 8.3 nm wavelength shift. However, if the observed response was due to either of these external parameters, the attenuation band would be expected to alter dramatically throughout the 25 min exposure as both temperature and relative humidity fluctuated during this time period.

The negative wavelength shift presented by the left-hand attenuation band associated with LP_{19} would indicate that there was an increase in coating refractive index. This change in response to CO_2 contradicts the data displayed in Section 7.2.1, where the ionic liquid produced a positive wavelength shift (thus a decrease in refractive index) from the left-hand attenuation band corresponding to the same cladding mode following exposure to CO_2. While the ionic liquid most likely increased in volume, thus producing the noted decrease in refractive index, a similar mechanism would not be possible in the ionogel since it possesses a rigid structure. Therefore rather than increasing in volume, it is speculated that the CO_2 molecules are absorbed within the ionogel causing an increase in density, thus producing the detectable positive change in refractive index.

Another aspect of the attenuation band's response which is apparent in Fig. 7.25 is the small fluctuations following the initial large shift. The perturbations equate to 0.3 nm changes centred around -8.3 nm. These changes are greater than the spectrometers resolution (0.13 nm) and are produced by noise in the spectrum. The resonance band monitored during this experiment presented adequate attenuation prior to ionogel coating (20% transmission difference in comparison to pre-fabrication values). However, following silanisation and ionogel deposition, the resonance feature's attenuation diminished dramatically (to 4%) compromising feature tracking. Although the initial wavelength shift to 20% CO_2 was large in comparison to the spectral noise, the presence of this would severely diminish the sensor's LoD.

To assess whether the ionogel coated LPG would demonstrate a repeatable response to subsequent CO_2 exposures, the experiment was extended so that the device was subjected to 25 min cycles of SA and CO_2. Similar to the data displayed in Fig. 7.25, the wavelength response of the attenuation band during the repeatability experiment was plotted alongside temperature and relative humidity (Fig. 7.26).

Fig. 7.26 shows that the attenuation band experienced an $\sim$8 nm wavelength shift when exposed to CO_2, however, when the LPG was subjected to SA, the wavelength shift produced by CO_2 was reversed, returning the attenuation band to its initial wavelength. This behaviour is produced by the fact that the CO_2 molecules are physically absorbed by the ionogel rather than being chemically bound (see Section 4.2.5), thus the absorption requires less energy to reverse the interaction. In this case, the decrease in partial pressure of CO_2 causes the ionogel coating to degas.

The response time of the ionogel coated LPG was of a similar magnitude to that observed in the previous experiment (90 s), where both CO_2 cycles elicited this response time. It is speculated that the response time of the device is highly dependent

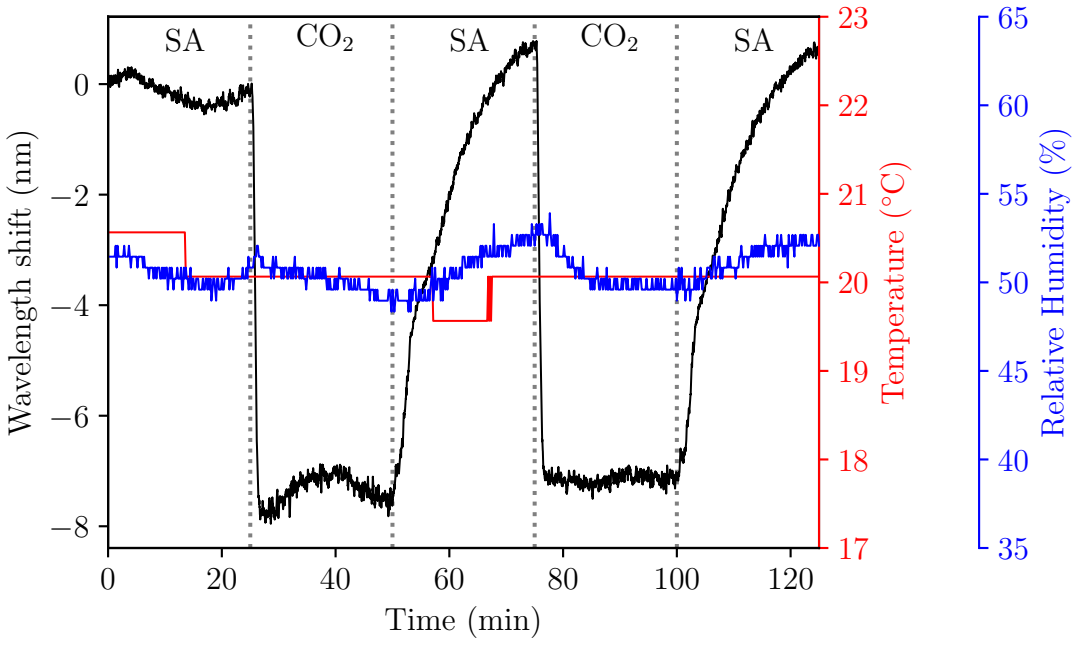

Figure 7.26: Wavelength response of attenuation band corresponding to LP_{19} from an LPG coated with $[C_6mim][Tf_2N]$ ionogel when exposed to 25 min cycles of SA and 20% CO_2. Temperature and relative humidity are also shown in order to provide a clear comparison. Lines are associated with their y-axis based on like colours

on the ability of the ionogel coating to allow the CO_2 molecules to permeate through the gel structure, where potentially a thinner coating may improve the response time. Nevertheless, the modified gas cell may also have influenced the response time witnessed here. Since the gas cell possesses an internal volume of 113 ml, it would take approximately 30 s for the 20% CO_2 to fully replace the SA inside the cell (based on a flow rate of 200 ml·min^{-1}). Since the LPG was suspended in the centre of the gas cell, the grating may not have been immediately exposed to CO_2 upon flow initiation, therefore the 90 s response time observed for the ionogel coated LPG may include a portion of the 30 s required to the fill the volume of the cell with CO_2. Interestingly, the ionogel coating required 25 min to fully degas and return to baseline values. Within the first 10 min of SA exposure, the attenuation band had shifted by 75% of the change seen in CO_2 (50 - 60 min in Fig. 7.26). However, the final 25% required 15 min before the attenaution band returned to its starting wavelength.

Similar to the results witnessed in Fig. 7.25, temperature and relative humidity do not appear to contribute significantly to the wavelength shift noted as both of these measurands fluctuated throughout the experiment.

7.5.2 Ionogel humidity response

Although $[C_6mim][Tf_2N]$ is hydrophobic, this material will still display some form of interaction with humidity, which may lead to a detectable response from the LPG. Consequently, the effect of humidity variation on the ionogel coated LPG was assessed.

Using the same ionogel coated fibre and experimental setup as described in the previous section (Section 7.5.1), the LPG was exposed to a 400 cc·min^{-1} flow of SA that cycled from 40% - 60% - 40% relative humidity in 25 min intervals. It took approximately 60 s for the humidity to stabilise at each level. A data logger was used to confirm the relative humidity change and monitor the internal temperature of the modified gas cell throughout the experimental procedure. The wavelength response of the same resonance feature monitored previously was once more tracked.

The results are presented in Fig. 7.27. A 5.5 nm wavelength shift (with a sensitivity of 0.275 nm·%$^{-1}$) was noted following a change in relative humidity from 40% to 60% which was confirmed by the data logger. Once the relative humidity returned to 40%, the resonance band responded accordingly, shifting back to the initial wavelength. Furthermore, the ionogel coated LPG required only ∼1 min to reach a steady wavelength, which considering the humidity generator required 1 min to change from 40% to 60%, would indicate that the ionogel coated LPG responded immediately to the changing humidity. This response was far quicker than observed by the data logger, which needed ∼5 min to establish the humidity change. The disparity between the response times of the two devices is most likely caused by the slower sampling rate of the data logger (20 s in comparison to 0.5 s of the LPG) and its location at the bottom of the gas cell in comparison to the LPG which was positioned in the centre.

The observed wavelength shift in response to a 20% relative humidity change is unexpected considering the hydrophobic nature of $[C_6mim][Tf_2N]$. However, even hydrophobic ionic liquids, such as $[Bmim][Tf_2N]$, have been shown to absorb atmospheric moisture, despite these molten salts possessing anion-cation pairs that promote a hydrophobic surface [46]. Although the structure of $[C_6mim][Tf_2N]$ reduces surface adsorption, water can favourably diffuse through the liquid regardless of the poor water interaction witnessed by the anion $[Tf_2N]^-$ [46]. This lack of hydrophilic attraction displayed by $[Tf_2N]^-$ is speculated to cause small water aggregates to form inside the ionic liquid which further promote the self-diffusion of water, exacerbating the issue [47].

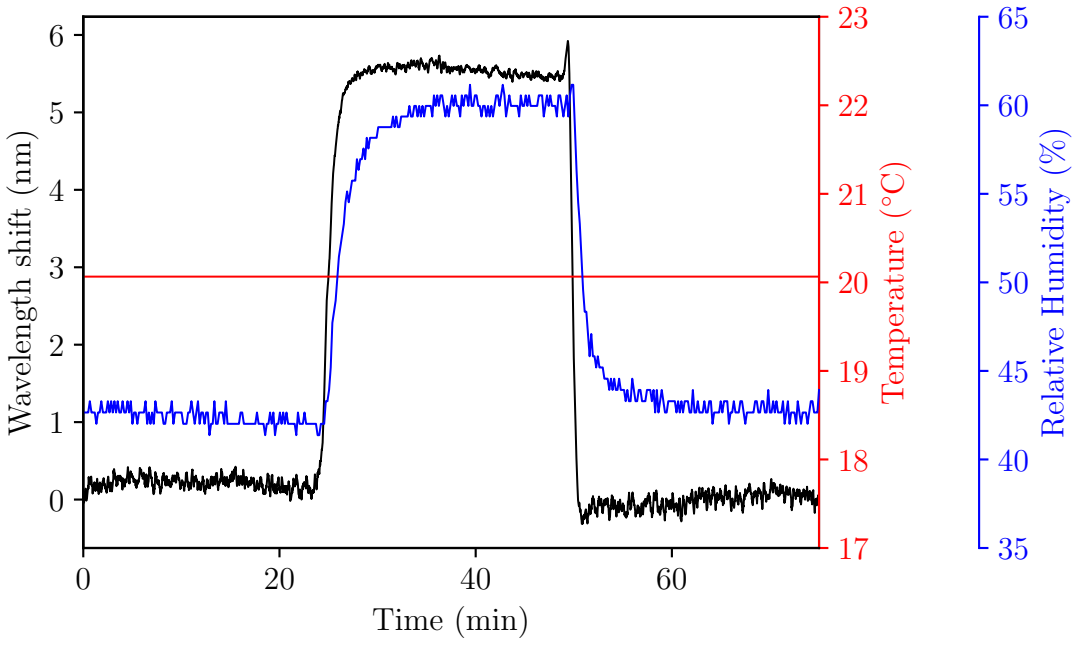

Figure 7.27: Wavelength response of attenuation band corresponding to LP_{19} from an LPG coated with $[C_6mim][Tf_2N]$ ionogel when humidity is changed from 40% - 60% - 40%. Relative humidity changes were monitored by the data logger and are also shown. Lines are associated with their y-axis based on like colours

Another important feature that is observable in Fig. 7.27 is the positive wavelength shift noted in response to increasing humidity. A red-shift in this case indicates that the surrounding refractive index of the LPG decreased. This reduction in refractive index is surprising, since, if the ionogel absorbed the atmospheric water the density of the gel would increase, thus a response similar to the one depicted in Fig. 7.25 (following absorption of CO_2) would be expected. Nevertheless, it could be speculated that the water molecules that diffuse through the ionogel coating are able to condense on the surface of the LPG. As the refractive index of water (1.333) is less than that of the ionogel (1.436), the LPG would therefore respond with a positive wavelength shift. Additionally, the role of the LMOG fibrous structure in which $[C_6mim][Tf_2N]$ is contained within the porous assembly may also influence the absorption of water. Previous studies examining oil composite 12-hydroxystearic acid gels have shown that water causes the gel structure to swell [48]. If the LMOG-based gel did increase in volume, a reduction in refractive index would be expected. However, all of these suggested mechanism require further examination to confirm their role in the humidity mediated wavelength shift.

7.5.3 Ionogel temperature response

To establish whether the ionogel deposition enhances an LPG's sensitivity to temperature, a coated and a non-coated LPG were subjected to a temperature increase. Typically, an LPG in standard telecommunications optical fibre has a temperature sensitivity in the range of 0.03 - 0.10 nm·°C^{-1} and up to 2.75 nm·°C^{-1} in photosensitive B-Ge codoped fibre [49]. However, the ionogel deposition is susceptible to a phase change near its sol-gel transition temperature and it is unclear whether there is a gradual change in gel structure that starts to occur far below this point which could influence the LPG's response.

A 40 mm long LPG was fabricated with a period and duty cycle of 113.8 μm and 50%, respectively, using the method described in Section 5.1. Following the silanisation protocol of Section 7.4.1, the LPG was coated with ionogel using a withdrawal speed of 30 mm·min^{-1} at a temperature of 80°C. A separate LPG was fabricated with the same length and duty cycle as the coated grating but with a period of 113.1 μm. The difference in periodicity was required in order to ensure that both the ionogel coated and non-coated LPGs coupled to the same cladding modes with associated attenuation bands operating at similar wavelengths. This guaranteed that they would both possess near-identical inherent sensitivities, an that any significant wavelength shifts could be confidently attributed to the addition of the ionogel coating.

Utilising a similar experimental arrangement as outlined in Fig. 6.2.1, the LPGs were placed inside the oven and their temperature sensitivities characterised in the range of 25 - 45°C in increments of 5°C, where each temperature was maintained for 30 min. This range of temperatures were selected as they are significantly below the sol-gel transition temperature (74°C). The gratings were interrogated throughout with a broadband source (LS-1, Ocean Optics) and a CCD spectrometer (HR4000, Ocean Optics) where the former was allowed to stabilise for 40 min. Each fibre was assessed three times and the attenuation band associated with LP_{19} was tracked using SIR software [29].

The wavelength response to variations in temperature for the ionogel coated and non-coated LPGs can be seen in Fig. 7.28. Temperature sensitivities of -0.93±0.07 nm·°C^{-1} and -1.03±0.04 nm·°C^{-1} were witnessed in the ionogel coated and non-coated LPGs, respectively. The similar sensitivities displayed by both LPGs indicates that the ionogel coating does not significantly influence the temperature response of the LPG. This demonstrates that the ionogel coating is physically stable up to at least 45°C, since any phase change would result in a slight alteration in the coating's refractive index, changing the effective index of the cladding inducing a resonance

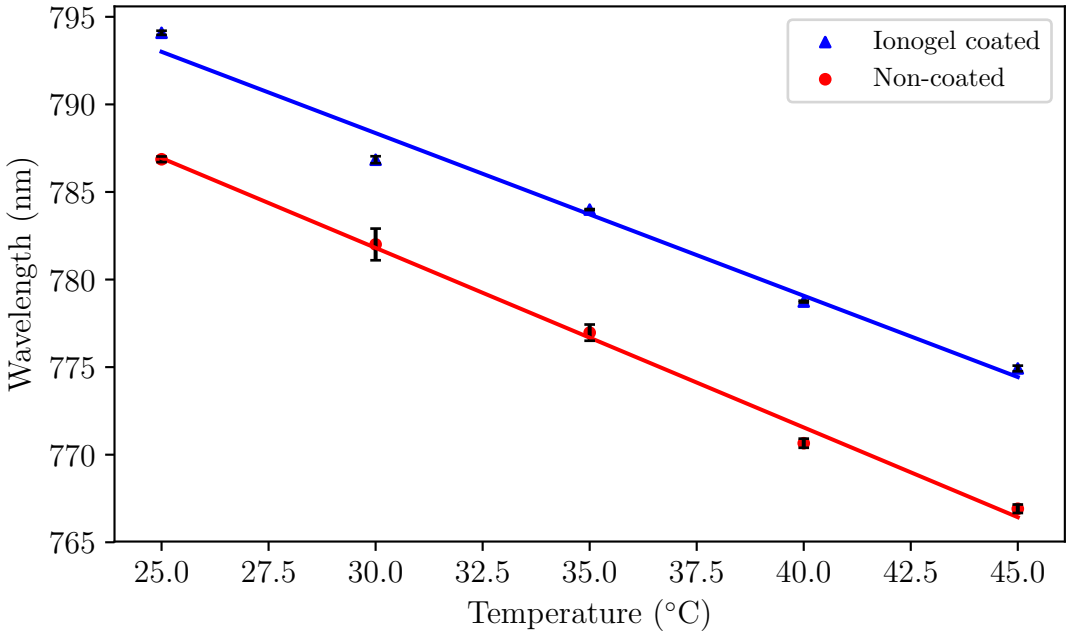

Figure 7.28: Wavelength response of attenuation band corresponding to LP_{19} for a non-coated and $[C_6mim][Tf_2N]$ ionogel coated LPG to a temperature change from 25 - 45°C. Method least squares used to calculate linear fit. Error bars represent SD

wavelength shift.

7.5.4 Silanisation CO_2 response

Since the pre-treatment material, AMPS, possesses structural amine groups, which demonstrate an affinity for CO_2 (see Section 4.2.1), it is important to confirm whether the CO_2 response witnessed in Section 7.5.1 was induced by the ionogel coating and not created via a silane mediated change. Therefore, the experimental procedure reported in Section 7.5.1 was repeated for a 40 mm long LPG with a period of 113.7 μm and a 50% duty cycle that had only received the silanisation process described in Section 7.4.1.

It is clear from Fig. 7.29 that an LPG treated with AMPS demonstrates no wavelength response when exposed to 20% CO_2. The minimal wavelength shift detected is below the resolution of the spectrometer (0.13 nm), thus indicating that the CO_2 mediated wavelength shift observed in Section 7.5.1 was produced by the ionogel coating rather than the AMPS pre-treatment process.

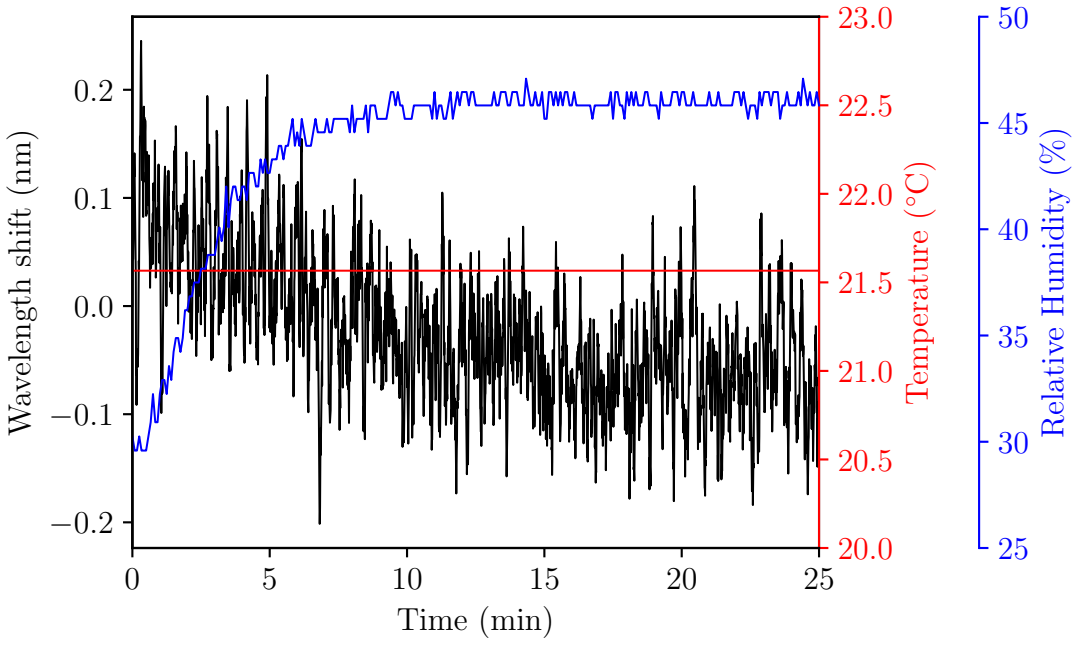

Figure 7.29: Wavelength response of attenuation band corresponding to LP_{19} from an LPG coated with AMPS when exposed to 20% CO_2. Temperature and relative humidity are also shown in order to provide a clear comparison. Lines are associated with their y-axis based on like colours

7.6 Summary and conclusion

The use of a composite PEI/SiO_2 deposition to create a CO_2 sensitive LPG coating was evaluated and found to be unsuitable due to its high humidity sensitivity. This led to subsequent investigations into the suitability of the ionic liquid $[C_6mim][Tf_2N]$ as a potential CO_2 sensitive LPG coating. It was found that exposure to gaseous CO_2 induced a refractive index change within 1 min that was detectable by an LPG. The ionic liquid was solidified into a gel using 12-hydroxystearic acid and a coating system was developed to allow the application of this ionogel to the surface of optical fibres. Following the analysis of eSEM images, the ionogel coated fibres presented inconsistent deposition and surface contamination. To alleviate these issues, the optical fibre was thoroughly cleaned and its surface silanated prior to coating. A preliminary investigation into the effect of fibre withdrawal speed on ionogel coating thickness was also conducted and it was found that coating thickness was inversely related to withdrawal speed. However, further work is required to establish a withdrawal speed that produces an ionogel coating with a minimal thickness. Finally, an ionogel coated LPG with a thickness of 500 nm demonstrated an 8.3±0.13 nm wavelength shift in response to 20% CO_2 which could be regenerated via a change in CO_2 partial pressure. The coated LPG did not show an enhanced temperature

response, however, a 5±0.13 nm wavelength shift was noted following a 20% change in relative humidity.

7.7 References

[1] J. Hromadka, B. Tokay, R. Correia, S. P. Morgan, and S. Korposh. Carbon dioxide measurements using long period grating optical fibre sensor coated with metal organic framework HKUST-1. *Sensors and Actuators B: Chemical*, 255(1):2483–2494, 2018.

[2] L. Melo, G. Burton, B. Davies, D. Risk, and P. Wild. Highly sensitive coated long period grating sensor for CO2 detection at atmospheric pressure. *Sensors and Actuators B: Chemical*, 202(1):294–300, 2014.

[3] A. Star, T.-R. Han, V. Joshi, J.-C. Gabriel, and G. Grüner. Nanoelectronic carbon dioxide sensors. *Advanced Materials*, 16(22):2049–2052, 2004.

[4] O. Kuzmych, B. L. Allen, and A. Star. Carbon nanotube sensors for exhaled breath components. *Nanotechnology*, 18(37):375502, 2007.

[5] S. S. Sabri, J. Guillemette, A. Guermoune, M. Siaj, and T. Szkopek. Enhancing gas induced charge doping in graphene field effect transistors by non-covalent functionalization with polyethyleneimine. *Applied Physics Letters*, 100(11):1–3, 2012.

[6] X. Xu, C. Song, J. M. Andresen, B. G. Miller, and A. W. Scaroni. Preparation and characterization of novel CO2 'molecular basket' adsorbents based on polymer-modified mesoporous molecular sieve MCM-41. *Microporous and Mesoporous Materials*, 62(1-2):29–45, 2003.

[7] Y. Lin, H. Lin, H. Wang, Y. Suo, B. Li, C. Kong, and L. Chen. Enhanced selective CO2 adsorption on polyamine/MIL-101 (Cr) composites. *Journal of Materials Chemistry A*, 2(35):14658–14665, 2014.

[8] S. Choi, J. H. Drese, and C. W. Jones. Adsorbent materials for carbon dioxide capture from large anthropogenic point sources. *ChemSusChem*, 2(9):796–854, 2009.

[9] Y. Lvov, K. Ariga, M. Onda, I. Ichinose, and T. Kunitake. Alternate assembly of ordered multilayers of SiO2 and other nanoparticles and polyions. *Langmuir*, 13(23):6195–6203, 1997.

[10] Z. Wang, F. Guo, C. Chen, L. Shi, S. Yuan, L. Sun, and J. Zhu. Self-assembly of PEI/SiO2 on polyethylene separators for Li-ion batteries with enhanced rate capability. *ACS Applied Materials and Interfaces*, 7(5):3314–3322, 2015.

[11] S. Korposh, S. W. James, S.-W. Lee, S. Topliss, S. C. Cheung, W. J. Batty, and R. P. Tatam. Fiber optic long period grating sensors with a nanoassembled mesoporous film of SiO2 nanoparticles. *Optics Express*, 18(12):13227–13238, 2010.

[12] S. Korposh, R. Selyanchyn, W. Yasukochi, S.-W. Lee, S. W. James, and R. P. Tatam. Optical fibre long period grating with a nanoporous coating formed from silica nanoparticles for ammonia sensing in water. *Materials Chemistry and Physics*, 133(2-3):784–792, 2012.

[13] N. D. Rees, S. W. James, R. P. Tatam, and G. J. Ashwell. Optical fiber long-period gratings with Langmuir–Blodgett thin-film overlays. *Optics Letters*, 27(9):686–688, 2002.

[14] S. W. James, I. Ishaq, G. J. Ashwell, and R. P. Tatam. Cascaded long-period gratings with nanostructured coatings. *Optics Letters*, 30(17):2197–2199, 2005.

[15] R. A. Zakaria. *NDIR instrumentation design for CO2 gas sensing*. Ph.D. thesis, Cranfield University, 2010.

[16] M. Partridge, S. W. James, and R. P. Tatam. Dissolved oxygen sensing using an optical fiber long period grating coated with hemoglobin. *Journal of Lightwave Technology*, 34(19):4506–4510, 2016.

[17] D. Viegas, J. Goicoechea, J. Corres, J. Santos, L. Ferreira, F. Araújo, and I. Matias. Humidity sensor based on a long-period fiber grating coated with a SiO2-nanosphere film. In *19th International Conference on Optical Fibre Sensors*, vol. 7004, p. 70044O. International Society for Optics and Photonics, 2008.

[18] J. W. Payne and B. F. Dodge. Rate of absorption of carbon dioxide in water and in alkaline media. *Industrial and Engineering Chemistry*, 24(6):630–637, 1932.

[19] S. Korposh, R. Wong, W. James, S, and P. Tatam, R. Temperature and thermo-optic coefficient measurements using optical fibre long period gratings operating at phase matching turning point. In *Fifth European Workshop on Optical Fibre Sensors*, vol. 8794, pp. 87942N–1–87942N–4. International Society for Optics and Photonics, 2013.

[20] J. Hromadka, S. Korposh, M. C. Partridge, S. W. James, F. Davis, D. Crump, and R. P. Tatam. Multi-parameter measurements using optical fibre long period

gratings for indoor air quality monitoring. *Sensors and Actuators B: Chemical*, 244(1):217–225, 2017.

[21] J. L. Anderson, J. K. Dixon, and J. F. Brennecke. Solubility of CO2, CH4, C2H6, C2H4, O2, and N2 in 1-Hexyl-3-methylpyridinium Bis(trifluoromethylsulfonyl)imide: Comparison to other ionic liquids. *Accounts of Chemical Research*, 40(11):1208–1216, 2007.

[22] K. A. Kurnia, C. M. Neves, M. G. Freire, L. M. Santos, and J. A. Coutinho. Comprehensive study on the impact of the cation alkyl side chain length on the solubility of water in ionic liquids. *Journal of Molecular Liquids*, 210(1):264–271, 2015.

[23] B. A. Voss, J. E. Bara, D. L. Gin, and R. D. Noble. Physically gelled ionic liquids: Solid membrane materials with liquidlike CO2 gas transport. *Chemistry of Materials*, 21(14):3027–3029, 2009.

[24] Y. Shimizu, Y. Ohte, Y. Yamamura, K. Saito, and T. Atake. Low-temperature heat capacity of room-temperature ionic liquid, 1-hexyl-3-methylimidazolium bis (trifluoromethylsulfonyl) imide. *The Journal of Physical Chemistry B*, 110(28):13970–13975, 2006.

[25] J. Valderrama and P. Robles. Critical properties, normal boiling temperatures, and acentric factors of fifty ionic liquids. *Industrial and Engineering Chemistry Research*, 46(4):1338–1344, 2007.

[26] R. D. Chirico, V. Diky, J. W. Magee, M. Frenkel, and K. N. Marsh. Thermodynamic and thermophysical properties of the reference ionic liquid: 1-hexyl-3-methylimidazolium bis[(trifluoromethyl) sulfonyl]amide (including mixtures). Part 2. Critical evaluation and recommended property values (IUPAC Technical Report). *Pure and Applied Chemistry*, 81(5):791–828, 2009.

[27] J. L. Anderson, J. K. Dixon, E. J. Maginn, and J. F. Brennecke. Measurement of SO2 solubility in ionic liquids. *The Journal of Physical Chemistry B*, 110(31):15059–15062, 2006.

[28] M. Klahn and A. Seduraman. What determines CO2 solubility in ionic liquids? A molecular simulation study. *The Journal of Physical Chemistry B*, 119(31):10066–10078, 2015.

[29] M. Partridge. Spectral processing software. Retrieved 23rd April 2017. https://github.com/MCeeP/SIR.

[30] D. Tosi. Review and analysis of peak tracking techniques for fiber Bragg grating sensors. *Sensors*, 17(10):2368, 2017.

[31] P. T. Nguyen, B. A. Voss, E. F. Wiesenauer, D. L. Gin, and R. D. Noble. Physically gelled room-temperature ionic liquid-based composite membranes for CO2/N2 separation: Effect of composition and thickness on membrane properties and performance. *Industrial and Engineering Chemistry Research*, 52(26):8812–8821, 2012.

[32] Z. Gu and Y. Xu. Design optimization of a long-period fiber grating with sol–gel coating for a gas sensor. *Measurement Science and Technology*, 18(11):3530, 2007.

[33] M. Faustini, B. Louis, P. A. Albouy, M. Kuemmel, and D. Grosso. Preparation of sol- gel films by dip-coating in extreme conditions. *The Journal of Physical Chemistry C*, 114(17):7637–7645, 2010.

[34] S. Korposh, S.-W. Lee, S. W. James, and R. P. Tatam. Refractive index sensitivity of fibre-optic long period gratings coated with SiO2 nanoparticle mesoporous thin films. *Measurement Science and Technology*, 22(7):1–10, 2011.

[35] S. W. James and R. P. Tatam. Fibre optic sensors with nano-structured coatings. *Journal of Optics A: Pure and Applied Optics*, 8(7):S430–S444, 2006.

[36] R. Charters, S. Staines, and R. Tatam. In-line fiber-optic components using Langmuir–Blodgett films. *Optics Letters*, 19(23):2036–2038, 1994.

[37] J. Cras, C. Rowe-Taitt, D. Nivens, and F. Ligler. Comparison of chemical cleaning methods of glass in preparation for silanization. *Biosensors and Bioelectronics*, 14(8-9):683–688, 1999.

[38] F. Canfarotta, A. Poma, A. Guerreiro, and S. Piletsky. Solid-phase synthesis of molecularly imprinted nanoparticles. *Nature Protocols*, 11(3):443, 2016.

[39] Y. Yuan and T. R. Lee. Contact angle and wetting properties. In *Surface Science Techniques*, pp. 3–34. Springer, 2013.

[40] D. Flinn, D. Guzonas, and R.-H. Yoon. Characterization of silica surfaces hydrophobized by octadecyltrichlorosilane. *Colloids and Surfaces A: Physicochemical and Engineering Aspects*, 87(3):163–176, 1994.

[41] G. T. Hermanson. *Bioconjugate Techniques*. Elsevier, London, UK, 3rd ed., 2013.

[42] C. Cheung, S. M. Topliss, S. W. James, and R. P. Tatam. Response of fiber-optic long-period gratings operating near the phase-matching turning point to the deposition of nanostructured coatings. *Journal of the Optical Society of America B*, 25(6):897–902, 2008.

[43] D. Grosso. How to exploit the full potential of the dip-coating process to better control film formation. *Journal of Materials Chemistry*, 21(43):17033–17038, 2011.

[44] Z. Wang, J. R. Heflin, R. H. Stolen, and S. Ramachandran. Analysis of optical response of long period fiber gratings to nm-thick thin-film coatings. *Optics Express*, 13(8):2808–2813, 2005.

[45] J. Hromadka, B. Tokay, S. W. James, and S. Korposh. Metal-organic framework thin films on a surface of optical fibre long period grating for chemical sensing. In *Optical Fiber Sensors Conference (OFS), 2017 25th*, pp. 1–4. IEEE, 2017.

[46] F. Di Francesco, N. Calisi, M. Creatini, B. Melai, P. Salvo, and C. Chiappe. Water sorption by anhydrous ionic liquids. *Green Chemistry*, 13(7):1712–1717, 2011.

[47] A.-L. Rollet, P. Porion, M. Vaultier, I. Billard, M. Deschamps, C. Bessada, and L. Jouvensal. Anomalous diffusion of water in [BMIM][TFSI] room-temperature ionic liquid. *The Journal of Physical Chemistry B*, 111(41):11888–11891, 2007.

[48] J.-T. Liang, H. Sun, and R. Seright. Why do gels reduce water permeability more than oil permeability? *SPE Reservoir Engineering*, 10(04):282–286, 1995.

[49] S. W. James and R. P. Tatam. Optical fibre long-period grating sensors: characteristics and application. *Measurement Science and Technology*, 14(5):R49–61, 2003.

Chapter 8

Conclusions and future work

During the course of this PhD project, a novel LPG-based CO_2 sensor using an ionic liquid deposition as the sensitive coating was developed. Since LPGs were an integral part of the sensing device, fabrication techniques to optimise the performance of these in-fibre elements were investigated. This chapter aims to summarise the key findings presented in this thesis and provide recommendations in which to extend the work presented here.

8.1 Summary

Initial work focussed upon assessing the repeatability of the overwrite LPG fabrication method to ensure the process was capable of repeatedly producing sensors with attenuation features at desired wavelengths. By creating LPGs with the same period, duty cycle, and total exposure time (6 cycles of 5 s), it was shown that it is possible to fabricate 3 LPGs that possessed attenuation band coupling to the LP_{14} mode with central wavelengths that were within ~4 nm of each other, a 6 nm improvement on previous work which explored the single exposure point-by-point method [1]. Furthermore, it was also demonstrated that the period of the LPG does not completely define the wavelength of attenuation bands, where two gratings of a slightly different period (113.0 μm and 113.2 μm) showed transmission spectra with attenuation features at the same wavelengths. This was achieved by exposing the LPG with a shorter period to more UV exposure cycles thus experiencing a larger refractive index modulation.

Using the overwrite method, 67 LPGs were fabricated with periods between 100 - 200 μm in optical fibre that possessed a short cut-off wavelength (620 nm) allowing

the features to be detected by a CCD spectrometer. The transmission data were subsequently displayed as an intensity plot in order to aid sensor design as it is possible to predict the period necessary to obtain an LPG with desired attenuation features. Moreover, this technique highlights additional features (e.g. 2^{nd} order coupling), which may not be so clearly identifiable via a single transmission spectrum. With the data mapped out as an intensity plot, all the PMTPs accessible for LPGs with a period in this range were clearly visible. LPG transmission data displayed in this manner is of particular use when designing LPGs. Although numerical modelling can typically be utilised for accurately predicting the presence of transmission features in standard telecommunication fibre (e.g. SMF28), LPGs that operate at the PMTP using non-standard optical fibre (e.g. PS750), or require the deposition of coatings where the thickness and refractive index is uncertain, are difficult to simulate accurately.

Following the identification of 2^{nd} order coupling features in the intensity plot which displayed sequential LPG transmission data, a theoretical and experimental investigation into the effects of the UV irradiation duty cycle during LPG fabrication was conducted, revealing that variations in this parameter determined which harmonic features were present in the transmission spectrum. It was demonstrated that an LPG fabricated with a 50% duty cycle maximised 1^{st} order coupling and did not possess features associated with 2^{nd} order coupling. However, producing an LPG with a 25% or 75% duty cyle created a grating which contained 2^{nd} order resonance bands with the greatest attenuation.

Previous work has exploited 2^{nd} order features for multi-parameter sensing [2] over a wavelength range of 600 - 1600 nm using an OSA. By utilising an LPG with a 181.5 μm period and a 25% duty cycle, it was shown here that a feature-rich spectrum which included 2^{nd} order attenuation bands was achievable within the wavelength range of a CCD spectrometer (550 - 1000 nm). Since CCD spectrometer-based interrogation is cheaper (in comparison to an OSA), the efficacy of multi-parameter sensing using the aforementioned LPG was evaluated. Following assessment of the sensitivity to environmental parameters (temperature, longitudinal strain, surrounding refractive index), the 1^{st} and 2^{nd} order attenuation features were numerically analysed for their feasibility to distinguish simultaneous parameters. Using a more rigorous numerical evaluation than [2], it was shown that accurate discrimination was not attainable via the use of 1^{st} and 2^{nd} order attenuation features associated with LP_{14} and LP_{22}, respectively.

To identify a suitable sensitive coating for the LPG CO_2 sensor, the feasibility of the

alkanoamine PEI was explored. This material demonstrates an affinity for CO_2 and has been utilised as an active sensing layer in previously cited devices [3]. Adopting the coating principle of LbL, PEI was deposited onto an LPG in a composite coating with SiO_2. It was expected that in the presence of CO_2 the coating would induce a detectable refractive index change. However, the PEI/SiO_2 coated LPG was extremely sensitive to variations in water vapour. As such, any response to CO_2 was ultimately masked by the influence of humidity.

Further investigation into an appropriate coating material resulted in the study of [C_6mim][Tf_2N]. Although this ionic liquid demonstrates CO_2 absorption [4], previous studies have not indicated if this uptake produces a refractive index change. Data presented here showed that a small refractive index alteration was induced from a subsequent 20% CO_2 exposure and that this change could be discerned by an LPG. Furthermore, this noted change was established to occur within 1 min of exposure. In order to apply [C_6mim][Tf_2N] to an optical fibre, the liquid was formed into a mechanically stable ionogel and a fibre coating system was developed based on the dip-coating technique. Initial inspection of the coated fibre revealed that the ionogel deposition displayed an inhomogeneous nature with a number of surface contamination issues. Through the use a methanol/HCl fibre wash and silanisation pre-treatment, the ionogel coating demonstrated a more consistent surface and thickness of 500 nm.

The [C_6mim][Tf_2N] coated LPG successfully responded to exposure of 20% CO_2, where this concentration produced an 8 nm wavelength shift with a response time of 90 s. Moreover, the CO_2 mediated change in the coating was easily reversible by decreasing the partial pressure of CO_2 allowing the sensor to return to baseline within 25 min. The ionogel coated LPG was also assessed for its sensitivity to temperature and humidity. Despite the fact that the coating did not influence the LPG's temperature sensitivity beyond inherent LPG values, the coated sensing element did demonstrate a humidity sensitivity of 0.275 nm·%$^{-1}$.

Finally, the overall aim of this project was to develop an LPG-based CO_2 sensor that could be operated in conjunction with an LPG breath ammonia sensor. As highlighted in Chapter 1, it was hoped the device would detect CO_2 in a concentration range of 0 - 15% with an accuracy of ±0.2% and a response time of <0.1 s. The CO_2 sensor created here demonstrated a response to 20% CO_2 in 90 s and was not however assessed in the desired concentration range. Nevertheless, based on the observed wavelength shift (8.3 nm) and the resolution of the spectrometer (130 pm), it is expected that the device would be able to detect a concentration of 1% (assuming a

linear response). It was also shown that the sensor did display a response to changing humidity, which would influence the device's CO_2 detection ability. In its current state, the CO_2 sensor does not meet the desired specification in order to fulfil the overall objective as CO_2 sensor suitable for breath analysis. However, a number of improvements and modifications have been suggested in Section 8.2 that would allow the CO_2 sensor designed here to achieve the overall objective.

Besides breath sensing, the device could be adapted and utilised in other applications, particularly those environments in which standard CO_2 sensors would not be able to access. These could include the detection of leaks in underground CO_2 storage reservoirs (where the sensor would be underground, allowing the instrumentation to remain on the surface) or to aid in mine safety (similarly exploiting the ability to have kilometres of fibre through mine shafts while keeping sensitive instruments at the entrance).

8.2 Future work

Although the main aim of the project, to develop an LPG-based CO_2 sensor, was achieved, a number of concepts and techniques presented here would benefit from further investigation and bring the sensor closer to the required specification.

8.2.1 LPG operation

During the fabrication of LPGs that contain 2^{nd} order resonance bands, the selection of an appropriate period ensures these features are distinct from the 1^{st} order attenuation bands. However, if the fibre is subjected to a significant environmental perturbation, i.e. a large change in temperature, the 2^{nd} order resonance band experiences a correspondingly large wavelength shift which often causes the band to merge with less sensitive 1^{st} order attenuation features, ultimately creating difficulties regarding wavelength tracking. As can be seen in Fig. 8.1, as the 2^{nd} order band coalesces with the 1^{st} order feature, the latter displays an intensity change. This alteration is most noticeable at the beginning and end of the attenuation band (Fig. 8.1), therefore, by developing a numerical method which compared the change in intensities at these regions, the wavelength of the merging feature could be more accurately determined.

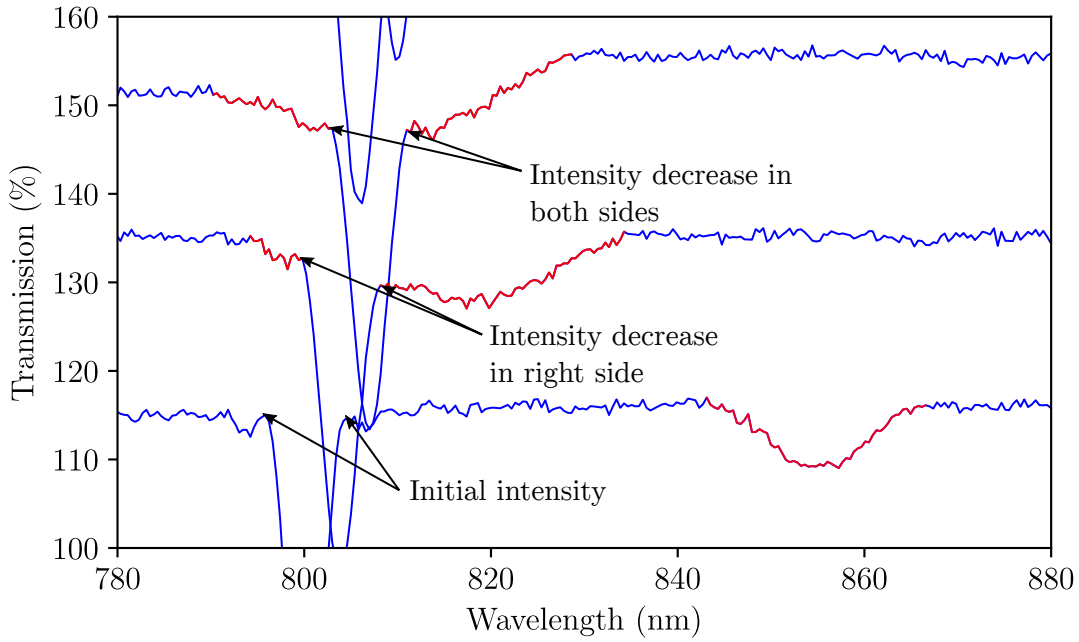

Figure 8.1: A portion of the offset transmission spectra from Fig. 5.9 highlighting the intensity decrease in 1^{st} order attenuation bands observed during the merging of 2^{nd} order resonance features. 2^{nd} order attenuation bands highlighted in red

8.2.2 Sensor fabrication

As mentioned in Chapter 7, the thickness of the ionogel coating applied to an optical fibre is dependant on the speed with which it is withdrawn through the solution. Although preliminary work was conducted on this aspect of the ionogel coating system (see Fig. 7.24), the relationship between withdrawal speed and coating thickness was not explored thoroughly. In a standard dip-coating process, the deposition material is suspended in a solvent and the correlation between withdrawal speed and coating thickness takes the form of a parabola, where a minimal deposition thickness can be obtained by using withdrawal speeds centred at the minimum [5]. However, it is unclear whether the ionogel will display a similar behaviour as this coating solidifies through a reduction in temperature rather than via an evaporation of the solvent. Therefore, by investigating the effect of slower withdrawal speeds (less than 18 mm·min^{-1}) on coating thickness, a greater understanding of the relationship between these variables can be established. Furthermore, this knowledge can be used to determine the speed at which a minimal coating thickness can be acquired. This is of particular importance as it is speculated that a thinner coating would produce a quicker response/recovery time via faster diffusion of CO_2 towards the coating region that is able to interact with the evanescent field.

The coating system developed in this thesis is very much of a prototype nature, thus the reproducibility and quality of the coating can vary between depositions. There a number of modifications which may improve the repeatability of the ionogel coating. Firstly, a technique which ensures the fibre is withdrawn perpendicular to the surface of the ionogel. This would produce an ionogel coating that possessed a consistent thickness for the entire circumference of the fibre. Although every effort was made to align the ionogel reservoir with the dip-coated arm (see Fig. 7.13 for details of the coating system) in such a way that the fibre would be withdrawn perpendicularly, this process was conducted by eye, therefore slight misalignment errors were inevitable. By using cameras that monitor the x- and y-plane prior to coating (Fig. 8.2 (a)), it would be possible to significantly reduce any discrepancies in perpendicular alignment.

Secondly, by reducing the temperature gradient between the ionogel reservoir and the ambient environment, the slower cooling effect experienced by the coating may influence the surface characteristics. This could be achieved by placing a copper sleeve round the fibre which would be seated on the aluminium block (Fig. 8.2 (b)). The high thermal conductivity of copper would create a passive temperature gradient which would be cooler at the distal end of the tube in relation to the aluminium block.

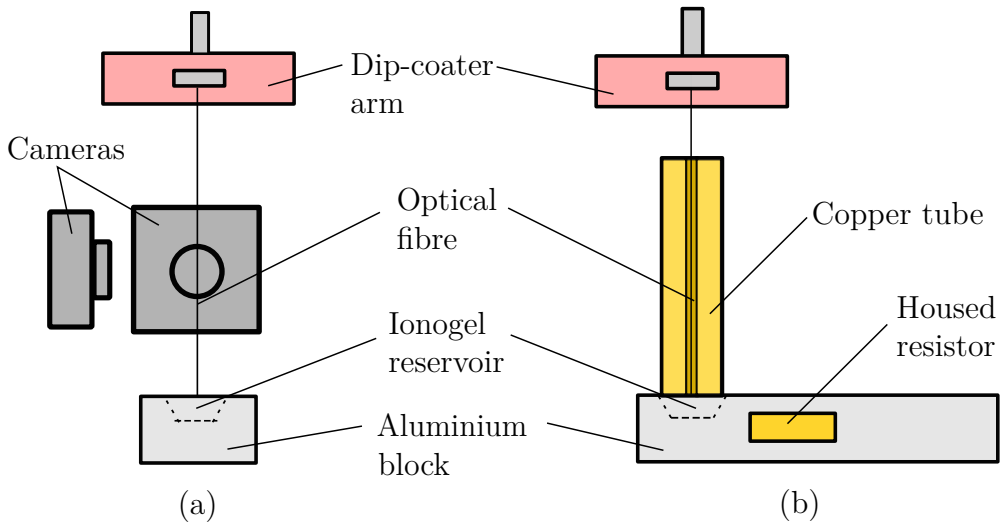

Figure 8.2: Illustration of the proposed improvements to the ionogel coating system for fibre alignment (a) and temperature offset (b)

8.2.3 Sensor performance

The detection of 20% CO_2 was achieved using the ionogel sensor in Chapter 7. While this result demonstrates that the ionogel coated LPG could be employed as a CO_2 sensing element, it is important from a sensor perspective that the LoD of this device be ascertained. The LoD is a key defining parameter of any sensor and helps determine the suitability of the device to particular applications. This could be accomplished by producing a concentration curve through measuring the wavelength response to decreasing concentrations of CO_2 and calculating the LoD using LoD = $3SD/b$, where b is the gradient of the calibration curve [6].

It has been shown in Chapter 7 that the ionogel sensor demonstrated a repeatable response to 3 cycles of CO_2 and SA. While this result indicates that the sensor has short-term stability (<2 h), it would be necessary to assess the device over a longer period of time. Initially, the stability of the ionogel coated LPG could be tested in a consistent concentration of CO_2 for a month. This would provide data on whether the coating slowly absorbs CO_2 over an extended period of time which was not noticeable in the short cycles (25 min) presented here. Furthermore, repeating the CO_2/SA cyclic experiment for a greater duration (>1 month) would highlight if any hysteresis occurs which was not witnessed in the short duration.

The CO_2 sensor developed here employed a single LPG as the transducing element, which simplified the fabrication procedure allowing the ionogel coating process and sensor characterisation to be prioritised. However, attenuation bands that are generated in the transmission spectrum of single LPGs typically possess minima with 1-2 nm width (up to 20 nm for features operating at the PMTP), creating issues regarding identification of the precise central wavelength of the resonance features necessary for sensing. Although this is does not pose an issue for sensing devices that require only course resolution, the increased band-width of the resonance features however limit the ability of the device to detect small wavelength shifts. Through the use of cascaded LPGs (see Section 3.6.2 for a description) this issue could be alleviated. The Mach-Zehnder interferometer created by the in-series LPGs produces attenuation features that contain a number of interference fringes, therefore providing finer features (in comparison to the relatively broad attenuation band) in which to monitor, ultimately improving the resolution of the device.

The humidity and temperature response displayed by the ionogel sensor severely affects the capability of the device for use in a practical situation. In order to remove the response to these environmental parameters the use of additional LPGs could be multiplexed in series to simultaneously measure temperature, humidity and CO_2.

Utilising a scheme proposed by Hromadka *et al.* [7], each LPG is fabricated with a slightly different period to facilitate wavelength division multiplexing and where individual gratings monitor only one measurand. Using the information gained from the LPGs responsible for humidity and temperature, it would be possible to adjust the response of the LPG designated for CO_2 sensing to compensate for these parameters.

In addition to the cross-sensitivity of humidity and temperature, $[C_6mim][Tf_2N]$ has also been demonstrated to show an affinity for other gases [8]. The solubility of CO_2 in $[C_6mim][Tf_2N]$ as an individual gas far surpasses that of other molecules (CH_4, O_2, N_2) [8], however there is evidence to suggest that the presence of CO_2 may enhance the uptake of these less soluble gases [9]. Furthermore, the solubility of hydrogen sulfide has been shown to be considerably larger in ionic liquids with the $[Tf_2N]^-$ anion [10]. Therefore, a number of experiments focussing on the cross-sensitivity of the ionogel sensor outlined in Chapter 7 would be necessary prior to assessment of the device in a realistic environment, where these gases would be present. Initially, the sensor should be exposed to each gas individually to determine if a response is elicited. This should be followed with a test to assess whether a mixture of CO_2 and each gas produces a synergistic mix which enhances the uptake of the cross-sensitive gas.

The creation of the ionogel CO_2 sensor presented in this thesis has demonstrated the capability of ionic liquids to be utilised as active coatings which display a refractive index change in response to a particular measurand. Moreover, this change was still noticeable following the mechanical stabilisation of the ionic liquid via the use of a gelling agent. These findings reveal the possibility that the ionogel used here could be adopted for other sensing schemes which operate via the detection of refractive index alterations. For example, use in an SPR CO_2 sensor where the ionogel could be deposited onto the intermediate metallic layer or coated onto optical fibre tapers. Furthermore, the use of ionogels for sensing could be extended for the detection of other analytes. Ionic liquids such as 1-methyl-3-butylimidazolium hexaflourophosphate are able to absorb VOCs [11]. Although the use of 12-hydroxystearic acid is only suitable for creating ionogels from imidazolium-based ionic liquids with large hydrophobic chains [12], the use of aspartame-based LMOGs has been shown to gel a greater number of ionic liquids [13]. The ability of these molten salts to absorb various analytes and be mechanically stabilised through simple LMOGs indicates that various new sensors could be potentially created through the incorporation of ionic liquids.

8.3 References

[1] M. Partridge, S. W. James, J. H. Barrington, and R. P. Tatam. Overwrite fabrication and tuning of long period gratings. *Optics Express*, 24(20):22345–22356, 2016.

[2] T. Allsop, L. Zhang, D. J. Webb, and I. Bennion. Discrimination between strain and temperature effects using first and second-order diffraction from a long-period grating. *Optics Communications*, 211(1-6):103–108, 2002.

[3] A. Star, T.-R. Han, V. Joshi, J.-C. Gabriel, and G. Grüner. Nanoelectronic carbon dioxide sensors. *Advanced Materials*, 16(22):2049–2052, 2004.

[4] C. Cadena, J. L. Anthony, J. K. Shah, T. I. Morrow, J. F. Brennecke, and E. J. Maginn. Why is CO2 so soluble in imidazolium-based ionic liquids? *Journal of the American Chemical Society*, 126(16):5300–5308, 2004.

[5] M. Faustini, B. Louis, P. A. Albouy, M. Kuemmel, and D. Grosso. Preparation of sol- gel films by dip-coating in extreme conditions. *The Journal of Physical Chemistry C*, 114(17):7637–7645, 2010.

[6] S. Korposh, S. W. James, R. P. Tatam, and S.-W. Lee. Fibre-optic chemical sensor approaches based on nanoassembled thin films: A challenge to future sensor technology. In *Current Developments in Optical Fiber Technology*. InTech, 2013.

[7] J. Hromadka, B. Tokay, S. W. James, and S. Korposh. Metal-organic framework thin films on a surface of optical fibre long period grating for chemical sensing. In *Optical Fiber Sensors Conference (OFS), 2017 25th*, pp. 1–4. IEEE, 2017.

[8] J. L. Anderson, J. K. Dixon, and J. F. Brennecke. Solubility of CO2, CH4, C2H6, C2H4, O2, and N2 in 1-Hexyl-3-methylpyridinium Bis(trifluoromethylsulfonyl)imide: Comparison to other ionic liquids. *Accounts of Chemical Research*, 40(11):1208–1216, 2007.

[9] D. G. Hert, J. L. Anderson, S. N. Aki, and J. F. Brennecke. Enhancement of oxygen and methane solubility in 1-hexyl-3-methylimidazolium bis(trifluoromethylsulfonyl)imide using carbon dioxide. *Chemical Communications*, 0(1):2603–2605, 2005.

[10] C. S. Pomelli, C. Chiappe, A. Vidis, G. Laurenczy, and P. J. Dyson. Influence of the interaction between hydrogen sulfide and ionic liquids on solubility:

Experimental and theoretical investigation. *The Journal of Physical Chemistry B*, 111(45):13014–13019, 2007.

[11] G. Quijano, A. Couvert, A. Amrane, G. Darracq, C. Couriol, P. Le Cloirec, L. Paquin, and D. Carrié. Potential of ionic liquids for VOC absorption and biodegradation in multiphase systems. *Chemical Engineering Science*, 66(12):2707–2712, 2011.

[12] B. A. Voss, J. E. Bara, D. L. Gin, and R. D. Noble. Physically gelled ionic liquids: Solid membrane materials with liquidlike CO2 gas transport. *Chemistry of Materials*, 21(14):3027–3029, 2009.

[13] P. T. Nguyen, B. A. Voss, E. F. Wiesenauer, D. L. Gin, and R. D. Noble. Physically gelled room-temperature ionic liquid-based composite membranes for CO2/N2 separation: Effect of composition and thickness on membrane properties and performance. *Industrial and Engineering Chemistry Research*, 52(26):8812–8821, 2012.

List of publications and outcomes

Journal Papers

1. J. H. Barrington, M. Partridge, S. W. James and R. P. Tatam. The effect of UV irradiation duty cycle on the 2^{nd} harmonic coupling efficiency in optical fiber long period gratings. *Optics & Laser Technology*, 109:227-232, 2018.
2. M. Partridge, S. W. James, J. H. Barrington and R. P. Tatam. Overwrite fabrication and tuning of long period gratings. *Optics Express*, 24(20):22345-22358, 2016.

Peer-Reviewed Conference Papers

3. J. H. Barrington, M. Partridge, S. W. James and R. P. Tatam. Experimental determination of 2^{nd} order phase matching turning points in long period gratings. *IEEE Sensors 2016, Florida, US*, 2016.

Conference Participation

6. J. H. Barrington, M. Partridge, S. W. James and R. P. Tatam. A novel approach to applying ionic liquids to the surface of optical fibres. *Ultra precision student conference, Cranfield, UK*, (Poster presentation), 2017.
7. J. H. Barrington, M. Partridge, S. W. James and R. P. Tatam. A novel approach to applying ionic liquids to the surface of optical fibres. *Ultra precision steering meeting, Cambridge, UK*, (Poster presentation), 2017.
8. J. H. Barrington, M. Partridge, S. W. James and R. P. Tatam. A precision fibre optic CO_2 sensor for gas analysis. *Rising Stars in Gas Sensing: The early career researchers meeting. 64^{th} Gas Analysis and Sensing Group Colloquium, Cranfield, UK*, (Poster presentation), 2016.

Appendix A

Python script for LPG phase matching curves

The following Python script was used to generate the phase matching curves depicted in Chapters 3 and 5.

```
from __future__ import division
import numpy as np
import scipy.special as sp
import matplotlib.pyplot as plt

### PS750 parameters
n1 = 1.4583
n2 = 1.4533
n3 = 1
r1 = 2.0e-6
r2 = 62.6e-6
n_min = 1.42
n_max = n1 - 1e-5

layers = 3
modes = 30
points = 20000
lambda_points = 400
lambda_min = 620e-9
lambda_max = 1100e-9
### wavelength range from lambda_min to lambda_max with
```

```
### lambda_points number of points
lambda_range = np.linspace(lambda_min, lambda_max, lambda_points)
### range of refractive index values to identify the effective
### refractive index for every wavelength
n = np.linspace(n_max, n_min, points)

### Function to calculate the effective refractive index for
### the core and cladding for a given wavelength
def zeros_calc(n, n1, n2, n3, r1, r2, wavelength):
    ko = 2*np.pi/wavelength
    beta = ko*n
    core_clad = []
    clad_air = []
    v = 0
    for y in beta:
        #### Calculating core and cladding boundries
        w1 = np.sqrt(np.abs(ko**2*n1**2-y**2))
        w2 = np.sqrt(np.abs(ko**2*n2**2-y**2))

        #### Numerals indicate from which layer e.g. dJ21 from
        #### cladding (2) to core (1)
        dJ11 = sp.jvp(v, (w1 * r1), 1)
        dY11 = sp.yvp(v, (w1 * r1), 1)
        dI11 = sp.ivp(v, (w1 * r1), 1)
        dK11 = sp.kvp(v, (w1 * r1), 1)
        dJ21 = sp.jvp(v, (w2 * r1), 1)
        dY21 = sp.yvp(v, (w2 * r1), 1)
        dI21 = sp.ivp(v, (w2 * r1), 1)
        dK21 = sp.kvp(v, (w2 * r1), 1)
        if y < ko*n1:
            Q1 = 2/(np.pi*r1)
            C11 = sp.j0(w1*r1)
            D11 = sp.y0(w1*r1)
            dC11 = dJ11
            dD11 = dY11
        else:
            Q1 = -1/(r1)
```

```
        C11 = sp.i0(w1*r1)
        D11 = sp.k0(w1*r1)
        dC11 = dI11
        dD11 = dK11

    if y < ko*n2:
        C21 = sp.j0(w2*r1)
        D21 = sp.y0(w2*r1)
        dC21 = dJ21
        dD21 = dY21
    else:
        C21 = sp.i0(w2*r1)
        D21 = sp.k0(w2*r1)
        dC21 = dI21
        dD21 = dK21

    m11 = (w1*dD11*C21-w2*D11*dC21)/Q1
    m12 = (w1*dD11*D21-w2*D11*dD21)/Q1
    m21 = (-w1*dC11*C21+w2*C11*dC21)/Q1
    m22 = (-w1*dC11*D21+w2*C11*dD21)/Q1

    M12 = np.matrix([[m11, m12], [m21, m22]])
    core_clad.append(M12[1, 1])
    ### Calculating cladding (2) and air (3) boundaries
    w3 = np.sqrt(np.abs(ko**2*n3**2-y**2))
    dJ22 = sp.jvp(v, (w2*r2), 1)
    dY22 = sp.yvp(v, (w2*r2), 1)
    dI22 = sp.ivp(v, (w2*r2), 1)
    dK22 = sp.kvp(v, (w2*r2), 1)
    dJ32 = sp.jvp(v, (w3*r2), 1)
    dY32 = sp.yvp(v, (w3*r2), 1)
    dI32 = sp.ivp(v, (w3*r2), 1)
    dK32 = sp.kvp(v, (w3*r2), 1)

    if y < ko*n2:
        Q2 = 2/(np.pi*r2)
        C22 = sp.j0(w2*r2)
```

```
        D22 = sp.y0(w2*r2)
        dC22 = dJ22
        dD22 = dY22

    else:
        Q2 = -1/(r2)
        C22 = sp.i0(w2*r2)
        D22 = sp.k0(w2*r2)
        dC22 = dI22
        dD22 = dK22

    if y < ko*n3:
        C32 = sp.j0(w3*r2)
        D32 = sp.y0(w3*r2)
        dC32 = dJ32
        dD32 = dY32

    else:
        C32 = sp.i0(w3*r2)
        D32 = sp.k0(w3*r2)
        dC32 = dI32
        dD32 = dK32

    m2_22 = (w2*dD22*C32-w3*D22*dC32)/Q2
    m2_23 = (w2*dD22*D32-w3*D22*dD32)/Q2
    m2_32 = (-w2*dC22*C32+w3*C22*dC32)/Q2
    m2_33 = (-w2*dC22*D32+w3*C22*dD32)/Q2

    M23 = np.matrix([[m2_22, m2_23], [m2_32, m2_33]])

    M = np.dot(M12, M23)
    ### For a finite fields M[1, 1] must equal 0
    clad_air.append(M[1, 1])
    ### Searches for zero crossing points returning the
    ### index of this value
    zeros_core = np.where(np.diff(np.sign(core_clad)))[0]
    zeros_clad = np.where(np.diff(np.sign(clad_air)))[0]
```

```
        clad_neff = []
        core_neff = n[zeros_core[0]]
        ### Adds to the list clad_neff the refractive
        ### index value based on the index values from zeros_clad
        for i in zeros_clad:
            clad_neff.append(n[i])
    return beta, core_neff, clad_neff, core_clad, clad_air, ko

### Function to return cladding effective refractive indices for
### all defined wavelengths and plot dispersion curves for required
### modes
def solution():
    print("Calculating zeros of claddding coefficient")
    clad_neff = []
    ### Calculates cladding effective refractive index for each
    ### wavelength and adds to the list clad_neff
    for i in lambda_range:
        clad_modes = zeros_calc(n, n1, n2, n3, r1, r2, i)
        clad_neff.append(clad_modes[2])
    ### Defines plot parameters
    fig = plt.figure("Dispersion curves",
    facecolor="white", edgecolor="white")
    ax = fig.add_subplot(1, 1, 1)
    ax.set_xlabel("Wavelength (nm)")
    ax.set_ylabel("Effective refractive index")
    plt.hold(True)
    ### Plots dispersion curves for defined number of modes
    for i in range(modes):
        ax.plot(lambda_range*1e9, clad_neff[i])
    # plt.show()
    return clad_neff

### Function to generate phase matching curves
def phase_matching_curve_plots(diffraction_order, core_neff, clad_neff):
    print("Plotting phase matching curves")
    ### Defines plot parameters
    fig = plt.figure("Phase matching curves",
```

```
    facecolor="white", edgecolor="white")
    ax = fig.add_subplot(1, 1, 1)
    ax.set_xlabel("Wavelength (nm)", fontsize=18)
    ax.set_ylabel("Period ($\mu$m)", fontsize=18)
    ax.tick_params(labelsize=14)
    ### Generates 1st order phase matching curves
    for i in range(modes):
        first_period = (lambda_range*diffraction_order /
                        (core_neff-clad_neff[i]))
        ax.plot(lambda_range*1e9, first_period*1e6, color='blue')
    ### Uncomment for addition of 2nd order phase matching curves
    # for i in range(modes):
    #     second_period = (lambda_range*(diffraction_order+1) /
    #                      (core_neff-clad_neff[i]))
    #     ax.plot(lambda_range*1e9, second_period*1e6, color='red')
    ### Uncomment if legend is required
    # ax.legend(handles, ylabels)
    # ax.legend(loc="upper right", fontsize=12)

plt.show()
return

### Defines the effective refractive index for all cladding modes
### as n_eff
n_eff = solution()
### Calls the phase matching curve function for core effective
### refractive index (n_eff[0]) and cladding effective refractive
### index (n_eff[1:])
phase_matching_curve_plots(1, n_eff[0], n_eff[1:])
```

Appendix B

Python script for square-wave Fourier analysis

In Chapter 6, a Fourier transform was applied to a square-wave, based on the UV irradiation pattern generated by the point-by-point method, to identify the harmonic content of this waveform with a 50% duty cycle. To achieve this, the following Python script was written which resulted in a single graph depicting the harmonics present in a square wave possessing a 50% duty cycle.

```
from scipy import signal
import numpy as np
import matplotlib.pyplot as plt

duty = 0.5
period = 0.001
length = 1000

### Resolution of square waveform
per = np.linspace(-length/2,length/2,np.int(length/period))
### Produces a square wave with a 50% duty cycle
sq = 1+(signal.square(2*np.pi*per*length/(period), duty))
### Applies an FFT to the square wave
ft = np.fft.fft(sq)
### Centres the transform
ftshift = np.fft.fftshift(ft)
### Plot parameters for the single plot for 50% duty cycle
fig = plt.figure(facecolor='white', edgecolor='white')
```

```
ax = fig.add_subplot(111)
ax.set_xlabel('Harmonic number', fontsize=18)
ax.set_ylabel('Amplitude (a.u.)', fontsize=18)
ax.set_xlim(-3.5, 3.5)
ax.tick_params(labelsize=14)
plt.plot(per, np.abs(ftshift))

plt.show()
```

Appendix C

Python script for harmonic intensity dependence on duty cycle in a square wave

To identify the influence duty cycle has on the generation of harmonics in a square wave, the following Python script was implemented in Chapter 6 to produce a single graph which shows harmonic intensity as a function of duty cycle.

```
from scipy import signal
import numpy as np
import matplotlib.pyplot as plt

duty = np.linspace(0, 1, 1001)
period = 0.01
length = 100

### Resolution of square waveform
per = np.linspace(-length/2,length/2,np.int(length/period))

ax.xaxis.set_major_locator(plt.MaxNLocator(12))

### Identifies the index of the 1st - 3rd harmonics
first_index = np.ravel(np.where(per>1))[0]
#print(first_index)
scnd_index = np.ravel(np.where(per>2))[0]
#print(scnd_index)
```

```
third_index = np.ravel(np.where(per>3))[0]
scnd_order = []
first_order = []
third_order = []

### Using the index found above, the value is applied to find
### the intensity of each required harmonic for every duty cycle
### iteration and added to their designated list
for dc in duty:
    sq = 1+(signal.square(2*np.pi*per*length/(period), dc))
    ft = np.fft.fft(sq)
    ftshift = np.fft.fftshift(ft)
    first_order.append(np.abs(ftshift[first_index]))
    scnd_order.append(np.abs(ftshift[scnd_index]))
    third_order.append(np.abs(ftshift[third_index]))

### Parameters for plotting area
fig = plt.figure(facecolor='white', edgecolor='white')
ax = fig.add_subplot(111)
ax.set_xlabel('Duty cycle (\%)', fontsize=18)
ax.set_ylabel('Intensity (a.u.)', fontsize=18)
ax.tick_params(labelsize=14)
y_ticks = [0, 10, 20, 30, 40, 50, 60]

### Plots all harmonic lists on a single plot
ax.plot(duty*100, first_order, label='1$^{st}$ order')
ax.plot(duty*100, scnd_order, label='2$^{nd}$ order')
ax.plot(duty*100, third_order, label='3$^{rd}$ order')
### Adds dotted lines for visual aid
plt.axvline(25, color='gray', linestyle=':')
plt.axvline(50, color='gray', linestyle=':')
plt.axvline(75, color='gray', linestyle=':')
### Applies a legend
handles, labels = ax.get_legend_handles_labels()
ax.legend(handles, labels)
ax.legend(loc='upper right', fontsize=14)
plt.show()
```

Appendix D

Calculation of fibre strain induced through aluminium frame thermal expansion

In order to ensure the LPG remained under tension during the temperature characterisation in Section 6.2.1, the fibre was attached to an aluminium frame. Nevertheless, the frame would expand with an increase in temperature, thereby applying additional strain to the fibre. The following calculation was used to identify the magnitude of this strain (by extension the maximal wavelength shift) and whether this would significantly influence temperature characterisation.

Initially, the change in length of the alumiunum frame (mm), ΔL, was calculated, assuming the frame was composed of pure aluminium, using [1],

$$\Delta L = \alpha L \Delta T, \tag{D.1}$$

where α is the approximate thermal expansion coefficient of aluminium (24×10^{-6} [1]), L is the initial length of the aluminium frame (mm) at 25°C, and ΔT is the change in temperature (K). Assuming the fibre did not slip in the frame and experienced the same ΔL, the applied strain, ϵ, was determined by [2],

$$\epsilon = \frac{\Delta L}{L} \tag{D.2}$$

D.1 References

[1] P. A. Tipler and G. Mosca. *Physics for Scientists and Engineers with Modern Physics*. Freeman, New York, 6th ed., 2008.

[2] N. Ni, C. Chan, X. Dong, J. Sun, and P. Shum. Cavity ring-down long-period fibre grating strain sensor. *Measurement Science and Technology*, 18(10):3135, 2007.